



**HAL**  
open science

# Propagation of light waves in correlated disordered media: density of states, transport, localisation

Romain J, M Monsarrat

► **To cite this version:**

Romain J, M Monsarrat. Propagation of light waves in correlated disordered media: density of states, transport, localisation. Disordered Systems and Neural Networks [cond-mat.dis-nn]. Université PSL, 2022. English. NNT: . tel-03765743

**HAL Id: tel-03765743**

**<https://hal.archives-ouvertes.fr/tel-03765743>**

Submitted on 31 Aug 2022

**HAL** is a multi-disciplinary open access archive for the deposit and dissemination of scientific research documents, whether they are published or not. The documents may come from teaching and research institutions in France or abroad, or from public or private research centers.

L'archive ouverte pluridisciplinaire **HAL**, est destinée au dépôt et à la diffusion de documents scientifiques de niveau recherche, publiés ou non, émanant des établissements d'enseignement et de recherche français ou étrangers, des laboratoires publics ou privés.

**THÈSE DE DOCTORAT**  
**DE L'UNIVERSITÉ PSL**

Préparée à l'Institut Langevin, ESPCI Paris - PSL, CNRS

**Propagation d'ondes lumineuses en milieux désordonnés  
corrélés : densité d'états, transport, localisation.**

Propagation of light waves in correlated disordered media:  
density of states, transport, localisation

Soutenue par

**Romain MONSARRAT**

Le 14 mars 2022

Directeur de thèse

**Arnaud TOURIN**

Encadrants de thèse

**Arthur GOETSCHY**  
**Romain PIERRAT**

École doctorale n°564

**Physique en Île-de-France**

Spécialité

**Physique**

Composition du jury :

Fabrice MORTESSAGNE Professeur, INPHYNI, Université Côte d'Azur	<i>Rapporteur</i>
Sergey SKIPETROV Directeur de recherche CNRS, LPMCM, Université Grenoble Alpes	<i>Rapporteur</i>
Jacqueline BLOCH Directrice de recherche CNRS, C2N, Université Paris-Saclay	<i>Examinatrice</i>
Dominique DELANDE Directeur de recherche CNRS, LKB, ENS - PSL, Sorbonne Université	<i>Président du jury</i>
Arnaud TOURIN Professeur, Institut Langevin, ESPCI Paris - PSL	<i>Directeur de thèse</i>
Arthur GOETSCHY Maître de conférence, Institut Langevin, ESPCI Paris - PSL	<i>Co-directeur de thèse</i>



# Remerciements

La thèse de doctorat présentée dans ce manuscrit n'est évidemment pas un travail purement personnel et de nombreuses personnes ont contribué de près ou de loin à cet ambitieux projet. Je tiens à remercier toutes les personnes qui, par leur contribution scientifique, technique ou humaine, ont permis la réalisation de ce travail.

La priorité est donnée à mes directeurs de thèse et à mes encadrants. Tout d'abord Arthur Goetschy et Romain Pierrat, qui m'ont proposé de travailler sur ce vaste sujet qu'est la propagation de la lumière dans des milieux ni complètement ordonnés, ni complètement désordonnés. Travailler avec eux a été très enrichissant, Arthur est un jeune chercheur brillant et très exigeant, mais toujours disponible pour échanger, parfois avec acharnement, et approfondir la compréhension physique d'un problème. Romain, numéricien autodidacte, qui avait déjà une expérience dans le domaine des milieux partiellement ordonnés, a profité de cette expérience pour me former aux méthodes numériques sur un cluster. Je garderai en mémoire son impressionnante capacité à voir en moins de 10 secondes la source d'un problème qui pouvait m'occuper pendant plusieurs jours, ou les nombreuses fois où j'ai interrompu son après-midi à l'improviste pour lui montrer avec enthousiasme de nouveaux résultats souvent trop frais. Je leur suis reconnaissant à tous les deux de m'avoir formé, et de m'avoir laissé une réelle liberté quant à l'orientation que je voulais donner à ce projet et aux différents axes explorés, même si cela était parfois déstabilisant.

J'ai également eu la chance d'avoir Arnaud Tourin en tant que directeur de thèse. Sa participation, initialement pour un besoin d'Habilitation à Diriger des Recherches, s'est avérée très intéressante tant sur le plan scientifique que sur le plan humain. Sa grande expertise en acoustique a apporté un regard extérieur et une ouverture sur des communautés qui nous étaient inconnues. Malgré son rôle de directeur de l'Institut Langevin, il reste disponible et désireux d'améliorer le quotidien du laboratoire. L'avoir comme directeur de thèse a aussi eu l'avantage d'avoir quelques réunions de travail au restaurant, ce qui est un beau bonus !

Poussé à la fois par un besoin de nouveauté et une certaine lassitude potentiellement liée à l'année 2020 plutôt difficile, j'ai eu l'occasion de travailler avec Fabrice Lemoult sur une application expérimentale de mes recherches. Je tiens à le remercier d'avoir consacré son temps à former un vulgaire théoricien à l'expérimentation en micro-ondes et je tiens à souligner son dynamisme, sa disponibilité et sa bonne humeur, en plus de ses grandes qualités de chercheur.

Je tiens également à remercier le groupe MeTheo et en particulier Rémi Carminati pour ses contributions techniques, les discussions intéressantes, et pour avoir maintenu le lien en période de confinement.

Je remercie également tous les membres techniques et administratifs de l'Institut Langevin pour leur soutien et leur sympathie.

Je remercie Fabrice Mortessagne et Sergey Skipetrov pour avoir rapporté ma thèse ainsi que Jacqueline Bloch et Dominique Delande pour avoir accepté de participer à ce prestigieux jury de thèse.

Une immense pensée va évidemment aux doctorants de l'Institut parmi lesquels je me suis

---

fait de vrais amis. J'y ai rencontré des personnes brillantes, sur le plan scientifique, mais aussi sur le plan humain. J'ai une estime particulière pour les membres passés ou présents du bureau R32 dans lequel j'ai passé plus de 3 ans : Clément R.-R. qui est parti trop tôt, Léo, Margaux, Mathieu, Kassandra, Loubnan, Maximilian, Clément dB., ... mais aussi certains membres des bureaux R31 et R33 où j'ai pu passer une partie importante de mon temps à discuter de science ou non : Benjamin, Chloé, Paul, Jules, Maxime, François, Guillaume, Alexandre, Arthur, Ahmed, Flavien, Hussam, Ulysse, ... Une pensée particulière va à Guillaume sans qui la thèse aurait été beaucoup moins drôle, mais aussi pour son soutien, notamment pour m'avoir évité de me retrouver à la rue avant la soutenance. Enfin, je te remercie, Jeanne, tu fais vraiment partie des belles rencontres de la thèse, elle n'aurait pas été la même sans toi. La vie à l'Institut Langevin est ponctuée de nombreux moments de convivialité particulièrement nécessaires, entre les pots ou les simples vendredis soirs passés "Aux Arènes". Pour tout cela, je remercie l'Institut Langevin.

Par ailleurs, je peux aussi compter sur mes amis de l'ESPCI qui sont restés pour une bonne partie en thèse : Alexandre, Bruno, J.-C., Victor, Vincent, Lucas, ... À la famille de la pression et plus particulièrement Cédric, Juliette et Victor. Enfin, je pense aussi à mes amis de Strasbourg et en particulier à Aline.

Outre la vie parisienne, j'ai la chance d'être soutenu par une famille aimante. Bien évidemment, mes parents qui m'ont soutenu lorsque j'étais engagé dans des études loin de chez moi. Malgré mon épanouissement dans cet environnement, je prends toujours beaucoup, et peut-être de plus en plus, de plaisir à revenir à la maison et pour cela je les remercie. Je pense aussi à mes grands-parents qui n'ont pas pu faire le déplacement pour la soutenance mais qui m'ont toujours accompagné, à mon frère et ma sœur ainsi qu'à ma marraine, qui ont fait tout leur possible pour assister à ma défense : pour tout cela, je les remercie.

Le dernier mot revient à Timothé, qui m'a soutenu dans les moments difficiles, mais qui était aussi là pour célébrer les bons moments, merci.

# Contents

<b>General introduction</b>	<b>7</b>
<b>1 Light in resonant spatially correlated media</b>	<b>11</b>
1.1 Resonant behaviour . . . . .	11
1.2 Introduction to scattering . . . . .	12
1.2.1 Scattering by individual particles . . . . .	12
1.2.2 Mean free path and transport . . . . .	13
1.3 Multiple scattering theory . . . . .	15
1.3.1 Green's formalism . . . . .	15
1.3.2 Scattering by an inhomogeneity and Lippmann-Schwinger equation . .	15
1.3.3 Scattering by inhomogeneities and Dyson equation . . . . .	17
1.3.4 Evaluation of the scattering length and transport regimes at low density	19
1.4 From the Bethe-Salpeter equation to the diffusion equation . . . . .	20
1.5 A fully microscopic description: the coupled dipoles method . . . . .	23
1.5.1 General approach . . . . .	23
1.5.2 Examples with two dipoles . . . . .	25
1.5.3 Example with $N \gg 2$ , density of states and inverse participation ratio	25
1.6 Introduction to Anderson localisation . . . . .	27
1.6.1 Weak localisation corrections . . . . .	27
1.6.2 Self-consistent approach to Anderson Localisation . . . . .	29
1.6.3 Scaling theory of Anderson localisation . . . . .	30
1.6.4 Dimensionality, polarisation and short-range . . . . .	32
1.7 Resonant photonic crystals . . . . .	36
1.7.1 Light in periodic media . . . . .	36
1.7.2 Dispersion relation in arrays of point resonators . . . . .	37
1.7.3 Scalar and vector fields versus TE and TM polarisation . . . . .	42
1.8 Spatially correlated materials . . . . .	44
1.8.1 What are spatial correlations? . . . . .	44
1.8.2 Natural occurrences and effect on the mean free path . . . . .	48
1.9 Opening of photonic band gaps and localisation . . . . .	49
1.10 Conclusion . . . . .	51
<b>2 Impact of spatial correlations on ensembles of resonators</b>	<b>53</b>
2.1 Hyperuniformity as knob to tune the degree of spatial correlations . . . . .	53
2.1.1 Properties and generation process . . . . .	53
2.1.2 Numerical procedure . . . . .	55
2.1.3 Remarks on the periodic structure found for $\chi \rightarrow 1$ . . . . .	56
2.1.4 Structural properties . . . . .	57
2.2 Hard-core correlations . . . . .	58
2.2.1 Generation process through a Monte-Carlo algorithm . . . . .	58

2.2.2	Statistical properties and comparison with stealthy hyperuniform point patterns . . . . .	60
2.3	Study of the photonic properties of hyperuniform ensembles of resonators through scalar couplings . . . . .	61
2.3.1	Low density regime . . . . .	61
2.3.2	High density regime, $k_0a \leq 3$ . . . . .	62
2.3.3	Phase diagram in density-frequency space . . . . .	62
2.3.4	Summary . . . . .	63
2.4	Effect of vector couplings . . . . .	65
2.4.1	Low density . . . . .	65
2.4.2	High density . . . . .	66
2.4.3	Intermediate density . . . . .	67
2.5	Localisation phase diagram . . . . .	67
2.6	Finite size effects and scaling approach of 2D TE collective resonances . . . . .	69
2.6.1	Finite size effects . . . . .	69
2.6.2	Scaling approach . . . . .	70
2.7	Short-range and polarisation effects . . . . .	72
2.8	Conclusion . . . . .	73
<b>3</b>	<b>Strongly correlated patterns seen as disordered crystalline structures</b>	<b>75</b>
3.1	Structural similarities between SHU patterns and crystals . . . . .	75
3.2	From the Hamiltonian to the dispersion relation . . . . .	76
3.2.1	Hamiltonian in Bloch space . . . . .	76
3.2.2	Regularisation of the crystalline Hamiltonian and large wavelength expansion . . . . .	77
3.3	Application to the triangular lattice . . . . .	78
3.3.1	Computation of the dispersion relation . . . . .	78
3.3.2	Computation of the density of states . . . . .	78
3.3.3	Comparison between triangular lattices and hyperuniform patterns . . . . .	79
3.4	Extension to other crystalline structures and average lattice . . . . .	81
3.5	The origin of band gaps in photonic crystals made of resonators . . . . .	83
3.5.1	Fine analysis of the opening and closing of band gaps in the triangular lattice . . . . .	83
3.5.2	General condition for the opening of band gaps . . . . .	86
3.5.3	Effect of the polarisation on the gaps . . . . .	87
3.5.4	Dispersion relation for hyperuniform patterns . . . . .	88
3.6	Expansion of the Hamiltonian in reciprocal space . . . . .	90
3.6.1	Long wavelength limit . . . . .	90
3.6.2	Higher order expansion . . . . .	92
3.7	Conclusion . . . . .	94
<b>4</b>	<b>Mesoscopic description of the density of states in partially ordered media</b>	<b>95</b>
4.1	Complex spectrum of $G$ in the thermodynamic limit . . . . .	95
4.2	DOS and resolvent of $G$ . . . . .	96
4.3	From the scattering operator to the resolvent . . . . .	97
4.4	Density expansion of the DOS . . . . .	98
4.4.1	Expression of the scattering operator to the self-energy . . . . .	99
4.4.2	Low density evaluation of the density of modes . . . . .	99
4.4.3	Density of states in 2D, beyond the ISA . . . . .	99
4.4.4	Expansion of the self-energy to second order in density and recurrent scattering . . . . .	100
4.4.5	Evaluation of $\Sigma_C$ . . . . .	101

4.4.6	Computation of $\Sigma_L$ . . . . .	102
4.4.7	Computation of $\Sigma_B$ . . . . .	103
4.5	Explicit evaluation of the density of states of 2D systems . . . . .	104
4.5.1	Evaluation of the average density of states for TE waves . . . . .	104
4.5.2	Evaluation of the average density of states for TM waves . . . . .	105
4.6	Single scattering versus double scattering . . . . .	106
4.7	Changes in the DOS seen as an interference process . . . . .	108
4.8	The DOS as $\text{Im } \mathbf{G}$ . . . . .	109
4.9	Conclusion . . . . .	111
<b>5</b>	<b>Strong localization phenomenon in correlated resonant systems</b>	<b>113</b>
5.1	Diffusion equation for vector fields . . . . .	113
5.1.1	Bethe-Salpether equation for vector Green's functions . . . . .	114
5.1.2	Diagonalization of the Bethe-Salpeter equation at large scales . . . . .	114
5.1.3	Diffusion equation . . . . .	117
5.2	Renormalisation of the diffusion constant using the self-consistent theory of localisation . . . . .	117
5.2.1	Study in 2D . . . . .	118
5.2.2	3D case . . . . .	119
5.3	Evaluation of the mean free paths . . . . .	119
5.3.1	The mean free paths given by the structure factor . . . . .	119
5.3.2	Density expansion of $\ell_s$ . . . . .	121
5.3.3	Density expansion of $\ell_t$ . . . . .	123
5.3.4	Impact of the mean free path on the localisation length . . . . .	125
5.4	Evaluation of $\xi$ and $\ell_s$ from numerical simulation . . . . .	125
5.4.1	Evaluation of $\xi$ and $\ell_s$ from transport simulation . . . . .	125
5.4.2	Evaluation of $\xi$ from the eigenvectors . . . . .	127
5.5	Comparison between theory and numerics . . . . .	130
5.6	Conclusion . . . . .	130
<b>6</b>	<b>Towards an experimental validation</b>	<b>133</b>
6.1	Two-dimensional propagation in a waveguide . . . . .	133
6.2	Resonance of high dielectric cylinders and the coupled dipole approach . . . . .	134
6.3	Numerical study of a system composed of two resonances . . . . .	136
6.3.1	Electromagnetic Green's function and generalised coupled-dipole method	136
6.3.2	Application to the first two Mie resonances . . . . .	139
6.4	Finite-element method . . . . .	140
6.5	Towards an experimental implementation . . . . .	141
6.6	Conclusion . . . . .	142
	<b>General conclusion</b>	<b>145</b>
<b>A</b>	<b>Polarizabilities in 2D and 3D for scalar and vector fields</b>	<b>147</b>
A.1	3D vector . . . . .	147
A.2	3D scalar . . . . .	147
A.3	2D vector . . . . .	147
A.4	2D scalar . . . . .	148
<b>B</b>	<b>Regularization of the crystalline Hamiltonian</b>	<b>149</b>
<b>C</b>	<b>Diagrammatic approach: drawing rules</b>	<b>151</b>
	<b>Bibliography</b>	<b>152</b>





# General introduction

In 1972, P.W. Anderson wrote “More is different”. The idea that collective behaviour is not the sum of isolated individual contributions, but is sometimes the result of elaborate and counter-intuitive interactions has been at the origin of the development of the field of complex systems. In the specific domain of wave-physics, researchers study the propagation of waves in complex media. The latter often consist in disordered ensembles of inclusions in a continuous matrix, like proteins in milk, an oil deposit in a sedimentary layer, up to a gas in an interstellar cloud. These media are all inhomogeneous, but wave propagation is only affected if the fluctuations of the material induce fluctuations of the propagation index. The milk proteins, for example, do not scatter sound wave in the liquid, but scatter visible light. The problem of light propagation in complex materials should not surprise any physicist. True homogeneous media are very rare, and as soon as matter is included, there exists at least one scale under which a structure is present, from the size of a grain of sand in the physics of a dune, to atomic length-scale in solid-state physics. In the same way, perfect arrangements do not exist and even crystals host defects. Even though all states of matter can always be viewed as disordered media at some infinitesimal scale, it is usually larger structures from the order of the micron for visible light to several meters for radio and sound-waves that perturb the propagation of waves in most uses. The phenomenon extends to any type of waves: in acoustics, the blur on an echograph image comes from scattering of sound waves in the tissues, while in seismology the waves are reflected by the complicated structures of Earth.

For light, it is often small scattering objects, with rather mild individual influence on light, but whose overall effect completely scramble an incoming field. It leads to the phenomenon of complex coherent interferences associated to random fluctuations of the field called a *speckle* pattern. Historically, the study of light in disordered structures began with the problem of light propagation in heterogeneous media. Lorentz and Lorenz were among the first to study the refractive index of fluids (Lorentz, 1880; Lorenz, 1869), followed some decades later by Rayleigh (1899), Mie (1908) and Maxwell Garnett (1904) who understood the microscopic origin of many of the observed properties. From the blue colour of the sky or some colloidal pigments to the blur in the fog, it all arises from the interaction of ensembles of small elements (air molecules, colloids, droplets, ...) with light. Most of the early works report results based on single particle effects that sum up to the macroscopic scale. Another generation of physicists including Kirkwood (1936) and Yvon (1937) laid out the first sketches of a multiple scattering framework. A big leap forward was achieved with Foldy (1945) and Lax (1951; 1952) with the development of the coupled-dipole method which will be extensively used in this manuscript.

The transport properties of light were studied a bit later by Chandrasekhar (1960) and Ishimaru (1985). Experimental evidence of coherent backscattering, a coherent effect in spatially disordered systems by Tsang and Ishimaru (1984), Van Albada and Lagendijk (1985) and Wolf and Maret (1985) led the community to pursue Anderson localisation, a peculiar transport regime where the intensity decays exponentially in every direction, for electromagnetic waves in three dimensional media. Theoretical predictions have been made a long time ago to treat the phenomenon of Anderson localization of scalar waves (Anderson, 1985; John,

1984) but the case of vector light remains, to this day, an open question even if recent work points to its absence in point-like scattering systems Skipetrov and Sokolov (2014); Skipetrov and Page (2016); van Tiggelen and Skipetrov (2021).

The field of photonics in disordered media really took off in the 80's-90's with the influence of researchers from the mesoscopic physics domain. The optical properties through complex media have been intensively studied in the past decades leading to the understanding of weak and strong localisation Skipetrov and van Tiggelen (2004, 2006) field correlations Shapiro (1986); Mello et al. (1988); Pnini and Shapiro (1989), the development of diffusing-wave spectroscopy (Pine et al., 1988), speckle correlations (Feng et al., 1988; Skipetrov et al., 2010), wavefront-shaping (Mosk et al., 2012). In these studies, no special attention has been given to the impact of spatial correlations on optical properties. The uncorrelated disorder hypothesis has proven relevant to many practical situations but fails at capturing some physical phenomena. For example, the bright blue colours of the feathers worn by some birds (Saranathan et al., 2012; Jacucci et al., 2020), or the transparency of the cornea (Maurice, 1957), have both been interpreted as a frequency-dependent interference effect controlled by partial order.

Spatially correlated arrangements have been observed to act as intermediaries between fully random ensembles and photonic crystals. They can host band gaps, a characteristic property of periodic lattices (John, 1987), yet preserve and even amplify the phenomenon of Anderson localisation, intrinsically linked to disorder. Although these effects have already been observed both numerically and experimentally (Jin et al., 2001; Miyazaki et al., 2003; Rockstuhl et al., 2006; Imagawa et al., 2010; Rechtsman et al., 2011; Vynck et al., 2012; Man et al., 2013; Conley et al., 2014; Froufe-Pérez et al., 2016, 2017; Sellers et al., 2017; Haberkorn et al., 2020; Zheng et al., 2020; Sgrignuoli and Dal Negro, 2021; Torquato and Kim, 2021; Klatt et al., 2021; Yu et al., 2021; Wan and Glotzer, 2021; Vynck et al., 2021), no convincing theory exists to explain the precise mechanisms taking place. The influence of the polarisation is also often overlooked as it adds a layer of complexity to the problem. It is yet a crucial element as it has been found to sometimes prevent the formation of gaps and localised states.

The object of the present thesis is to study light scattering in 2D and 3D media composed of resonant sub-wavelength particles (Fraden and Maret, 1990; Lagendijk and van Tiggelen, 1996) in order to elucidate the origin of band gaps and strong localisation in correlated photonic structures.

The first chapter presents a state of the art of the physical phenomena we will study and their modelling. We start by summarising important properties of fully disordered arrangements of resonators, with an emphasis on the treatment of Anderson localisation. Transport properties are discussed by means of statistical quantities like the scattering mean free path or the refractive index. We present the effective Hamiltonian derived from the coupled-dipole method, which describes our main research model and discuss how to analyse the information contained in its collective resonances. After a brief summary of the physics of disordered systems, the chapter goes on to describe photonic crystals as references for perfect order. We present the basic tools required to study periodic structures, and in particular the concept of band structures. The dispersion relation contains, in addition to the frequencies of the collective excitations of the structure, spatial information embedded in the wavevector. We show how the gaps in the band structure of crystals made of resonators, are driven by polaritonic effects and not only by Bragg ones. This chapter ends by a focus on partially ordered structures, presenting their spatial properties, as well as some of their photonic properties.

The second chapter uses the coupled dipole framework to numerically study the effect of spatial correlations on the collective resonances. This approach allows to include both the resonant character of the particles and the field polarisation. It provides informations about the collective resonances of the ensemble, such as their frequencies and lifetimes. We present a systematic analysis over frequencies, densities and correlation ratios (all the way from full

disorder to complete order), of 2D and 3D structures, and for both vector and scalar couplings between resonators. We pay particular attention to the density of states to characterise the formation of gaps, and to the lifetimes of the resonances, to reveal strongly confined localised modes.

The third chapter develops a photonic crystal framework to model the density of states of highly correlated arrangements. Strong similarities between correlated patterns and periodic structures lead us to model partially ordered ensembles as patches of small crystals. We compare in particular the density of states of the two types of structure, and study the dispersion relations of different lattices to understand the conditions for the opening and closing of gaps in disordered but correlated systems.

The fourth chapter proposes an alternative model for the effect of spatial correlations on the density of state. The framework of photonic crystal is left aside in favour of a mesoscopic physics approach. We derive an equation relating the density of states to the total scattering operator of the system and the self energy. Spatial correlations are included in the model, as well as recurrent scattering up to second order in density. Among the numerous scattering events involved in recurrent scattering, we identify the dominant ones and show how the changes in the density of states can be understood as an interference process.

Chapter 5 addresses the question of the origin of Anderson localisation in spatially correlated and resonant ensembles. We begin by studying the effect of polarisation on long-range transport in disordered dilute 2D systems. We then use the frequency-dependent self-consistent theory of localisation to relate the density of state depletion to the observation of localised modes. A comparison between our predictions and simulations will be presented after obtaining theoretical predictions for the scattering and transport mean free paths which take into account spatial correlations and polarisation.

In chapter six, we present our preliminary work on a setup designed to test some of the predictions made in the previous chapters. We focus in particular on 2D arrangements of resonators with vector coupling. This configuration is achieved by putting high index ceramic cylinders in a metallic planar waveguide and using the first Mie resonances of the cylinders to access different polarisation couplings. We also simulate the physical system composed of particles supporting two resonances in the frequency range of interest, first by adapting the coupled-dipole method to include both resonances, and then by means of a finite element method. The experimental implementation of the setup has, to this day, not reproduced numerical and theoretical results, but solutions are being explored to solve these issues.



# Chapter 1

## Light in resonant media: Spatial correlations as a bridge between disordered systems and photonic crystals

This chapter is intended to be a partial review of the different concepts, models or phenomena that will be considered and used in this thesis. Since this work focuses on systems made out of resonators, we will in particular emphasise the characteristics of resonant versus non-resonant elements in terms of wave scattering. We will then introduce the basic concepts of multiple scattering theory and lay out some theoretical tools used throughout this manuscript to describe the propagation of waves through disordered media. These concepts will be applied to 2D and 3D ensembles of resonant scatterers. A special focus will be put on the phenomenon of Anderson localisation as its observation and behaviour in the presence of partial structural order is an important aspect of this work. In our study of the effect of partial order on wave propagation in disordered systems, we will also explore the opposite end of the order spectrum: the limit of photonic crystals. We will then highlight some important results obtained in spatially correlated ensembles of scatterers that will serve as stepping stones for the following chapters which hold new findings on the subject. A reader already familiar with all these topics may scroll down to the next chapter.

### 1.1 Resonant behaviour

We define a resonance as a selective and relatively strong response of a system from an external stimulation close to its *natural* frequency. This ubiquitous behaviour is very familiar when thinking about musical instruments, but much less when thinking about optics. Yet, the ground principles are the same for all waves. When a wave propagates in a medium (vacuum included), it is influenced by two aspects, the intrinsic properties of the constituents of the material given by its refractive index and the boundary conditions, given by geometry. An optical system can thus be resonant from the material itself. Examples of such resonances include the infra-red absorption of carbon dioxide in the atmosphere acting as a green house gas or the sharp frequency response of a cloud of cold atoms in vacuum. But even with a non-dispersive index, resonance is possible through shape.

The general idea is that you can confine an excitation through an index mismatch, inducing locally a steady-state accumulation of energy. The extreme example is the laser cavity. Light is strongly confined by semi-transparent mirrors between which it bounces back and forth a great number of times. The phase mismatch between the waves coming from multiple round-

trips leads to destructive interferences if the cavity length does not coincide with multiples of the wavelength, creating a Fabry-Perrot like system which is known to hosts very sharp resonances (Fabry and Perot, 1899). The lasing process *per se* occurs when a gain medium is added in order to compensate for the losses of the cavity, and one or more of the resonances of the cavity will light on. An example of the full treatment of a 2D lasing setup based on the Steady-state Ab initio Laser Theory (SALT) developed in Ref. Ge et al. (2010) is shown in Fig. 1.1. To emphasise the importance of the resonance of the cavity, the laser setup can be inverted, the gain turning into losses creating a coherent perfect absorber (Chong et al., 2010) at the initial laser frequency. The example of the laser will be the only occurrence in this manuscript where gain or absorption are considered.

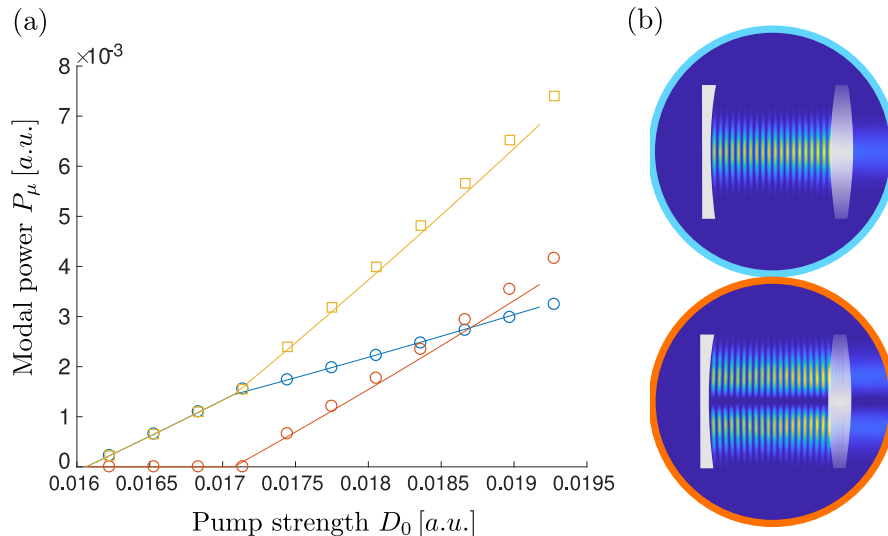


Figure 1.1: (a) Output power of the first two modes (blue and orange) and total output power (yellow) with increased pump strength obtained using the SALT approach. (b) Intensity profile of the first two modes of the cavity composed of a perfect curved mirror (left) and a lens (right) delimiting the uniformly pumped region. The two modes minimise their spatial overlap to optimise the energy provided by the pump. (Monsarrat and Stone, 2016, unpublished)

The concept of cavity can actually be extended to any object of arbitrary shape as long as it can be described with a different index than its environment. Our target system is not *per se* a cavity as it consists in an open medium with inclusions and could better be seen as an *inverse cavity*. The field propagates in the host medium and scatters on the heterogeneities. This process is usually described within the framework of multiple scattering theory.

## 1.2 Introduction to scattering

### 1.2.1 Scattering by individual particles

Before considering the complex scattering by ensembles of particles, let us recall the already interesting behaviour of individual scatterers. Because of the small wavelength of optical light, the interaction of light with large objects was understood first in the form of the classical theory of diffraction (Huygens et al., 1900). Macroscopic objects have the tendency to mostly scatter in the forward direction with, depending on the precise wavelength and the shape of the object, some strong secondary lobes. It corresponds to the green domain of Fig. 1.2.

At the other end of the spectrum, the case of particles much smaller than the wavelength has been first studied by Rayleigh (1899). He modelled the interaction of light with the atoms

as an off-resonance elastic process. The field polarises the particles, creating a dipole moment orthogonal to the incident wave-vector. Hence, the radiation pattern is the one of a single electric dipole with a characteristic “doughnut” shape as seen in Fig. 1.2 (b). Because the drive is off resonance, the scattered intensity has the known  $\lambda^{-4}$  dependence which gives rise to the sky’s blue colour.

The intermediate regime of objects whose size is of the same magnitude as the wavelength, has been considered by Mie (1908). By performing a spherical harmonic expansion of the field both inside and outside of the particle, the scattering cross-section can be computed for simple shapes like spheres and ellipsoids. The theory requires only two parameters: the size of the particle and the ratio of indices between the particles and the environment. It means that given a frequency, the normalised scattering cross-section for different sizes of particles, or conversely the frequency behaviour of the same particle is simply a rescaling of the same master function. An example of Mie theory for particles of index  $n = 1.33$  (simplified non dispersive model of a droplet of water in air) is shown in Fig. 1.2. Interestingly all three regimes of size parameter  $kr_p$  ( $k = \omega/c$  is the wavevector and  $r_p$  the radius of the particle) are captured by Mie theory. It is nonetheless not used in practice in the limiting cases as it requires the computation of a series whose acceptable cut-off increases with the size parameter (the larger a particle, the more modes it can host).

The case of the simplified water droplet from Fig. 1.2 shows that even without a dispersive material, the scattering by an object can be resonant.

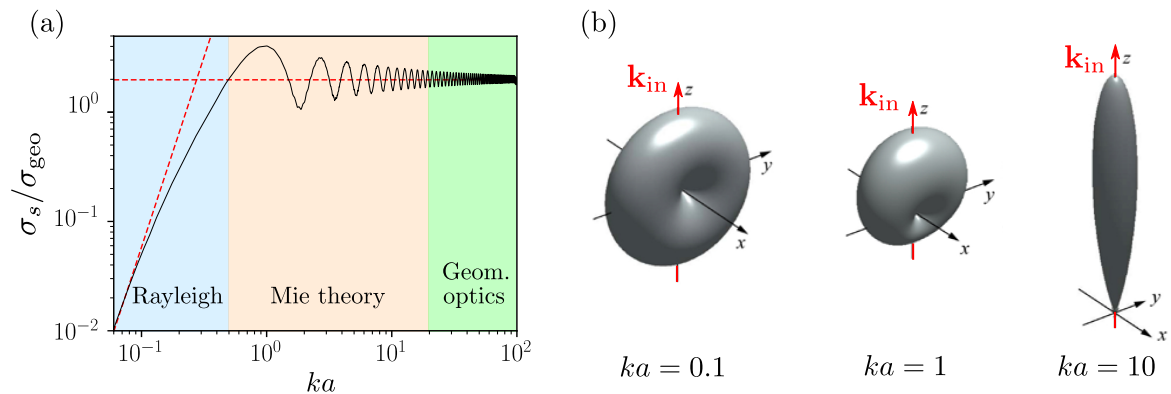


Figure 1.2: (a) Scattering cross-section of a sphere of index  $n = 1.33$ , normalised by its geometrical cross-section with respect to the size parameter  $ka$ . The red dashed lines are the asymptotic behaviour for small particle (Rayleigh) or very large ones (geometrical optics). (b) Radiation patterns in the three different regimes of (a). The incident field is propagating along the  $z$  direction and polarised along  $x$ . The patterns have been taken from Bekshaev et al. (2013).

### 1.2.2 Mean free path and transport

The transition from single scattering to multiple scattering is in general complicated as cooperative effects may take place. As a first approximation, we may consider that the total scattering of a system composed of different particles is simply the sum of independent scattering events. It is convenient and turns out to be rigorous at low density or small thickness of the medium. It is relevant to assess if, in a given ensemble, the interaction between the light and the particles is strong enough to impede the propagation through the system or not. Comparing the typical distance between two scattering events with the size of the medium can give us that information. The former typical distance is called the scattering mean free



path  $\ell_s$ . The different transport regimes are summarised in Fig. 1.3. For either very dilute ensembles or weakly scattering particles (large  $\ell_s$ ) in a sample of extension  $L$ , the light barely interacts with the medium and the propagation can still be thought of as ballistic light ( $\ell_s > L$ ). At higher density (small  $\ell_s$ ), we go from a small portion of ballistic light (blurry image with a lower contrast), to random wave propagation (completely altered image) for  $\ell_s \lesssim L$ . At even higher densities of particles, when the wavelength covers many scatterers distant by  $a$ , the precise structure disappears and the waves travel through a homogeneous medium described by an effective index ( $\lambda \gg a$ ).

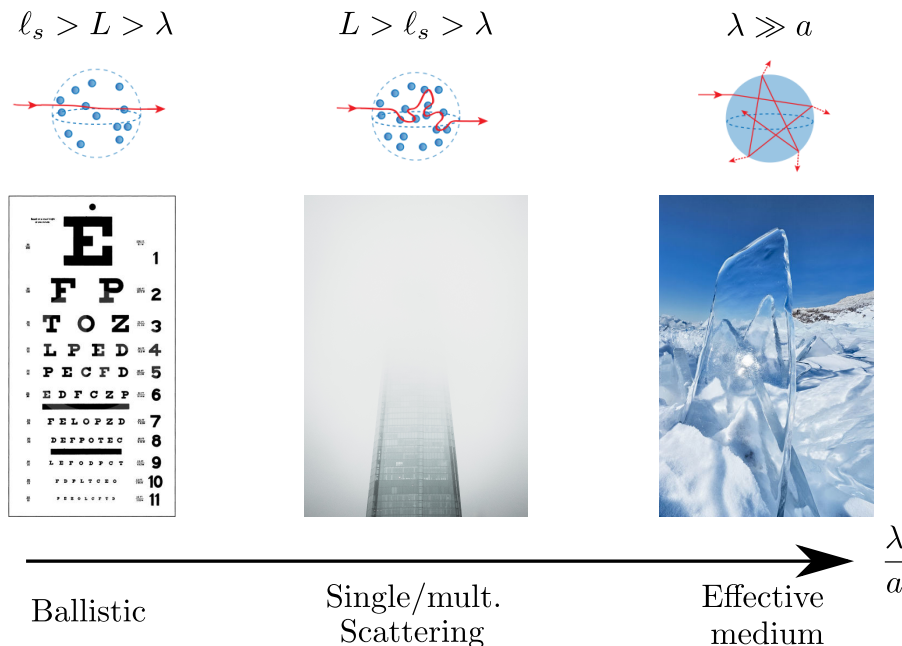


Figure 1.3: Transport regime with respect to the inter-particle distance  $a$ , the mean free path  $\ell$ , the system size  $L$  and the wavelength  $\lambda$ . (Image credits : American Academy of ophthalmology <https://www.aao.org> and <https://unsplash.com>.)

Conventional imaging works in the ballistic or in the single scattering regime with aberration correction methods to take out the continuous index variations. In the multiple scattering regime, there exists no direct imaging technique. Some recent methods using speckle correlations have been developed to circumvent this issue but the limitations are still strong (Katz et al., 2014; Puyo et al., 2019; Badon et al., 2020).

The transport properties described in this thesis, like the amount of ballistic light and hence the contrast of an image, rely on the evaluation of the scattering mean free path. It is a delicate quantity to access experimentally and its computation requires to go deeper into the theory of multiple scattering. For that, we need to lay down some theoretical tools based on the Green's formalism.

## 1.3 Multiple scattering theory

### 1.3.1 Green's formalism

Let us start by defining the convention we will use in the rest of this manuscript. We define the free-space Green's function in both the scalar and vector cases as

$$\left[ \nabla^2 + \frac{\omega^2}{c^2} \right] G_0(\mathbf{r} - \mathbf{r}', \omega) = \delta(\mathbf{r} - \mathbf{r}'), \quad (1.1)$$

$$\left[ -\nabla \times \nabla \times + \frac{\omega^2}{c^2} \right] \mathbf{G}_0(\mathbf{r} - \mathbf{r}', \omega) = \mathbf{1} \delta(\mathbf{r} - \mathbf{r}'), \quad (1.2)$$

where  $\omega$  is the frequency of the wave, and  $c$  the light celerity.  $G_0$  and  $\mathbf{G}_0$  are respectively the Green's function and Green's tensor in two or three dimensions,  $\delta(\mathbf{r})$  is the canonical Dirac delta function and  $\mathbf{1}$  denotes the identity operator. In free space, where  $\varepsilon(\mathbf{r}) = 1$  (or a constant at the cost of a renormalisation of the frequency), the explicit expression of the Green's functions in both Fourier and real space are given by

$$G_0(\mathbf{q}, k) = \frac{1}{k^2 - q^2}, \quad (1.3)$$

$$\mathbf{G}_0(\mathbf{q}, k) = \frac{\Delta_q^\perp}{k^2 - q^2} + \frac{\Delta_q^\parallel}{k^2}, \quad (1.4)$$

where  $k = \omega/c$ ,  $\mathbf{q}$  is the Fourier parameter and  $\Delta_q^{\perp, \parallel}$  are respectively the transverse or longitudinal projector along  $\mathbf{q}$  such that  $\Delta_q^\perp = \mathbf{1} - \mathbf{q} \otimes \mathbf{q}/q^2$  and  $\Delta_q^\parallel = \mathbf{q} \otimes \mathbf{q}/q^2$ . Using Eqs. (1.3) and (1.4), we can write the real space expression of their retarded version for scalar waves,

$$G_0(\mathbf{r}, k) = \begin{cases} \frac{-i}{4} H_0^{(1)}(kr) & \text{in 2D,} \\ \frac{-e^{ikr}}{4\pi r} & \text{in 3D,} \end{cases} \quad (1.5)$$

where  $H_\alpha^{(1)}$  is the Hankel function of the first kind and of order  $\alpha$ . For vector waves, we have

$$\mathbf{G}_0(\mathbf{r}, k) = \begin{cases} \frac{-i}{4} \left[ \Delta_r^\perp H_0^{(1)}(kr) + \left( \Delta_r^\parallel - \Delta_r^\perp \right) \frac{H_1^{(1)}(kr)}{kr} \right] + \mathbf{1} \frac{\delta(\mathbf{r})}{2k^2} & \text{in 2D,} \\ \frac{-e^{ikr}}{4\pi r} \left[ \Delta_r^\perp + \left( 2\Delta_r^\parallel - \Delta_r^\perp \right) \frac{1 - ikr}{k^2 r^2} \right] + \mathbf{1} \frac{\delta(\mathbf{r})}{3k^3} & \text{in 3D.} \end{cases} \quad (1.6)$$

It can be noted that the convention used for the Green's functions is the one used in condensed matter rather than in optics. They both differ by an overall sign.

### 1.3.2 Scattering by an inhomogeneity and Lippmann-Schwinger equation

In a more formal fashion than in the previous section, the scattering properties of an object can be computed from Eq. (1.1). The most simple situation is an inclusion of dielectric constant  $\varepsilon$ . The electric field is given by the Lippmann-Schwinger equation (Lippmann and Schwinger, 1950)

$$\mathbf{E}(\mathbf{r}, k) = \mathbf{E}_0(\mathbf{r}, k) - k^2 \int d\mathbf{r}' [\varepsilon(\mathbf{r}', k) - 1] \mathbf{G}_0(\mathbf{r} - \mathbf{r}', k) \mathbf{E}(\mathbf{r}', k), \quad (1.7)$$

where  $\mathbf{E}_0$  is the input or incident field. This self-consistent equation can be written in an operator picture

$$\mathbf{E} = \mathbf{E}_0 + \mathbf{G}_0 \mathbf{V} \mathbf{E}, \quad (1.8)$$

where  $\mathbf{E}$ ,  $\mathbf{E}_0$  and  $\mathbf{V}$  stand for the total field, the input field and the interaction operator between the fields and the particle defined in Eq. (1.7). Explicitly, they read

$$\mathbf{G}_0 : \mathbf{E} \rightarrow \int d\mathbf{r}' \mathbf{G}_0(\mathbf{r} - \mathbf{r}', \omega) \mathbf{E}(\mathbf{r}') \quad (1.9)$$

$$\mathbf{V} : \mathbf{E} \rightarrow -k^2 [\varepsilon(\mathbf{r}) - 1] \mathbf{E}(\mathbf{r}). \quad (1.10)$$

Equation (1.8) can be iterated and resummed so as to obtain the total scattering operator of the particle  $\mathbf{T}$  (Carminati and Schotland, 2021):

$$\begin{aligned} \mathbf{E} &= \mathbf{E}_0 + \mathbf{G}_0 \mathbf{V} \mathbf{E} = \mathbf{E}_0 + \mathbf{G}_0 \mathbf{V} \mathbf{E}_0 + \mathbf{G}_0 \mathbf{V} \mathbf{G}_0 \mathbf{V} \mathbf{E} = \mathbf{E}_0 + \sum_{j=1}^{\infty} (\mathbf{G}_0 \mathbf{V})^j \mathbf{E}_0 \\ &= \mathbf{E}_0 + \mathbf{G}_0 \frac{\mathbf{V}}{\mathbf{1} - \mathbf{G}_0 \mathbf{V}} \mathbf{E}_0 = \mathbf{E}_0 + \mathbf{G}_0 \mathbf{T} \mathbf{E}_0. \end{aligned} \quad (1.11)$$

Computing  $\mathbf{T}$  analytically is in general difficult. Two noticeable exceptions are the case of spherical particles of constant index leading to Mie theory and the case of small objects compared to the wavelength (including the wavelength inside the particle). In the first case, the total scattering operator can be expressed on a spherical (3D) or cylindrical (2D) harmonics basis and computed for every mode leading to the well known Mie theory. In the latter, the field is supposed to be constant inside the particle and the integral in Eq. (1.7) sums up to an integral of the Green tensor over the particle's volume. From Eq. (1.7), for a small particle located at  $\mathbf{r}_0$ , we end up with

$$\mathbf{T}(\mathbf{r}, \mathbf{r}', \omega) = -k^2 \alpha(\omega) \delta(\mathbf{r} - \mathbf{r}_0) \delta(\mathbf{r}' - \mathbf{r}_0) \mathbf{1}. \quad (1.12)$$

For example, it takes for vector waves in 3D the form

$$\alpha(\omega) = \frac{\alpha_0(\omega)}{1 - i \frac{k^3}{6\pi} \alpha_0(\omega)}, \quad (1.13)$$

is the polarisability of the particle,  $\alpha_0(\omega) = 3\delta V \frac{\varepsilon(\omega) - 1}{\varepsilon(\omega) + 2}$  is the static polarisability in 3 dimensions with  $\delta V$  the volume of a particle. It can be noted that the small particle assumption amounts to truncating the Mie series after the first dipolar term.

The complete frequency behaviour of an object is complicated as dispersion can come from the index itself, but also from the shape. A good model for the polarisability of a non-absorbing system close to a resonance ( $|\omega - \omega_0| < \omega_0$ ) is given by a Lorentzian functions

$$\alpha(\omega) \propto \frac{-\Gamma_0}{\omega - \omega_0 + i\Gamma_0/2}, \quad (1.14)$$

where  $\omega_0$  the central frequency and  $\Gamma_0$  the linewidth of the resonance. The prefactor depends on both the dimension of space and on the number of field degrees of freedom (Novotny and Hecht, 2012). The different polarisabilities are summarised in appendix A. This model is exact in the case of a two-level atoms far from saturation (Labeyrie et al., 1999). The scattering behaviour of an isolated particle can then be fully described using Eq. (1.11). We treat the case of several particles in the next section.

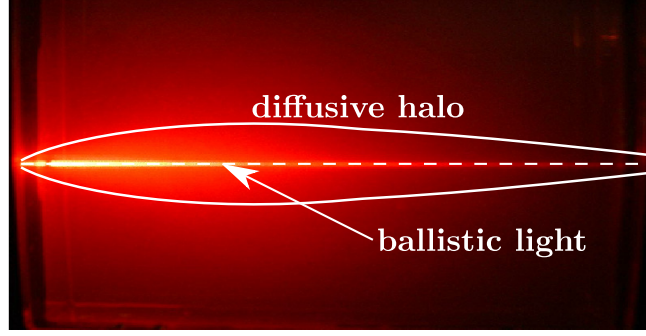


Figure 1.4: Laser light shining through a suspension of polystyrene beads in water showing the ballistic light being attenuated with the depth and transferred into the diffusive halo (EM2C laboratory, École Centrale Paris, CNRS).

### 1.3.3 Scattering by inhomogeneities and Dyson equation

Let us now consider an ensemble of scatterers which can each be described using a scattering matrix  $\mathbf{T}$ . In the single scattering approximation, each particle can scatter the incident wave and the total scattered field is thus the sum of each event:

$$\mathbf{E} = \mathbf{E}_0 + \sum_j \mathbf{G}_0 \mathbf{T}_j \mathbf{E}_0, \quad (1.15)$$

where  $\mathbf{T}_j$  is the scattering operator of scatterer  $j$ . The above expression considers scattering sequences where each object only scatters once. It is called the single or Born scattering approximation and is adapted to very dilute ensembles or thin samples compared to the mean free path. In general, the scattered field can still interact with the system and the equation becomes

$$\mathbf{E} = \mathbf{E}_0 + \sum_j \mathbf{G}_0 \mathbf{T}_j \mathbf{E}. \quad (1.16)$$

This equation can be iterated in what is referred as the Born series

$$\mathbf{E} = \mathbf{E}_0 + \sum_j \mathbf{G}_0 \mathbf{T}_j \mathbf{E}_0 + \sum_j \sum_{l \neq j} \mathbf{G}_0 \mathbf{T}_l \mathbf{G}_0 \mathbf{T}_j \mathbf{E}_0 + \sum_j \sum_{l \neq j} \sum_{m \neq l} \mathbf{G}_0 \mathbf{T}_m \mathbf{G}_0 \mathbf{T}_l \mathbf{G}_0 \mathbf{T}_j \mathbf{E}_0 + \dots \quad (1.17)$$

The above equation gives a deterministic expression of the field in a given system in terms of the location of the scattering elements. It can be used to derive, for small particles, the coupled dipole method, which will be intensively applied in this work and developed in Sec. 1.5.1.

A perfect knowledge of the behaviour of a given system can be useful for some applications, but most of the time it is the average or typical properties of a given type of medium that is accessible. Figure 1.4 shows the example of self-averaging intensity due to Brownian motion of the particles. The image is composed of two distinct parts, first the attenuated ballistic light highlighting the mean-field and secondly the diffusive halo which exists due to multiple scattering. The field is thus ensemble-averaged over the disorder degrees of freedom leading to

$$\langle \mathbf{E} \rangle = \mathbf{E}_0 + \sum_j \mathbf{G}_0 \langle \mathbf{T}_j \rangle \mathbf{E}_0 + \sum_j \sum_{l \neq j} \mathbf{G}_0 \langle \mathbf{T}_l \mathbf{G}_0 \mathbf{T}_j \rangle \mathbf{E}_0 + \sum_j \sum_{l \neq j} \sum_{m \neq l} \mathbf{G}_0 \langle \mathbf{T}_m \mathbf{G}_0 \mathbf{T}_l \mathbf{G}_0 \mathbf{T}_j \rangle \mathbf{E}_0 + \dots, \quad (1.18)$$

where the brackets denotes, throughout this manuscript, an ensemble average over the disorder degrees of freedom. This equation can be rewritten as

$$\langle \mathbf{E} \rangle = \mathbf{E}_0 + \mathbf{G}_0 \mathbf{\Sigma} \langle \mathbf{E} \rangle. \quad (1.19)$$

It is called the Dyson equation (Carminati and Schotland, 2021), which defines the self-energy  $\Sigma$  enclosing all the complexity of the problem. More precisely,  $\Sigma$  encloses every non-factorisable scattering sequences such as the ones presented below in diagrammatic form:

$$\Sigma = \text{Diagram 1} + \text{Diagram 2} + \text{Diagram 3} + \text{Diagram 4} + \text{Diagram 5} + \dots$$

$$+ \text{Diagram 6} + \text{Diagram 7} + \text{Diagram 8} + \text{Diagram 9} + \text{Diagram 10} + \dots \quad (1.20)$$

Here, a hollow circle represent a scattering operator  $\mathbf{T}$ , an horizontal line stands for a Green's function between scattering particles, a crooked line connects two identical particles while a dashed line specifies the statistical correlation between the positions of the scatterers (the rules are summarised in App. C. The incident field  $\mathbf{E}_0$  can be chosen as the one produced by a point source in order to obtain an equation on the average Green's function  $\langle \mathbf{G} \rangle$ . In Fourier space, it reads

$$\langle \mathbf{G}(\mathbf{q}, k) \rangle = \mathbf{G}_0(\mathbf{q}, k) + \mathbf{G}_0(\mathbf{q}, k) \Sigma(\mathbf{q}, k) \langle \mathbf{G}(\mathbf{q}, k) \rangle \quad (1.21)$$

$$= \frac{1}{\mathbf{G}_0(\mathbf{q}, k)^{-1} - \Sigma(\mathbf{q}, k)}$$

$$= \begin{cases} \frac{1}{k^2 - q^2 - \Sigma(\mathbf{q}, k)} & \text{for scalar fields,} \\ \frac{\Delta_{\mathbf{q}}^{\perp}}{k^2 - q^2 - \Sigma^{\perp}(\mathbf{q}, k)} + \frac{\Delta_{\mathbf{q}}^{\parallel}}{k^2 - \Sigma^{\parallel}(\mathbf{q}, k)} & \text{for vector fields,} \end{cases} \quad (1.22)$$

where  $\Sigma^{\perp}$  and  $\Sigma^{\parallel}$  are respectively the transverse and longitudinal parts of the self-energy. The computation of the self-energy gives access to all the information about the propagation of the average field in that medium.

In a non-absorbing medium, the scattering mean free path informing about the transport regime is given by the attenuation length of the intensity of the mean-field. We thus need to perform a Fourier transform of Eq. (1.22). It is in general complicated because  $\Sigma$  may depend on  $\mathbf{q}$  in a complicated fashion. A first simplification comes from the fact that, for vector fields, only the transverse part of the Green's function carries a far-field contribution. The longitudinal part of  $\langle \mathbf{G} \rangle$  can thus be neglected, and both the scalar and the vector expressions have the same structure. The second approximation is called the *on-shell* approximation. It states that if the self-energy is small compared to  $k^2$ , it will only contribute significantly if  $q = k$ , effectively freezing the wavevector dependence in  $\Sigma$  at  $k$ . We end up for scalar (vector) fields with

$$\langle G^{\perp}(\mathbf{q}, k) \rangle = \frac{1}{k^2 \left( 1 - \frac{\Sigma^{\perp}(k, k)}{k^2} \right) - q^2} = \frac{1}{k_{\text{eff}}^2 - q^2}, \quad (1.23)$$

where  $k_{\text{eff}}(k) = kn(k) = k \sqrt{1 - \frac{\Sigma^{\perp}(k, k)}{k^2}}$  defines the effective index  $n = n' + in''$ . Under these assumptions, the average Green's function can be written by simply swapping  $k$  with  $k_{\text{eff}}$  in Eq. (1.5). In the far field,  $\langle G_0(\mathbf{r}, k) \rangle \propto \exp(inkr) = \exp(ikn'r) \exp(-n''kr)$  such that we can extract the scattering mean free path from  $|\langle \mathbf{E} \rangle|^2 \sim e^{-r/\ell_s}$  as

$$\frac{1}{\ell_s} = 2kn''(k) = 2k \text{Im} \sqrt{1 - \frac{\Sigma^{\perp}(k, k)}{k^2}} \simeq -\frac{\text{Im} \Sigma^{\perp}(k, k)}{k}. \quad (1.24)$$

The right side of Eq. (1.24) has been obtained from a first order expansion of the square root which is a good approximation in very dilute systems. The next section provides an example of the computation of the scattering mean free path for point-like resonators in a very dilute assembly.

### 1.3.4 Evaluation of the scattering length and transport regimes at low density

The self-energy can be computed at low density by truncating Eq. (1.20) after the first term. It is called the Independent Scattering Approximation (ISA) and will be denoted  $\Sigma_{\text{ISA}}$ . If we consider identical scatterers, we can write  $\mathbf{T}_j(\omega, \mathbf{r}, \mathbf{r}') = t(\omega)\delta(\mathbf{r} - \mathbf{r}_j)\delta(\mathbf{r}' - \mathbf{r}_j)\mathbb{1}$ , where  $t(\omega)$  is the one particle scattering operator. The self energy reads

$$\Sigma_{\text{ISA}}(\mathbf{r}, \mathbf{r}', \omega) = \left\langle \sum_j \mathbf{T}_j(\omega, \mathbf{r}, \mathbf{r}') \right\rangle = N\mathbb{1} \int d\mathbf{r}_j p[\mathbf{r}_j] t(\omega) \delta(\mathbf{r} - \mathbf{r}_j) \delta(\mathbf{r}' - \mathbf{r}_j) = \mathbb{1} \rho t(\omega) \delta(\mathbf{r} - \mathbf{r}'), \quad (1.25)$$

where the distribution of scatterers  $p(\mathbf{r})$  has been assumed uniform ( $p[\mathbf{r}] = 1/V$ , with  $V$  the volume of the system) and where  $\rho = N/V$  is the density of scatterers. In Fourier space we have

$$\begin{aligned} \Sigma_{\text{ISA}}(\mathbf{q}, \mathbf{q}', \omega) &= \int d\mathbf{r} d\mathbf{r}' \Sigma_{\text{ISA}}(\mathbf{r}, \mathbf{r}', \omega) e^{-i\mathbf{q}\cdot\mathbf{r}} e^{i\mathbf{q}'\cdot\mathbf{r}'} \\ &= \mathbb{1} \rho t(\omega) \int d\mathbf{r} e^{-i\mathbf{r}\cdot(\mathbf{q}-\mathbf{q}')} = \mathbb{1} \rho t(\omega) (2\pi)^d \delta(\mathbf{q} - \mathbf{q}'). \end{aligned} \quad (1.26)$$

The final-delta term accounts for the fact that the ISA self-energy only carries contribution for identical incoming and outgoing wavevector, but the  $\mathbf{q} - \mathbf{q}'$  structure is a more general feature of translationally invariant media. The usual expression of the self-energy appearing in Eq. (1.24) differs from Eq. (1.26) in the way that the  $(2\pi)^d \delta(\mathbf{q} - \mathbf{q}')$  is set aside. The self energy used throughout this thesis is defined through the relation  $\Sigma(\mathbf{q}, \mathbf{q}', \omega) \equiv \Sigma(\mathbf{q} - \mathbf{q}', \omega) (2\pi)^d \delta(\mathbf{q} - \mathbf{q}')$ .

Let us now look at the mean free path, using as an example the polarisability of a two level atom embedded in a three dimensional space, with vector couplings. Using Eqs. (1.24), (1.12) and (1.26) and  $\alpha(\omega) = -\frac{3\pi}{k_0^3} \frac{\Gamma_0}{\omega - \omega_0 + i\Gamma_0/2}$ ,  $k_0 = \omega_0/c$  (see appendix A), we obtain

$$\ell_s = \frac{-k}{\rho \text{Im}[t(\omega)]} = \frac{k_0^3}{6\pi k \rho} \left[ 1 + \frac{4(\omega - \omega_0)^2}{\Gamma_0^2} \right]. \quad (1.27)$$

In the following, we will use normalised variables, such as the detuning from the bare resonance  $\delta = 2(\omega - \omega_0)/\Gamma_0$  as a frequency variable and the resonant wavevector normalised by the mean distance  $a$  between two scatterers as a density variable  $k_0 a$ . Equation (1.27) becomes in the limit of small detuning and large quality factor

$$k_0 \ell_s = \frac{(k_0 a)^3}{6\pi} (1 + \delta^2). \quad (1.28)$$

With the values of the mean free path obtained in Eq. (1.28), we can build a transport phase diagram for given quality factor and density parameters. The results are shown in Fig. 1.5.

One may notice that we are missing the *effective medium* regime from Fig. 1.3. It corresponds to a regime where the ISA approximation breaks down for at least two reasons. First because at high density high order contributions in Eq. (1.20) cannot be neglected, second because the wavelength becomes much larger than the mean distance between the scatterers. The wave cannot scatter on a range much smaller than its wavelength even if it encompasses many diffusers. In a very high density regime ( $k_0 a \ll 1$ ) the effect of the inhomogeneities is not perceived, resulting in an effective homogeneous medium. A good model to find the

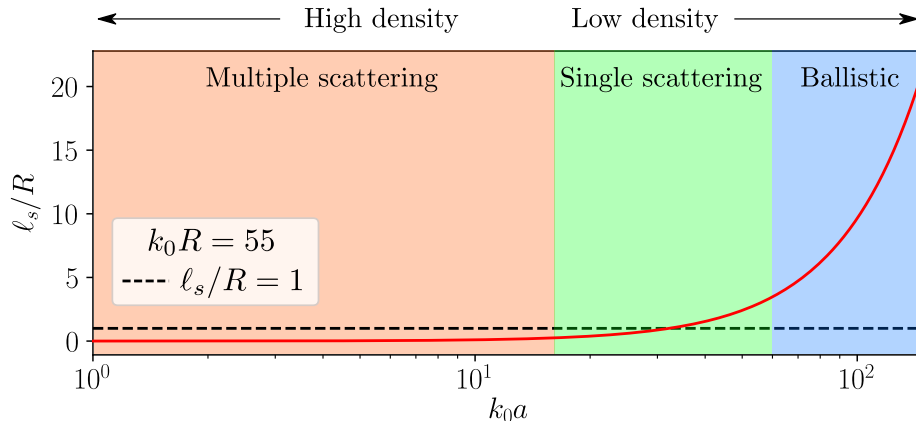


Figure 1.5: Scattering mean free path normalised by a system size  $R$ , computed using Eq. (1.28), at  $\delta = 0$  and for  $k_0 R = 55$ . The condition  $\ell_s/R = 1$  is highlighted as it is the pivot value regarding the transport. At low density (large  $k_0 a$  on the right), the scattering mean free path is easily larger than the system and scattering is rare, we are in the ballistic regime. As we increase the density (smaller  $k_0 a$  on the left), scattering is more likely,  $\ell_s$  decreases.

effective index associated with this regime can be found from the Maxwell Garnett equation (Maxwell Garnett, 1904) where the effective permittivity  $\varepsilon_{\text{eff}} = n^2$  obeys

$$\frac{\varepsilon_{\text{eff}} - 1}{\varepsilon_{\text{eff}} + 2} = \phi_i \frac{\varepsilon_i - \varepsilon_m}{\varepsilon_i + 2\varepsilon_m}. \quad (1.29)$$

Here  $\varepsilon_i$  and  $\varepsilon_m$  are the permittivity of the inclusions and of the medium, and  $\phi_i$  is the volume fraction of the inclusions. This equation only works for heterogeneities which can be described by an index. In the case of point-like resonators described above, the Lorenz-Lorentz formula also called Clausius-Mossotti links the effective index to a polarisability and gives in three dimensions

$$\frac{\varepsilon_{\text{eff}} - 1}{\varepsilon_{\text{eff}} + 2} = \frac{\rho\alpha(\omega)}{3}. \quad (1.30)$$

Equation (1.30) can be obtained by including scattering between particle having a delta-like repulsion. Explicitly it amounts to including in the self-energy the diagrams

$$\Sigma = \text{---} \circ \text{---} \circ \text{---} + \text{---} \circ \text{---} \circ \text{---} \circ \text{---} + \text{---} \circ \text{---} \circ \text{---} \circ \text{---} \circ \text{---} + \text{---} \circ \text{---} \circ \text{---} \circ \text{---} \circ \text{---} \circ \text{---} + \dots \quad (1.31)$$

It can also be derived by considering recurrent scattering in fully uncorrelated ensembles. In the last situation, it is the delta-divergence of the Green's function which bring this Lorenz-Lorentz correction, thus specific to vector fields. The derivation is done in Ref. Legendijk and van Tiggelen (1996). Until now, we analysed light transport by considering only the average field which usually corresponds to the ballistic part of the field. However in large samples or deep into the scattering medium, when the ballistic light has been damped, the mean-field description does not seem relevant. A solution is to work with the average intensity which keeps a non-zero value deep inside a medium as illustrated on the diffusive halo in Fig. 1.4. We develop this approach in the next section.

## 1.4 From the Bethe-Salpeter equation to the diffusion equation

Scattered light can be accessed by looking at the average intensity. Before considering anomalous behaviour, let us first discuss the usual behaviour of the intensity in a disordered medium:

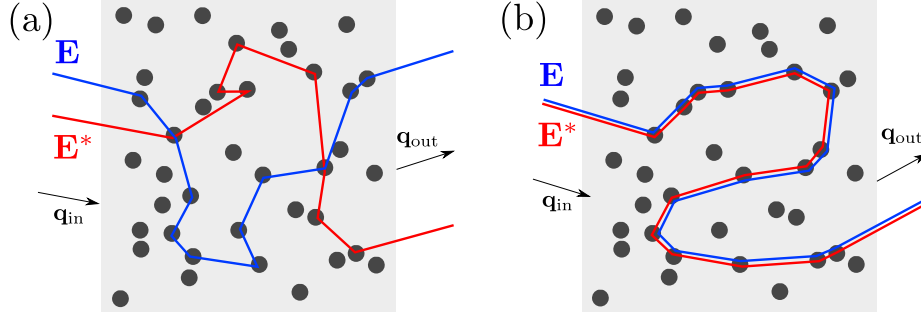


Figure 1.6: Schematic approach showing diffusion sequences in a disordered medium in the general case (a) and in the ladder approximation (b) where the field and its conjugate follow the same path.

diffusion. To derive a diffusion equation for the average intensity in the dilute regime, we use an equation similar to the Dyson equation (1.19) but for the average intensity: it is called the Bethe-Salpeter equation (Lagendijk and van Tiggelen, 1996). This equation takes into account all possible combination of diffusion paths in the medium as seen on Fig. 1.6 (a). It reads

$$\begin{aligned} \langle \mathbf{G}(\mathbf{r}, \mathbf{r}_0, \omega) \mathbf{G}^*(\boldsymbol{\rho}, \boldsymbol{\rho}_0, \varpi) \rangle &= \langle \mathbf{G}(\mathbf{r}, \mathbf{r}_0, \omega) \rangle \langle \mathbf{G}^*(\boldsymbol{\rho}, \boldsymbol{\rho}_0, \varpi) \rangle \\ &+ \int \langle \mathbf{G}(\mathbf{r}, \mathbf{r}', \omega) \rangle \langle \mathbf{G}^*(\boldsymbol{\rho}, \boldsymbol{\rho}', \varpi) \rangle \mathbf{U}(\mathbf{r}', \mathbf{r}'', \boldsymbol{\rho}', \boldsymbol{\rho}'', \omega, \varpi) \langle \mathbf{G}(\mathbf{r}'', \mathbf{r}_0, \omega) \mathbf{G}^*(\boldsymbol{\rho}'', \boldsymbol{\rho}_0, \varpi) \rangle d\mathbf{r}' d\mathbf{r}'' d\boldsymbol{\rho}' d\boldsymbol{\rho}'', \end{aligned} \quad (1.32)$$

where  $\mathbf{U}$  is the irreducible vertex and is the two-field counterpart of the self energy  $\boldsymbol{\Sigma}$ . It contains every irreducible scattering event involving two fields as shown in Fig. 1.6 (a). Some elements of the vertex  $\mathbf{U}$  are drawn diagrammatically below,

$$\mathbf{U} = \begin{array}{c} \circ \\ | \\ \circ \end{array} + \begin{array}{c} \circ \\ \vdots \\ \circ \end{array} + \begin{array}{c} \circ \\ \text{---} \\ \circ \end{array} + \begin{array}{c} \circ \\ \text{---} \\ \circ \end{array} + \begin{array}{c} \circ \text{---} \circ \\ | \\ \circ \end{array} + \begin{array}{c} \circ \text{---} \circ \\ | \\ \circ \end{array} + \begin{array}{c} \circ \text{---} \circ \\ | \\ \circ \end{array} + \begin{array}{c} \circ \text{---} \circ \\ | \\ \circ \end{array} + \dots \quad (1.33)$$

The reading rules described after Eq. (1.20) apply in each field in the upper or lower part of the diagram. In addition vertical and tilted lines connect two identical or spatially correlated scatterers. The simplest way to derive a diffusion equation for the intensity is to make the following simplifying assumptions. First, we simplify the Bethe-Salpeter equation (1.32), by taking  $\mathbf{r} = \boldsymbol{\rho}$  and  $\mathbf{r}_0 = \boldsymbol{\rho}_0$  and writing frequencies as  $\omega \rightarrow \omega + \Omega/2 \equiv \omega^+$  and  $\varpi \rightarrow \omega - \Omega/2 \equiv \omega^-$ , where  $\omega$  and  $\Omega$  have different physical meanings. When  $\Omega \ll \omega$ , the *slow* frequency  $\Omega$  can be seen as the frequency rate of the envelope of  $\langle \mathbf{G} \mathbf{G}^* \rangle$  conjugated with the travel time, and  $\omega$  as the fast carrier frequency. Diffusion occurs at long time which is equivalent to evaluating the correlator for small  $\Omega$  compared to  $\omega$ . Second, we consider the simplest diffusion sequences for the intensity called the *ladder* approximation, where we assume that both fields follow the same path as shown in Fig. 1.6 (b). Third, we assume scalar field propagation. The intensity vertex is then simplified as

$$U_0(\mathbf{r}, \mathbf{r}', \boldsymbol{\rho}, \boldsymbol{\rho}, \omega, \Omega) = \begin{array}{c} \circ \\ | \\ \circ \end{array} = \rho t(\omega^+) t^*(\omega^-) \delta(\mathbf{r} - \mathbf{r}') \delta(\boldsymbol{\rho} - \boldsymbol{\rho}') \delta(\mathbf{r} - \boldsymbol{\rho}) \quad (1.34)$$



where  $t$  is the particle scattering operator. Combining Eqs. (1.32) and (1.34) and defining  $I(\mathbf{r}, \omega, \Omega) \equiv \langle G(\mathbf{r}, \mathbf{r}_0, \omega + \Omega/2) G^*(\mathbf{r}, \mathbf{r}_0, \omega - \Omega/2) \rangle$  with  $\mathbf{r}_0 = \mathbf{0}$  for simplicity, we can write

$$I(\mathbf{r}, \omega, \Omega) = \langle G(\mathbf{r}, \omega^+) \rangle \langle G^*(\mathbf{r}, \omega^-) \rangle + \rho t(\omega^+) t^*(\omega^-) \int d\mathbf{r}' \langle G(\mathbf{r} - \mathbf{r}', \omega^+) \rangle \langle G^*(\mathbf{r} - \mathbf{r}', \omega^-) \rangle I(\mathbf{r}', \omega, \Omega) \quad (1.35)$$

which simplifies in Fourier space as

$$I(\mathbf{q}, \omega, \Omega) = \text{FT} [\langle G(\mathbf{r}, \omega^+) \rangle \langle G^*(\mathbf{r}, \omega^-) \rangle] (\mathbf{q}) + \rho t(\omega^+) t^*(\omega^-) \text{FT} [\langle G(\mathbf{r}, \omega^+) \rangle \langle G^*(\mathbf{r}, \omega^-) \rangle] (\mathbf{q}) I(\mathbf{q}, \omega, \Omega), \quad (1.36)$$

where  $\text{FT}[f](q)$  denotes the Fourier transform of  $f$  taken at  $q$ . We are left with the evaluation of the Fourier transform of the incoherent intensity, which can be computed exactly recalling results from Sec. 1.3.3, with  $\langle G(\mathbf{r}, \omega^\pm) \rangle \simeq e^{i\omega n'(\omega^\pm)r/c} e^{\pm i n'(\omega^\pm)\Omega r/2c} e^{-r/2\ell_s} / 4\pi r$  in 3D. At first order in  $\Omega/\omega$  the contribution coming from correction in the real part of the optical index can be summarised as

$$\langle G(\mathbf{r}, \omega^+) \rangle \langle G^*(\mathbf{r}, \omega^-) \rangle \simeq \frac{e^{i\tilde{\Omega}r/c} e^{-r/\ell_s}}{16\pi^2 r^2}, \quad (1.37)$$

with

$$\tilde{\Omega} \equiv \Omega \left[ 1 + \frac{\delta}{2k_0\ell_s} - \frac{c}{\Gamma_0\ell_s} \left( 1 - \frac{2}{\delta^2 + 1} \right) \right]. \quad (1.38)$$

Here, we have assumed a small detuning and a large quality factor to be consistent with the expression of the polarisabilities. Finally, we have in Fourier space

$$\begin{aligned} \text{FT} [\langle G(\mathbf{r}, \omega^+) \rangle \langle G^*(\mathbf{r}, \omega^-) \rangle] (\mathbf{q}) &\simeq \int d\mathbf{r} \frac{e^{i\tilde{\Omega}r/c} e^{-r/\ell_s}}{16\pi^2 r^2} e^{-i\mathbf{q}\cdot\mathbf{r}} \\ &\simeq \frac{1}{4\pi q} \text{atan} \left( \frac{q\ell_s}{1 - i\tilde{\Omega}\ell_s/c} \right) \\ &\simeq \frac{\ell_s}{4\pi} \left( 1 + i\tilde{\Omega}\ell_s/c \right) \left( 1 - \frac{q^2\ell_s^2}{3} \right), \end{aligned} \quad (1.39)$$

where we expanded Eq. (1.39) at small  $\Omega$  to obtain the long time limit and identified the mean free path  $k\ell_s(\omega) = 1/\rho \text{Im}[\alpha(\omega)]$  and noticed that  $|\alpha(\omega)|^2 = \text{Im} \alpha(\omega) 4\pi/k_0^3$  in the resonant scatterers such as the ones defined in Eq. (1.27). We then obtain

$$\alpha \left( \omega + \frac{\Omega}{2} \right) \alpha^* \left( \omega - \frac{\Omega}{2} \right) \simeq |\alpha(\omega)|^2 \left( 1 + \frac{2i\Omega}{\Gamma_0} \frac{1}{\delta^2 + 1} \right). \quad (1.40)$$

Finally, when inserting Eqs. (1.40) and (1.39) in Eq. (1.36), we end up with

$$\left[ \frac{q^2\ell_s^2}{3} - i\Omega \left( \frac{\ell_s}{c} + \frac{1}{\Gamma_0} \right) \right] I(\mathbf{q}, \omega, \Omega) = I_0(\mathbf{q}, \omega, \Omega), \quad (1.41)$$

where  $I_0(\mathbf{q}, \omega, \Omega) \equiv \text{FT}[\langle G(\mathbf{r}, \omega^+) \rangle \langle G^*(\mathbf{r}, \omega^-) \rangle] (\mathbf{q})$  can be viewed as a source term. Equation (1.41) is a diffusion equation for the average intensity. The left-hand side of Eq. (1.41) can be rewritten as  $[\partial_t - D(\omega)\nabla^2] I(\mathbf{r}, t, \omega)$  where

$$D(\omega) = \frac{\ell_s^2}{3} \left[ \frac{\ell_s}{c} + \frac{1}{\Gamma_0} \right]^{-1} = \frac{\ell_s^2}{3} \frac{1}{\tau_s + \tau_r}. \quad (1.42)$$

Here  $\tau_s = \ell_s/c$  is the mean time between scattering events and  $\tau_r = 1/\Gamma_0$  close to resonance.

This simple model gives two scattering regimes. Far from the resonance, the energy velocity  $v_E$ , defined by  $D = \ell_s v_E / 3$  in 3D is simply the celerity of light. Close to the resonance, the scattering time is dominated by the trapping inside the particle such that  $v_E \simeq \ell_s \Gamma_0$ .

Using only the Bethe-Salpeter equation and exact results for diluted systems, we showed that the average intensity satisfies a diffusion equation and computed its diffusion coefficient. Equation (1.32) is actually more general as it involves two fields evaluated at different positions and different frequencies. It can be used to derive, without any assumption on the shape of  $\mathbf{U}$ , the radiative transfer equation as well as a diffusion equation (Carminati and Schotland, 2021) for the general two-fields correlator. In this more complete approach, the mean free path for the average intensity can be different from the one of the average field  $\ell_s$  because of scattering anisotropy. Precisely, we assumed an isotropic scattering process in  $\mathbf{U}_0$  but for larger objects with more complicated  $\mathbf{T}$ -operator or when including more complicated scattering path, the isotropy hypothesis does not hold. The transport mean free path  $\ell_t$  and  $\ell_s$  are linked through an anisotropy factor  $g$  by

$$\ell_t = \frac{\ell_s}{1 - g}, \quad (1.43)$$

where  $g \in [-1, 1]$ . We will go back to the computation of  $g$  in Chap. 5

In the last two sections, we restricted our analysis to the low density regimes ( $\Sigma \simeq \Sigma_{\text{ISA}}$  and  $\mathbf{U} \simeq \mathbf{U}_0$ ). Going beyond requires to expand  $\Sigma$  to higher order in density. Several methods can be used to go beyond the low density approximation of the self energy ( $\Sigma \simeq \Sigma_{\text{ISA}}$ ). The first one is to continue the density expansion giving rise to the ISA, up to higher order. This approach will be studied in the framework of correlated disorder in Chap. 4. Alternatively, we can also switch from a *macroscopic* description of the problem in terms of the mean-field quantities where the constituting details of the system have been erased to a *microscopic* description. In the next section, we will develop a fully microscopic description of the resonances of a system and try to solve it exactly. It is called the coupled dipoles or the Foldy-Lax method.

## 1.5 A fully microscopic description: the coupled dipoles method

This section aims at describing the coupled dipole method used intensively in this work. It allows to compute (numerically) the collective complex frequencies of an ensemble of coupled point-dipoles in a medium. The approach requires the positions of the resonators, their response to an exciting field and the free-field Green's function to be known.

### 1.5.1 General approach

In this study, we consider light propagation at frequency  $\omega = ck$  in an ensemble of  $N$  identical resonant scatterers characterised by their polarisability  $\alpha(\omega)$ . The field  $\mathbf{E}_i$  exciting a scatterer  $i$  is the sum of the input external field  $\mathbf{E}_0(\mathbf{r}_i)$  and the fields radiated by scatterers  $j \neq i$ :

$$\mathbf{E}_i = \mathbf{E}_0(\mathbf{r}_i) - k^2 \alpha(\omega) \sum_{j \neq i} \mathbf{G}_0(\mathbf{r}_i, \mathbf{r}_j, \omega) \mathbf{E}_j. \quad (1.44)$$

Here,  $\mathbf{G}_0$  is the free space Green's function of the wave equation, propagating the field between different scatterers. The excitation fields  $\mathbf{E}_i$  can be linked to the induced dipole moment  $\mathbf{p}_i$  according to  $\mathbf{p}_i = \varepsilon_0 \alpha(\omega) \mathbf{E}_i$ . The derivation of the coupled dipole equations (1.44) (CDE), in a semi-classical Foldy (1945); Lax (1951) or full quantum framework Lehmberg (1970); Goetschy (2011), shows that  $\alpha(\omega)$  also depends on the field polarisation. Equation (1.44) defines a closed set of equations which once inverted gives the total field at any position  $\mathbf{r}$  as

$$\mathbf{E}(\mathbf{r}) = \mathbf{E}_0(\mathbf{r}) - k^2 \alpha(\omega) \sum_i \mathbf{G}_0(\mathbf{r}, \mathbf{r}_i, \omega) \mathbf{E}_i. \quad (1.45)$$

The equation above can be used to compute for example the mean-field response of an ensemble of scatterers simply by averaging the field obtained in each disordered realisation, as in Rohfritsch et al. (2020) to evaluate the effective index numerically without any assumption. It is not the scheme we pursued. In this thesis, we will be particularly interested in the collective complex resonances of the system. By definition, resonances of the scattering problem are solutions  $\omega$  in the absence of external excitation ( $\mathbf{E}_0 = \mathbf{0}$ ). According to Eq. (1.44) they satisfy the equation

$$\det [\mathbb{1} + k^2 \alpha(\omega) \mathbb{G}_0(\omega)] = 0, \quad (1.46)$$

where  $\mathbb{G}_0(\omega)$  is a  $\beta N \times \beta N$  matrix ( $\beta = 1$  for scalar waves and  $\beta = 2, 3$  for vector waves in 2D or 3D) with element  $ij, i \neq j$  equal to  $\mathbf{G}_0(\mathbf{r}_i, \mathbf{r}_j, \omega)$  and element  $ii$  equal to  $\mathbf{0}$ . Equation (1.46) rigorously captures all the poles of the total scattering operator, except those associated to peculiar field solutions that are zero on each scatterer ( $\mathbf{E}_i = 0$  for all  $i$ ). The latter, which behave as free field without matter, may exist in crystals because of the periodicity (Klugkist et al., 2006; Antezza and Castin, 2009a) but are unlikely for disordered materials. In the following, the polarisability of each scatterer is assumed to have a single resonance at  $\omega_0$  and a radiative decay rate  $\Gamma_0$ . For  $|\omega - \omega_0| \ll \omega_0$ , it takes the form  $\alpha(\omega) = \tilde{\alpha}(\omega) c_d / k_0^d$ , with  $c_d$  a constant depending only on the dimensions of space and of the field type (scalar or vector) taking the values

$d$	2	3
scalar	4	$4\pi$
vector	8	$6\pi$

and  $\tilde{\alpha}$  defined as

$$\tilde{\alpha}(\omega) = \frac{-\Gamma_0/2}{\omega - \omega_0 + i\Gamma_0/2}. \quad (1.47)$$

The resonance condition (1.46) is then conveniently expressed in terms of an effective Hamiltonian  $\mathcal{H}(\omega)$  as  $\det [\omega \mathbb{1} - \mathcal{H}(\omega)] = 0$ , with

$$\mathcal{H}(\omega) = \left( \omega_0 - i \frac{\Gamma_0}{2} \right) \mathbb{1} - \frac{\Gamma_0}{2} \tilde{\mathbb{G}}_0(\omega), \quad (1.48)$$

and  $\tilde{\mathbb{G}}_0(\omega) = -c_d k^2 k_0^{-d} \mathbb{G}_0(\omega)$ . In this way, light-matter interaction is entirely characterised by an effective potential proportional to the Green's matrix  $\tilde{\mathbb{G}}_0(\omega)$  (Akkermans et al., 2008; Antezza and Castin, 2009b; Goetschy, 2011). For  $N \gg 1$  scatterers, the frequency dependence of  $\tilde{\mathbb{G}}_0(\omega)$  makes the search for resonances a cumbersome non-linear problem, which can be treated exactly for periodic point patterns (see discussion in Sec.1.7.2), but not for the broad class of disordered patterns considered in this work. In the following, we will address the case of scattering resonators with large quality factor ( $Q = \omega_0/\Gamma_0 \gg 1$ ), for which the coupling term in Eq. (1.48) can be treated as a perturbation. This amounts to freezing the frequency of  $\tilde{\mathbb{G}}_0(\omega)$  at the resonance frequency  $\omega_0$ . This is an excellent approximation for light scattering in atomic systems, which we expect to hold as well for Mie-type resonators with  $Q \gtrsim 10$ . In this situation, there are  $\beta N$  complex resonances  $\omega_n - i\Gamma_n/2$  given by

$$\begin{cases} \omega_n = \omega_0 - \frac{\Gamma_0}{2} \text{Re}\Lambda_n, \\ \Gamma_n = \Gamma_0 (1 + \text{Im}\Lambda_n), \end{cases} \quad (1.49)$$

where  $\Lambda_n$  are the eigenvalues of the Green's matrix  $\tilde{\mathbb{G}}_0(\omega_0)$ . For finite-size systems,  $\Lambda_n$  occupy an extended domain in the complex plane, with  $\text{Im}\Lambda_n > -1$  (Skipetrov and Goetschy, 2011).  $\text{Re}\Lambda_n$  represent the collective Lamb shifts and  $\text{Im}\Lambda_n$  the collective decay rates. For simplicity

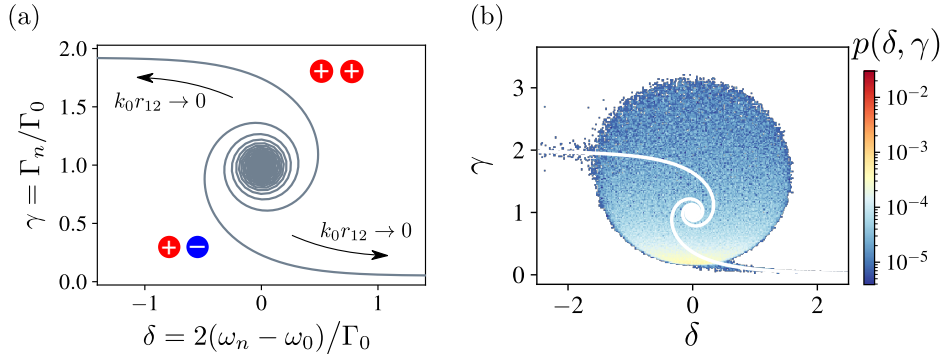


Figure 1.7: (a) Eigenvalues of the Hamiltonian (1.51) with respect to the only free parameter  $k_0 r_{12}$  for 2D scalar coupling. The upper spiral describes a symmetric excitation (double plus sign) whose detuning becomes negative for  $k_0 r_{12} \rightarrow 0$  and the linewidth plateaued out at twice the initial linewidth, while the lower one, an anti-symmetrical one (plus and minus sign) with a positive detuning and a vanishing linewidth. (b) Distribution of eigenvalues of  $N = 4000$  particles and  $k_0 a = 7$  in 3D with a scalar coupling. The two particles trajectory has been added to highlight the reminiscence of (a), even in a case where  $N \gg 2$ .

and if not explicitly stated otherwise, in the rest of the thesis we will work with high quality factor and reduced frequency variables such that

$$\delta_n = 2 \frac{\omega_n - \omega_0}{\Gamma_0} = -\text{Re } \Lambda_n \quad \text{and} \quad \gamma_n = \frac{\Gamma_n}{\Gamma_0} = 1 + \text{Im } \Lambda_n, \quad (1.50)$$

where  $\delta_n$  is the detuning and  $\gamma_n$  the normalised linewidth.

### 1.5.2 Examples with two dipoles

The simplest Hamiltonian (1.48) we can write involves two particles and a scalar coupling field leading to  $2 \times 2$  matrix:

$$\mathcal{H}(r_{12}, \omega_0) = - \begin{pmatrix} i & \tilde{G}_0(r_{12}, \omega_0) \\ \tilde{G}_0(r_{12}, \omega_0) & i \end{pmatrix}, \quad (1.51)$$

where  $\tilde{G}_0(r_{12}, \omega_0) = -c_d k^2 k_0^{-d} G_0(r_{12}, \omega_0)$  and  $r_{12}$  is the distance between the two resonators. Even though the Hamiltonian is non hermitian, it is still easily diagonalisable with  $\delta_n^\pm = \mp \text{Re } \tilde{G}_0(r_{12}, \omega_0)$  and  $\gamma_n^\pm = 1 \pm \text{Im } \tilde{G}_0(r_{12}, \omega_0)$ . The two eigenvalues only depend on the reduced parameter  $k_0 r_{12}$ . Each eigenvalue describes a spiral in the complex plane when  $k_0 r_{12}$  is changed, leading to the spectrum shown in Fig. 1.7(a). The direct observation of the symmetrical and anti-symmetrical mode described by each branch can be found in Ref. Michaelis de Vasconcellos et al. (2011)

### 1.5.3 Example with $N \gg 2$ , density of states and inverse participation ratio

When we consider a larger number of resonators, the spectrum cannot be simply computed as in the previous section, and each realisation of the disorder will give a new set of modes, completely different from one another. It is thus interesting to come up with aggregated observables that can be averaged out over the disorder. In this case, we can define the joint probability density of eigenvalues in  $\{\delta, \gamma\}$  space as in Fig. 1.7(b). Explicitly we define

$$p(\delta, \gamma) = \frac{1}{\beta N} \left\langle \sum_{n=1}^{\beta N} \delta(\delta - \delta_n) \delta(\gamma - \gamma_n) \right\rangle, \quad (1.52)$$

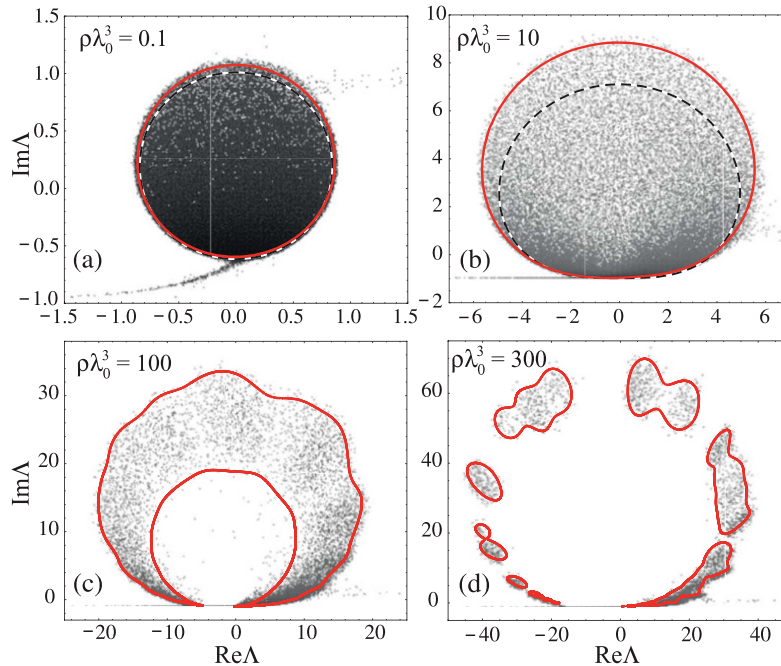


Figure 1.8: Distribution of eigenvalues in the complex plane of fully disordered ensembles of  $N = 10^4$  resonators coupled by a scalar field in 3D at different density regimes characterised by  $\rho\lambda^3$ . The predictions for the border of the distribution are shown in red and are found to be a two parameter function depending only on  $N$  and  $\rho\lambda^3$ . Figure from Goetschy and Skipetrov (2011a).

where  $p(\delta, \gamma)$  is the joint probability of  $\delta$  and  $\gamma$  and  $\beta$  the dimension of the field (1 for scalar fields and  $d$  for vector fields in  $d$ -dimensions). Often, we will be interested in the marginal distribution of the frequencies  $p(\omega)$  such that we also define

$$p(\omega) = \frac{1}{\mathcal{V}} \left\langle \sum_{n=1}^{\beta N} \delta(\omega - \omega_n) \right\rangle = \frac{2\beta\rho}{\Gamma_0} p(\delta), \quad (1.53)$$

where  $\mathcal{V}$  is the  $d$ -dimensional volume occupied by the disordered sample, and  $p(\delta)$  is the distribution of the normalised detuning. In the thermodynamic limit ( $N \rightarrow \infty$ ,  $\mathcal{V} \rightarrow \infty$ , at fixed density  $\rho = N/\mathcal{V}$ ), almost all complex eigenvalues  $\omega_n - i\Gamma_n/2$  collapse on the real axis and the definition (1.53) coincides with the density of modes of the Hamiltonian (1.48). The distribution of  $\Lambda_n$  in the complex plane has been characterised theoretically in details for scalar and vector waves in 3D fully disordered systems (Skipetrov and Goetschy, 2011; Goetschy and Skipetrov, 2011a,b; Goetschy, 2011). Examples of predictions of the bounds of the distributions is given in Fig. 1.8 from dilute and diffusive systems up to densities leading to homogenisation. These works highlighted the role of the finite mode life-times due to finite system size, as they offer valuable information about localisation properties of the corresponding eigenstates (Goetschy and Skipetrov, 2011a; Skipetrov and Sokolov, 2014; Bellando et al., 2014; Skipetrov, 2016).

The obvious symmetry of the eigenmodes  $|\psi_n\rangle$  or  $\mathcal{H}$  for  $N = 2$  also disappears with large system. An observable called the Inverse Participation Ratio (IPR) is used to characterise the spatial extension of a mode  $|\psi_n\rangle$ , and is defined for scalar fields as (Mirlin, 2000)

$$\text{IPR}_n = \frac{\sum_i^N \|\psi_{n,i}\|^4}{\left(\sum_i^N \|\psi_{n,i}\|^2\right)^2}, \quad (1.54)$$

where  $\psi_{n,i}$  is the component of  $|\psi_n\rangle$  at position  $r_i$ . For vector fields,  $\psi_{n,i} \equiv \sqrt{\psi_{n,i} \cdot \psi_{n,i}}$  where  $\boldsymbol{\psi}_{\mathbf{n},i}$  is the vector polarisation field on particle  $i$  for the  $n^{\text{th}}$  mode. The IPR goes from  $1/N$  if the mode is equally spread over all the scatterers, to 1 if it is only carried by a single resonator. This observable is particularly useful to characterise localised states (see Sec. 1.6.4).

A keen reader may have noticed that up to now, we did not talk about the regime of localisation, where the field exists in the form of localised modes in the bulk of a material. This regime, which can be observed using the coupled dipoles method described above, cannot be captured by the mean-field approach developed in Sec. 1.3.3. However it can be accessed in the framework of the average two-fields correlators studied in Sec. 1.4, as we will see in the next section and in particular in Sec. 1.6.2.

## 1.6 Introduction to Anderson localisation

This section will introduce the principles of Anderson localisation as well as some useful theoretical models used to describe it. Anderson localisation is a phenomenon where disorder is strong enough to impede the propagation of a wave due to multiple scattering. The complex interference effect creates an exponential attenuation of the average intensity over a lengthscale called the localisation length  $\xi$ . In this section we will pay a particular attention to the effect of dimensionality as Anderson localisation has been found to strongly depend on the space dimension. While in three dimensions the propagation of scalar waves in disordered potentials is known to exhibit a real phase transition between a diffusive regime and an Anderson localised regime with the scattering mean free path as the order parameter, in one and two dimensions localisation always occurs over a certain extend. Anderson localisation or strong localisation may yet be difficult to observe in finite-sized samples if the attenuation length is not much smaller than the observed system size. At first we will focus on the corrections to regular diffusion theory used to characterise what is called *weak localisation*: a precursor to strong localisation. We will then show that this approach can be extended to capture strong localisation through a self-consistent renormalisation of the diffusion coefficient. It will give us the range of parameters where the Anderson transition is expected to occur in 3D, or the localisation length in lower dimensions. To finish the theoretical description of strong localisation, special light will be shed on a scaling analysis which will uphold the dimensionality effects of the phenomenon.

The rest of the section will present recent numerical and experimental work on the topic, with particular spotlight on the physical aspects which can promote or deter localisation.

### 1.6.1 Weak localisation corrections

We showed using the Bethe-Salpeter equation that considering two fields  $\mathbf{E}$  and  $\mathbf{E}^*$  propagating along the same sequence will lead to a diffusion equation for the average intensity. The first sequences which result in a weak localisation effect are called cooperons. In a cooperon, the two fields still scatter on the same resonators, but not in the same order. Figure 1.9 (a) features such a sequence. There is an exchange site represented by a yellow region where the two paths deviate and end up following a sequence in reverse order before rejoining at the crossing site. The phase mismatch between the two paths is given by the path difference at the crossing site. The contribution of a cooperon will therefore be important if the scatterers involved in the exchange are close. To take this effect into account, we first consider a ladder sequence with a crossing, and then every additional sequences where the loop in the cooperon is of arbitrary length. On top of  $\mathbf{U}_0$ , we need to include in the irreducible vertex the following terms:

$$\mathbf{U}_C = \begin{array}{c} \text{Diagram 1} \\ \text{Diagram 2} \\ \text{Diagram 3} \\ \text{Diagram 4} \end{array} + \dots \quad (1.55)$$

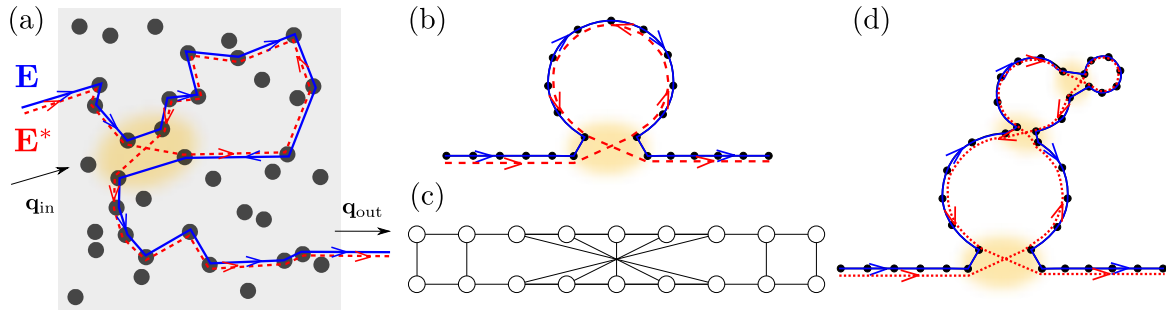


Figure 1.9: (a) Real space representation of a diffusion sequence involved in weak localisation corrections. The field and the conjugated one follow the same path as in regular diffusion, except in a loop where an exchange happens after which they follow the diffusion sequence in reverse order. The exchange site is highlighted by a yellow domain and this kind of exchange loop are called a cooperon. (b) Schematic representation of the events of (a). (c) Equivalent diagrammatic representation of the sequence with ladders surrounding the cooperon loop. (d) Iterated version of the cooperon happening inside a cooperon loop.

This first correction induces a negative correction in the diffusion constant involving the return probability of a random walk in the considered system (Müller and Delande, 2016) as

$$\frac{1}{D} = \frac{1}{D_0} \left[ 1 + \frac{1}{\pi p(\omega) D_0} \int \frac{d\mathbf{q}}{(2\pi)^d} \frac{1}{q^2 - i0^+} \right]. \quad (1.56)$$

It can be rewritten by considering that the correction to  $D$  are small as  $D = D_0 - D_0 P_0$  where  $P_0$  is the return probability of the diffusion kernel at infinite time. Indeed, integrating the diffusion Green's function in Fourier space amounts to evaluating the diffusive propagator from the origin to the origin. Taking the limit of vanishing frequency leads to consider the sum over all possible return times, and thus the integral includes all possible paths returning to the origin after any given time. This correction is responsible for the well known Coherent Back Scattering effect (CBS), studied in Akkermans et al. (1986). In the context of localisation, the above equation can give us insight on the behaviour of the wave. We assumed in this case the free space density of states in  $p(\omega)$  and expressed the Boltzmann diffusion coefficient in non resonant systems such that  $D_0 = \ell_t c/d$ , to obtain

$$D = D_0 \left( 1 - \frac{d}{\pi k^{d-1} \ell_t} \int_0^\infty dq \frac{q^{d-1}}{q^2 - i0^+} \right). \quad (1.57)$$

In 3D, the integral can be computed by setting a cut-off at large  $q$ , which can be taken as  $1/\ell_t$  as the smallest length-scale where diffusion takes place. The diffusion coefficient becomes  $D \simeq D_0 (1 - 3/\pi(k\ell_t)^2)$ . For large values of the mean free path, it gives accurate estimates of the diffusion coefficient but we see that it breaks down when  $k\ell_t = \sqrt{3/\pi} \sim 1$ , predicting a negative diffusion coefficient. This criterion called the Ioffe-Regel criterion (Ioffe and Regel, 1960) gives an estimate of the onset of strong localisation.

Interestingly, one cannot derive such conditions in less than 3D. In 1D, the integral is computed using a small  $q$  cut-off of  $1/R$ , where  $R$  is the system size and gives  $D = D_0 (1 - R/2\ell_t)$ . The diffusion constant is expected to go to zero as the system size grows, leading to the prediction that light always localises in 1D. This equation is not valid for large systems, but the transport regime prediction turns out to be accurate as we will show later in Sec. 1.6.2.

In two dimensions, one needs to use both the small and the large  $q$  cut-off to obtain the diffusion coefficient  $D \simeq D_0 \left[ 1 - \frac{2}{\pi k \ell_t} \ln \left( \frac{R}{\ell_t} \right) \right]$ . This formula also predicts a vanishing diffusion constant for large systems but compared to the 1D case, the rate depends strongly

on the mean free path. This rough preliminary result also predicts a localised behaviour of waves in infinite systems, in agreement with the more elaborate scaling theory developed later.

Weak localisation as a bulk phenomenon only occurs in 3D where the diffusion coefficient only depends on bulk variables. At lower dimension, the weak localisation correction is only meaningful for (very) small systems where  $L \ll \ell_t$  in 1D and  $R \ll \exp(\pi k \ell_t / 2)$  in 2D. The limits of the weak localisation approach come from two aspects, first in the computation of the return probability in Eq. (1.56) we assumed a diffusive transport regime which by definition cannot catch a localised regime. It is particularly problematic in one and two dimensions where the transport may not be diffusive. Another issue is the truncated expansion of the irreducible vertex  $\mathbf{U}$ . Only the maximally crossed diagrams have been included while localisation is a highly collective effect which cannot be approximated by such an expansion. A solution has been brought by Wölfle and Vollhardt (2010) with the use of a self-consistent approach.

### 1.6.2 Self-consistent approach to Anderson Localisation

The idea of the self consistent theory of localisation is to keep the renormalised diffusion coefficient in the right hand side of Eq. (1.56) and to keep the frequency dependence. This actually amounts to allowing a *cooperon* to form inside a first *cooperon* loop as described in Fig. 1.9 (d). Another simplification has been to take the density of states  $p(\omega)$  at its free space value. This seemingly strong hypothesis is relevant in the case of non dispersive systems, but will lead to some important corrections in resonant systems as we will show in Chap. 5. Instead of looking at finite-size effects we can look at time dynamics in infinite bulk systems by keeping the frequency as a variable. One ends up with

$$\frac{1}{D(\omega)} = \frac{1}{D_0} \left[ 1 + \frac{1}{\pi p(\omega)} \int \frac{d\mathbf{q}}{(2\pi)^d} \frac{1}{D(\omega) q^2 - i\Omega} \right]. \quad (1.58)$$

**1D case** In 1D, the integral is regular for finite  $\Omega$  and leads to

$$\frac{D(\omega)}{D_0} = \frac{\sqrt{1 - 16i\Omega\tau - 1}}{\sqrt{1 - 16i\Omega\tau + 1}} \underset{\Omega\tau \ll 1}{\simeq} -4i\Omega\tau, \quad (1.59)$$

where  $\tau = \ell_t^2 / D_0$  is the scattering mean free time. The now purely imaginary diffusion coefficient obtained in the long time, small  $\Omega$  limit in Eq. (1.59) changes the diffusion kernel  $1/(-i\Omega + D(\omega)q^2) \rightarrow i/\Omega \times 1/(1 + 4\ell_t^2 q^2)$  such that in real space the average intensity behaves as  $\exp(-r/\xi)$  with  $\xi = 2\ell_t$  which is the exact result for the localisation length.

**2D case** In two dimensions we can calculate the integral of Eq. (1.58) using the same large  $q$  cut-off as in Sec. 1.6.1. The diffusion coefficient is given by the implicit equation

$$\frac{D(\omega)}{D_0} = 1 - \frac{1}{\pi k \ell_t} \ln \left[ 1 - \frac{D(\omega)}{D_0} \frac{1}{2i\omega\tau} \right]. \quad (1.60)$$

Even if the renormalised self-consistent diffusion coefficient depends on  $k\ell_t$ , it does not influence the fact that at short time ( $\omega\tau \ll 1$ ), we have a diffusive kernel with  $D \simeq D_0$ , and localisation at long time. The localisation length  $\xi$  reads

$$\xi = \ell_t \sqrt{\exp(\pi k \ell_t) - 1} \simeq \ell_t \exp\left(\frac{\pi k \ell_t}{2}\right), \quad (1.61)$$

which is the usual formula used in 2D systems, *e.g.* in Laurent et al. (2007a) or Conley et al. (2014). The exponential dependence of  $\xi$  on  $k\ell_t$  is interesting to turn a localised system into an effective diffusive one by a simple adjustment of  $k\ell_t$ .



**3D case** The 3D case is the most complicated as the implicit equation obtained from Eq. (1.58),

$$\frac{D(\omega)}{D_0} = 1 - \frac{3}{\pi(k\ell_t)^2} \left[ 1 - \frac{\pi}{2} \sqrt{\frac{-3i\omega\tau}{D(\omega)/D_0}} \right], \quad (1.62)$$

highlights three different regimes and a real phase transition characterised by a critical value of the order parameter,  $k\ell_c = \sqrt{3/\pi} \sim 1$  (Ioffe-Regel's criterion). Above the critical value ( $k\ell_t > k\ell_c$ ), the diffusion coefficient goes to a constant at long time, indicating a diffusion behaviour. Equation (1.62) can then be used to evaluate the correction to the Boltzmann diffusion constant  $D_0$ , correction which is always negative. Below the critical value  $k\ell_t < k\ell_c$ , the diffusion constant vanishes at long time leading to exponential localisation with

$$D(\omega) \simeq -i\omega\xi^2 \quad \text{and} \quad \xi \simeq \frac{1}{k\ell_c - k\ell_t}. \quad (1.63)$$

A knowledgeable reader may notice that the localisation transition exhibits a critical exponent of  $\nu = 1$ . This observation is in contradiction with numerical simulations which give  $\nu = 1.58 \pm 0.01$  (see Refs. Slevin and Ohtsuki (1999) and Lemarié et al. (2009)). The third regime lies at the critical point itself. The diffusion coefficient reads  $D(\omega) \sim (-i\omega)^{1/3}$ , leading to a sub-diffusive behaviour  $\langle r^2(t) \rangle \propto t^{2/3}$ .

The self-consistent approach to Anderson localisation has the merit to pinpoint the role of some scattering process such as the maximally crossed diagrams. At the transition, the system becomes critical and many types of scattering events are expected to participate to localisation. We can cite in particular the ones involved in the coherent forward scattering (Karpiuk et al., 2012; Ghosh et al., 2014; Hainaut et al., 2018) which, even though weaker than the cooperon in general, can play a role near the critical point. These other families of scattering events were, to our knowledge, not taken into account into a self-consistent diffusion theory. Their consideration may give a values closer to numerical simulations for the critical exponent for the localisation length.

Through a self-consistent renormalisation of the diffusion coefficient, we obtain quantitative predictions for the diffusion coefficient and the localisation length. A more general approach, uses the renormalisation group and scaling theory.

### 1.6.3 Scaling theory of Anderson localisation

The scaling approach of Anderson localisation falls into the more general renormalisation group methods. The general approach is to infer the behaviour of a system from the dependence of the parameters of a model with respect to the size of its constituting elements or the overall size. An historical example is the Ising model for spins connected through a network. We look for new effective couplings connecting groups of spins with each-others. It can be viewed as a decimation process of the initial graph to obtain the behaviour of an effective *zoomed-out* version of the initial system (Cardy, 1996). The derivation can be iterated to obtain the macroscopic behaviour of such system from first principles parameters. In our situation, we suppose that our system can be described solely by a dimensionless conductance called the Thouless conductance  $g$  in reference to Thouless (1974). The latter can be defined as:

$$g = \frac{\gamma(\omega)}{\langle \omega_{n+1} - \omega_n \rangle_n}, \quad (1.64)$$

where  $\gamma(\omega)$  is the typical linewidth of a mode, and  $\langle \omega_{n+1} - \omega_n \rangle_n$  is the mean spacing between two neighbouring modes. The behaviour of the conductance with the system size is evaluated from basic physical arguments following Abrahams et al. (1979). If the conductance is large, most of the modes spectrally overlap, the macroscopic diffusive transport theory is valid, leading to Ohmic transport. Therefore we have  $g(R) \sim \sigma R^{d-2}$  with  $\sigma$  the bulk conductivity

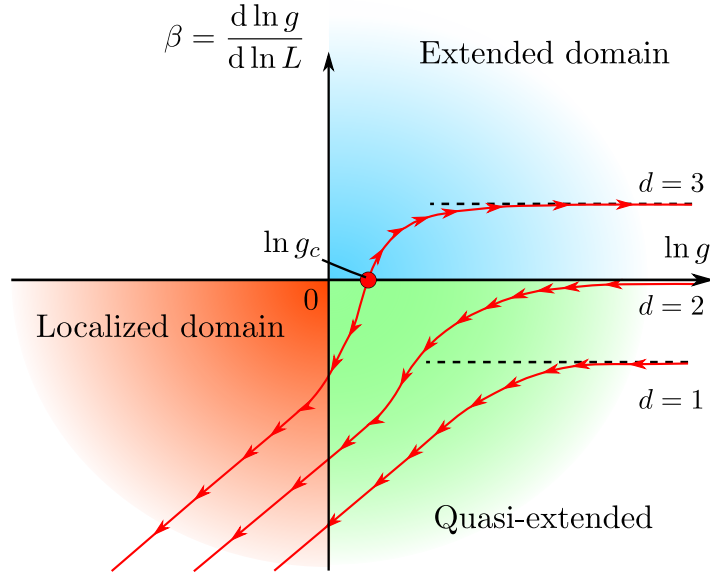


Figure 1.10: Renormalisation flow of the dimensionless conductance  $g$  (solid red line), in different dimensions. The domain of positive  $\beta$  and positive  $\ln g$ , indicates that the conductance grows with the system size, it corresponds to a metallic or diffusive regime in blue. The domain of small conductance and negative  $\beta$  corresponds to a localised regime in red. The last one is intermediary, as it has decent values of the conductance, yet negative values for  $\beta$ . It means that in infinite systems, the conductance should decrease to zeros, hence the name quasi-extended regime. It exists only in finite-size systems. The graph has been adapted from Ref. Abrahams et al. (1979).

in the material,  $R$  the system size and  $d$  the spatial dimension (Thouless, 1974). By defining a scaling function as

$$\beta(g) = \frac{d \ln g}{d \ln R}, \quad (1.65)$$

we find  $\lim_{g \rightarrow \infty} \beta_d(g) = d - 2$ . If we now consider the regime of very low conductivity ( $g \ll 1$ ), we expect the modes to be spatially localised leading to  $g \simeq g_\xi e^{-R/\xi}$ , where  $\xi$  is the localisation length and  $g_\xi$  is depending only of  $\xi$ . It directly leads to  $\lim_{g \rightarrow 0} \beta = \ln\left(\frac{g}{g_\xi}\right)$ . The two asymptotics are shown in Fig. 1.10, and the rest can be roughly extrapolated by continuity. The existence of inflexion points as well as the slope of the first corrections from the limit cases were obtained in Abrahams et al. (1979) through microscopic consideration on the relevant physical processes involved, but it goes beyond the scope of this introducing chapter.

The plot in the  $\left\{ \ln g, \frac{d \ln g}{d \ln R} \right\}$  space defines a renormalisation flow meaning that a given system is described by a point in the parameter space and depending on its location, we can extrapolate the behaviour of a larger version of the same system. Explicitly, a positive  $\beta$  indicates that a scale factor will increase the value of  $g$ . In one and two dimensions, the theory predicts that no matter the starting point, the fields will localise above a certain size  $R$ . This is in striking contrast with the 3D case and in perfect agreement with other approaches based on transfer matrix theory (Beenakker, 1997). In 2D though, we can notice that if the conductance is high enough the scaling function  $\beta$  is very close to zero, hinting on a good transport regime only because the system is not large enough to develop a localised behaviour at its full extent. This is in agreement with the self-consistent theory where the localisation only occurs at long time, or over a exponentially large length scale [see Eq. (1.61)]. The 3D case is maybe the most interesting because by merely using a continuity condition and two

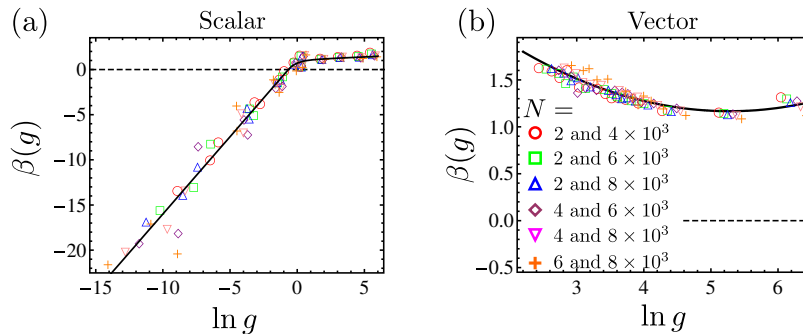


Figure 1.11: Finite-size scaling in 3D for a scalar coupling (a) and for vector coupling (b) taken from Skipetrov and Sokolov (2014). The values of  $\beta(g)$  and  $\ln g$  are obtained using the coupled dipoles method at fixed frequency ( $\delta = 1$ ) for different densities. The scalar system has the typical shape described in Fig. 1.10 where a localisation transition occurs. Above  $\beta(g) = 0$  the modes will stay delocalised in infinite samples, while below 0 they will exponentially decay over a given lengthscale. The situation differs for vector fields as  $\beta(g)$  stays always positive, suggesting the absence of localisation in infinite systems.

limit cases, we can predict the existence of a critical value of the conductance dividing two drastically different behaviour for the transport. Below the threshold,  $\beta$  is negative and we recover the same localisation behaviour as in one and two dimensions for large systems. On the other hand, above a critical value,  $\beta$  is positive and the modes remain extended even in infinite media. The explicit values of the localisation lengths, or the critical conductance value can be obtained with the full use of renormalisation group theory and microscopic parameters such as the mean free path. The localised domain shown in red in Fig. 1.10 is fairly easy to discriminate experimentally as the conductance is really low and decreases exponentially with the sample size. The extended and quasi-extended regimes are more problematic to distinguish as one can think of being in the extended one simply because the system is smaller than the spatial extension of a localised bulk mode. Finite-size effects are therefore very important when working with 2D systems, even more than in 3D.

#### 1.6.4 Dimensionality, polarisation and short-range

The main interest of the scaling approach to Anderson localisation is that it gives simple predictions on localisation as a function of the space dimension. Nevertheless it has only been fully derived in the case of scalar fields in the context of the quantum treatment of electrons in solids (Zdetsis et al., 1985). Light can only be viewed as a scalar field under some stringent approximations and need in general to be treated as a fully vector field described by a dyadic Green's function [see Eqs. (1.4) and (1.6)]. This first change from the canonical scaling theory has already driven some controversy over the possibility for vector light to localise (Wiersma et al., 1997; Scheffold et al., 1999). A numerical framework based on the eigenmodes of the Green's matrix (Sec. 1.5.1) has been developed in Skipetrov and Sokolov (2014) and Skipetrov (2016) to evaluate the behaviour of the conductance in finite-size systems. We can define the conductance of each mode of the Green's matrix by

$$g_n = \frac{\gamma_n}{\langle \omega_{n+1} - \omega_n \rangle_n}, \quad (1.66)$$

where we used Eq. (1.64) and the values of linewidth and mean spacing given by Eq. (1.49). The  $\beta$ -function is then evaluated by computing  $\ln g$  (or its average over fractions of its distribution) for different system sizes.

In 3D, this approach predicts a localisation transition for scalar waves triggered by Ioffe-Regel's criterion with a perfect agreement with the scaling approach introduced in the previous

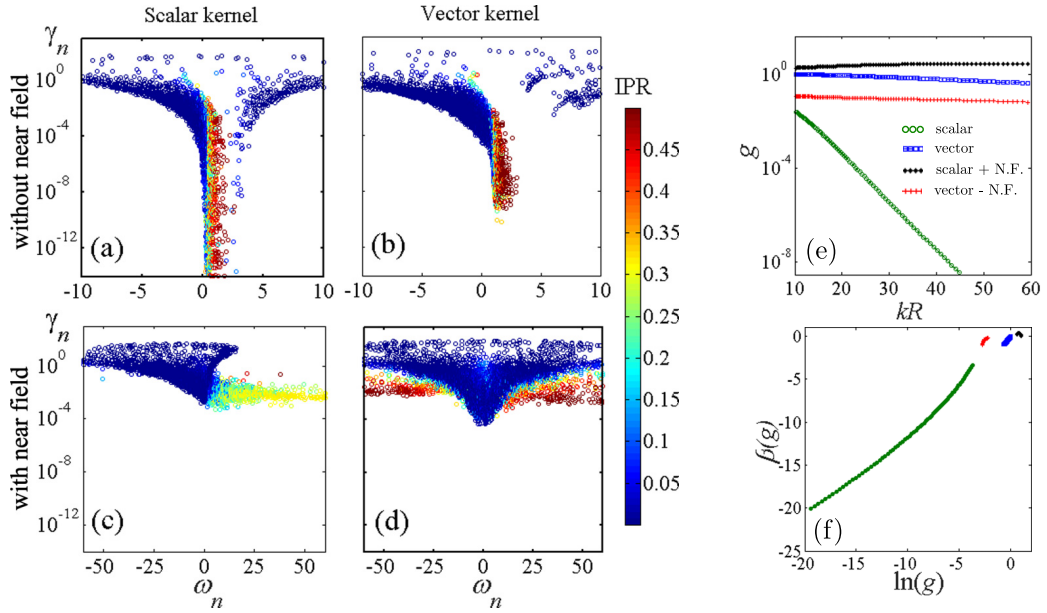


Figure 1.12: Spectra of the Green matrix for 2D systems with a scalar (a) or vector (d) coupling. Figure (b) accounts for the vector situation where the near-field part of the Green’s function has been removed to mimic the short-range behaviour of the scalar setup, while in contrary (c) describes the scalar situation with vector-like near-field. The conductance computed from the spectra (a)-(d) are shown on (e) and the corresponding  $\beta$  function in (f). The figures were taken from Máximo et al. (2015) and highlight the role of near-field effect.

section. This localisation condition can be played with either by changing the frequency at fixed density or at fixed detuning by varying the density (Fig. 1.11). Moreover, the plot of  $\beta(\ln g)$  has the exact same shape as the one in Fig. 1.10. Switching to the full vector description drastically changes the picture. The conductance always increases with the system size, no matter the parameter range. Hence an always positive  $\beta$  function is seen in Fig. 1.11 (b). This has been confirmed theoretically in van Tiggelen and Skipetrov (2021) where it was shown that near-field coupling opened, at high enough density, a new transport channel increasing the diffusion coefficient and destroying localisation. Reference Máximo et al. (2015) made similar observation in 2D: there is no localisation transition in 2D for scalar wave and no localisation has been found at all for vector waves.

Strongly localised modes are visible for scalar couplings in 2D [Fig. 1.12 (a)] and a scaling analysis reveals a negative  $\beta$  function, compatible with Fig. 1.10. On the other hand, the vector spectrum does not possess the usual localisation features characterised by a combination of very small linewidths and strong IPR. The conductance remains rather high, even if slightly lower than 1, and its derivative with the system size is also close to zero but by lower values. The scaling approach is here hardly conclusive as  $\ln g$  is only sampled over a narrow range. The authors concluded in an absence of localisation. One of the interests of the article is to highlight the effect of near-field and polarisation. Indeed, the vector Green’s function is characterised by both a vector kernel and a stronger near-field contribution. Figure 1.12 (c) shows that adding vector-like near-field contribution to the scalar situation prevents visible localisation on the spectrum and actually leads to a now positive  $\beta$  at large conductance. On the other hand, removing the near-field from the vector situation seems to create some localised modes in the distribution in a similar fashion as the regular scalar mode. Yet, the  $\beta$  function remains barely negative even if the conductance has reduced. The fact that the only values of  $g$  probed by Máximo et al. (2015) are high while  $\beta(\ln g)$  is close to zero but negative is still compatible with the scaling result for scalar waves of Fig. 1.10.

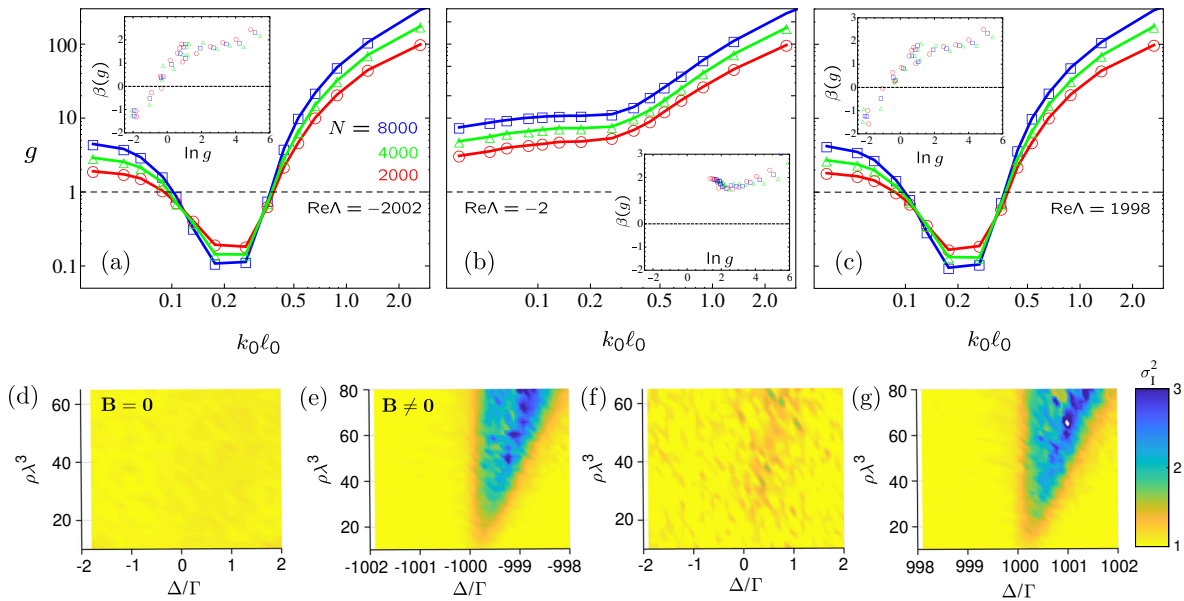


Figure 1.13: Finite-size scaling analysis of the transition  $|f, J = 0\rangle \rightarrow |e, J = 1\rangle$  with full vector coupling and including a Zeeman shift, taken from Skipetrov and Sokolov (2015) (top). Analogous results obtained from intensity fluctuations  $\sigma_I \equiv \langle I - \langle I \rangle \rangle$  with  $I$  the intensity, taken from Cottier et al. (2019) (bottom). The magnetic field is strong enough that the level spacing between the three Zeeman shifted resonances is much larger than the bare linewidth of the transition. The transitions  $|f, m = 0\rangle \rightarrow |e, m = \pm 1\rangle$  are shown in (a,e) and (c,g) respectively and both exhibit localisation features. The  $|f, m = 0\rangle \rightarrow |e, m = 0\rangle$  transition on (b,f) is similar to the system with  $\mathbf{B} = 0$ .

The potential relevance of a near-field propagation channel discussed in details in Refs. Nieuwenhuizen et al. (1994); Skipetrov and Sokolov (2014); van Tiggelen and Skipetrov (2021) and leads to the search for physical systems with different short-range behaviour. The first one was the case of elastic waves in 3D and has been treated in Ref. Skipetrov and Beltukov (2018). The Green's function for the propagation of elastic waves is more complicated than in optics but there are two convenient limits. In the far-field, it can be decomposed in two independent propagation channels, a longitudinal one (compression or p-waves) and a transverse one (shear or s waves). Each channel has a  $r^{-3}$  short-range behaviour, similar to the optical case, yet they compensate in the total Green's function leading to a  $r^{-1}$  dependence as in the scalar case, allowing a localisation transition.

The second one is the propagation of electromagnetic light in cloud of resonant atoms, with the addition of a magnetic field inducing a Zeeman shift. The two-levels atom initially modelled is complexified by considering a transition from a ground state  $|f, J = 0\rangle$  whose total angular momentum is  $J = 0$  to a triply degenerated state with  $J = 1$ , leading to a Zeeman splitting depending on the projection  $m = 0$  or  $\pm 1$  of the excited states. In the absence of magnetic field, this setup is equivalent to the usual 3D vector problem and localisation does not occur as seen in Fig. 1.13 (d). With a strong enough external magnetic field, the three transitions occur in disjointed sets of the frequency range. The two transitions  $|f, m = 0\rangle \rightarrow |e, m = \pm 1\rangle$  exhibit a localisation transition with a distinctive  $\beta(\ln g)$  function (see Fig. 1.13- a,c). The  $|f, m = 0\rangle \rightarrow |e, m = 0\rangle$  transition displays a strictly increasing conductance with the system size, as in the absence of magnetic field. These observations have been corroborated in Cottier et al. (2019) by looking at the intensity fluctuation in such systems. In the limit where the Zeeman frequency shift  $\Delta$  is much larger than the bare linewidth  $\Gamma_0$ , the three transitions can be seen as almost independent and can each be described by an effective Hamiltonian with different behaviours. Apart from a shift in the

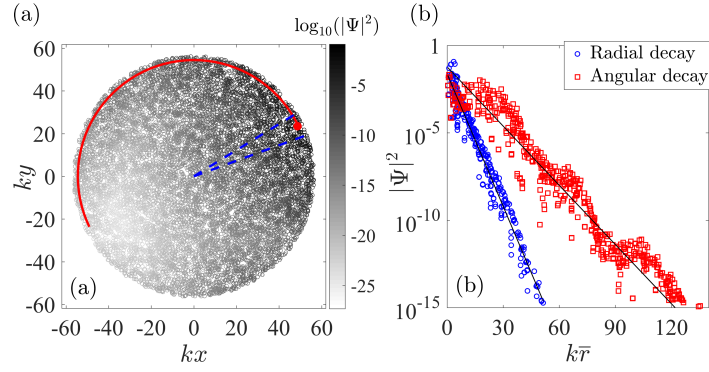


Figure 1.14: Study of localised modes for light on the edges of samples in both 2D and 3D, from Maximo et al. (2019). (a) Spatial profile of the intensity of a mode centred on the edge, and (b) intensity profile along the radial and angular direction. The localisation length of these edge modes is closely related to the behaviour of the bulk mode in  $d - 1$  dimension.

detuning due to  $\mathbf{B}$ , both the far field and the near-field terms accounting for the transition  $m = 0$  to  $m = \pm 1$  are more similar to the scalar case than the  $m = 0$  to  $m = 0$  transition. In particular the near-field terms are two times weaker in the first situation, hence the greater similarity with the scalar case.

Until now we essentially focused on Anderson localisation as a bulk phenomenon. We can cite one more interesting, yet more peculiar, result: the case of localised edge modes behaving as bulk modes in lower spatial dimension. It has been done in Maximo et al. (2019) and an example is shown in Fig. 1.14. The localisation lengths of these vector edges modes, in both 2D and 3D ensembles, show good agreements with localised bulk modes in respectively dimension one and two. Even though Anderson localisation is a bulk phenomenon and that by definition, the proportion of these edges states tends to zero in infinite systems, it is still interesting to note that the cooperative effects needed to obtain localised states could occur in vector systems under particular conditions.

In this section we shed a special light on the problem of Anderson localisation in disordered media. We reviewed the basis of the self-consistent theory, highlighting the elementary processes favouring localisation of waves. We then presented the scaling approach which uses a heuristic approach with renormalisation concepts to characterise the transport regimes, with the dimension of space as a critical parameter. It emphasised the fact that localisation always occurs in less than 3D, and that above it exhibits a real phase transition from a diffusive regime to a localised one. Potential polarisation effects due to the dimension of the field have not been taken into account in these theories but numerical results obtained from the coupled dipoles method suggest their strong influence. In particular vector light has not been observed to localise neither in 2D nor in 3D. The precise role of polarisation is put to question either by modifying of the short range coupling using artificial setups or by looking at physical systems with different near-field behaviour. We saw that localisation can be restored with tempered near-field coupling. In the next chapters we will analyse how spatial correlations can change the picture described so far. For that purpose, in the rest of the present chapter we will move away from the physics of fully disordered systems and study the effect of order. At first we will focus on perfectly ordered ensembles : photonic crystals, before moving to recent works on partially correlated patterns.

## 1.7 Resonant photonic crystals

### 1.7.1 Light in periodic media

In our path to understand the physics of resonant correlated disordered systems, we started from purely disordered ensembles of resonators. Let us now describe the opposite end of the spectrum : perfect order and photonic crystals. It all started with Yablonovitch (1987) and John (1987) who had the idea that light could be controlled as electrons in semiconductors through periodic structures. Creating optical circuits to replace electronics would have many advantages, starting by reduced losses by the much weaker coupling of light with itself. The evident drawback is that reduced coupling also means a more difficult control. Strong interaction between light and matter requires materials with strong dielectric index mismatch, or with resonant objects like Mie particles or cold atoms.

To understand the modification of the photonic properties of a medium when periodicity is added, we need some tools such as the notion of lattice and reciprocal lattice, and the Brillouin zone. A periodic system is invariant under discrete translations and the smallest closed set of these translations forms the basis vectors of the lattice, usually denoted  $\{\mathbf{a}_i\}$ . The reciprocal lattice is simply the Fourier transform of the direct lattice, and its basis vectors are labelled  $\{\mathbf{b}_i\}$ . The basis vectors in momentum space are related to the real space ones as

$$\mathbf{a}_i \cdot \mathbf{b}_j = 2\pi\delta_{i,j}. \quad (1.67)$$

The last key ingredient is the Brillouin zone. In periodic structure, the smallest distance between the atoms defines the largest elementary cell in Fourier space, called the first Brillouin Zone, often abbreviated BZ. Its importance comes from the fact that the entire photonic band structure exists in the first Brillouin Zone. A more formal definition of the Brillouin zone is obtained in term of the Wigner-Seitz cell of the reciprocal lattice. Now that the basic tools have been briefly laid out and summarised in Fig. 1.15, let us start with the easiest example of a system periodised along only one direction as shown in Fig. 1.16.

We consider a non dispersive medium where  $\omega = c_1k$ . This linear dispersion relation can be plotted with an artificial periodicity, effectively folding the dispersion relation at  $ka/\pi$  as in Fig. 1.16 (a). If we now interchange every couple of layer separated by  $a$  in Fig. 1.16 (a) by a medium with a different permittivity where  $\omega = c_2k$  in the bulk, the folding of the dispersion relation becomes physical, and partial reflections take place at the interfaces. The strongest interaction occurs at  $k = \pi/a$  where destructive interferences happen between modes with identical frequencies and opposite wave-vectors. The initial degeneracy is lifted and a gap opens where no mode at a given frequency can propagate, no matter the wave-vector. This weak effect in the case of a GaAs/GaAlAs multilayer shown in Fig. 1.16 (b) can be greatly

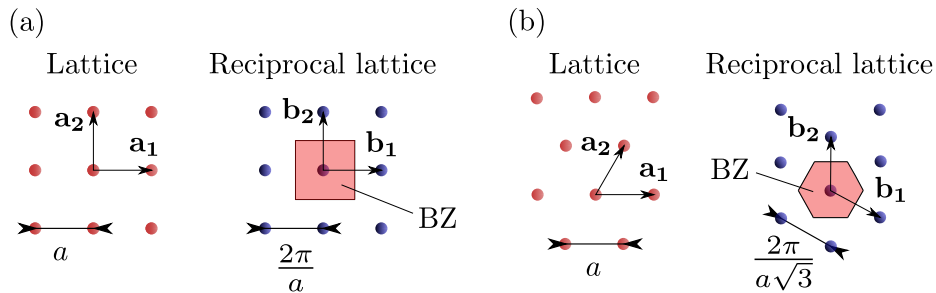


Figure 1.15: Lattice and reciprocal lattice for square (a) and triangular (b) lattice. The direct vectors are noted  $\mathbf{a}_1$  and  $\mathbf{a}_2$  while the reciprocal ones are denoted by  $\mathbf{b}_1$  and  $\mathbf{b}_2$ , and the Brillouin zone (BZ) is shown in red.

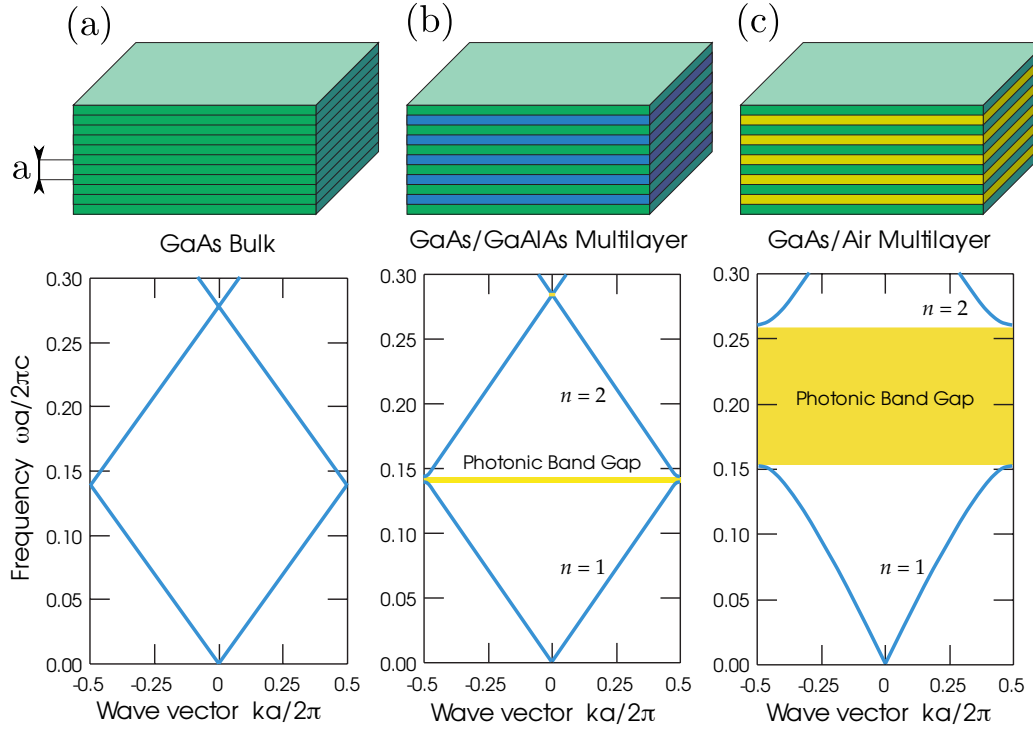


Figure 1.16: Illustration of the effect of the index mismatch on the band structure adapted from Joannopoulos et al. (2008), showing stacked layers of GaAs forming a bulk system (a), GaAs/GaAlAs multilayer (b) and GaAs/air multilayer (c) with their corresponding band structure below. The larger the index discrepancy, the larger is the gap.

improved by increasing the index mismatch between the different layers. The index of GaAs at 632 nm is around  $n = 3.86$ , while GaAlAs is  $n = 3.81$  hence a weak effect in Fig. 1.16 (b) and a much stronger one where GaAlAs has been replaced by an air layer of index  $n = 1$  in Fig. 1.16 (c).

A band gap may not seem particularly interesting as it is a forbidden frequency window for propagation, but one of its interesting aspects is that defects in the structure create peculiar modes trapped around the imperfections, and which lie precisely in these band gaps as shown in Fig. 1.17. Point defects are known to host localised modes and can be used as cavities, whereas line defects tend to guide light along the fracture line as in Fig. 1.17 (c) and are thus good candidates for wave-guides (Russell, 2003; Xiong et al., 2019), and surface defects act as mirrors. The basis of optical circuits has been laid out, but many challenges still exist in both nano-fabrication, scalability and even in the precise physical understanding of many of their properties. Their usefulness is still being discussed.

One of the difficulties in the field of photonic crystals, is the usually small difference of index between the different elements, leading to rather weak light-matter interactions and less efficient interference processes. Resonant materials can be of help in that regard.

### 1.7.2 Dispersion relation in arrays of point resonators

Resonant elements with complicated geometries are beyond the scope of this thesis. Here we will limit our analysis to periodic ensembles of point-like resonators.

The most basic difference between resonant and non-resonant system is the dispersion relation of isolated or bulk material. On the one hand, the dispersion is linear and periodicity induces changes mostly near the Bragg points at  $q = m\pi/a$ , with  $m \in \mathbb{Z}$  (Fig. 1.18 b).



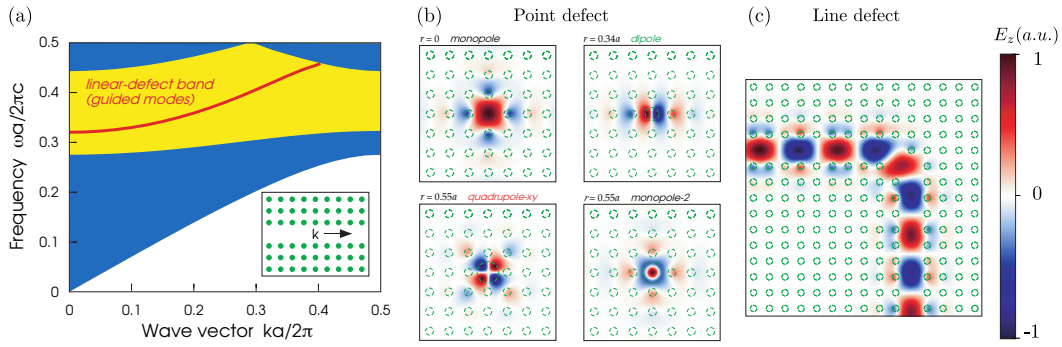


Figure 1.17: (a) Schematic band structure of a 2D array on infinite cylinder in a square lattice exhibiting a band gap and a linear-defect band of guided modes existing inside the bulk gap. (b) Point defect trapping the field, where a cylinder has a different radius (or index) than the others, (c) Line defect where a set of consecutive cylinders have been removed effectively guiding the field. (adapted from Joannopoulos et al. (2008))

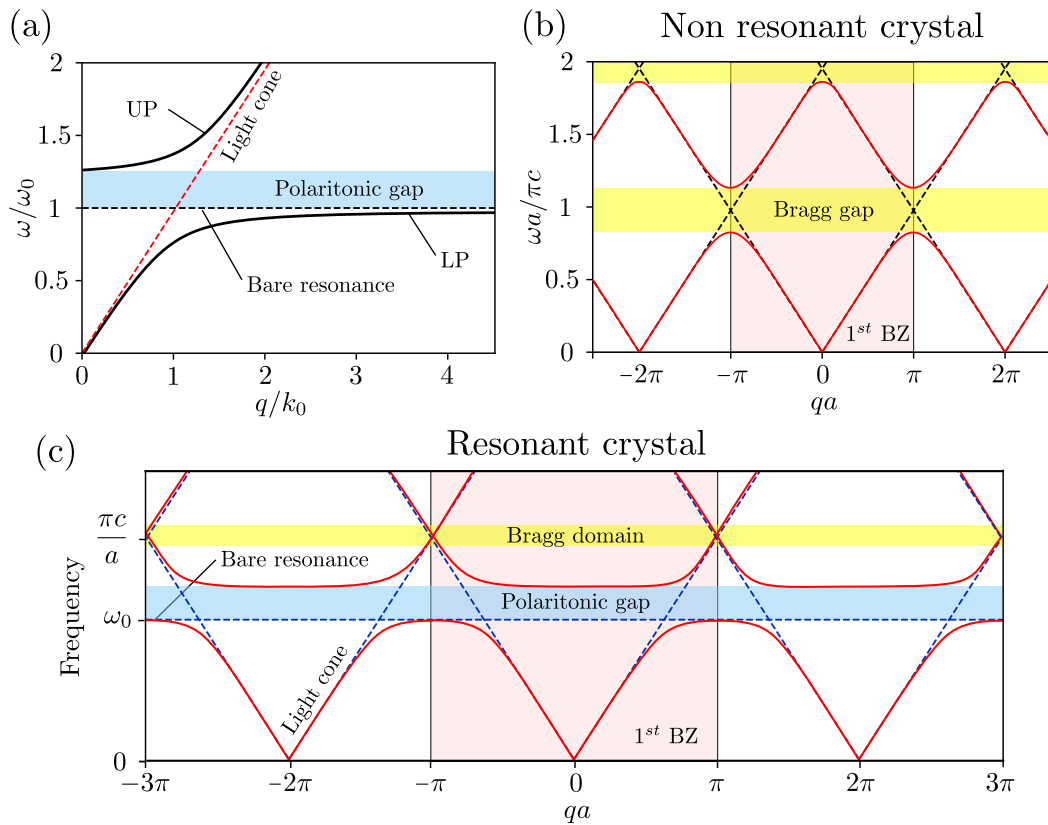


Figure 1.18: (a) Schematic representation of a polaritonic dispersion relation, showing the difference with a non-resonant dispersion curve with the light cone in dashed red. Its top band is called the upper polariton (UP) while the bottom band is the lower polariton (LP). (b) Illustrative representation of the dispersion relation of a non-resonant and (c) resonant 1D crystal of periodicity  $a$ . The dispersion relation of the uncoupled system is shown in dark blue dashed line and the interacting system in plain red. The light pink area is the first BZ, the blue regions are polaritonic gaps and the yellow ones are Bragg areas.

On the other hand, in resonant materials, the elementary dispersion relation is polaritonic, with the characteristic shape of Fig. 1.18 (a), arising from the coupling between a linear dispersion relation (light) and a resonance carried by the matter, at a frequency  $\omega_0$  (flat line). There already exists a band gap in the last case and periodicity can have very different effect depending on the ratio between the Bragg frequency  $\pi c/a$  and  $\omega_0$ . The structure is more complicated since there is an extra degree of freedom and the initial dispersion relation contains two bands.

**Remarks on band folding in polaritons:** A keen observer of Fig. 1.18 (c) may notice that the periodisation of the lower polaritonic band does not result in a band fold at the crossing, contrary to the upper polariton which behaves as the non resonant case. It is actually not a mathematical artefact but a property of the physical system. At large  $\mathbf{q}$ , near the edge of the first BZ, the upper polariton is mostly light-like, meaning that the field it is supported by is continuous, hosting arbitrarily large wave-vectors. On the contrary, the lower polariton is *matter*-like and hence physically lives on a discrete set: the resonators. The smallest wavelength is given by the lattice spacing meaning that wave-vectors larger than  $\pi c/a$  do not exist and the lower polariton actually stops at the edge of the first Brillouin zone without folding. This phenomenon is specific to the case of the propagation in fields living on discrete structures where the edge of the first BZ is truly a wave-vector limit. Indeed, the smallest wave-length is the distance between two neighbour elements. In contrast, in continuous fields infinitely small wavelength can exist. In this case, the band folding can simply be seen as an under-sampling of a mode at a wave-vector larger than the sampling limit  $\pi c/a$ .

## Model

One of the first band structure computation in resonant ensembles of dipoles can be found in van Coevorden et al. (1996) where the band structure of the face-centred cubic lattice has been computed in the dipole approximation for vector light. The authors predicted an omnidirectional photonic band gap which has been first refuted in Klugkist et al. (2006) and later by Antezza and Castin (2009a). Their computation is based on the same Hamiltonian introduced in Eq. (1.48).

For infinite Bravais lattices, eigenstates of the Hamiltonian (1.48) taken at resonance are Bloch modes that can be labelled by a vector  $\mathbf{q}$  in the first Brillouin zone Antezza and Castin (2009b). The corresponding eigenvalues are noted  $\omega_{\mathbf{q}}$ . Using the periodicity of the lattice, the eigenvalue problem reduces to  $\det[\omega_{\mathbf{q}}\mathbb{1} - \mathcal{H}_{\mathbf{q}}(\omega_0)] = 0$ , where the  $\beta \times \beta$  matrix  $\mathcal{H}_{\mathbf{q}}(\omega_0)$  is

$$\mathcal{H}_{\mathbf{q}}(\omega_0) = \left( \omega_0 - i \frac{\Gamma_0}{2} \right) \mathbb{1} - \frac{\Gamma_0}{2} \tilde{\mathbb{G}}_0(\mathbf{q}, \omega_0), \quad (1.68)$$

with  $\tilde{\mathbb{G}}_0(\mathbf{q}, \omega_0) = -c_d k_0^{2-d} \sum_{\mathbf{R} \neq \mathbf{0}} \mathbf{G}_0(\mathbf{R}, \omega) e^{-i\mathbf{q} \cdot \mathbf{R}}$ . Since the free space Green's function  $\mathbf{G}_0$  decays slowly in real space, it is not possible to perform a nearest-neighbour-type approximation of the summation involved in  $\tilde{\mathbb{G}}_0(\mathbf{q}, \omega_0)$ . Using Poisson's formula instead, we convert the sum over lattice positions  $\mathbf{R}$  into a sum over reciprocal lattice vectors  $\mathbf{Q}$ ,

$$\tilde{\mathbb{G}}_0(\mathbf{q}, \omega_0) = -c_d k_0^{2-d} \left[ \rho \sum_{\mathbf{Q}} \mathbf{G}_0(\mathbf{q} - \mathbf{Q}, \omega_0) - \mathbf{G}_0(\mathbf{R} = \mathbf{0}, \omega_0) \right], \quad (1.69)$$

where the Fourier transform of the Green's function is given by Eq. (1.4). The formulation (3.2) is more appropriate for computation because convergence is much faster in momentum space. The price to pay is the necessity to regularise  $\mathbf{G}_0$  since the two terms in Eq. (3.2) diverge, whereas their difference does not and has been derived in Antezza and Castin (2009b); Perczel et al. (2017). The detail of the regularisation procedure will be shown

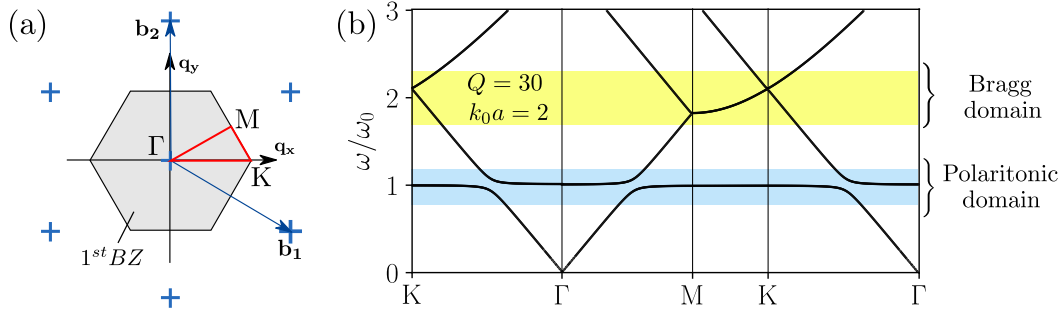


Figure 1.19: (a) First Brillouin zone of the triangular lattice showing the special points  $\Gamma$ ,  $M$  and  $K$  and the basis vectors  $\mathbf{b}_1$  and  $\mathbf{b}_2$ . (b) Band structure over the path  $K-\Gamma-M-K-\Gamma$ , with scalar coupling at high density ( $k_0a = 2$ ), and a quality factor of  $Q = 30$ . The domain where the upper polaritons meet is referred to as the Bragg domain (yellow) while the region near  $\omega_0$  is called polaritonic (light blue).

in Chap. 3. The obtained Hamiltonian is parametric in  $\mathbf{q}$ , and can thus be diagonalised over the first Brillouin zone (BZ).

Hamiltonian (3.2) is actually a high quality factor approximation of the more general equation (Antezza and Castin, 2009a). Assuming high  $Q$  allowed to use a simplified expression for the polarisability, as well as to freeze the frequency dependence in the Green's function. When both constrains are lifted, the more general expression becomes

$$\det \left[ \mathbb{1} + \alpha_Q(\omega_{\mathbf{q}}) \frac{\omega_{\mathbf{q}}^2}{c^2} \sum_{\mathbf{R} \neq 0} \mathbf{G}_0(\mathbf{R}, \omega_{\mathbf{q}}) e^{-\mathbf{q} \cdot \mathbf{R}} \right] = 0, \quad (1.70)$$

with  $\alpha_Q(\omega) = \frac{c_d}{Q} \frac{\omega_0^2}{\omega^2 - \omega_0^2 + i\omega^3/Q\omega_0}$  in 3D and  $\frac{c_d}{Q} \frac{\omega_0^2}{\omega^2 - \omega_0^2 + i\omega^2/Q}$  in 2D where  $c_d$  has been defined in Eq. (1.48). In this case, it is important to keep the frequency dependence in both the generalised polarisability and the Green's function to accurately capture the propagation far from resonance. This last approach is then no longer a linear eigenvalue problem, and require more numerical work. A minimisation of the magnitude of the determinant of Eq. (1.70) for different initial frequencies is usually enough. The procedure needs to be adjusted to be able to distinguish two close bands with arbitrary precision. The degeneracy degree of a band can be obtained once a solution has been found. We then evaluate Hamiltonian (1.70) for the solution we found, and the degeneracy of our solution is given by the number of zero eigenvalues of this matrix.

### Example of the triangular lattice in 2D

To justify our description of the band structures obtained by adding periodic spatial structures onto resonant system, we applied the generalised Eq. (1.70) to a 2D triangular lattice with scalar coupling. We computed the solution of Eq. (1.70) along the irreducible path  $\Gamma-M-K-\Gamma$  in the first Brillouin zone [see Fig. 1.19 (a)]. Figure 1.19 (b) displays the two distinct frequency domains respectively related to the polaritonic part of the band structure ( $\omega/\omega_0 \sim 1$ ), and the Bragg domain at the crossing of the dispersion relations at the edges of the first Brillouin zone ( $q \sim \pi/a \Rightarrow \omega/\omega_0 \sim 4/k_0a \sim 2$ ). As expressed when considering Fig 1.18, only the upper polariton with its quasi-linear dispersion relation exhibit band folding at the edge of the first BZ, while the lower polariton does not. Interestingly, the crossing of the UP near the  $M$  and  $K$  points do not result in the opening of a Bragg gap. For this illustration, the density has been chosen such that the polaritonic and the Bragg domain are well separated. At high enough densities, ( $k_0a < 3$ ), the polaritonic band structure always lies below the first

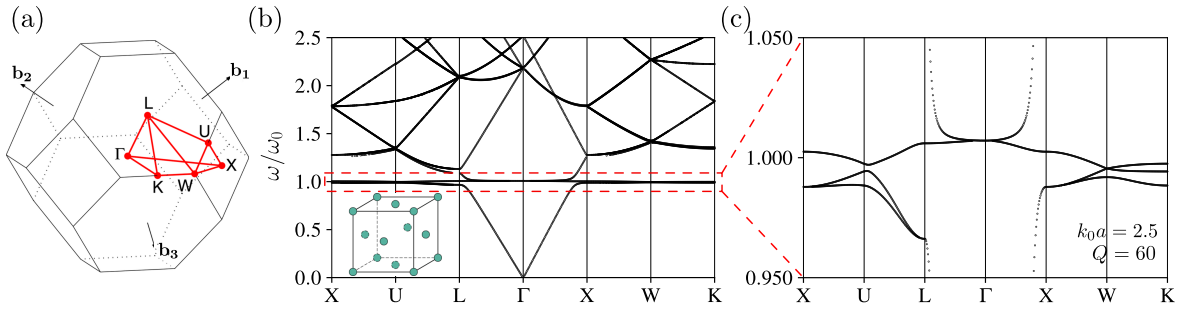


Figure 1.20: (a) First Brillouin Zone of the FCC lattice, and the irreducible domain enclosed by the red polyhedra with six non-equivalent vertices. (b) Band structure of the FCC lattice using the full vector Green's function, at  $k_0a = 2.5$  and for a quality factor of 60, over a large range of frequencies and (c) a zoom around the bare resonance ( $\omega = \omega_0$ ). Results re-adapted and based on Ref. Antezza and Castin (2009a)

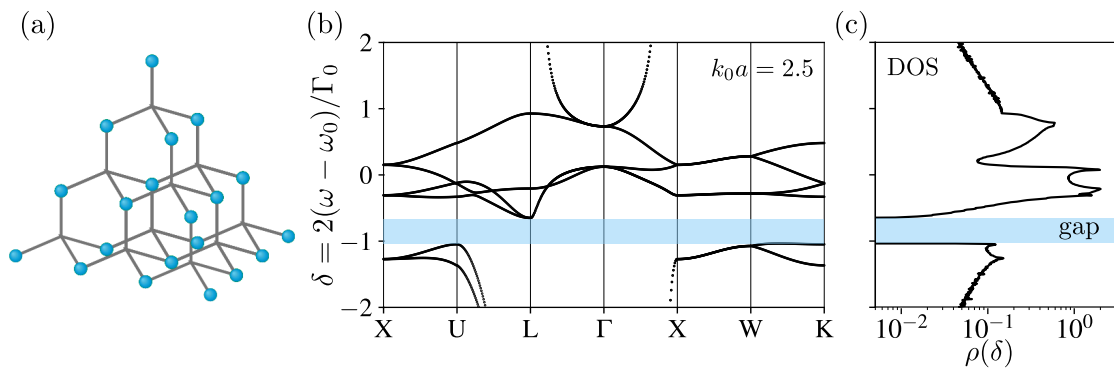


Figure 1.21: (a) Diamond lattice in real space, its Brillouin zone being the same as the FCC lattice. (b) Dispersion relation under the high quality factor assumption, at  $k_0a = 2.5$  along the path X-U-L-Γ-X-W-K. (c) Density of states computed from a sampling procedure of the BZ over the same frequency range.

Bragg foldings of the structure. Interesting physics happens when the two overlap, it will be the topic of Chap. 3

### Existence of gaps for vector light in 3D structures

The models described above have been used in particular to study the existence and the properties of photonic band gaps in periodic lattices.

**Band gaps in FCC lattices** The approach described above has also been used to answer the question of the existence of photonic band gaps in Face-Centred Cubic (FCC) lattices for vector light. This question requires the computation of the dispersion relation along numerous paths of the more complicated first BZ of the lattice [see Fig. 1.20 (a)].

At the densities considered in Refs. van Coevorden et al. (1996); Klugkist et al. (2006); Antezza and Castin (2009a) the Bragg domain is still well separated from the polaritonic one, and the dispersion relation obtained in Fig. 1.20 (c) is the same as the one, we obtain using Eq. (3.2). In the latter, the possible gap existing along X-U-L-Γ is closed between X-W-K. There is no omnidirectional gap in the FCC structure for vector light.

**Band gaps in diamond lattices** Even if the densest lattice in 3D does not permit a full band gap for the propagation of vector light, some more hollow lattices do. It is in particular

the case of the diamond lattice which is presented in Fig. 1.21. The structure (a) looks very different from the FCC but it can actually be obtained from the latter by adding four extra atoms in the structure. They thus share the same first Brillouin Zone. Hamiltonian (3.2) is more complicated as there are more atoms in the structure and a system with a high quality factor will still require to work with a  $6 \times 6$  operator. Nonetheless, we can still compute its band structure along the different paths, giving Fig. 1.21 (b) which shows a full band gap. This is confirmed by numerically computing the DOS by sampling the volume of the first BZ and performing a count of the resonances. This robustness of the gap with respect to disorder has been studied in Refs. Antezza and Castin (2013); Hasan et al. (2018); Skipetrov (2020).

Photonic crystals made of resonators are studied in the optics of controlling and trapping light. Cold atoms trapped in external periodic potentials are good candidates for implementing such crystals. A full 3D control is still quite difficult and instead of triply periodic crystals, two-dimensional arrays have been used. In a realistic experiment the system is of finite-size, which leads to finite lifetimes of the excitations. It has been shown in Facchinetti et al. (2016) that strongly sub-radiant modes can be found in such structure, allowing to trap light over time much larger than the propagation time in a non-resonant sample. The same kind of setup has been deployed to study topological effects leading to very robust and stable channels as in Perczel et al. (2017).

### 1.7.3 Scalar and vector fields versus TE and TM polarisation

In 2D photonic crystals, we can distinguish two types of wave propagation, that differ through their polarisation. Because the linear coupling between a vector field and polarisable material mathematically decouples the fields aligned along the invariance direction (*out-of plane*) with the one orthogonal to it (*in plane*), the two polarisations can be effectively treated independently. We call Transverse Magnetic (TM) polarisation the setup where the electric field is aligned with the invariance direction, and Transverse Electric (TE) the one where the field lies within the orthogonal plane.

Even in the TE polarisation, where the propagation of the electric field seems to be a full vector problem as the wave-vector  $\mathbf{k}$  also lies within the same plane. Yet, in the case of material object described by a dielectric constant, the field can always be written in term of a scalar wave equation on either the electric field  $\mathbf{E}$  or with the magnetic field  $\mathbf{H}$ . The full equations satisfied by  $\mathbf{E}$  and  $\mathbf{H}$  are

$$\nabla \times \nabla \times \mathbf{E}(\mathbf{r}) = \frac{\omega^2}{c^2} \varepsilon(\mathbf{r}) \mathbf{E}(\mathbf{r}), \quad \text{and} \quad \nabla \times \left( \frac{1}{\varepsilon(\mathbf{r})} \nabla \times \mathbf{H}(\mathbf{r}) \right) = \frac{\omega^2}{c^2} \mathbf{H}(\mathbf{r}). \quad (1.71)$$

When either  $\mathbf{E}$  or  $\mathbf{H}$  lies within the plane, the other points out. The in-plane field satisfies Eq. (1.71) where the differential operators live in 2D, while the complementary field obeys scalar equations of the form:

$$\left[ \nabla^2 E_z(\mathbf{r}) + \varepsilon(\mathbf{r}) \frac{\omega^2}{c^2} \right] E_z(\mathbf{r}) = 0, \quad \text{and} \quad \left[ -\nabla \cdot \frac{1}{\varepsilon(\mathbf{r})} \nabla + \frac{\omega^2}{c^2} \right] H_z(\mathbf{r}) = 0. \quad (1.72)$$

But when considering locally resonant systems modelled using a polarisability the equivalence between the study of  $\mathbf{E}$  and  $\mathbf{H}$  is broken. In the TM polarisation the out-of plane dipoles can be viewed as coupled monopoles and can be modelled by the scalar coupled-dipole method where the magnetic field is obtained through a curl of the electric field but still depends on the 1D induced dipole moment of each particle. In the TE polarisation, the excitation field is a 2D vector lying in plane, and even if the magnetic field is a scalar field, it depends strongly on the two components of the excitation field. In the limiting case when only the first dipole resonance exists, the TM polarisation folds onto a scalar setup, while the TE polarisation describes the full vector problem.

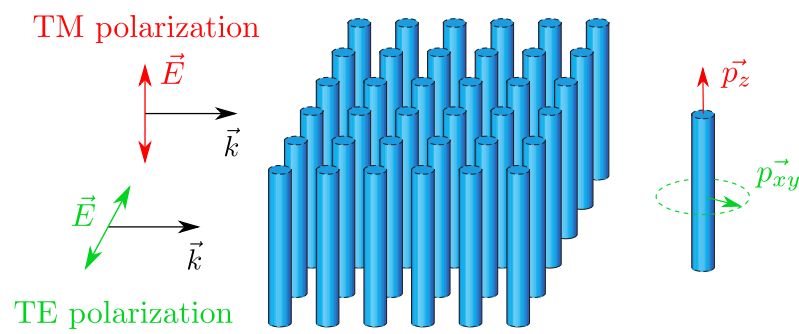


Figure 1.22: Sketch of the splitting between the TM and TE polarisation. (adapted from Joannopoulos et al. (2008))

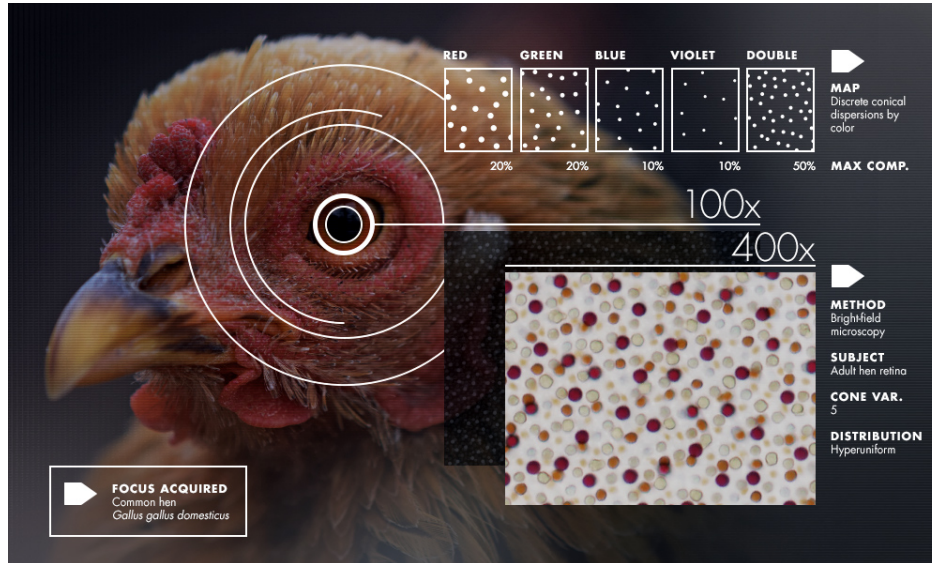


Figure 1.23: Distribution of the photoreceptors in a chicken’s eye displaying partial order for each kind of cell as seen in inset (taken from “A Bird’s-Eye View of Nature’s Hidden Order”, <https://www.quantamagazine.org/>).

## 1.8 Spatially correlated materials

After laying the basis for the study of fully disordered and completely ordered photonic systems in the last two sections, we can finally move onto the continuum spanning between the two. We will first present briefly special types of systems showing partial order and how to characterise them, namely hyperuniform and hard-core point patterns. A particular attention will be thrown upon two quantities widely used to describe spatial correlations: the pair correlation function and its Fourier counterpart, the structure factor. We will present natural occurrences of the correlated patterns we will study, as well as their physical implications in terms of colouration for example. The study of the mean free path in these systems has already led to some understanding of their photonics properties. On the other hand, other aspects of correlated materials remain elusive to the understanding, with for example the opening of photonic band gaps, a property commonly seen in photonic crystals. The second facet we will focus on, and which turns out to be linked to the opening of gaps in the density of states, is Anderson localisation. The theory developed in Sec. 1.6 does not include spatial correlations, but the field has yet become a playground for numerical studies.

### 1.8.1 What are spatial correlations?

It is not clear whether completely uncorrelated material exist in nature as there at least exists a physical repulsion between its elementary units. Hence as soon as interactions are present, the distribution of the elements deviates from pure randomness. Even a snapshot of a dilute gas where the particles seem to be located without order has at least the core repulsion between the molecules themselves. Short-range correlations are easy to comprehend, with hard-core like potential as the most common example. A less intuitive type of quasi-ordered structure are long-range correlations. The latter have been the target of a lot of recent work due to the recent development of the concept of hyperuniformity by S. Torquato and coworkers (Torquato and Stillinger, 2003; Torquato et al., 2021). A natural example of such correlated pattern can be seen in the retina of chickens when looking at the location of the photoreceptors as in Fig. 1.23. Statistical correlations in a set of random variables can simply be viewed as deviations from statistical independence. In uncorrelated patterns the probability of finding

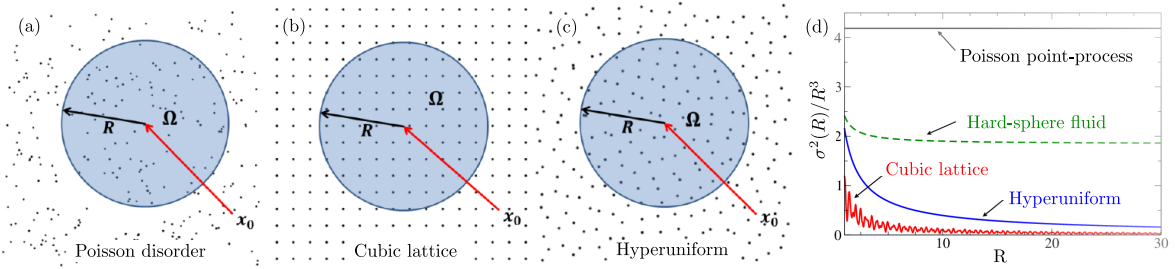


Figure 1.24: Point pattern of a Poisson disordered (a), cubic lattice (b), and hyperuniform (c) ensemble with the related number variance exhibiting different scaling laws (d). Figures adapted from Torquato (2018)

a particle at any given distance of a first one is always the same. In the case of short-range repulsion, it is rather intuitive that very close to the reference particle the probability of finding another object is lower than in the absence of interactions. We also expect this perturbation to disappear far from the first particle. This seemingly intuitive result is much more difficult to predict in the case of long range order. This is why we need to define some correlation functions that can be evaluated and compared for different type of partially ordered patterns.

Let us first understand the characteristics of full disorder. A fully disordered point pattern is called a Poisson point-process because the number of object  $N$  in a given volume  $V$  follows a Poisson distribution

$$p(N = n) = \frac{\Lambda^n}{n!} e^{-\Lambda}, \quad (1.73)$$

where  $\Lambda = \rho V$  with  $\rho$  the average density of particle and  $V$  the volume. Order can change this distribution, and in particular its variance. For a Poisson disorder, the variance is equal to the mean  $\Lambda = \rho V \propto R^d$ , while in crystals it is much smaller and has been shown (Huxley (2003)) to behave as  $\sigma^2 \propto R^{2t}$  with  $t \lesssim 0.63$  in 2D and  $t \lesssim 1.22$  in 3D leading to a sub-Poissonian behaviour as seen in Fig. 1.24 (a,b). Among the many other classes of spatial correlations which have sub-Poissonian statistics, we can mention two of them which will be of importance in the rest of this manuscript: hard-core like potentials and hyperuniformity. The number variance of the latter, shown on Fig. 1.24 (c), has a much closer behaviour to the fully crystalline ensembles rather than with the other disordered systems. This is an example of long-range effects due to correlations. The end of the section aims at providing a proper definition of the two concepts.

To characterise the above distributions, we need to define the probability of finding particles at given positions. At first order, we have  $p(\mathbf{r}_1) = 1/V$  and at second order

$$\begin{aligned} p(\mathbf{r}_1, \mathbf{r}_2) &= p(\mathbf{r}_1)p(\mathbf{r}_2)g_2(\mathbf{r}_1, \mathbf{r}_2) \\ &= p(\mathbf{r}_1)p(\mathbf{r}_2) [1 + h_2(\mathbf{r}_1, \mathbf{r}_2)] \end{aligned} \quad (1.74)$$

where we assumed a homogeneous media (statistically invariant under translation), Eq. (1.74) defines the pair correlation function  $g_2$  and the total correlation function  $h_2$ . In general, we define the  $n$ -point correlation function as  $p(\mathbf{r}_1, \mathbf{r}_2, \dots, \mathbf{r}_n) = p(\mathbf{r}_1)p(\mathbf{r}_2)\dots p(\mathbf{r}_n)g_n(\mathbf{r}_1, \mathbf{r}_2, \dots, \mathbf{r}_n)$ . The  $n$ -points correlation function  $g_n$  has positive values and indicates whether a configuration  $\{\mathbf{r}_1, \mathbf{r}_2, \dots, \mathbf{r}_n\}$  is more (value larger than one) or less likely (between zero and one) in this system than in an fully random pattern.

Hard-core point patterns (HC) can be directly defined through their pair correlation-function. Explicitly,  $g_2$  needs to cancel around the origin, highlighting the complete repulsion under a critical distance. This behaviour is shown in Fig. 1.25 (a) where the pair correlation function cancels for both the low and high correlation ratios  $\phi$ , defined as the volume fraction of the exclusion volume over the total volume.



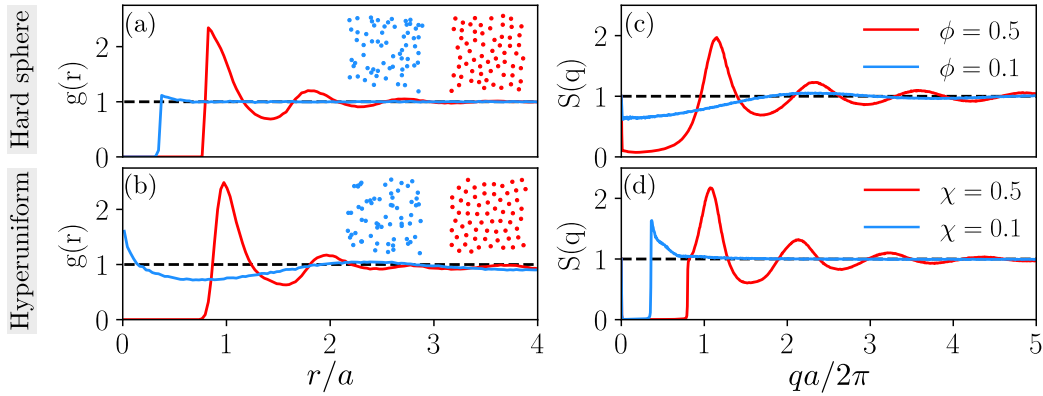


Figure 1.25: Examples of pair correlation functions and structure factor for 2D hard spheres, respectively (a) and (c), and stealthy hyperuniform point patterns, respectively (b) and (d) for a correlation ratio of 0.1 (blue) and 0.5 (red). Examples of patterns are shown in insert with the same colour-code.

Regarding Stealthy Hyper-Uniform point-patterns (SHU), the simplest definition involves the reciprocal version of  $g_2$ , called the structure factor  $S$ . In practice  $S$  is computed from the Fourier transform of the point pattern as

$$S(\mathbf{q}) = \left\langle \frac{1}{N} \left| \sum_{j=1}^N e^{-i\mathbf{q}\cdot\mathbf{r}_j} \right|^2 \right\rangle \quad (1.75)$$

$$\begin{aligned} &= 1 + (N-1) \int d\mathbf{r}_j d\mathbf{r}_m p(\mathbf{r}_j, \mathbf{r}_m) e^{-i\mathbf{q}\cdot(\mathbf{r}_j - \mathbf{r}_m)} \\ &\simeq 1 + \rho g_2(\mathbf{q}). \end{aligned} \quad (1.76)$$

Stealthy hyperuniform point patterns are then patterns for which the structure factor cancels over a finite domain around the origin. Here the correlation  $\chi$  is related to the volume  $V_K$  in reciprocal space where  $S(\mathbf{q})$  as  $\chi = V_K (L/2\pi)^d$ , is cancelled. Similarly as for HC ensembles, the correlation ratio is bounded between 0 and 1 and a value of 0.5 already characterise strong spatial correlations. For detailed expressions of the correlations ratios, the reader may refer to Eqs. (2.7) of Chap. 2.

Examples of the structure factor of SHU patterns are given in Fig. 1.25 (d). We can notice a kind of duality between HC and SHU patterns, where a condition of cancellation of a correlation function either applies in direct space ( $g_2(\mathbf{r})$ ) or in the Fourier domain ( $S(\mathbf{q})$ ). Correlations are visible in the form of oscillations of the structure factor  $S$  or of the pair correlation functions  $g_2$ . Both  $g_2$  and  $S$  are plotted for hard-core correlations and hyperuniform point patterns in Fig. 1.25. In weakly correlated ensembles [see the blue lines in Fig. 1.25 (a,b)] the correlation function stay close to their uncorrelated value (equal to 1) apart from a usually small domain in real or momentum space. The particular case of hard spheres shows that at low correlations, even if the two point patterns shown in insert of Fig. 1.25 (a,b) look similar, their correlations function do not. The radial distribution function  $g_2$  only exhibits a short-range interaction while hyperuniformity seems to alter the pair correlation function over a much larger distances. However in both cases, if the correlations are strong (see the red lines) the functions develop sharp peaks and a series of damped oscillations characteristics of both short and long-range interactions.

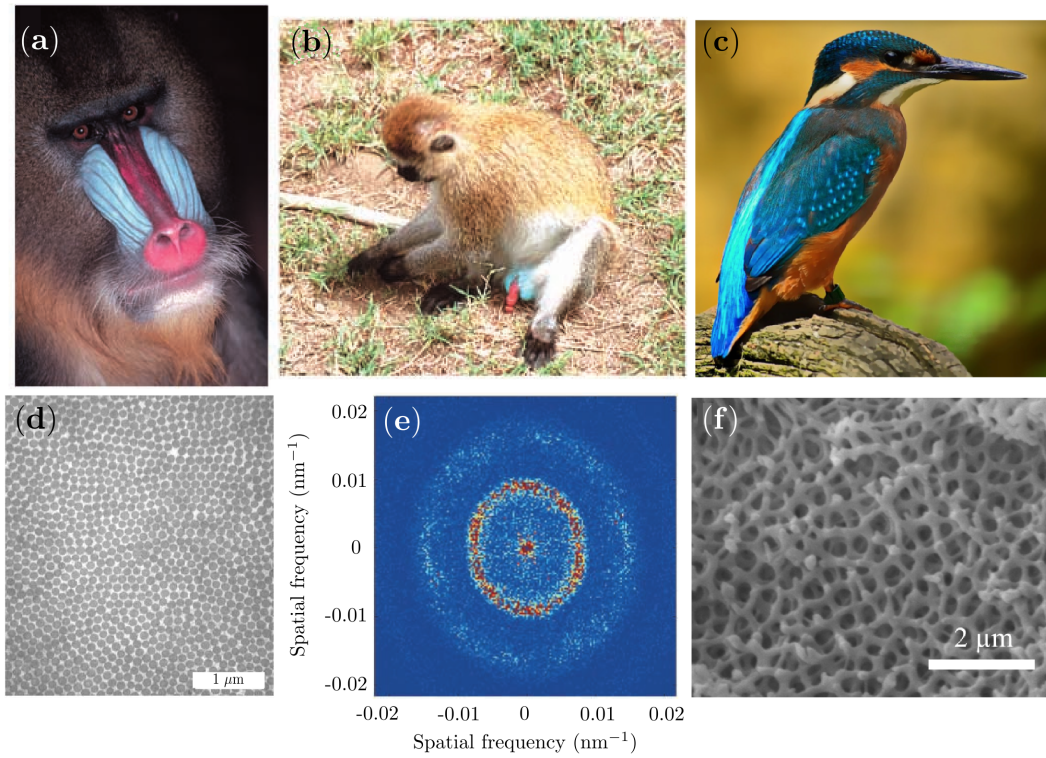


Figure 1.26: Structurally blue colour of a mandrill's nose (a), a monkey's scrotum (b) and kingfisher's feathers (c). Microscope view of the arrangement of collagen fibres responsible for the colouration of the mandrill's nose (d) with the associated structure factor (e), adapted from Prum and Torres (2004) and microscope view of the 3D network structure in the kingfishers' feathers (f), adapted from Stavenga et al. (2011).

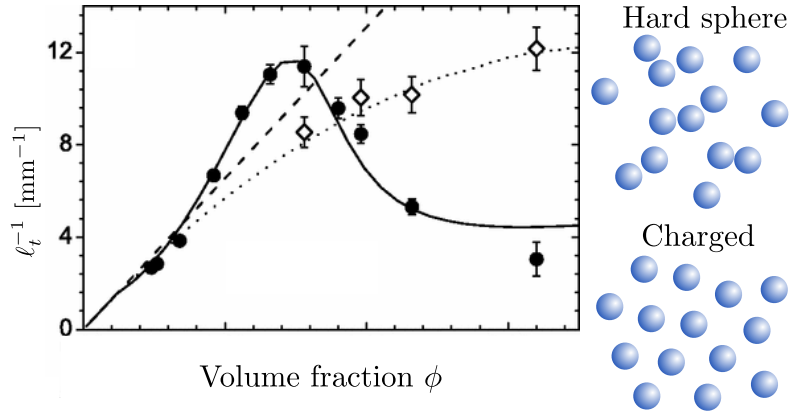


Figure 1.27: Impact of spatial correlation on the inverse transport mean free path in a colloidal suspension with hard-sphere repulsion (white diamonds) or electrostatic interactions (black dots). The continuous and dotted lines show the theoretical predictions of Eq. (1.77) with the appropriate structure factor and the dashed line shows the prediction for uncorrelated pattern. The results are taken and adapted from Rojas-Ochoa et al. (2004).

### 1.8.2 Natural occurrences and effect on the mean free path

Spatially correlated structures are not the appanage of synthetic man-made materials but have naturally been selected by evolution, sometimes for their photonic properties. Indeed, strong partial order have been found to give rise to structural colouration, and in particular to most of the blue colours in the animal kingdom with iconic examples among monkeys, birds [Fig. 1.26 a,c] and insects. While evidences from Jiao et al. (2014) showed that the arrangement of the cones in the retinas of chickens follow hyperuniform order, the structure likely emerged because of the property of hyperuniform patterns to be disordered yet homogeneous meshes. A hyperuniform pattern thus provides an optimal way to arrange photoreceptors in retinas.

Figure 1.26 (d) and (f) show that given the presence of a collagen fibre (d) or a pattern hole (f), the direct neighbourhood is strongly influenced with in particular a favoured distance with the next particle. This translates into  $g_2$  which acquires a low value inside the particle's volume and a larger value at the typical neighbour's distance. The effect on the structure factor are shown in Fig. 1.26 (e) where sets of rings develop due to correlations. Structural colouration has been understood as a frequency dependent modification of the transport mean free path (1.43), due to spatial correlations. The transport mean free path can be expressed as in Fraden and Maret (1990)

$$\frac{1}{\ell_t} \simeq \rho \int_0^{2k} dq F(q) S(q), \quad (1.77)$$

where  $F$  is a function proportional to the form factor of the particle and describes its intrinsic anisotropy, and  $k = \omega/c$ . Equation (1.77) has an explicit dependence on the frequency, which gives in the situation of Fig. 1.26 (e), an increase of the scattered intensity when  $k$  reaches the first maximum of the structure factor. A direct graphical estimation gives a peak of  $S$  around  $q \sim 0.7 \text{ nm}^{-1}$ , leading to stronger scattering for frequencies of 200 – 300 nm. This rough evaluation gives a value in the UV range, which is already a decent approximation for the observation of blue colours. If we were to evaluate the transport mean free path for frequencies below the first maximum of the structure factor, we would obtain a larger value for the mean free path. In addition to the fact that cooler wavelengths are more scattered, warmer colours are less scattered in spatially correlated media. Figure 1.27 shows the same behaviour, but at a fixed frequency and when varying the correlation ratio. At a given frequency, charged interactions which tends to produce similar patterns to hyperuniform

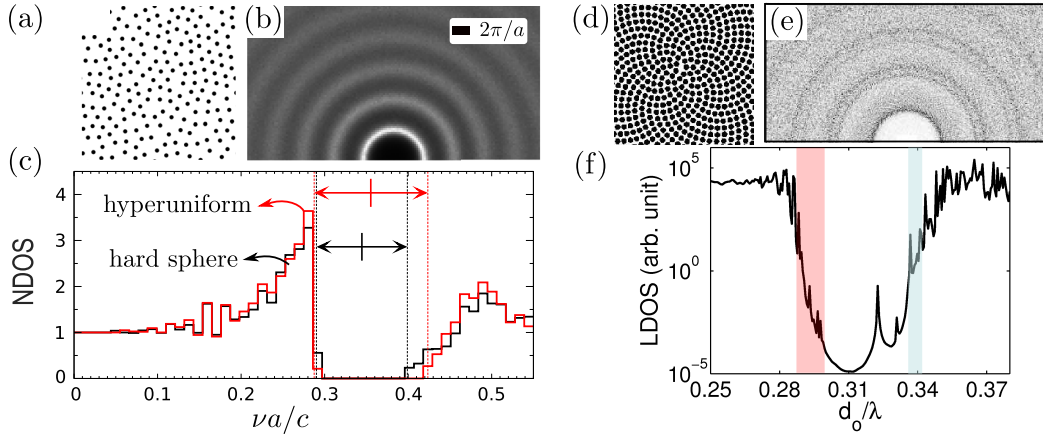


Figure 1.28: (a) Point pattern of a highly correlated disordered (hard core-potential), (b) its structure factor and (c) numerical photonic density of states of the corresponding setup dressed with infinite dielectric silicon cylinders, showing an almost identical DOS compared to SHU systems. Figure adapted from Froufe-Pérez et al. (2016). Same analysis in point pattern made of Vogel's spirals (d) with similar structure factor as in SHU systems (e) and a gap in the DOS (f). The results come from Liew et al. (2011)

ones, increase the correlation ratio and create a dip in  $S$  followed by a peak. The position of the peak moves toward the observation frequency until it reaches it, increasing  $\ell_t^{-1}$  as seen in the maximum of the plain line in Fig. 1.27. The peak then moves past the working frequency and the integration range of Eq. (1.77) only overlaps the domain of small structure factor, leading to the low values of  $\ell_t^{-1}$  observed for higher correlation ratios.

## 1.9 Opening of photonic band gaps and localisation

In addition to altering the transport mean free path, spatial correlations were found to modify the density of states and even open full band gaps which were thought to be the endowment of complete order. In two dimensional arrangements of point-resonators, coupled with a scalar field, several families of partial order exhibit band gaps triggered by correlations (Liew et al., 2011; Dal Negro et al., 2019; Froufe-Pérez et al., 2016, 2017). Figure 1.28 shows hard sphere and hyperuniform ensembles which, when sufficiently correlated, show an almost identical DOS with a profound gap which were attributed to a Bragg-type condition due to the first peak of the structure factor. However the gapped region lies in the frequency window of the first resonances of the cylinder computed using Mie theory ( $\nu_{\text{Bragg}}a/c \sim 1$  and  $\nu_{\text{Mie}}a/c \sim 0.15 - 0.3$ ), hinting that the phenomenon is of polaritonic nature rather than of Bragg origin. Photonic bandgap has also been observed in more regular, yet aperiodic structures known as Vogel spirals (see Fig. 1.28) which turn out to have a very similar structure factor as the Correlated Disordered (CD) systems we described above.

In addition, the neighbourhood of the gaps in these correlated materials displays some characteristic features of Anderson localisation with a small conductance and a strong attenuation of the spatial extension of the mode profiles (see Fig. 1.30 for an example in SHU patterns).

Previous numerical predictions in 2D SHU systems have been confirmed experimentally in the microwave regime in a wave-guide geometry to mimic a two dimensional setup by Dalichaouch et al. (1991), Laurent et al. (2007b) and Aubry et al. (2020). The transmission in the bulk is strongly reduced by the addition of spatial correlations [see Fig. 1.30 (b)], due to a vanishingly small number of accessible modes in the considered frequency range [Fig. 1.30 (c)]. Moreover, localisation takes place around the gap, which exists near the first Mie resonance of the individual cylinders.

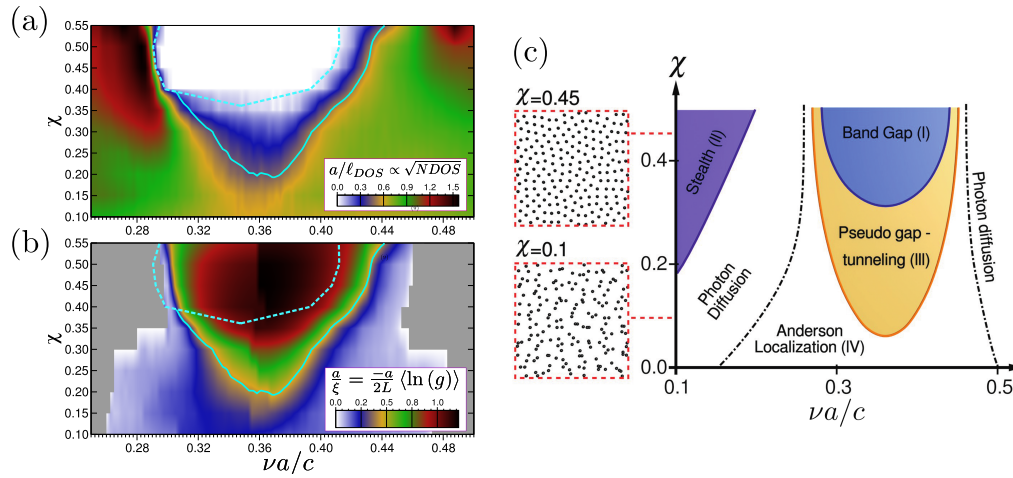


Figure 1.29: (a, b) Concomitance of DOS depletion and localisation for 2D scalar wave propagation in SHU pattern. (c) Heuristic phase diagram deduced from (a) and (b) showing transitions between Anderson localisation, diffusion and a fully gapped system. Adapted from Ref. (Froufe-Pérez et al., 2017)

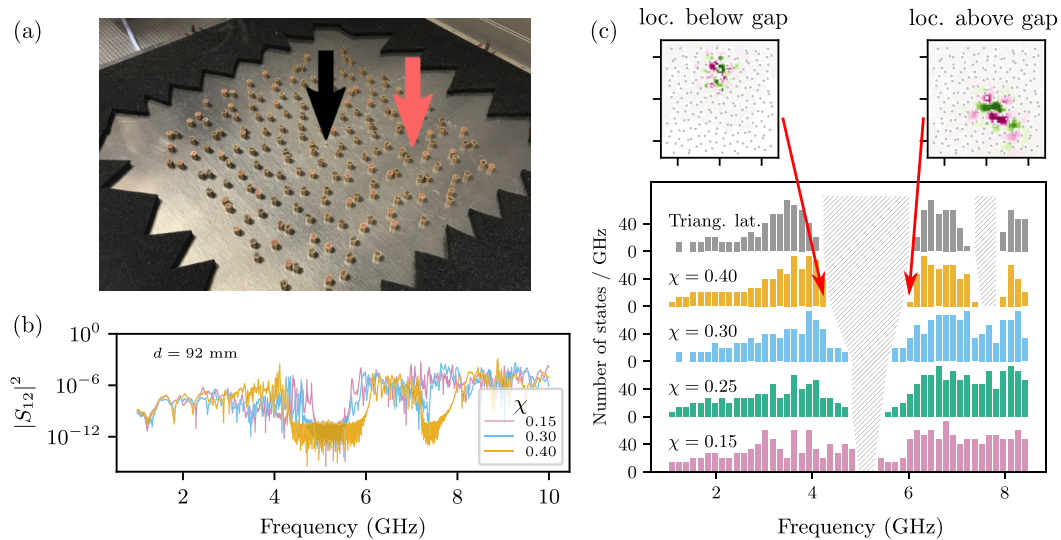


Figure 1.30: Experimental evidence using dielectric resonators (Mie cylinders of  $n \simeq 6$  and diameter 5mm) in an effective 2D geometry coupled with micro-waves (a). Correlations induces the opening of drops in transmission (b,  $S_{12}$ ) due to band gaps (c). Localised modes are found near the edges of the gaps. (Aubry et al., 2020)

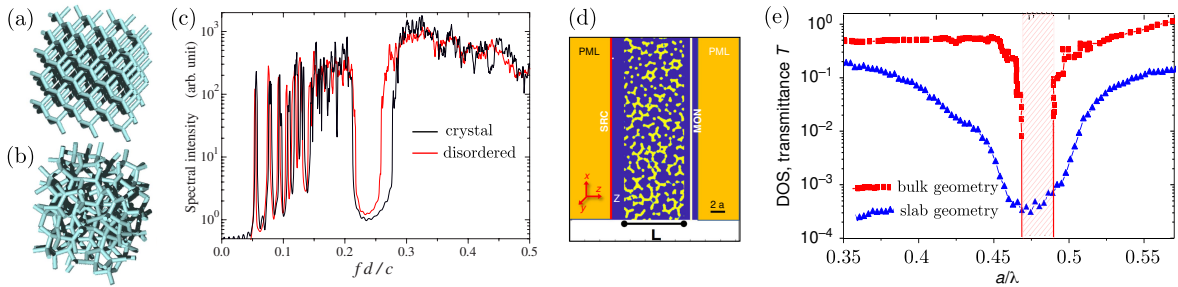


Figure 1.31: Comparison between the photonic properties of a dielectric network following the edges of a perfect diamond lattice (a) and those of an amorphous system which preserves the coordination, as well as the typical distance between neighbours of the ordered structure (b). Fig.(c) shows that both densities of states are similar and host a similar band gap (Edagawa et al., 2008). (d, e) Numerical experiment of the same material as in (b) in a slab geometry showing similar DOS depletion (Haberko et al., 2020)

We think that all previous observations in 2D can be interpreted in terms of coupled monopolar, or *out-of plane* resonances and can then be described by the scalar coupled dipole method (TM polarisation). When the field lies within the plane of the resonators (TE polarisation), no gap nor localisation features are seen. In this polarisation, the behaviour of spatially correlated systems is similar to the one of the uncorrelated patterns described in Sec. 1.6.4.

If in general no omnidirectional band gap are found in 3D crystals, there exists an exception: the diamond lattice. This effect has been used to create disordered structures which locally preserve the symmetry of the diamond lattice. Figure 1.31 (a,c) shows a dielectric network architecture with the same local tetrahedral environment than the diamond lattice. Both the ordered and amorphous structures exhibit the same band gap when coupled by light. This is still visible when instead of an infinite bulk material, a slice is used in a slab geometry (d-e). Nano-fabrication techniques can now produce these structure such as in Scheffold's group, see Muller et al. (2017). Even if diamond crystals made of point resonators also exhibit an omnidirectional gap (Skipetrov, 2020; Antezza and Castin, 2013, 2009a), the relevance of the model for previously mentioned network structures is arguable. The potential effects of correlations on Anderson localisation of light in 3D is still an undergoing investigation and as of now, few numerical or experimental evidence has been put forward.

In two dimensional systems, correlations have been found to induce changes in the DOS potentially leading to photonic band gaps. They seem to reveal the underlying polaritonic properties due to resonances and hidden in uncorrelated ensembles. Bragg gaps are unlikely to play a crucial role in these disordered structures and neither serious microscopic explanation nor theory of the phenomenon exists to this day. The fundamental reason for occurrence of Anderson localisation in the vicinity of these gaps also remains an elusive question. We aim at answering these questions in the following chapters.

## 1.10 Conclusion

In this section we laid the foundations of the different fields and approaches we will use in this manuscript. As the main goal of this work is to better understand the effects of correlated disorder in photonics systems, we first presented the two limiting cases in the order spectrum: complete disorder and photonic crystal. We introduced the mathematical tools used to describe the physics of waves in disordered ensembles with a particular focus on the notion of averages over the disorder. We showed how using a macroscopic vision of the system we could access the mean free path, the energy velocity or the diffusion coefficient. On the

other hand, we also demonstrated how a microscopic framework based on the coupled dipoles method allows to access the properties of the individual mode of a given disorder pattern. This powerful tool can easily be used to compute density of states, and to infer the spatial properties of the collective resonances.

It naturally leads us to consider the peculiar transport regime of Anderson localisation where the modes are exponentially localised inside the system. We highlighted the strong influence of dimensionality in the physics of localisation using both the perturbative approach of weak localisation and the self-consistent theory. The predictions, in agreement with the scaling approach of localisation, expressed the existence of a phase transition in 3D between a diffusive and a strongly localised regime, while localisation is always expected to occur in less than 3D. These results have been observed through a review of the recent work on the subject, but it has also been pointed out that the simplified model used to treat light did not take into account polarisation effects and near-field. It has been observed to change drastically the physics of the problem often leading to a vanishing of localisation.

After reviewing some of the physics of fully disordered systems, we also needed to understand the physics of complete order as another reference situation. We sketched the basic features of crystals giving rise to their photonic properties. We emphasised the key differences between resonant and non resonant structures with a highlight on the distinction between Bragg and polaritonic gaps.

Finally we presented some of the most representative work on the effect of correlated disorder on the photonic properties. In particular we emphasise the observations of band gaps in these structures. The effect of correlations in the Anderson localisation problem is also not understood and both aspects remain open problems we will try to answer.

## Chapter 2

# Impact of spatial correlations on ensembles of resonators

This chapter aims at describing the influence of spatial correlations on ensembles of coupled resonators in the framework introduced in Sec. 1.5.1. To probe these effects, we will mostly work with a class of correlations called Stealthy HyperUniform (SHU) and sometimes with a Hard-Core like correlations labelled HS (Hard Sphere) in 3D or HD (Hard Disks) in 2D. Two dimensional systems will be used to illustrate the discussion but everything is straightforwardly adapted to 3D and when it is not, explicit expressions for both cases will be given. We will point out the differences and similarities between both types of correlations and discuss the generality of our findings for other classes of spatial correlations. In particular we will highlight the effects of partial order on both the density of states (DOS) and on Anderson localisation, while the theoretical description of these effects will be left to the following chapters.

### 2.1 Hyperuniformity as knob to tune the degree of spatial correlations

The concept of hyperuniformity has been first introduced in Torquato and Stillinger (2003) as a mathematical solution of the maximally random jammed packing of sphere. As mentioned in Sec. 1.8, HU is found in living organisms as an arrangement that allows for specific mechanical or optical properties like in the retina (Jiao et al., 2014) or as the optimal distribution of immune system receptors in the stored immunity Mayer et al. (2015). The partial order in the cornea's fibres arrangements also shares some properties with hyperuniform arrangements (Salameh et al., 2020). SHU is a special class of HU, which allows to introduce a tunable amount of HU correlation through a variable number of constraints imposed to the structure. Contrary to HS systems with small packing fraction, SHU patterns with a small number of constraints are dominated by long-range correlations. Yet, when the number of constraints in SHU and the packing fraction in HS are large, both patterns display a rather homogeneous density of points as seen in Fig. 2.1. Let us describe here their basic properties and the generation process.

#### 2.1.1 Properties and generation process

Hyperuniform point patterns are characterised by cancellation of the structure factor in the limit of vanishing wave-vector [ $S(\mathbf{q}) \rightarrow 0$  for  $q \rightarrow 0$ ]. It corresponds in real space to a strong reduction of the number variance at large scale as already mentioned in Fig. 1.24. As mentioned above, we will study a sub-class of hyperuniform systems where the structure factor not only cancels at low  $q$ , but is zero over a finite domain around  $\mathbf{q} = \mathbf{0}$ . To preserve the



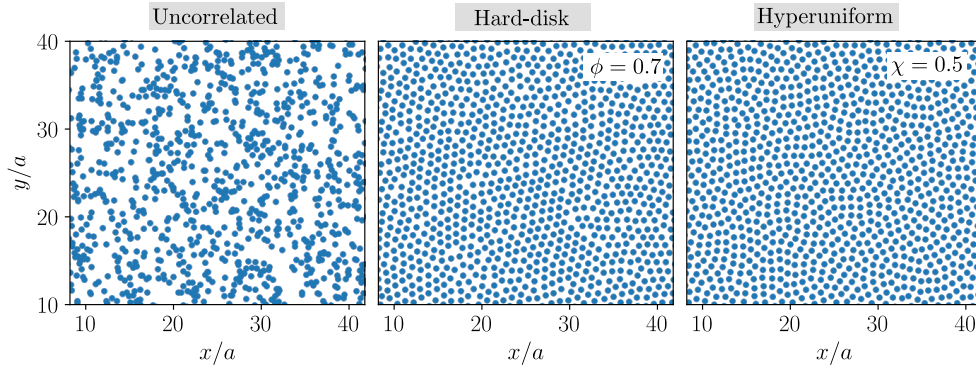


Figure 2.1: Comparison at fixed particle density between an uncorrelated pattern, a strongly correlated hard-disk and a hyperuniform pattern in 2D.

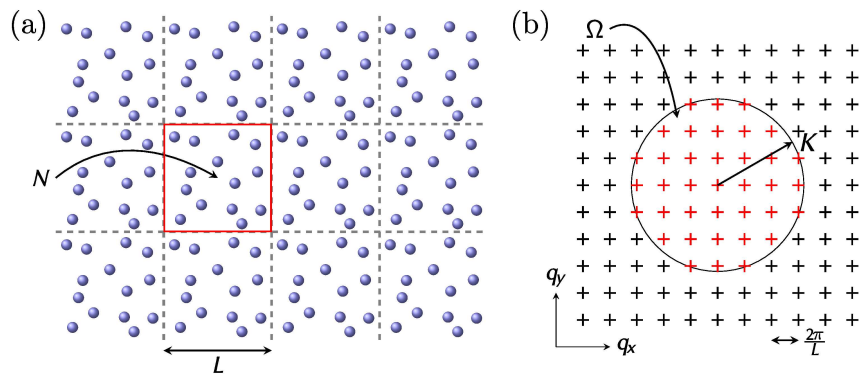


Figure 2.2: (a) Periodisation procedure used to mimic an infinite point pattern. A unit-cell containing  $N$  points is copied onto a square lattice leading to a discretised structure factor in Fourier space, (b) the Stealthy domain is a disk of radius  $K$  and is denoted  $\Omega$ . The discrete lattice points enclosed in the domain are drawn in red.

maximum number of symmetries, we will only consider patterns for which the domain, called *stealthy domain*, is a sphere (or a disk in 2D). Naturally, the latter cannot be of arbitrary size. To understand the limits, let us consider an infinite pattern made of identical copies of an elementary one as shown in Fig. 2.2 (a). Due to periodicity, there is a finite number of degrees of freedom, and thus a finite number of addressable constrains. If  $N$  is the number of points in the elementary cell, there will be  $d(N - 1)$  degrees of freedom with  $d$  the space dimension (the minus one accounts for the invariance under a global translation but will be neglected later on). The number of available constrains can be obtained by looking at the structure factor

$$S(\mathbf{q}) = \frac{1}{N} \left| \sum_{j=1}^N e^{i\mathbf{q}\cdot\mathbf{r}_j} \right|^2 \text{III}_{1/L}(\mathbf{q}), \quad (2.1)$$

where  $\text{III}_{1/L}(\mathbf{q})$  is a Dirac comb over the  $d$ -dimensional space and of spacing  $2\pi/L$ . Each discrete point where  $S$  may be non-zero in reciprocal space accounts for a degree of freedom. If we fix the value of  $S$  to zero over a sphere of radius  $K$ , we then impose a number of constraints equal to

$$\# \text{of constrains} = \begin{cases} \frac{1}{2} \pi K^2 \frac{1}{(2\pi/L)^2} & \text{in 2D,} \\ \frac{1}{2} \frac{4\pi K^3}{3} \frac{1}{(2\pi/L)^3} & \text{in 3D,} \end{cases} \quad (2.2)$$

where the  $1/2$  accounts for the symmetry  $S(-\mathbf{q}) = S(\mathbf{q})$ . Since this number cannot be higher than the total number of degrees of freedom, we can compute a correlation ratio  $\chi$  as the ratio between the number of constraints and the total number of degrees of freedom as

$$\chi = \frac{\# \text{of constrains}}{\# \text{of dof}} = \begin{cases} \frac{(Ka)^2}{16\pi} & \text{in 2D,} \\ \frac{(Ka)^3}{9\pi} & \text{in 3D,} \end{cases} \quad (2.3)$$

where we used  $\rho = NL^{-d} = a^{-d}$ .

A small value of  $\chi$  corresponds to a small  $K$ -domain and hence to a low amount of correlations. On the other hand, a value higher than  $0.4 - 0.5$  will be considered high and relates to strongly correlated patterns as shown in Fig. 2.3. Above some critical value of  $\chi$ , the system loses statistical isotropy and will eventually crystallise. A regular arrangement like a cubic lattice will have Bragg peaks at  $2\pi/a$  which is equivalent to a  $\chi$  of  $0.78$ . The maximum value for  $\chi$  will be given by the lattice toward which the procedure used to generate SHU pattern will converge.

### 2.1.2 Numerical procedure

To generate SHU patterns, we follow the method already used in Torquato et al. (2006); Leseur et al. (2016) and introduce the following potential defined as the integral of the structure factor over the stealth region as

$$\Phi(\{\mathbf{r}_i\}) = \int_{q < K} d\mathbf{q} S(\mathbf{q}) \equiv \sum_{i,j} u(\mathbf{r}_i - \mathbf{r}_j), \quad (2.4)$$

where

$$u(\Delta\mathbf{r}) = \begin{cases} 2\pi K \frac{J_1(K\Delta r)}{\Delta r}, & \text{in 2D} \\ 2\pi K \frac{j_1(K\Delta r)}{\Delta r}, & \text{in 3D} \end{cases} \quad (2.5)$$

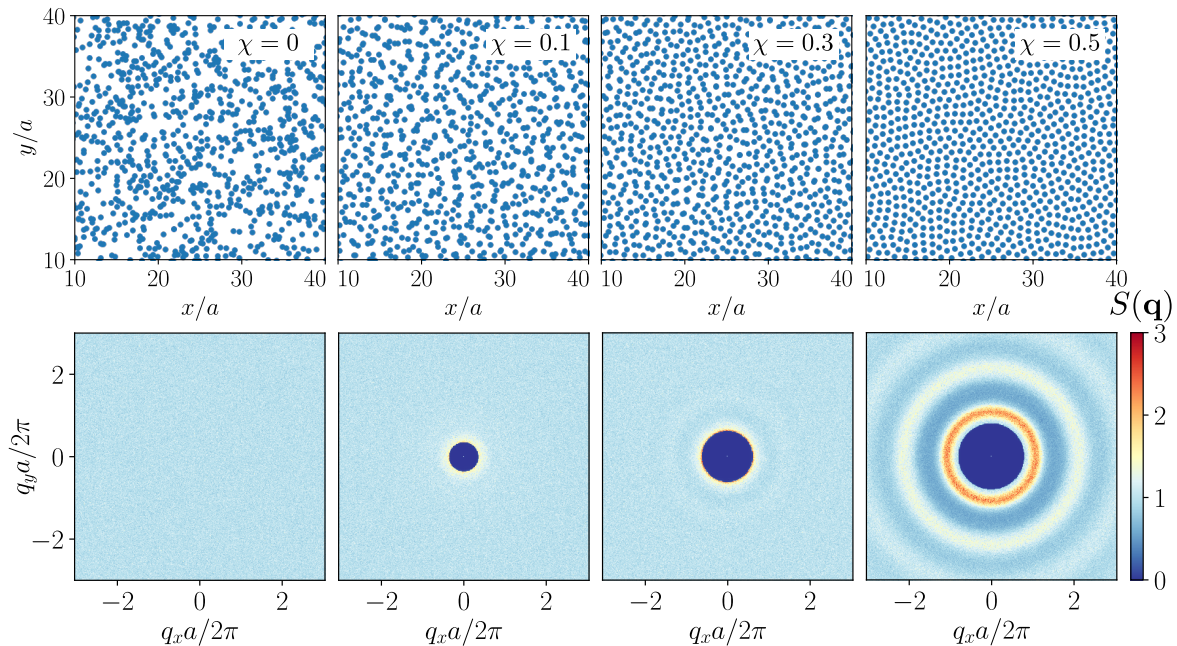


Figure 2.3: SHU point pattern and associated structure factor from  $\chi = 0$  to  $\chi = 0.5$ . The values of  $S$  have been averaged over 128 configurations of  $N = 20000$  points.

where  $j_1$  and  $J_1$  are the spherical and cylindrical Bessel functions of order 1 in the limit of  $R \rightarrow \infty$ . The SHU configurations are by definition sets of positions satisfying  $\Phi(\{\mathbf{r}_i\}) = 0$ . They are found by using a gradient descent method on the potential  $\Phi$ . More elaborated methods have been used in Froufe-Pérez et al. (2016); Torquato (2018) relying on a simulated annealing procedure. However, we found by comparing both methods that the improvement is not significant enough to have any impact on the optical properties discussed later on. It also greatly increases the computation time.

### 2.1.3 Remarks on the periodic structure found for $\chi \rightarrow 1$

As mentioned above, the SHU patterns found in the limit of large  $\chi$  strongly depends on the generation procedure itself, rather than on an intrinsic property of the type of correlations. At high enough  $\chi$ , all the degrees of freedom will be fixed and the system must crystallise, but in which lattice? Previous works in 2D (Leseur, 2016; Froufe-Pérez et al., 2016) observed a crystallisation in a square lattice from  $\chi = 0.6 - 0.7$  and up. In the first reference, the domain of cancellation of  $S$  was also chosen as a square but not in the second reference where it was chosen as a disk. We hint that in the generation process, the only element with a cartesian symmetry was the periodisation used to mimic infinite ensembles. We then apply a procedure where the periodisation can be done along any lattice. The example of a triangular periodisation is shown in Fig 2.4(a). To facilitate the crystallisation into a more specific lattice, we also decided to remove the Bragg peaks of the target lattice to prevent any conflict between the target potential and the lattice. The last condition is mostly relevant for hollow lattices where the Bragg points can be reached at reasonable values of  $\chi$ . In the case of the square and triangular lattices in 2D, the critical values where this overlap happens are respectively  $\chi = 0.79$  and  $\chi = 0.95$ . Our procedure allows for a crystallisation in a richer variety of lattices. Above  $\chi = 0.65$ , there seems to be a main lattice structure, with defects. We see in Fig. 2.4(b-c) a mainly square lattice at  $\chi = 0.7$  and a triangular one at  $\chi = 0.75$ . Different patterns seem to exist in different correlation ranges and a further analysis would be required to explore this phenomenon. Since our work dealt with ensembles with maximum

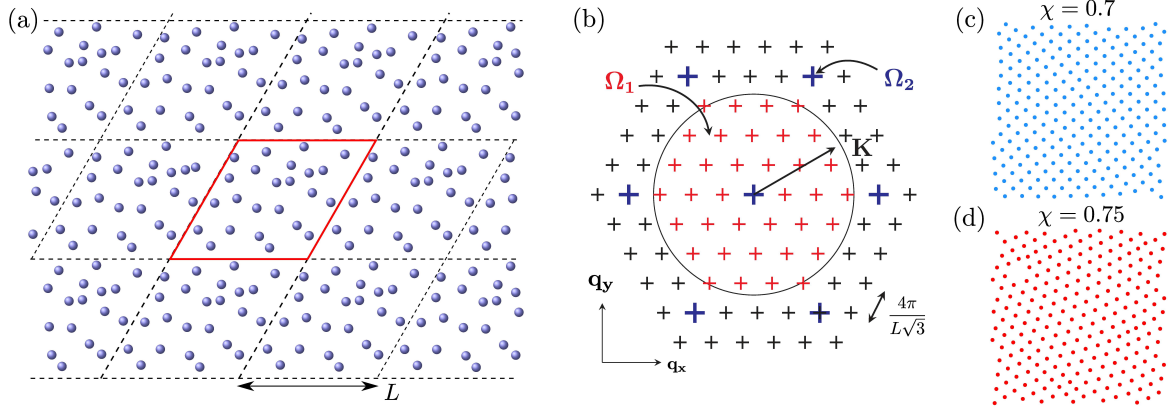


Figure 2.4: (a) Generalised version of Fig. 2.2 (b) where periodisation has been made along a triangular lattice, showing the reciprocal triangular Dirac comb in (b). The stealth domain of radius  $K$  is denoted  $\Omega_1$  and the set of Bragg peaks separated by  $4\pi/a\sqrt{3}$  of the target lattice as  $\Omega_2$ . (c) and (d) show the obtained pattern for respectively  $\chi = 0.7$  and  $0.75$  where we can go from a seemingly square lattice to a triangular one.

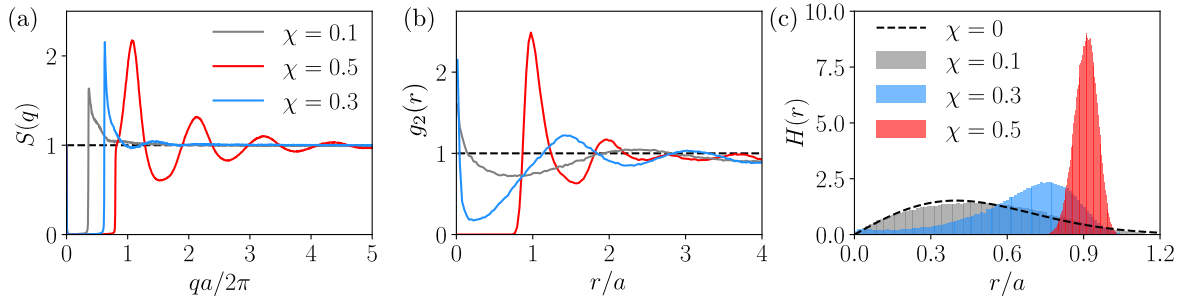


Figure 2.5: (a) Structure factor and (b) pair correlation function for SHU patterns at  $\chi = 0.1$ ,  $0.3$  and  $0.5$ . (c) shows the first neighbour distribution  $H(r)$  evaluated for  $\chi = 0$ , to  $0.5$ . The dashed line corresponds to the theoretical prediction for the Poisson distribution  $H(r) = 2\pi r \exp(-\pi r^2)$  which still fits the weakly correlated case. The values of every distribution have been averaged over 128 configurations of  $N = 20000$  points.

correlation ratios of  $0.5$ , these observations are more of a curiosity than critical.

### 2.1.4 Structural properties

As seen on both Fig. 2.3 and 2.5, when increasing the correlation ratio  $\chi$ , the structure factor is first characterised by a dip at small  $\mathbf{q}$  values and then develops some ripples extending far beyond the stealthy domain. The pair correlation function  $g_2$ , defined in Sec. 1.8.1, initially displays a long-range modulation at  $\chi = 0.1$  which is difficult to interpret on its own. It is nonetheless this feature that is linked to the strong damping of the variance in the number statistics as described in Ref. Torquato (2018). The slow and weak oscillations of  $g_2$  observed even at low correlation ratios become stronger and their frequency increases with the correlations ratio. We can notice that above  $\chi = 0.4$ , the system exhibits an effective hard sphere behaviour. The radial distribution function goes to zero below  $0.8a$  meaning a complete exclusion radius. This is better seen on the first neighbour distribution  $H(r)$  plotted in Fig. 2.5 (c) which goes from a Weibull distribution (Philip J. and Francis C., 1954) to something looking like a Gaussian distribution centred around  $r = 0.9a$  and of width  $0.15a$ . Indeed, at high  $\chi$  every point seems to have a relatively similar environment with a large exclusion volume and a first set of neighbours at a fixed distance. This property is very

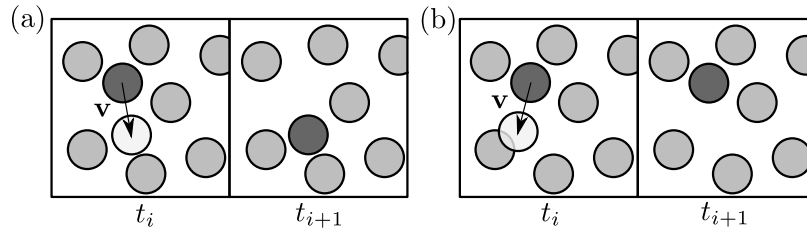


Figure 2.6: The two possible choices for the Monte-Carlo algorithm to generate a hard-disk ensemble. The random displacement of a particle either arrives in a new area without any overlap with other particles (a), or if there are, the particle will stay at its initial place (b).

similar to what is found with HD of large packing fraction. In the next section we will present the HD generation process and describe the differences and similarities with SHU patterns.

## 2.2 Hard-core correlations

Hard-core correlations are easily understandable as they rely on a hard-wall repulsion in real space, rather than on a condition in momentum space as is the case for SHU patterns. Every solid object we interact with has an exclusion domain, from the location of the sand grain in a sandstorm, to a more arranged pile of oranges on a market stall, or a tight Mayan wall. Here, for simplicity, we will only consider isotropic objects (i.e. spheres or disks). If hard-core structures naturally emerge from simple mechanics, it is quite complicated to replicate them numerically.

### 2.2.1 Generation process through a Monte-Carlo algorithm

We can define in the same way as for SHU pattern a potential whose minima are hard-core ensembles. Explicitly we have:

$$\Phi(\{\mathbf{r}_i\}) = \sum_i \Phi_i(\{\mathbf{r}_j\}) = \sum_i \sum_j \mathbb{1}_{\mathcal{B}(\mathbf{r}_i, 2r_0)}(\mathbf{r}_j), \quad (2.6)$$

where  $\mathbb{1}_{\mathcal{B}(\mathbf{r}_i, 2r_0)}(\mathbf{x})$  is the indicator function for a ball centred at  $\mathbf{r}_i$  and of radius  $2r_0$ , with  $r_0$  the hard core radius and  $\Phi_i$  is the one-particle potential. Even though the potential is well defined, it is not regular enough to compute its gradient and cannot be treated as the potential for SHU patterns.

To find the minima of such functions we need to introduce a stochastic procedure, in the same fashion as in Froufe-Pérez et al. (2016). Since the one particle potential increases by steps and simply counts the number of overlapping neighbours, each minimisation sequence will try to reduce to the total number of overlaps. It is more and more difficult to do as we increase the volume fraction defined as the ratio of the volume of the objects over the total volume

$$\phi = \begin{cases} \frac{N\pi r_0^2}{4V}, & \text{in 2D} \\ \frac{N\pi r_0^3}{6V}, & \text{in 3D} \end{cases} \quad (2.7)$$

where  $r_0$  is the minimal distance between two points.

For low volume fraction, we can generate non-overlapping configurations by adding one particle at a time. Volume fraction of  $\phi < 0.4$  can be directly obtained from this method. In order to tend towards a global minimum of the potential  $\Phi$  for higher volume fractions  $\phi$ , we cannot simply move the overlapping particles and try to find an empty spot. We need to immerse

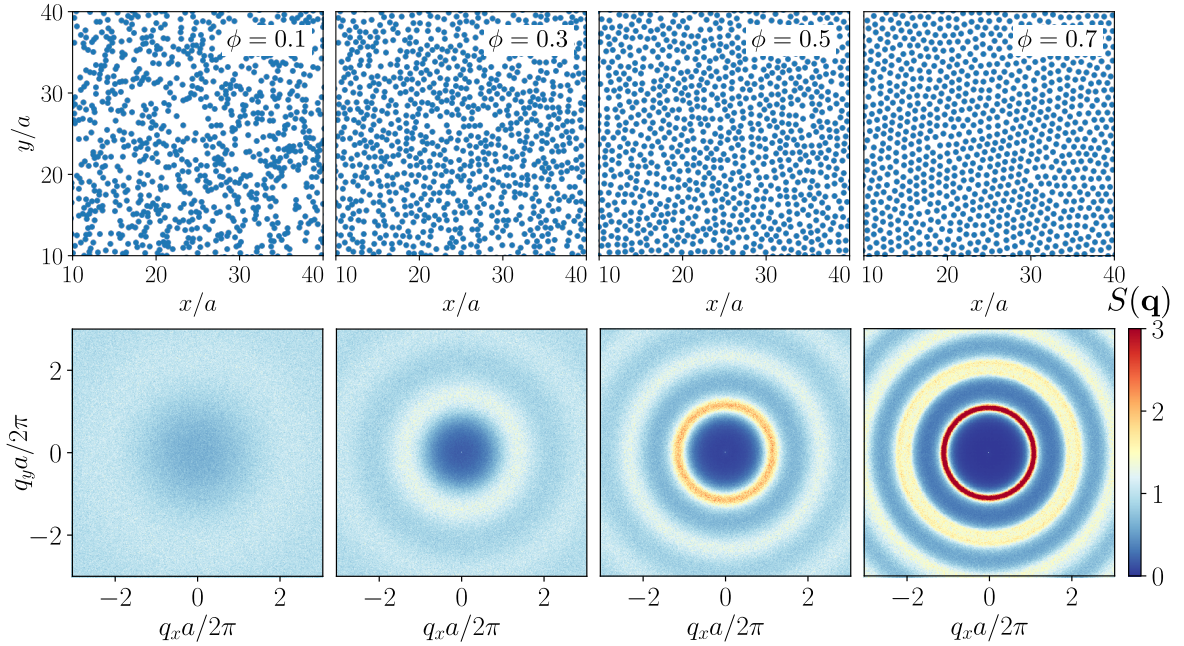


Figure 2.7: Hard disk point pattern and associated structure factor from  $\phi = 0.1$  to  $\phi = 0.7$ . The values of  $S$  have been averaged over 128 configurations of  $N = 10000$  points.

the particles in a thermal bath, where the particles move randomly. At each step, this is done by moving a fraction (usually above 95%) of the particles by a displacement  $\mathbf{v}$ , taken in a Gaussian distribution associated to an effective temperature  $T$  without consideration for possible overlaps. For the rest of the particles, we follow the procedure described in Fig. 2.6, where we either move the particles to a less crowded place or if we cannot find any, we let them at their initial locations. The system should on average be at thermal equilibrium, with yet a decrease of the global potential at each step. We iterate this process while lowering the effective temperature to converge towards a global minima.

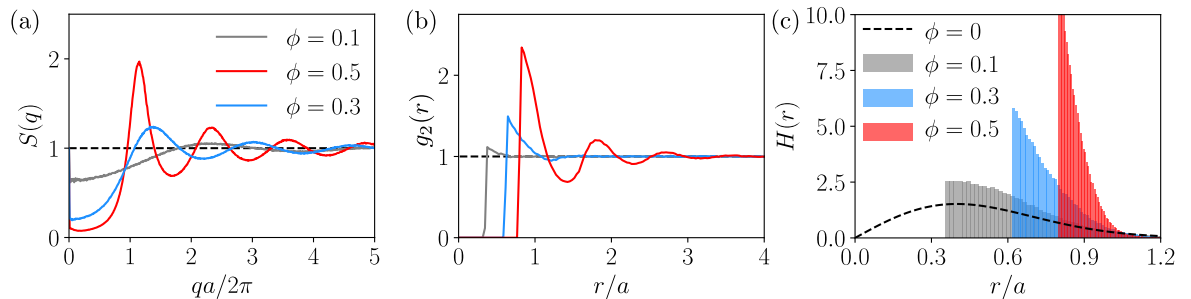


Figure 2.8: (a) Structure factor and (b) pair correlation function for HD patterns at  $\phi = 0.1$ , 0.3 and 0.5. Fig.(c) shows the first neighbour distribution  $H(r)$  evaluated for  $\phi = 0$ , to 0.5. The dashed line corresponds to the theoretical prediction for the Poisson distribution  $H(r) = 2\pi r \exp(-\pi r^2)$  which do not fit the weakly correlated case, contrary to SHU correlation. Results have been obtained with 128 configurations of  $N = 10000$  points.

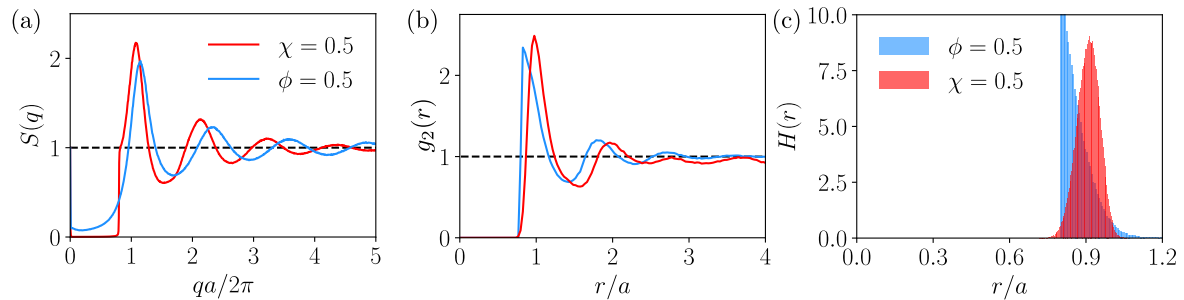


Figure 2.9: (a) Comparison of the structure factor and (b) pair correlation function for HD (blue) and SHU (red) patterns at  $\phi = 0.5$  and  $\chi = 0.5$  respectively. Fig.(c) shows the first neighbour distribution  $H(r)$  evaluated for both ensembles.

### 2.2.2 Statistical properties and comparison with stealthy hyperuniform point patterns

Using the same observables as for stealthy hyperuniform patterns, we can obtain Figs. 2.7 and 2.8. The pair correlation function displays the typical hard-core behaviour with only short-range correlations up to rather large values of  $\phi$ . When the volume fraction reaches  $\phi = 0.4$ , the pattern develops long-range correlations with larger oscillations of the  $g_2$  function and a *hyperuniform-like* behaviour where the structure factor is strongly suppressed over a domain around  $\mathbf{q} = \mathbf{0}$ . The shape of both the pair correlation function and the structure factor have been mathematically modelled leading respectively to the Percus-Yevick (Percus and Yevick, 1958) and the Baus-Colot approximation (Baus and Colot, 1987). These formulas are complicated when the correlation ratio is large, and a direct numerical estimation is often preferred for accuracy and simplicity reasons.

HD and SHU distributions of points share a lot of features in highly correlated ensembles. Figure 2.9 compares the structure factor, the pair correlation function and the nearest neighbour distribution of a SHU pattern at  $\chi = 0.5$  and a HD ensemble at  $\phi = 0.5$ . The height of the maxima of  $S(q)$  and  $g_2(r)$ , their locations, and the period of their oscillations are similar. The two nearest-neighbour functions also overlap. Even if they do not reach their maxima at the same values, they have a compact domain centred around the same value. Similar results have been obtained in Ref. Froufe-Pérez et al. (2016) where they propose a condition to align the two correlation ratios.

The strong similarities between HD and SHU correlations hint that the photonic properties of SHU systems discussed later on can be generalised to hard-core point patterns or any correlated ensemble with similar pair-correlation function. While this section was mostly a description of the point patterns on their own with a particular attention to their generation and elementary properties, the following sections will explore their photonic properties. Even though we used 2D patterns to illustrate this section, we carried the same work in 3D. In the following sections, we will discuss the photonic properties of 2D and 3D SHU correlated point patterns, made of resonant scatterers coupled by scalar or vector waves. We will highlight the similarities and differences between the different configurations, with a special attention for Anderson localisation.

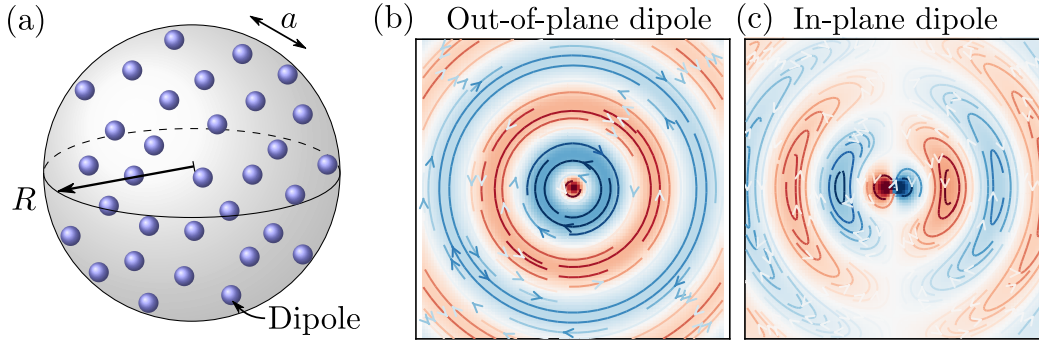


Figure 2.10: (a) Schematic representation of the scattering system. Resonators (blue dots) are distributed in a 2D or 3D open domain of radius  $R$ , and separated by a mean distance  $a$ . (b,c) Amplitude of the electric field (colour map) and field lines of the magnetic field, generated in 2D system by a dipole placed at the centre. In (b) the dipole moment is out-of plane, leading to an effective in-plane monopolar behaviour, while it is in plane in (c).

## 2.3 Study of the photonic properties of hyperuniform ensembles of resonators through scalar couplings

Here we use the coupled-dipole framework to study the influence of spatial correlations on the photonic properties of ensembles of resonators, as represented in Fig. 2.10. We first consider the case of scalar coupling in 2D and 3D. We remind that it corresponds to a coupling between resonators mediated by the Green's function of the scalar wave equation in 2D or 3D. The vector case, illustrated in Fig. 2.10, (c) correspond to a dipole radiation pattern. In 2D, scalar coupling can be physically implemented by placing the dipoles out-of-plane, as in Fig. 2.10 (b). The latter can represent the first dipole mode of a Mie cylinder in the TM or TE polarisation described in Sec. 1.7.3. Both the low and high density regime will be considered and the latter will allow us to study the occurrence of Anderson Localisation in these patterns.

In our simulations, we will keep the system size constant and vary the density through the number of resonators. In 2D, we use a system size of  $k_0R = 55$  and vary the number  $N$  of resonators between 200 and 2500, while in 3D we take  $k_0R = 25$  and vary  $N$  between 200 and 8000.

### 2.3.1 Low density regime

Let us first take a look at the distribution in the complex plane of the collective resonances of the system defined in Sec. 1.5.1 for fully disordered ensembles ( $\chi = 0$ ) at low density. Figure 2.11 (left) shows a distribution composed of a bulk of delocalised modes [low IPR encoded in the colour map, see Eq. (1.54)] centred around the values  $\delta = 0$ ,  $\gamma = 1$ . There also exist two families of resonances with very high IPR of roughly  $1/2$  that corresponds to the modes of pairs of dipoles described in Sec. 1.5.3. The upper branch of super-radiant modes is visible in 3D but not in 2D. Indeed, the two setups differ by their coupling strength. The 2D coupling scales as  $\sim r^{-1/2}$  and as  $r^{-1}$  in 3D. Thus, two particles at the same distance will be more strongly coupled in 3D than in 2D. The difference of coupling strength also explains the different shapes of the sub-radiant branches.

The addition of strong correlations leaves the bulk of the distribution almost unchanged, while suppressing the proximity resonances. This is due to the short-range repulsion induced by SHU correlations which prevents pairs of points to be arbitrarily close from one another as shown in Fig. 2.5 (c). We also represent in Fig. 2.11 the DOS  $p(\delta)$ , showing that correlations have almost no influence on the DOS in the regime of low density  $k_0a \gtrsim 5$ .



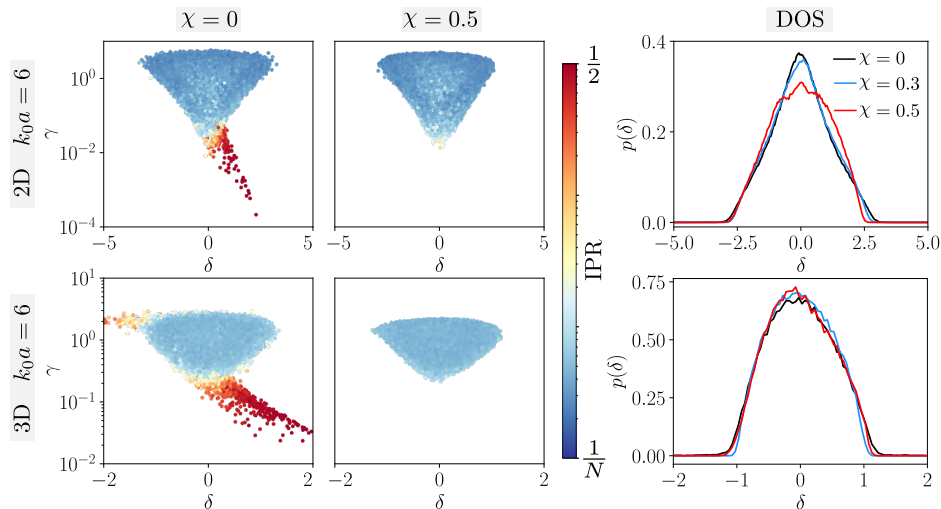


Figure 2.11: Complex spectra obtained using the coupled-dipole method in 2D (top) and 3D (bottom), for  $k_0 a = 6$ . The fully disordered case is shown on the left and the values for  $\chi = 0.5$  are in the middle. The colormap shows the Inverse Participation Ratio (IPR). The marginal distributions of the collective detuning are drawn on the right. The distributions have all been normalised to 1, and were sampled on over  $10^5$  eigenvalues. Each realisation of the disorder holds between 250 and 300 resonators, leading to a system size of  $k_0 R = 55$  in 2D and  $k_0 R = 25$  in 3D, with  $R$  the radius of the disk or the sphere containing the resonators.

### 2.3.2 High density regime, $k_0 a \leq 3$

The high density case is interesting because it leads to the formation of pseudo-gap in the DOS and to the localisation of some of the eigenstates of the effective Hamiltonian. We choose two slightly different values of density in 2D and 3D in order to exhibit the same behaviour for each  $\chi$ -value. As seen in Fig. 2.12, at  $\chi = 0$ , the complex spectrum still resembles the one at  $k_0 a = 6$ , but with modes with higher IPR and slightly longer lifetime  $\tau = \gamma^{-1}$ . It is the expected behaviour in the scalar case when we reach the onset of localisation. Indeed, increasing the density leads to a reduction of the transport mean free path, which translates into a rapid drop of the localisation length in 2D that may become smaller than the system size, and into a transition towards a localised phase in 3D in the frequency range where  $k\ell_t \lesssim 1$ . In both cases, strong localisation is achieved at higher densities, but the intermediate regime shown in Fig. 2.12 is interesting because it also clearly reveals an impact of correlation on the DOS and localisation.

As seen in Fig. 2.12, localisation features are enhanced when  $\chi$  goes from 0 to 0.3, with a set of modes with a strong IPR and long lifetime  $\gamma^{-1}$ . For even stronger correlations, these localised modes seem to disappear and a pseudo-gap opens instead. This is corroborated when looking at the density of states which shows a movement from a distribution locally similar to a Lorentzian to a gapped one as  $\chi$  increases. These observations, found in both 2D and 3D, in the range of density and  $\chi$ , suggests that localisation could be reached not only by tuning the mean free path but also by modifying the DOS.

### 2.3.3 Phase diagram in density-frequency space

In order to have an overview of the evolution of the spectra with correlations, we need to aggregate our data, composed of large sets of complex eigenvalues, into meaningful observables adapted to the description of the density of modes and localisation. We decided to focus our analysis on the marginal distribution of detuning  $p(\delta)$ , as well on the minimal value of the collective linewidth,  $\gamma^{\min} \equiv \langle \min \gamma \rangle$ . The latter is an excellent indicator of localisation

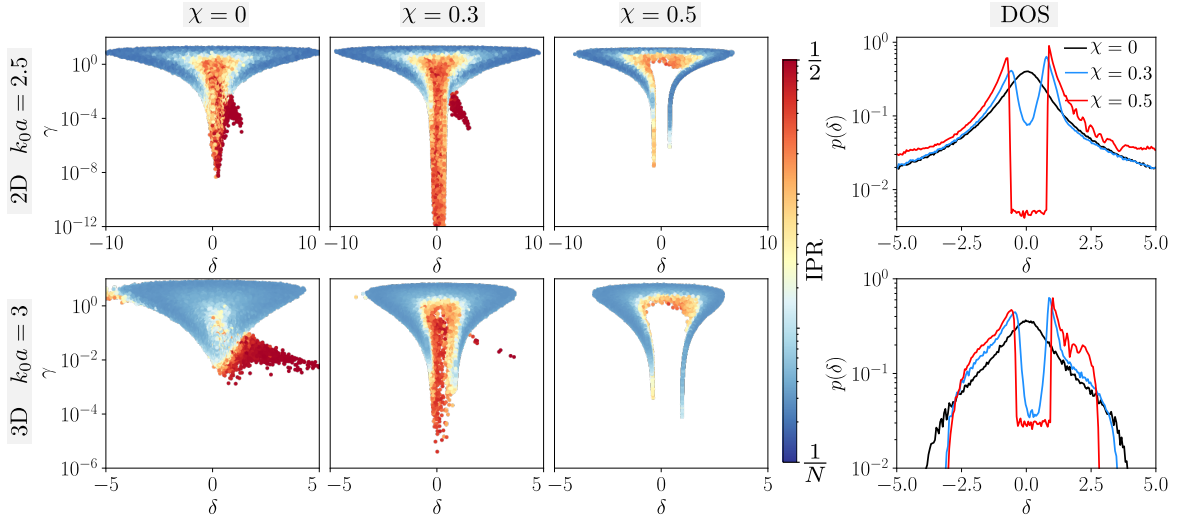


Figure 2.12: Distributions of collective resonances in the plane (detuning, decay rate), obtained using the coupled-dipole method in 2D (top) and 3D (bottom), for  $k_0a = 2.5$  (2D) and  $k_0a = 3$  (3D) and for different degrees of correlation ( $\chi = 0, 0.3, 0.5$ ). The colourmap shows the IPR. The marginal distributions of the collective detuning are drawn on the right. They are built from  $10^5$  eigenvalues and normalised to unity. Each realisation of the disorder holds between 1500 and 2500 resonators, which corresponds to a system size of  $k_0R = 55$  in 2D and  $k_0R = 25$  in 3D.

as modes with very small radiative decay rates are necessarily associated to localised states. These two observables are also the ones characterising the smallest dimensionless conductance described in Sec. 1.6.3, defined as the linewidth over the mean spacing. The relevance of these observables will be corroborated by a scaling analysis of the problem.

The maps of density of states  $p(\delta)$  and  $\gamma^{\min}$  as function of detuning and density are shown in Figs. 2.13 and 2.14. We recover the results described in the dilute and high density regime, but with a wide view of the phenomenon. In the absence of correlation, the DOS becomes progressively asymmetric as density is increased, with a maximum that shifts towards positive detuning. At high density, a pseudo-gap develops in a spectral region where localised modes are found. This effect is visible in Figs. 2.14 and 2.15 for 2D systems, but not for 3D systems because it occurs at  $k_0a < 2$ ; a 3D spectrum at  $k_0a = 1$  is shown in Fig. 2.15 (a). In both 2D and 3D, we see that correlations increase the phase-space extent of the localised domain. Both changes in the DOS and in  $\gamma^{\min}$  follow the same patterns in phase space with a rhombus shape stopping above  $k_0a \sim 3$  and surrounded by lines of high DOS. At  $\chi \gtrsim 0.4$ , the localised modes mostly disappear apart from some small domains very close to the edges of the rather large pseudo-gap appearing in the DOS.

There are elements suggesting that the deep pseudo-gap observed for  $\chi > 0.4$  could turn into a full Photonic Band Gap (PBG) in an infinite system. In particular, we observe that the modes directly inside the pseudo-gap have a short lifetime and are localised on the edges of the sample as seen in Fig. 2.15 (b). These modes should by definition disappear in a borderless sample, effectively opening the gap.

### 2.3.4 Summary

In the case of scalar coupling between resonators, the 2D and 3D setups present strong similarities. At low density of resonators, spatial correlations have small impact on the mode distribution: the bulk of the distribution remains almost unaltered while the branches accounting for proximity resonances are suppressed when short-range repulsion becomes dominant. On

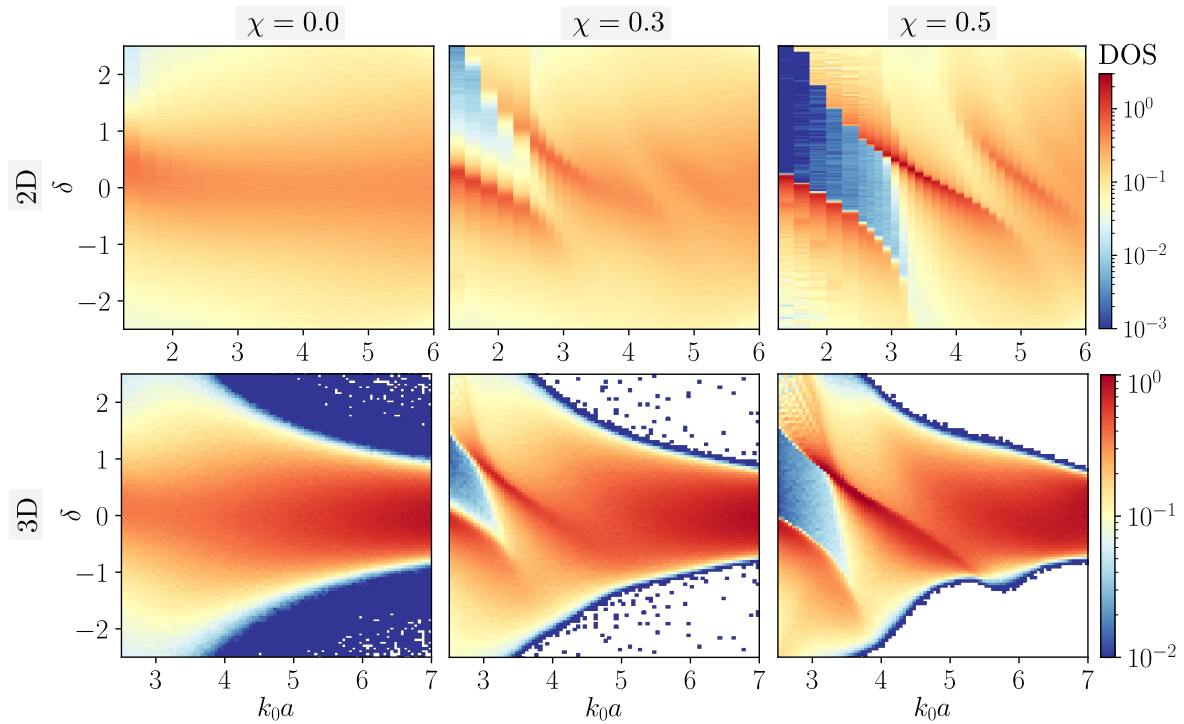


Figure 2.13: Density of states  $p(\delta)$  as a function of  $k_0a$  and  $\delta$  of ensembles of resonators in 2D (top) and 3D (bottom), for different degrees of correlation:  $\chi = 0$  (left),  $\chi = 0.3$  (centre),  $\chi = 0.5$  (right). The white domain corresponds to the phase-space domain that extends beyond the finite support of  $p(\delta)$ .

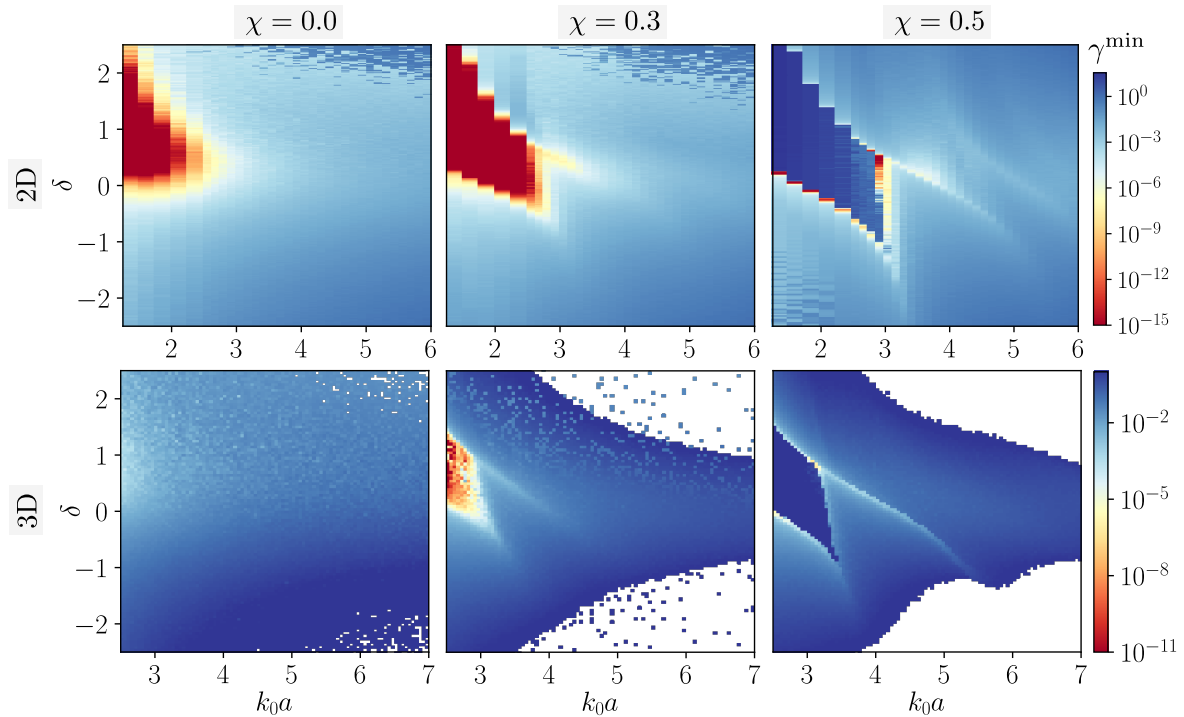


Figure 2.14: Minimum decay rate  $\gamma^{\min}$ , as a function of  $k_0a$  and  $\delta$  in 2D (top) and 3D (bottom), for different degrees of correlation:  $\chi = 0$  (left),  $\chi = 0.3$  (centre),  $\chi = 0.5$  (right).

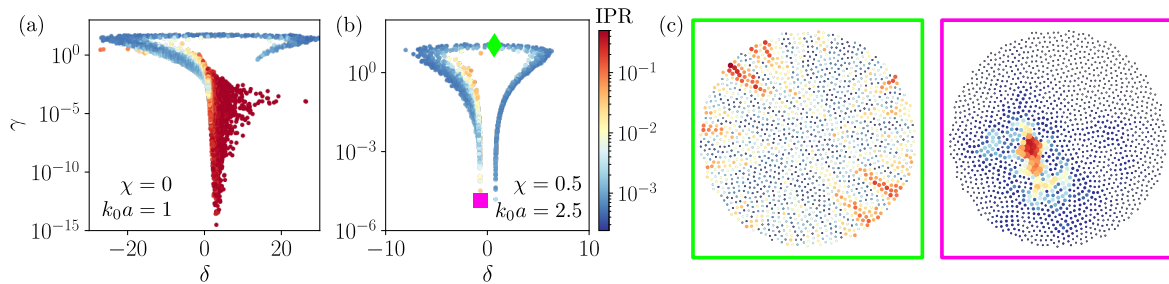


Figure 2.15: (a) Distributions of resonances for an uncorrelated 3D ensemble of  $N = 4180$  resonators ( $k_0R = 25$ ) at  $k_0a = 1$  displaying strongly localised mode with large IPR and small  $\gamma$ . (b) Distribution of resonances for a strongly correlated 2D ensemble of  $N = 1520$  resonators ( $k_0R = 55$ ), at  $\chi = 0.5$ , showing a pseudo-gap with very few localised modes on the side. (c) Spatial distribution of the eigenvectors, associated to resonances located inside the pseudo-gap (green diamond) and on its lower edge (magenta square).

the other hand, both the density of states and the localisation are affected by correlation at high density. Spatial order brings the localised regime to lower densities, especially in 3D, and opens a band gap with a characteristic shape (see Figs. 2.13 and 2.14), which is similar in 2D and 3D. This striking resemblance between the physics of two and three-dimensional ensembles should not prevent us from remembering that they behave differently regarding Anderson localisation. We will come back to this aspect in the next chapters.

## 2.4 Effect of vector couplings

In this section, we will describe the behaviour of correlated ensembles of resonators in both 2D and 3D, but with now vector couplings. In 3D, this is in fact the only rigorous model for light interacting with resonant dipoles. In 2D, it corresponds to propagation of in-plane electromagnetic waves, often referred to as the TE polarisation. In this configuration, both the field and the dipole moment lie in the same plane (see Fig. 1.22 in Sec. 1.7.3).

We will first analyse the low and high density limit for both the 2D and the 3D system as they have similar behaviour, and then focus of the intermediate regime where they differ. Here again, we will mostly focus on two complementary observables: the density of states and the smallest linewidth as an indicator of Anderson Localisation. A complete picture of the behaviour of both the 2D and 3D systems can then be drawn from the plot of these two observables over the entire density-frequency phase space.

We will show that ensembles of resonators embedded in 3D space do not host Anderson localisation no matter the correlation strength, while the equivalent ensembles in 2D will exhibit a window of strong localisation opened by spatial order. To validate this finding, we will perform a scaling analysis as introduced in the previous chapter.

### 2.4.1 Low density

Let us start with the low density regime ( $k_0a \gtrsim 6$ ) which shows similar behavior to the scalar setup. For scalar coupling, the distributions in Fig. 2.11 were characterised by a bulk of eigenvalues surrounded by branches, associated to modes located on pairs of points which disappear due to the repulsion created by correlations. The exact same thing happens with vector couplings in Fig. 2.16, except that now there are four branches. The overall density of states is only marginally affected by spatial correlations and the bulk modes are delocalised within the extent of the finite system.

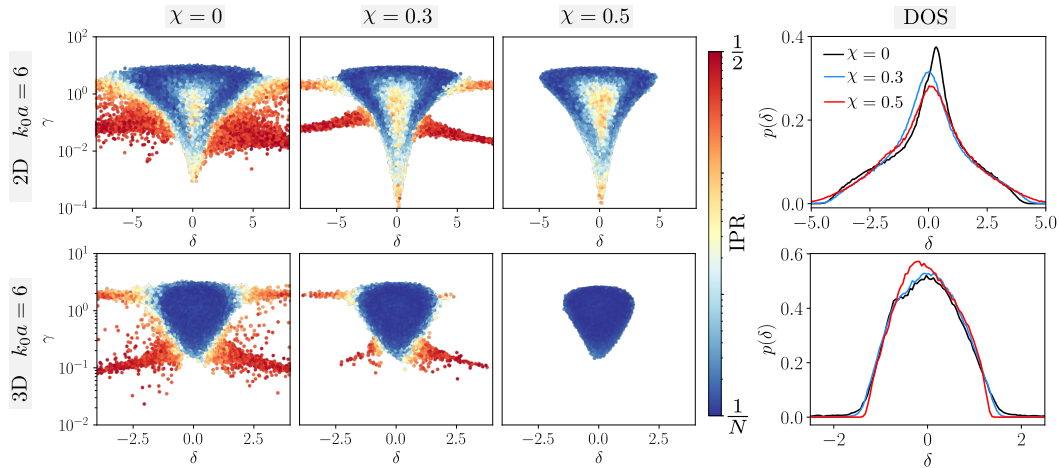


Figure 2.16: Distributions of resonances obtained for vector waves at low density  $k_0a = 6$  in 3D (top) and 2D (bottom) for  $\chi$  varying from 0 to 0.5. The colormap shows the IPR of each mode and the DOS are shown on the right in both cases.

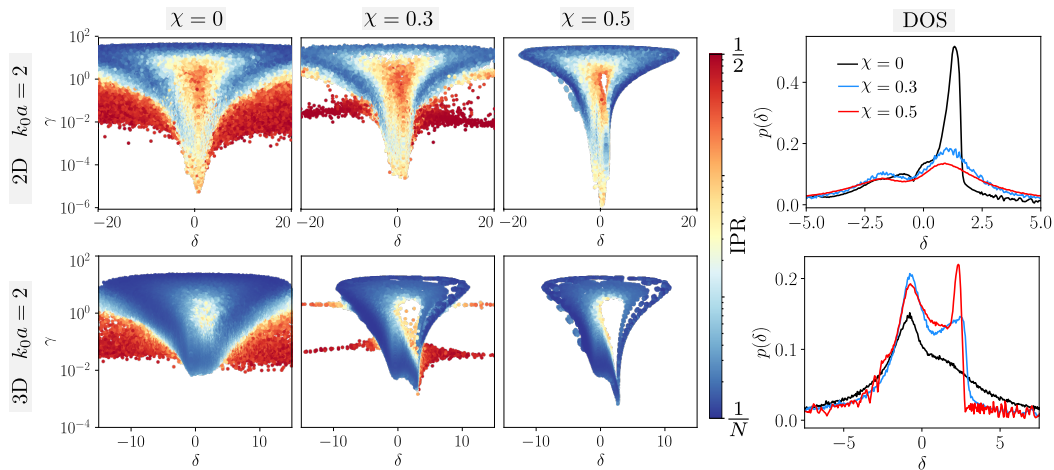


Figure 2.17: Distribution of resonances for vector fields at high density ( $k_0a = 2$ ) in 3D (top) and 2D (bottom) for  $\chi$  varying from 0 to 0.5. The colormap shows the IPR of each mode and the distribution of the detuning are shown on the right in both cases.

## 2.4.2 High density

The high density limit was interesting in the scalar case because that was the limit where Anderson localisation occurs in 3D or starts to be visible in 2D. When taking into account the full vector description of the problem in 3D at  $\chi = 0$ , strong localisation disappears as shown in Sec. 1.6.4. Whereas in the scalar case, spatial correlations favoured an already possible localisation, things look different here. Figure 2.17 displays a complicated evolution of the spectra. At  $\chi = 0$  and high density, the complex plane is much more populated by proximity resonances which are removed by correlations. For the most correlated patterns, a hole opens in the complex plane which translates into a depletion in the density of states. However, we can notice the absence of gap both in 2D and 3D, no matter the correlation strength. The evolution of the DOS under the influence of spatial correlation is studied in Chap. 4. In addition, there is no mode with a sufficiently small linewidth nor a high enough IPR to signal a localised state in the bulk. The situation is thus different from the scalar case. In the lineage of Skipetrov and Sokolov (2014); Máximo et al. (2015) localisation of vector waves do not seem possible at high density. The story does not end here and there is still one regime

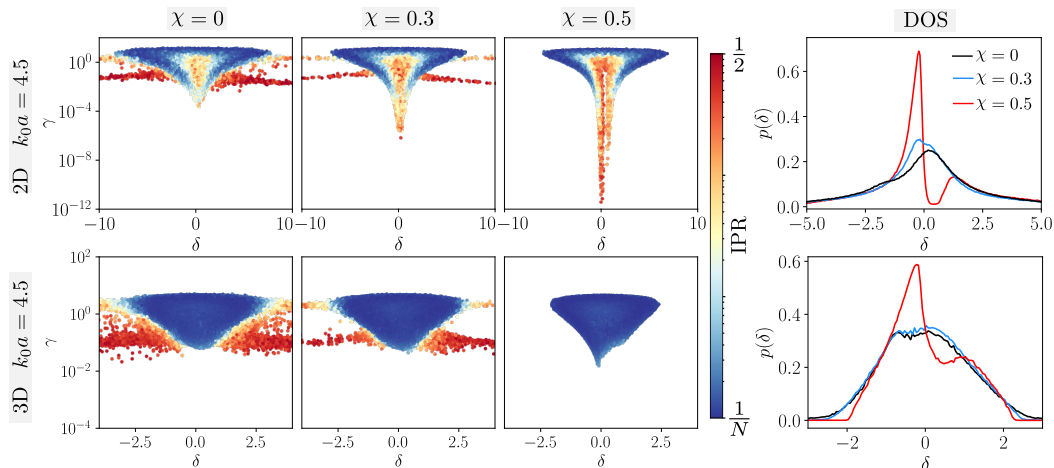


Figure 2.18: Distribution of resonances obtained at intermediate density  $k_0a = 4.5$  in 3D (top) and 2D (bottom) for  $\chi$  varying from 0 to 0.5. The colormap shows the IPR of each mode and the distribution of the detuning are shown on the right in both cases.

of interest left to explore.

### 2.4.3 Intermediate density

Around a density of  $k_0a \sim 4.5$ , the situation differs now between both the vector and the scalar cases, but also between the 2D and the 3D setups. When looking at Fig. 2.18, we can notice that in the absence of correlations, the 2D and 3D setups have spectra similar to the ones found in the low density limit. As soon as the correlation ratio increases, the 3D distribution is only stripped of its branches without much qualitative changes. Regarding the 2D situation at  $\chi = 0.3$ , there exists a set of modes in the middle of the distribution with intermediate values of IPR but not so small  $\gamma$ . Increasing  $\chi$  rearranges this domain of the spectrum by pulling the collective linewidth toward vanishingly small values, and visibly increasing the IPR in the direct vicinity. The complex spectrum at  $\chi = 0.5$  seems to exhibit a cut near  $\delta = 0$  which is seen on the DOS as a pseudo-gap. A map of the intensity profile of the modes shows [Fig. 2.19 (b-c)] a very different behaviour without and with correlations, going from a diffusive and extended mode to a strongly localised one at  $\chi = 0.5$ . We thus make the same observations as in the high density limit for scalar waves: a pseudo-gap develops in the DOS near which spatially localised modes with very long lifetime exist. There is thus an Anderson localised domain for 2D vector waves in a density regime where scalar wave is not observed to localise in our finite-sized setup (even though TM waves are expected to always be localised in infinite samples). It is to our knowledge the first occurrence of the observation of localised electromagnetic vector waves in 2D.

A systematic study of the problem is presented in the next section. We build a localisation phase diagram and emphasise the link between Anderson localisation and a collapse of the DOS.

## 2.5 Localisation phase diagram

Previously, we characterised localisation using the IPR and the collapse of the linewidths of the collective modes. Yet, a high IPR does not unequivocally refer to an exponentially localised mode as proximity resonances and or modes located at the sample boundary may have large IPR without being related to Anderson localisation. We will thus use  $\gamma$ , and in particular its minimum value per frequency range as a robust indicator for Anderson Localisation, as was

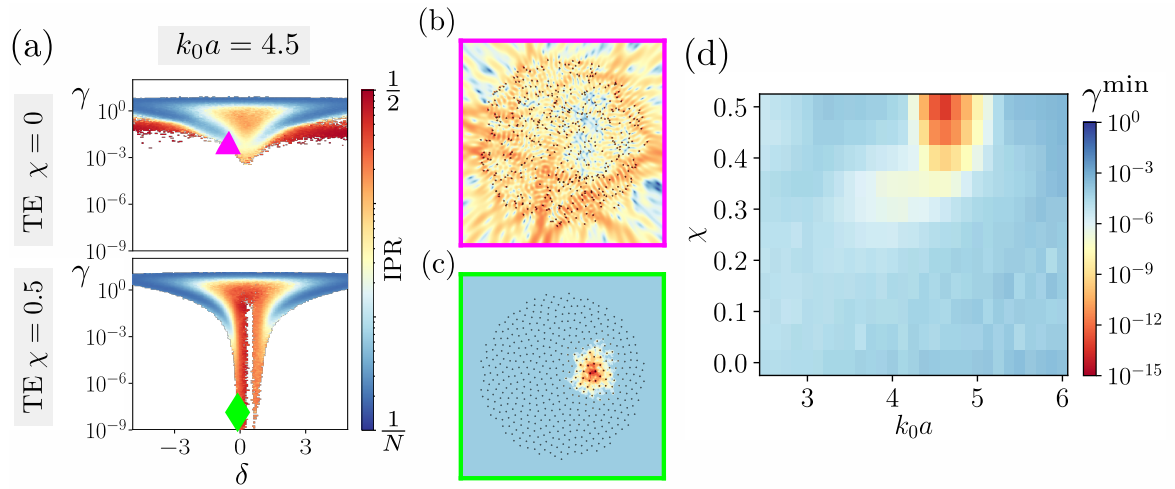


Figure 2.19: (a) Comparison between the complex spectrum computed at  $k_0a = 4.5$  in the TE polarisation at  $\chi = 0$  and  $\chi = 0.5$ . (b, c) Examples of the spatial profiles of modes taken in each distribution, showing a delocalised mode in the fully disordered pattern (b) and (c) a localised one for the most ordered one. (d) Minimal value of the linewidth as a function of density and correlation. According to Fig. (d), the localised regime seems to appear above  $\chi \gtrsim 0.35$ .

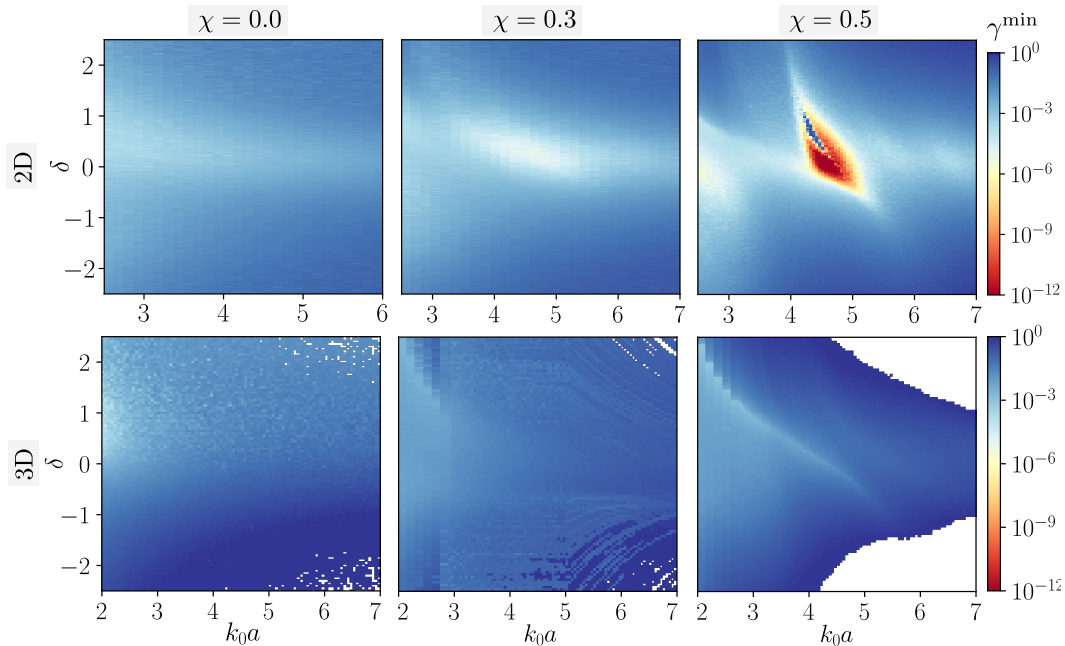


Figure 2.20: Map of the minimal value of  $\gamma$  in the density-frequency ( $k_0a, \delta$ ) space for  $\chi$  ranging from 0 to 0.5 in both 2D (top) and 3D (bottom).

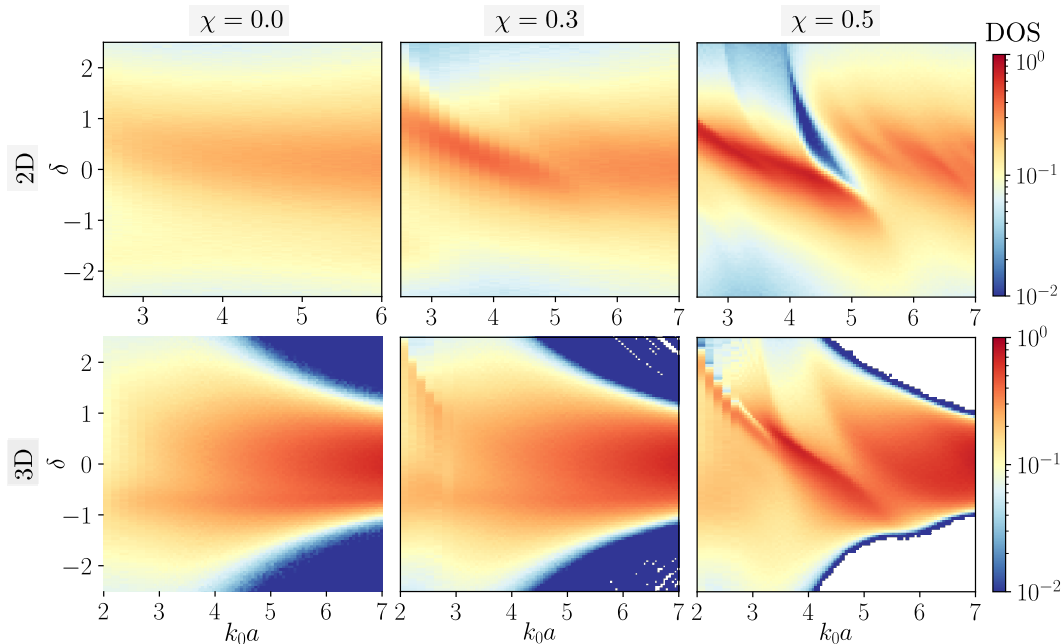


Figure 2.21: Map of the density of states for vector waves in the density-frequency  $(k_0 a, \delta)$  space for  $\chi$  ranging from 0 to 0.5 in both 2D (top) and 3D (bottom).

already done in Sec. 2.3.3. The results are shown in Fig. 2.20 in both the 3D and the 2D situations. In the 3D case, we see that the linewidths remain large, no matter the density, frequency or correlation ratio. In the 2D case though, we see that a window of localised modes with very small linewidths opens between  $k_0 a = 4$  and 5, for mostly positive detunings. The small cut of large  $\gamma^{\min}$  inside the localised domain occurs for modes located at the center of the pseudo-gap, associated to eigenstates localised at the sample boundaries and described in Fig. 2.15. Such eigenstates quickly leak out and thus have a large  $\gamma$ .

Furthermore, we also show the DOS map in Fig. 2.21. In the 3D case, no significant reduction of the DOS appears in the presence of correlations and only weak features, correlated with the map of minimum linewidths, can be seen in the most correlated situation. Nonetheless, in 2D we can see a sharp decrease of the DOS in the region  $4 < k_0 a < 5$ , described above as a localisation domain.

The coincidence between the existence of a pseudo-gap in the DOS and a localised regime was already seen for scalar waves in Figs. 2.14 and 2.13. It will be explored and explained theoretically in the next chapters. In the meantime, let us focus on the properties of the localised domain for 2D vector waves.

## 2.6 Finite size effects and scaling approach of 2D TE collective resonances

In this section we will analyse the behaviour of the system as its size is increased. We will confirm through a scaling analysis that our observations indeed correspond to Anderson localisation and question the existence of a phase transition as in the 3D scalar configuration.

### 2.6.1 Finite size effects

We computed maps of both  $\gamma^{\min}$  and the DOS for three different values of the system size  $k_0 R$ . Compared to Figs. 2.20 and 2.21, we doubled the size of the system each time to reach respectively  $k_0 R = 55$ , 110 and 220 in the largest case. We focused on the region of interest



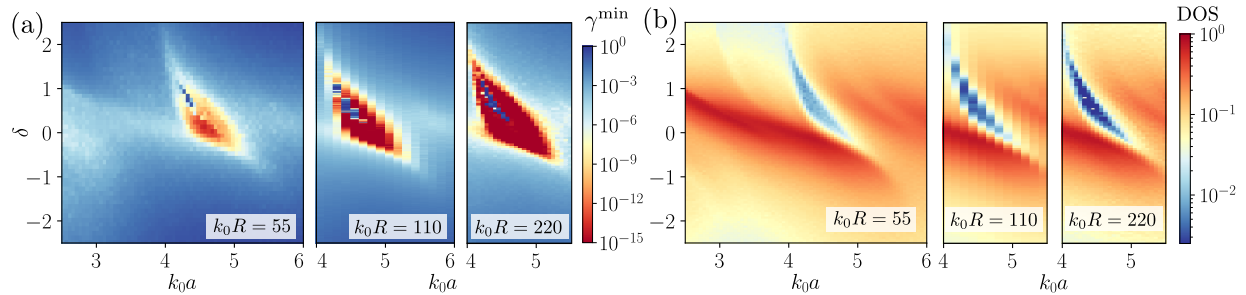


Figure 2.22: Evolution of  $\gamma^{\min}$  (a) and of the density of states (b) in the TE polarisation of the most correlated point patterns in 2D ( $\chi = 0.5$ ) as function of the system size  $k_0 R$ . The statistical analysis has been performed with at least  $10^5$  eigenvalues for each set of parameters.

for localisation because higher densities became out of reasonable reach at these sizes. The values of  $\gamma^{\min}$  [Fig. 2.22 (a)] decrease from around  $10^{-12}$  to  $10^{-15}$  and below the machine precision. The domain over which the linewidths collapse also expands a bit while its edges become sharper. The density of states [Fig. 2.22 (b)] is left almost unchanged apart from a deepening of the gap and the phase-space extent of the domain where we have a complete band gap remains small. These results strongly indicate that localisation is preserved in the infinite size limit. This will be confirmed in the next section by a finite-size scaling analysis.

## 2.6.2 Scaling approach

We perform here a scaling analysis (see Sec.1.6 for an introduction), following the approach developed in Ref. Skipetrov (2016) for 3D scalar waves. For this, we define the dimensionless conductance as

$$g = \frac{\gamma}{\langle \omega_{n+1} - \omega_n \rangle}. \quad (2.8)$$

It has been shown in Refs. Skipetrov (2016); Skipetrov and Sokolov (2014) that the entire distribution of  $g$  does not follow the one-parameter scaling required by the theory of Abrahams et al. (1979). To solve this issue, we can look at the part of the distribution accounting for the smallest conductances. We thus define the quantile  $q$  of the distribution such that

$$q = \int_0^{g_q} p(g) dg, \quad (2.9)$$

where  $p(g)$  is the normalised distribution of the conductance and  $g_q$  the pivot value. We then perform the statistical analysis only on the part of the distribution accounting for a given quantile, meaning that values above  $g_q$  are not considered. A  $q$  value of 0.5 turns  $g_q$  into the median, and if  $q = 1$ ,  $g_q$  gives the upper edge of the distribution. By extension, we also define  $g_{q=0} = \min g$

Based on Refs. Skipetrov (2016); Skipetrov and Sokolov (2014), we choose  $q$ -values ranging from  $10^{-4}$  to  $10^{-3}$ , without noticeable differences between them, and computed the derivative with the system size

$$\beta(g) = \frac{d \ln g_q}{d \ln R}, \quad (2.10)$$

where  $R$  is the size of our system which varies in our case from  $k_0 R = 55$  to  $k_0 R = 110$ . About  $10^6$  eigenvalues have been used for each size, meaning respectively 533 and 133 disordered configurations of  $N = 469$  and  $N = 1877$  resonators. The values of  $g_q$  are computed for each frequency in window of width  $\delta \pm 0.01$  surrounding the gapped region at  $k_0 a = 4.5$ , first in the absence of correlations giving Fig. 2.23 (a). We do not access very small values for  $g_q$  in our system and the  $\beta$  function is quite noisy due to the small number of eigenvalues in

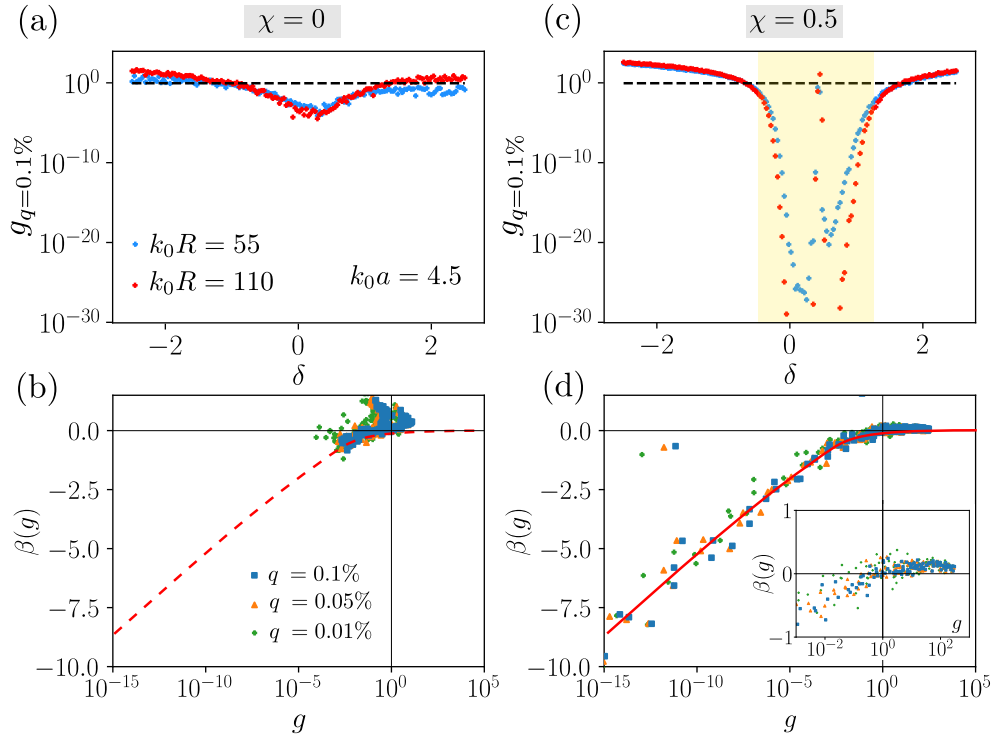


Figure 2.23: Values of  $g_{q=0.01\%}$  versus detuning  $\delta$ , for 2D vector waves at  $k_0a = 4.5$ . The uncorrelated case ( $\chi = 0$ ) and highly correlated one ( $\chi = 0.5$ ) are shown in (a) and (c). Blue markers correspond to a system size of  $k_0R = 55$  and the red ones of  $k_0R = 110$ . The yellow domain in (c) corresponds to the frequency range where a pseudo-gap is present. Plots of  $\beta(\ln g_q)$  for  $\chi = 0$  (b) and  $\chi = 0.5$  (d). The blue squares account for  $q = 0.1\%$ , the orange triangles for  $q = 0.05\%$  and the green crosses for  $q = 0.01\%$ . The solid lines are illustrative and the inset of (c) is a zoom of the region around  $\beta \sim 0$ .

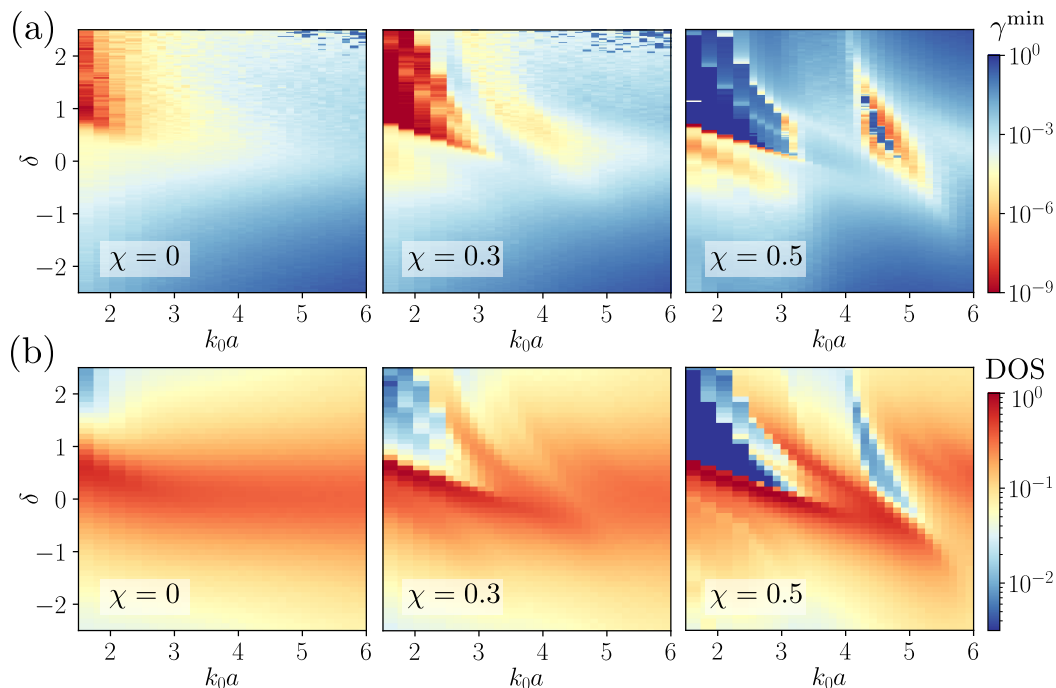


Figure 2.24: Maps of  $\gamma^{\min}$  (a) and of the density of states (b) in 2D sets of uncorrelated ( $\chi = 0$ , left) to strongly correlated ( $\chi = 0.5$ , right) resonators, coupled via the transverse Green's function (2.12). The system size is  $k_0 R = 55$ .

the pseudo-gap leading to large statistical fluctuations. It covers both positive and negative values, and as a result there is no clear evidence of a phase transition.

In the case of strongly correlated patterns, the conductance  $g_q$  collapses faster in the localised region for large systems, as seen in Fig. 2.23 (c). The plot of the scaling function in Fig. 2.23 (d) has the characteristic profile of a localised phase (see Fig. 1.10). We have a characteristic exponential scaling for small values of the conductance, and a stabilisation towards a constant value of  $\beta$  for larger conductances. It is difficult to assess, even when looking at the zoom over the region  $g \sim 1$ , if the system exhibits a phase transition because the values remain noisy and  $\beta$  stays close to 0. Outside of the localised frequency window, the conductance has little to no dependence on the system size. The values of positive  $\beta$  are also the most subject to fluctuations when changing  $q$  or the width of the frequency window. These results show that 2D TE systems exhibit Anderson localisation in the presence of correlation, but are not sufficiently precise to assess the existence of a phase transition or not.

## 2.7 Short-range and polarisation effects

The question of the origin of the hindrance to localisation of vector waves in fully disordered patterns has been tackled already in Refs. Máximo et al. (2015); Skipetrov and Sokolov (2014). The crucial role of short-range effects has been pointed out in Refs. Skipetrov and Sokolov (2015); Skipetrov and Beltukov (2018) and Ref. Máximo et al. (2015) suggested the idea to use an artificially modified Green's function to test separately the influence of the vector nature of the field and of its near-field components. We carried out a similar analysis for spatially correlated ensembles by substituting from the full dyadic Green's tensor its transverse component in Fourier space. There are indeed several ways to discard the short-range  $r^{-d}$  divergence. The simplest one is to use the far-field expression. Alternatively one can notice that the divergence is brought by the longitudinal part of the Green's function  $G^{\parallel}$ . This is the choice we did to preserve some of the non-transverse polarisation component. Using the

expression of the total Green's tensor,

$$\mathbf{G}_0(\mathbf{q}, \omega) = G_0^\perp(\mathbf{q}, \omega)\mathbf{\Delta}_\mathbf{q}^\perp + G_0^\parallel(\mathbf{q}, \omega)\mathbf{\Delta}_\mathbf{q}^\parallel, \quad (2.11)$$

the modified Green's function reads

$$G_0^\perp(\mathbf{r}, \omega) = \begin{cases} -\mathbf{\Delta}_\mathbf{r}^\perp \frac{e^{ik_0r}}{4\pi r} + (2\mathbf{\Delta}_\mathbf{r}^\parallel - \mathbf{\Delta}_\mathbf{r}^\perp) \left[ \frac{i}{k_0r} \frac{e^{ik_0r}}{4\pi r} + \frac{1}{k_0^2 r^2} \frac{1 - e^{ik_0r}}{4\pi r} \right] & \text{in 3D} \\ -\mathbf{\Delta}_\mathbf{r}^\perp \frac{i}{4} H_0^{(1)}(k_0r) + (\mathbf{\Delta}_\mathbf{r}^\parallel - \mathbf{\Delta}_\mathbf{r}^\perp) \left[ \frac{1}{2\pi k_0^2 r^2} - \frac{i}{4} \frac{H_1^{(1)}(k_0r)}{k_0r} \right] & \text{in 2D} \end{cases} \quad (2.12)$$

In the 2D case, we observe in Fig. 2.24 (a) for uncorrelated patterns a similar behaviour as for 2D waves in TM polarization (see Fig. 2.10) in Fig. 2.14, with a system already partially localised at large densities. At these densities, correlations play the same role as for scalar waves, facilitating localisation and opening a band-gap at positive detuning. More interestingly, we can see that at intermediate densities, we recover the behaviour of the TM configuration, with both the localised domain and the pseudo-gap around  $k_0a = 4.5$ . Hence the longitudinal part of the Green's function and in particular its short-range components has no influence in the intermediate density range where localisation of TE waves is observed. This is not surprising since at intermediate density and in arrangements where the distance with one's first neighbour is close to  $0.9a$ , the short-range terms are already weaker than the far-field contribution.

## 2.8 Conclusion

The present chapter intended to explore numerically the physics of spatially correlated ensembles of resonators. We first described the properties and the generation processes of such correlated patterns. We highlighted the similarity between strongly correlated ensembles of both hard sphere-like and hyperuniform systems, which both share a narrow nearest neighbour distribution. This similarity justified our choice to mostly focus on stealthy hyperuniform ensembles as a robust model for strongly correlated materials.

We first simulated the behaviour of patterns with diverse degrees of partial order, coupled by the scalar Green's propagator. We observed that Anderson localisation is visible in finite-size systems of high density in both 2D and 3D space even in the absence of correlations. Partial order has been noticed to push the system further toward localisation, and coincidentally opens a pseudo-gap in the DOS. The 2D and 3D gaps occur around the same values of densities and frequencies and have the same rhombus shape. Their common origin will be studied in Chap. 3.

As a second step, we looked at the more complicated situation where the resonators are coupled through the full vector problem. Localisation of light at high density is known to be hindered by the opening of a transport channel mediated by short-range interactions, and spatial correlations do not alter this mechanism. No localisation can be seen in the 3D setup at any density, while it occurs in 2D for highly correlated ensembles of moderate density. We confirmed through a scaling approach that this phenomenon can be attributed to Anderson localisation. Yet, we could not discern whether the system exhibits a phase transition as is the case for 3D scalar waves, or if the situation is identical to the 2D scalar configuration. Using only the transverse part of the dyadic Green's tensor, we showed that the localisation window at intermediate density was an effect of the polarisation alone and that near-field contributions can be neglected.

This numerical study brought several questions. First, how do spatial correlations influence the density of states? We will try to answer this problem by two different approaches. The first one consists in regarding correlated patterns as sets of weakly disordered crystals that can be

treated within the photonic crystal framework introduced in Sec. 1.7. This will be the subject of Chap.3. The second approach is based on a mesoscopic physics picture, where we will identify an unexpected relation between the DOS and the self-energy of the wave propagator and perform a low density expansion of the self energy, exact up to the second order. It will allow to compute analytically the DOS and predict the effect of spatial correlations. This will be the topic of Chap. 4. The second question is the link between the DOS and the properties of localisation of such media. This will be addressed in Chap. 5 by means of the self-consistent theory of localisation, adapted to the non-trivial case of vector waves propagating in strongly correlated and resonant systems.

## Chapter 3

# Strongly correlated patterns seen as disordered crystalline structures

The aim of this chapter is to show the relevance of the study of photonic crystals for the understanding of correlated disordered systems. We will use the properties of the spatial correlations functions of strongly correlated SHU patterns and crystalline lattices to justify the similarities found in their DOS. We will focus on simple 2D lattices, such as the triangular or square lattice, to understand the photonic properties of crystals of various densities, for both scalar (TM polarisation) and vector (TE polarisation) couplings. We will show that the density of states of 2D lattices, and in particular the triangular one, shares a lot of similarities with the strongly correlated point patterns described in Chap. 2. Yet, there is no particular reason why the triangular lattice should provide a better description of SHU ensembles than the square one, or any other lattice. We will show that SHU ensembles can be viewed as patches of different crystalline structures with a variety of orientations and lattice parameters and, as a result, we will make the hypothesis that the SHU DOS can be recovered by averaging the DOS of the different crystalline patches. We assume that all of the lattices sharing the same statistical properties will participate to the photonic structure of disordered patterns which should exhibit an average behaviour. This approach will turn out to be accurate, capturing in particular the opening of gaps. This model will also give insights into the physics involved. By studying the conditions for the opening and the closing of the gaps in different lattices, we will understand the fundamental differences between the scalar and vector cases regarding both the high and low density gaps. We will show that the conditions for the existence of gaps in the structure can be modelled using only the interplay between up to three Brillouin zones, allowing to further simplify the study. The crucial role of polarisation effects in the gap physics will be particularly emphasised.

This study, mainly focused on 2D systems, will be extended to 3D ensembles to give general predictions for 3D SHU patterns.

### 3.1 Structural similarities between SHU patterns and crystals

The link between a perfect crystal with infinite-range correlations and a strongly correlated but still disordered system is not obvious. In particular, one cannot derive a proper dispersion relation in the case of a disordered ensemble. Yet strongly hyperuniform point patterns exhibit well defined short-range order. This becomes even clearer if we draw unit cells on the pattern, as is done for perfect lattices. The result is shown in Fig. 3.1 (a). The disordered pattern looks like a patchwork of small crystals with their own orientation, in contrast with the perfect crystal which preserves orientational order. The microcrystals are composed on average of a few dozens of unit cells at  $\chi = 0.5$ . The similarity is reinforced by the analysis of the first neighbour distribution and the pair-correlation function, as shown in in Fig. 3.1 (b). Both

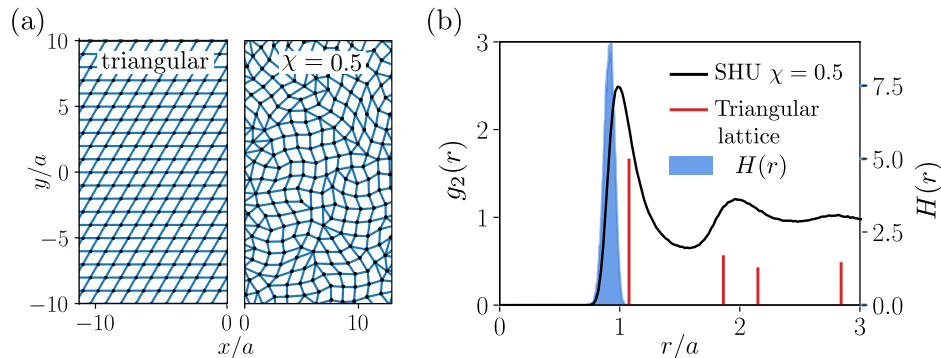


Figure 3.1: (a) Connected point patterns of a triangular lattice (left) and a SHU configuration at  $\chi = 0.5$  (right). (b) Pair correlation function  $g_2(r)$  (left axis) and nearest neighbour distribution  $H(r)$  (right axis) of a SHU configuration at  $\chi = 0.5$ . The function  $g_2(r)$  of a triangular lattice is superimposed for comparison.

of them are peaked, indicating strong short-range order, similar to the one found in lattices (see  $g_2$  of the triangular lattice in red). These observations suggest that a strongly correlated disordered pattern can be seen as an assembly of small crystals, with orientation and lattice parameters that fluctuate while preserving a large packing fraction. The study of photonic crystals is thus justified, both as the limiting case of perfectly correlated systems and as a potentially good model for strongly correlated ones.

## 3.2 From the Hamiltonian to the dispersion relation

In this section, we will derive the equation giving the dispersion relation  $\omega = f(\mathbf{q})$  for any Bravais lattice in 2D made of resonators. Our approach is inspired by the analysis of 3D atomic lattices developed in Refs. Antezza and Castin (2009b,a). The Hamiltonian used in Eq. (1.48) to obtain the complex spectrum in the coupled-dipole method applies for all kinds of spatial arrangements and can thus be used to treat photonic crystals. The approach simply consists in expressing Eq. (1.48) in a Bloch basis, which turns a  $\beta N \times \beta N$  Hamiltonian into a  $\beta \times \beta$  effective Hamiltonian, where  $\beta$  is the dimension of the field and  $N$  the number of coupled resonators.

### 3.2.1 Hamiltonian in Bloch space

For infinite Bravais lattices, eigenstates of the Hamiltonian (1.48) taken at resonance are Bloch modes that can be labelled by a vector  $\mathbf{q}$  in the first Brillouin zone. The corresponding eigenvalues are noted  $\omega_{\mathbf{q}}$ . Using the periodicity of the lattice, the eigenvalue problem reduces to  $\det[\omega_{\mathbf{q}}\mathbb{1} - \mathcal{H}_{\mathbf{q}}(\omega_{\mathbf{q}})] = 0$ , where the  $\beta \times \beta$  matrix  $\mathcal{H}_{\mathbf{q}}(\omega_{\mathbf{q}})$  is given by

$$\mathcal{H}_{\mathbf{q}}(\omega_{\mathbf{q}}) = \left( \omega_0 - i \frac{\Gamma_0}{2} \right) \mathbb{1} - \frac{\Gamma_0}{2} \tilde{\mathcal{G}}_0(\mathbf{q}, \omega_{\mathbf{q}}), \quad (3.1)$$

where  $\tilde{\mathcal{G}}_0(\mathbf{q}, \omega_{\mathbf{q}}) = -c_d k_0^{2-d} \sum_{\mathbf{R} \neq \mathbf{0}} \mathbf{G}_0(\mathbf{R}, \omega_{\mathbf{q}}) e^{-i\mathbf{q} \cdot \mathbf{R}}$  is the Green's matrix expressed in terms of Bloch waves. Since the free space Green's function  $\mathbf{G}_0$  decays slowly in real space, it is not possible to perform a nearest-neighbour-type approximation of the summation involved in  $\tilde{\mathcal{G}}_0(\mathbf{q}, \omega_{\mathbf{q}})$ . Using Poisson's formula instead, we convert the sum over lattice positions  $\mathbf{R}$  into a sum over reciprocal lattice vectors  $\mathbf{Q}$ ,

$$\tilde{\mathcal{G}}_0(\mathbf{q}, \omega_{\mathbf{q}}) = -c_d k_0^{2-d} \left[ \rho \sum_{\mathbf{Q}} \mathbf{G}_0(\mathbf{q} - \mathbf{Q}, \omega_{\mathbf{q}}) - \mathbf{G}_0(\mathbf{R} = \mathbf{0}, \omega_{\mathbf{q}}) \right], \quad (3.2)$$

where the Fourier transform of the Green's function is given by Eq. (1.4). The formulation (3.2) is more appropriate for computation because convergence is much faster in momentum space. The price to pay is the necessity to regularise  $\mathbf{G}_0$  since the two terms in Eq. (3.2) diverge, whereas their difference does not. In the following, we adapt to 2D scalar and vector waves the regularisation procedure introduced in Antezza and Castin (2009b); Perczel et al. (2017).

### 3.2.2 Regularisation of the crystalline Hamiltonian and large wavelength expansion

As mentioned above, Poisson's formula requires the evaluation of the Green's function at its singularity. This can be circumvented by introducing a Gaussian cut-off in momentum space, which smoothens the real space divergence at the origin. Explicitly we use the following relation derived in Ref. Antezza and Castin (2009a)

$$\sum_{\mathbf{R} \neq \mathbf{0}} \mathbf{G}_0(\mathbf{R}, \omega) e^{-i\mathbf{q} \cdot \mathbf{R}} \simeq \lim_{b \rightarrow 0} e^{\frac{k_0^2 b^2}{2}} \left[ \rho \sum_{\mathbf{Q}} \mathbf{G}_0^*(\mathbf{Q} - \mathbf{q}, \omega) - \mathbf{G}_0^*(\mathbf{R} = \mathbf{0}, \omega) \right], \quad (3.3)$$

where the regularised Green's function in momentum space is simply

$$\mathbf{G}_0^*(\mathbf{q}, \omega) = \mathbf{G}_0(\mathbf{q}, \omega) e^{-\frac{q^2 b^2}{2}}, \quad (3.4)$$

with  $b$  is regularisation parameter. Using Eqs. (3.3) and (3.4), we can rewrite Eq. (3.3) as a sum of finite terms

$$\tilde{\mathbf{G}}_0(\mathbf{q}, \omega) = -\frac{4\beta\omega^2}{\omega_0^2} e^{\frac{k_0^2 b^2}{2}} \left[ \frac{1}{V_L} \sum_{\mathbf{Q}} \mathbf{G}_0^*(\mathbf{q} - \mathbf{Q}, \omega) - \mathbf{G}_0^*(\mathbf{R} = \mathbf{0}, \omega) \right], \quad (3.5)$$

which becomes independent of  $b$  for  $b \ll a$ . For the 2D TM polarisation, the last term of Eq. (3.5) reads

$$\begin{aligned} \mathbf{G}_0^*(\mathbf{R} = \mathbf{0}, \omega) &= -\frac{i}{4} \int d\mathbf{r} H_0^{(1)}(k_0 r) \frac{e^{-\frac{r^2}{2b^2}}}{2\pi b^2} \\ &\underset{k_0 b \ll 1}{\simeq} -\frac{1}{\pi} \left[ \gamma + \ln \left( \frac{k_0^2 b^2}{2} \right) \right] - \frac{i\mathbb{1}}{4}. \end{aligned} \quad (3.6)$$

Here the Hankel function has been approximated at small values by

$$H_0^{(1)}(x) \underset{x \ll 1}{\simeq} 1 + \frac{i}{\pi} \left[ 2\gamma + \ln \left( \frac{x^2}{4} \right) \right], \quad (3.7)$$

where  $\gamma$  is the Euler's constant. In the TE polarisation, using  $\int_0^{2\pi} d\theta (\mathbb{1} - \hat{\mathbf{r}} \otimes \hat{\mathbf{r}}) = \pi\mathbb{1}$  and  $\int_0^{2\pi} d\theta (\mathbb{1} - 2\hat{\mathbf{r}} \otimes \hat{\mathbf{r}}) = 0$  where  $\hat{\mathbf{r}} = \mathbf{r}/r$ , we get

$$\begin{aligned} \mathbf{G}_0^*(\mathbf{R} = \mathbf{0}, \omega) &= -\frac{i\pi\mathbb{1}}{4} \int_0^\infty dr r H_0^{(1)}(k_0 r) \frac{e^{-\frac{u^2}{2b^2}}}{2\pi b^2} + \frac{\mathbb{1}}{4\pi k_0^2 b^2} \\ &\underset{k_0 b \ll 1}{\simeq} -\frac{1}{2\pi} \left[ \gamma + \ln \left( \frac{k_0^2 b^2}{2} \right) \right] - \mathbb{1} \left( \frac{i}{8} - \frac{1}{4\pi k_0^2 b^2} \right). \end{aligned}$$

The expressions for 3D ensembles are given in App. B. For small enough  $b/a$ , the Hamiltonian computed with Eq. (3.5) is independent of the regularisation parameter  $b$ . In practice, we set  $b/a = 0.01$ , and checked that we can safely truncate the sum over the reciprocal lattice without affecting the result by keeping  $\mathbf{Q}$  which satisfy  $|\mathbf{q} - \mathbf{Q}| \lesssim 7/b$ . In order to generate dispersion relations such as that shown in Fig. 3.2, we use the large quality factor approximation which amounts to replacing  $\omega_q$  by  $\omega_0$  in Eq. (3.1) and diagonalize the resulting Hamiltonian for  $\mathbf{q}$  belonging to an irreducible path of the first Brillouin zone (BZ).



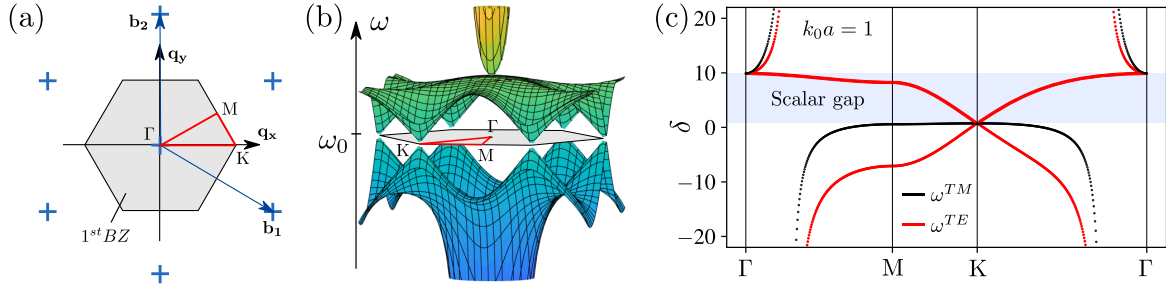


Figure 3.2: (a) First Brillouin zone of the 2D triangular lattice showing in red the irreducible domain with the symmetry points  $\Gamma$ , the centre of the BZ,  $K$  its corner and  $M$  the middle of the edges. (b) Dispersion relation for vector waves over the entire Brillouin zone, showing Dirac cones at the vertices of the hexagon. (c) Dispersion relation of the 2D triangular lattice along the irreducible path  $\Gamma$ - $M$ - $K$ - $\Gamma$  for vector waves (red) and scalar waves (black). The Dirac cones at  $K$  are clearly visible for vector waves.

### 3.3 Application to the triangular lattice

#### 3.3.1 Computation of the dispersion relation

In this section, we compute the dispersion relation of a triangular lattice composed of resonant dipoles in both the TM (scalar) and TE (vector) polarisation. The direct and reciprocal lattice parameters are given by

$$\mathbf{a}_1 = a^* \begin{pmatrix} 1 \\ 0 \end{pmatrix} \quad \mathbf{a}_2 = a^* \begin{pmatrix} 1/2 \\ \sqrt{3}/2 \end{pmatrix} \quad \mathbf{b}_1 = \frac{2\pi}{a^*} \begin{pmatrix} 1 \\ -1/\sqrt{3} \end{pmatrix} \quad \mathbf{b}_2 = \frac{2\pi}{a^*} \begin{pmatrix} 0 \\ 2/\sqrt{3} \end{pmatrix}, \quad (3.8)$$

where  $a^*$  is the distance between neighbouring resonators. It is related to  $a = V^{1/d}$  through  $a^2 = |\det(\mathbf{a}_1, \mathbf{a}_2)| = (a^*)^2 \sqrt{3}/2$ . The reciprocal lattice, as well as the first Brillouin zone of the structure, are shown in Fig. 3.2 (a).

For each  $\mathbf{q}$  in the first BZ, we compute Eq. (3.5) and obtain the band structure  $\omega = f(\mathbf{q})$ . The result for TE polarisation is shown in Fig. 3.2 (b). We identify three bands although we have two eigenvalues only. This is due to the polaritonic structure captured near the resonance, as both the lower and the upper polaritons (see also Fig. 1.18) are described by a single eigenvalue through the divergence of a hyperbolic function.

As we can see in Fig. 3.2 (b), the symmetries make the representation over the entire BZ redundant. A computation along the edges of what is called an irreducible domain, represented in red in Fig. 3.2 (a), is enough to describe the entire band structure. The dispersion relation along the path  $\Gamma$ (centre of the first BZ)- $M$ (middle of an edge)- $K$ (vertex) in both TE and TM is given in Fig. 3.2(c). It gives a clear representation of the three bands found in the vector case, and the two polaritonic bands in the scalar one. This representation emphasizes the existence of Dirac cones at the point  $K$ , which closes the gap observed for scalar fields. Dirac cone connecting a polaritonic band and a flat band have been reported in the case of micropillar optical cavities arranged in a honeycomb lattice in Ref. Jacqmin et al. (2014).

#### 3.3.2 Computation of the density of states

For photonic crystals, the density of states  $p(\omega)$  can be straightforwardly obtained from the band structure. The eigenvalues of Eq. (3.1) are computed for each  $\mathbf{q}$  in the first BZ and the number of solutions  $\omega(\mathbf{q})$  in a given frequency range is counted. Explicitly

$$p(\omega) = \sum_n \int_{\mathbf{q} \in \text{BZ}} d\mathbf{q} \delta[\omega - \omega_n(\mathbf{q})], \quad (3.9)$$

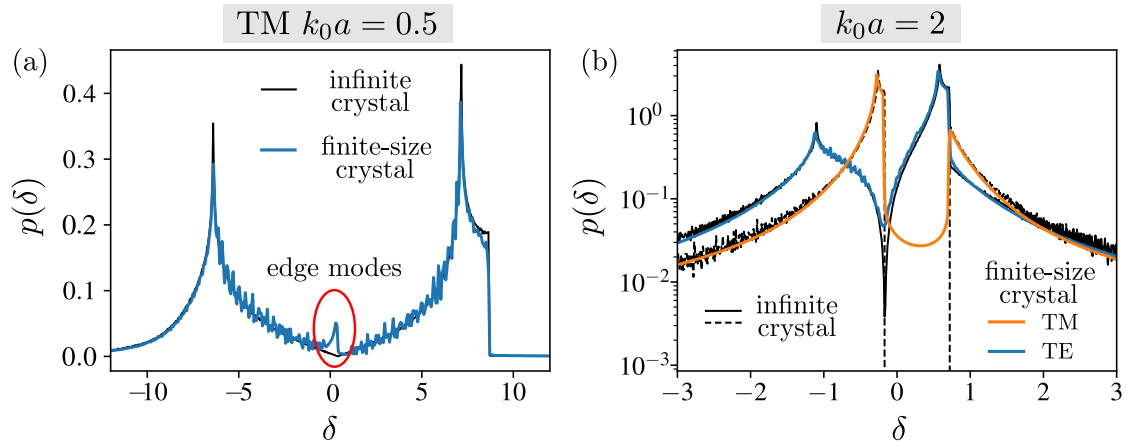


Figure 3.3: Density of states of triangular lattices at  $k_0a = 0.5$  (a) and  $k_0a = 2$  (b). In each case, the black lines account for the solutions associated to Eq. (3.1), while the blue and orange lines are obtained from brute-force diagonalization of the coupled-dipole Hamiltonian in respectively the TE and TM polarisation. The spectra are computed from the diagonalization of the Green’s matrix for  $N = 10^4$  resonators. The agreement between the two is excellent except at low values of  $p(\delta)$ , because of residual leaking in finite-size samples.

where  $n$  runs over the different bands and  $\omega_n$  are the eigenvalues of the Hamiltonian 3.1 associated to each band.

In Fig. 3.3 we compare, the DOS of the the triangular lattice evaluated from Eq. (3.5), to the DOS computed from a direct diagonalization of the Hamiltonian 1.48 with  $N = 10^4$ . As expected, the agreement between the two approaches is excellent. We can point out two differences. The first difference is the existence of edge modes in the finite-size system [see Fig. 3.3 (a)], which are not predicted from Eq. (3.1) because the latter assumes infinite system size. The second difference is the presence of residual DOS for finite-size system, in the TM gap predicted for infinite systems. This has also been observed, yet less drastically, for TE waves, at the crossing of the Dirac cones of Fig. 3.2, where the density of modes is minimal. This finite-size effect has been modelled in Ref. Hasan et al. (2018), by assuming that the linewidth of the crystalline modes is given by the inverse of the ballistic propagation time throughout the sample. This prediction has been confirmed for crystals of resonators in Ref. Skipetrov (2020).

Apart from these small differences, Eq. (3.5) is thus expected to give results identical to those obtained with the brute-force diagonalization.

### 3.3.3 Comparison between triangular lattices and hyperuniform patterns

Let us now compare the DOS of crystals and SHU disordered systems. Following our approach of Chap. 2, we computed the density of states of the triangular lattice over a large range of densities and detunings and place it in regards to the one describing strongly correlated SHU patterns ( $\chi = 0.5$ ) for TM and TE coupling. Figure 3.4 shows that the two TM DOS share a lot of features, and in particular a large gap at high densities surrounded by maxima of  $p(\delta)$ . They differ around  $k_0a \geq 4$  inasmuch as the triangular lattice exhibits a small band gap, which is absent in correlated ensembles. Nonetheless, the shape of the high density gap looks identical for both patterns.

In the TE polarisation [see Fig. 3.4, (c,d)], the high density gap is absent in both situations, while a gap exists at intermediate densities ( $k_0a \in [4, 5.5]$ ) with a distinctive sickle shape. It is however much smaller in hyperuniform ensembles than in the triangular lattice. Weaker features, with in particular a maximum of the DOS below the gap and extending at higher

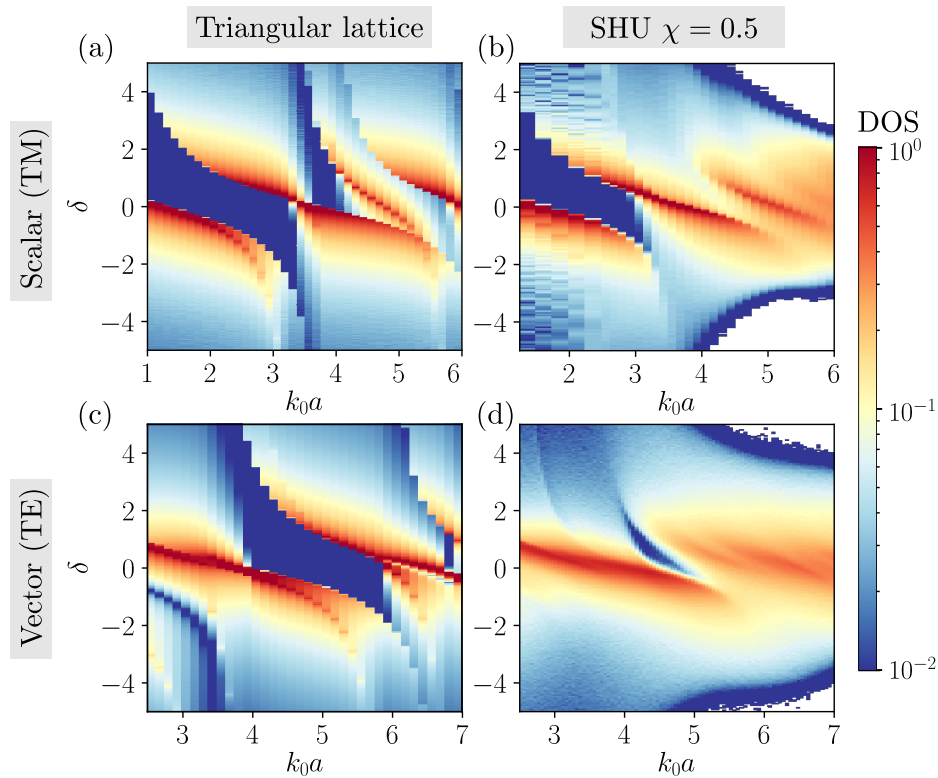


Figure 3.4: Comparison between the DOS of the triangular lattice (a,c) obtained from a sampling of the dispersion relation over the first Brillouin zone, and the DOS of hyperuniform patterns (b,d) using the coupled-dipole method, for respectively scalar (TM) and vector (TE) couplings. In the TM polarisation, both the periodic lattice and the disordered pattern exhibit a strong gap in the DOS at high densities ( $k_0 a < 3$ ) and detunings of few linewidths. In the TE polarisation, no high density gap is found in neither systems, but both support a gap of different size at intermediate densities. Even though this gap is much larger in the crystal than in SHU ensembles, it preserves the same characteristic sickle shape.

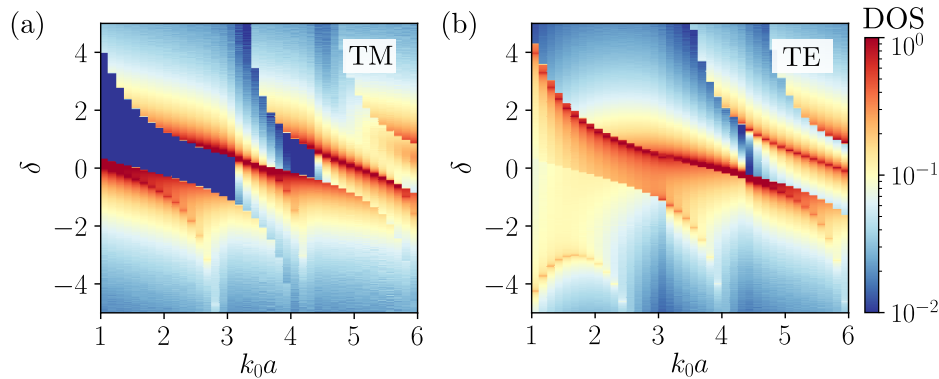


Figure 3.5: Density of states of the square lattice computed using Eq. (3.1), in TM and TE polarisation, over the density-frequency space parametrised by  $k_0a$  and  $\delta$ . The TM DOS of the square lattice is similar to the triangular one, apart from the small gap at  $k_0a \sim 4$  being more stocky. On the other hand, in the TE polarisation, there is no gap contrary to the triangular lattice. The narrow domain centred at  $k_0a \sim 4.5$  where the DOS is small, can be interpreted as a remain of the large photonic band gap of the triangular lattice.

densities, are also shared between the two systems.

### 3.4 Extension to other crystalline structures and average lattice

The previous analysis based on the triangular lattice has the merit of providing similar DOS compared to hyperuniform patterns. Yet, the choice of the triangular array may seem arbitrary, as it is not the dominating lattice in Fig. 3.1. We have represented in Fig. 3.5 the DOS of scalar and vector waves in a square lattice. For scalar waves, the DOS looks very similar to the triangular lattice result. However it is not the case for vector waves; in particular, the gap at intermediate density is barely visible in the square arrangement. In this respect, the SHU pattern seems to behave half-way between the triangular lattice and the square lattice.

Figure 3.1 tends to indicate that the two lattices mentioned above are only two of the many which can be locally found in SHU patterns. Therefore, we calculated the DOS of a wide range of lattices to obtain an average behaviour that should resemble the partially ordered configuration.

For the sake of simplicity, we restricted ourselves to the study of a subclass of 2D lattices called orthorhombic lattices. They are characterised by a single parameter, the relative angle between the two basis vectors of equal length, as shown in Fig. 3.6. To remain consistent with the statistical properties of SHU ensembles, and in particular their first neighbour distribution, we exclude lattices with a low packing fraction. The averaging procedure is summarised in Fig. 3.6, where the lattices taken into account are included in the hashed domain.

Let us give the general expressions of the reciprocal basis vectors of orthorhombic lattices. Reciprocal and direct basis vectors are related through the relation

$$\mathbf{B} = 2\pi (\mathbf{A}^T)^{-1}, \quad (3.10)$$

where  $\mathbf{A}$  ( $\mathbf{B}$ ) is a matrix whose columns are the direct (reciprocal) basis vectors. Using the parametrisation for the orthorhombic lattices and Eq. (3.10), we directly get

$$\mathbf{a}_1 = a^* \begin{pmatrix} 1 \\ 0 \end{pmatrix} \quad \mathbf{a}_2 = a^* \begin{pmatrix} \cos \theta \\ \sin \theta \end{pmatrix} \quad \mathbf{b}_1 = \frac{2\pi}{a^*} \begin{pmatrix} 1 \\ -\cos \theta / \sin \theta \end{pmatrix} \quad \mathbf{b}_2 = \frac{2\pi}{a^*} \begin{pmatrix} 0 \\ 1 / \sin \theta \end{pmatrix}. \quad (3.11)$$

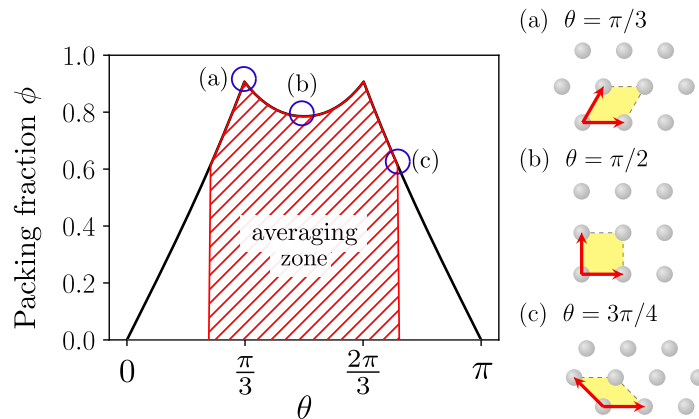


Figure 3.6: Packing fraction  $\phi$  of orthorhombic lattices with respect to the relative angle  $\theta$  between the two basis vectors. The fraction  $\phi$  is defined as the ratio between the area of packed non-interpenetrating disks placed on the lattice and the total area. Examples of unit cells are shown on the right: triangular lattice (a) with  $\phi = 0.90$ , square lattice (b) with  $\phi = 0.78$ , and a less compact oblique lattice (c) with  $\phi = 0.60$ . The dashed domain shows the range of angles used to obtain the average DOS of Fig. 3.7 (a,c) and corresponds to  $\phi \leq 0.6$ .

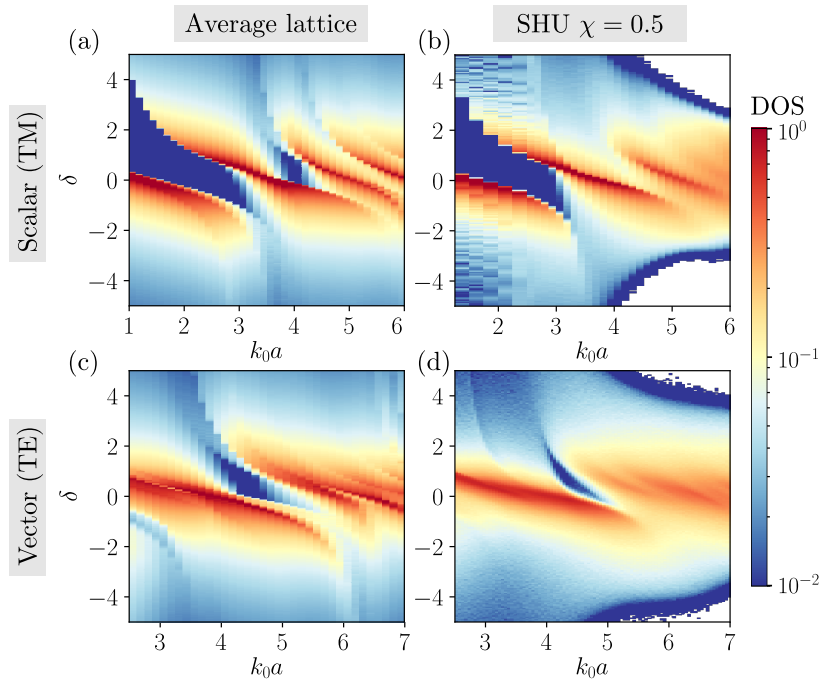


Figure 3.7: Comparison between the density of states of photonics crystals averaged over the lattice parameters, as defined in Fig. 3.6, (left column) and the one obtained for SHU systems (right column). The system in TM polarisation is shown on the upper line and the TE polarisation on the bottom line. The DOS are very similar in both polarisations, with the only difference being a small gap for scalar waves centred at  $k_0a = 4$ , absent in the disordered systems.

Here  $a^*$  is the vector length in the direct basis. It can be expressed in terms of the mean distance  $a = 1/\rho^{1/2}$  as  $a = a^* \sqrt{|\sin \theta|}$ . We computed the dispersion relation for 40 different lattices such that  $\theta \in [\pi/4.25, \pi/2]$  and packing fraction  $\phi > 0.6$ , and averaged their DOS to obtain Fig. 3.7.

For scalar waves, this averaging procedure does not modify in depth the results already found with the triangular and square lattices. However it leads to a better agreement with the SHU DOS, in particular at high density. At lower densities, the DOS still possesses rather sharp fluctuations that are smoothed out in the disordered case. Another difference is the existence of a small gap in the crystalline structures at  $k_0a = 4$  which is absent in the hyperuniform setup. Its position nonetheless coincides with a local minimum of the DOS of the SHU patterns. In the TE configuration, the averaging procedure leads to more significant effects. The large gap observed at intermediate density in the triangular lattice is shrunk and is now comparable to the one observed in SHU patterns. Most of the other weaker features of the DOS of SHU ensembles are also visible, but with finer details, as it was the case for the TM polarisation. These small discrepancies may be due to the approximation consisting in only considering orthorhombic lattices, which only span a subset of all possible 2D lattices.

In any case, the description of the strongly correlated SHU patterns in terms of ensembles of crystals whose lattice parameters and orientations fluctuate seems to hold. This incites us to study in more details photonic crystals, to elucidate in particular the conditions for the opening and closing of the gaps.

## 3.5 The origin of band gaps in photonic crystals made of resonators

This section will present an analysis of the band structure of the triangular lattice as function of the number density. We will focus on the existence of band gaps and will relate their opening and closing conditions to special combinations of polaritonic dispersion relations associated to different Brillouin zones.

### 3.5.1 Fine analysis of the opening and closing of band gaps in the triangular lattice

Figures 3.8 and 3.9 display the band structure in both TM (black) and TE (red), as well as the first BZ of the triangular lattice and the intersection of the light-cone with the resonant frequency ( $|\mathbf{q}| = \omega_0/c$ ) for densities varying from  $k_0a = 2$  to  $k_0a = 7.5$ . At high densities ( $k_0a \leq 3$ ), the scalar dispersion relation is polaritonic-like, with a full band gap between the lower polariton plateauing around  $\delta = 0$ , and the upper polariton whose minimum lies around  $\delta = 2$  (see Sec. 3.6.1 for a theoretical justification). This TM gap then closes around  $k_0a = 3.4$ , where a band folds at the point M. The existence of a high density gap corresponds to the density range where the light circle is completely included in the first Brillouin zone. And a contact at M between the light circles associated to two neighbouring BZ sets the closing condition for the high density gap. No large gap subsists in TM polarisation beyond this crossing.

Regarding the TE polarisation, the high density band structure looks similar to the TM one, apart from an extra relatively flat band closing the polaritonic structure. The same kind of folding happens for the lower and upper polariton near the point M, but the structure remains gap-less. One needs to wait until the density decreases enough to allow a crossing of three light circles at the point K to witness the opening a gap for the vector system. Interestingly, the TM band structure is gap-less in this density regime. The TE setup maintains a gap up to  $k_0a \sim 5.85$ , which coincides with the next contact between light circles coming from next to nearest neighbours BZ. This contact occurs at M. The structure then becomes

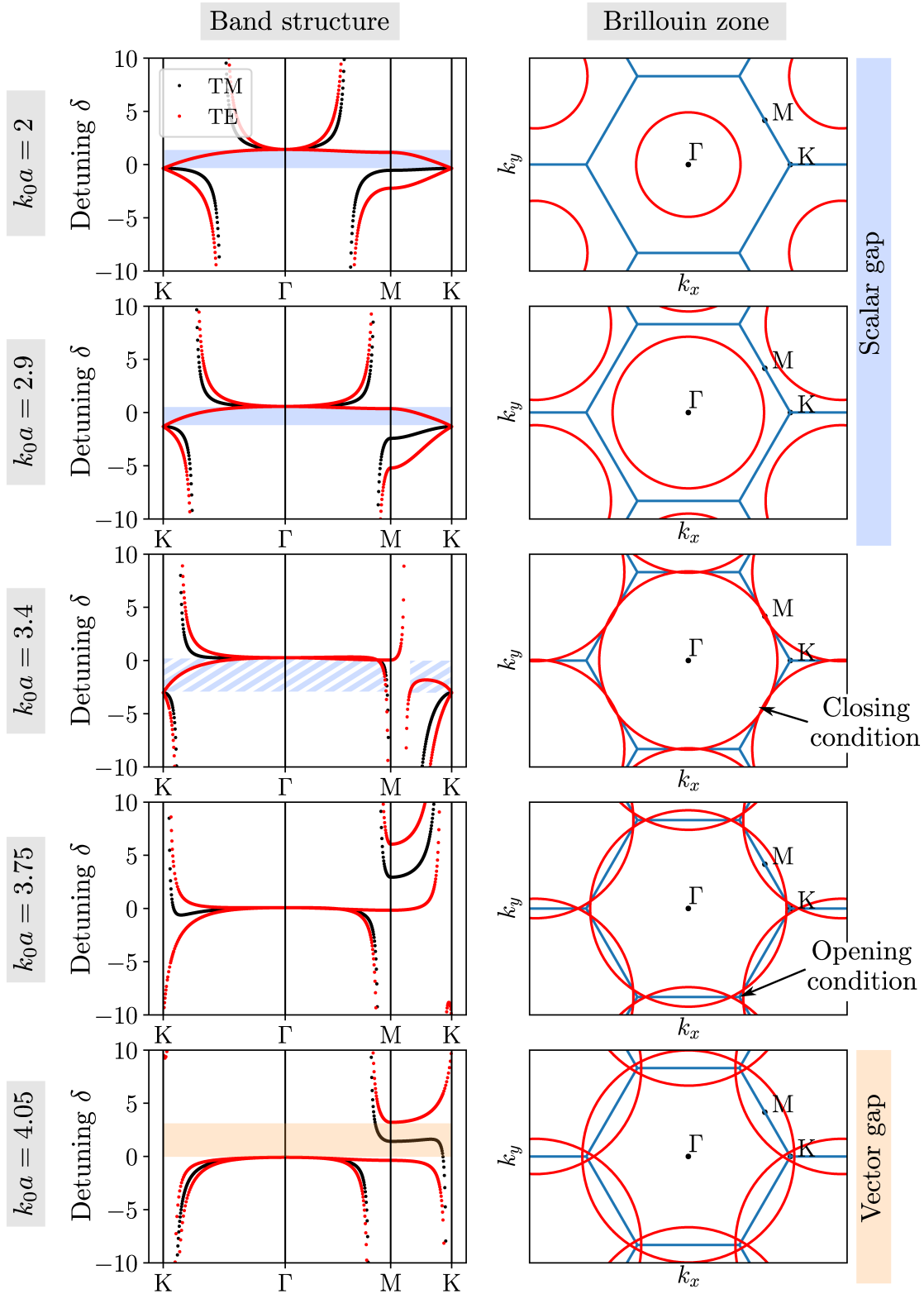


Figure 3.8: Dispersion relation of the triangular lattice in TM polarisation (black) and in TE (red) and representation of the Brillouin zone superimposed with the light circle (intersection of the light cone with the resonance at  $\omega_0$ ). The density decreases as we go down. The scalar gap is drawn in light blue, and the vector one in orange. For each of them we link the opening and closing condition of the gaps to overlaps between different light circles. In particular, the closing of the TM gap occurs when the light circles associated to adjacent BZ touch at M, near  $k_0a \sim 3.4$ , and the opening of the TE gap when three circles overlap at K.

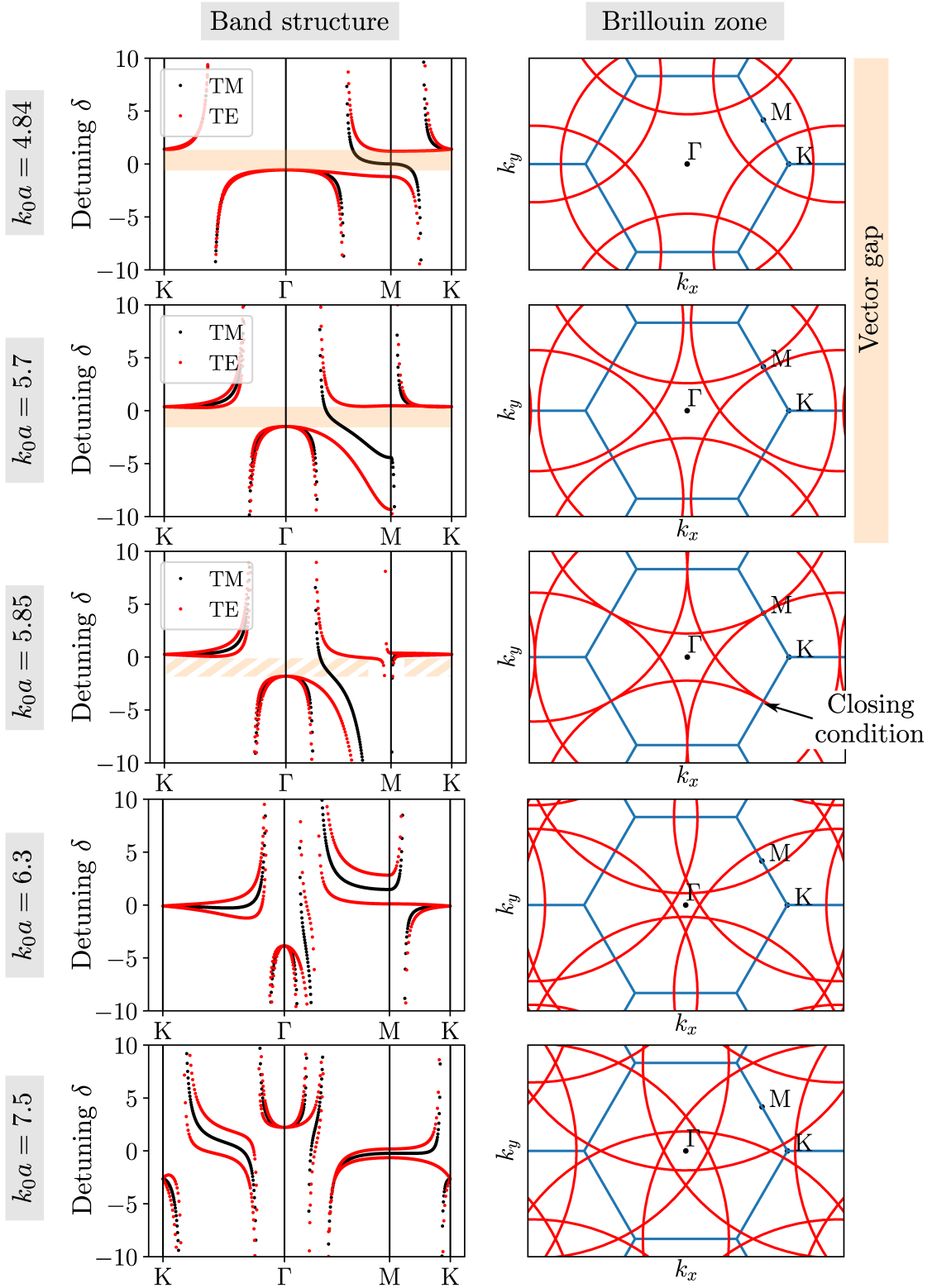


Figure 3.9: Continuation of Fig. 3.8 at lower densities. In this frequency range, the closing of the TE gap occurs when two light circles associated to next nearest neighbouring BZ, overlap at the point  $M$ , for densities close to  $k_0 a = 5.85$ . The complexity of the band structure increases at lower densities, making the opening of gaps less likely.



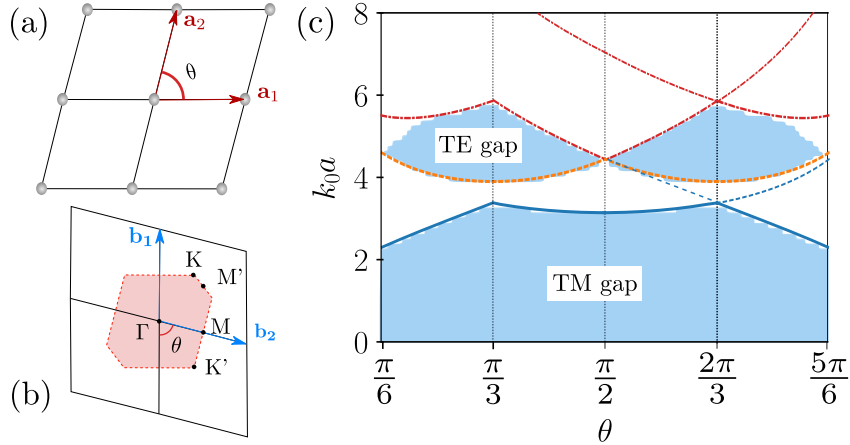


Figure 3.10: (a) Direct orthorhombic lattice parametrised by  $\theta$  and generated by the vectors  $\mathbf{a}_1$  and  $\mathbf{a}_2$ , and (b) the reciprocal lattice spanned by  $\mathbf{b}_1$  and  $\mathbf{b}_2$ . The symmetry points are specified and a prime denotes two non equivalent symmetry points (in the triangular lattice M and M', as well as K and K' share the same dispersion relation, contrary to less symmetrical lattices). (c) Critical values  $k_0a$  defining the gap regions as function of the direct lattice angle  $\theta$ . The TM gap disappears when the light circle reaches the closer inner edge of the first Brillouin zone (see inset), either in M or M' depending on  $\theta$ . The TE gap opens when the light circle reaches the outer edges in K and K'. It closes when the light circles associated to two non-adjacent Brillouin zones first meet, either in M or M'. The blue domain corresponds to bandgaps found numerically for the different lattices. The agreement between the theoretical predictions of Eqs. 3.12,3.13 and 3.14 and the numerics is excellent. TM and TE gaps are found in non-overlapping regimes of density. The range of density for the existence of the TE gap is maximal for the triangular lattice ( $\theta = \pi/3$ ) and minimal for the square lattice ( $\theta = \pi/2$ ).

very complicated as many band-foldings occur and each BZ is swept by the light circles of its six adjacent BZ. No large and clear band gap has been identified above this values of  $k_0a$ .

### 3.5.2 General condition for the opening of band gaps

Previous analysis of the triangular lattice shows that the opening and the closing of the gaps are linked to the geometrical overlap between light circles associated to different BZ. We can extend these conditions to other lattices to obtain general expressions for the existence of gaps in both TM and TE systems. There is no high density bound for the existence of the TM gap. This will be shown in detail in Sec. 3.6.1. Its lower bound is given by the intersection of two light circles coming from adjacent BZ at M. It corresponds to the critical value,

$$k_0a^* = \frac{\pi}{|\sin \theta|} \min \left( 1, \sqrt{2 - 2\cos \theta} \right), \quad (3.12)$$

where the contact is reached either at M or M' of Fig. 3.10 (b). The TE gap opens when the light circle reaches the outer edges in K and K'. It corresponds to

$$k_0a^* = \frac{\pi}{(1 + \cos \theta) |\sin(\theta/2)|}, \quad (3.13)$$

the points K and K' being at the same distance from  $\Gamma$ . The TE gap closes for

$$k_0a^* = \min \left( \frac{\pi}{|\sin(\theta/2)|}, \frac{\pi |\sin \theta|}{\sqrt{5 - 4 \cos \theta}} \right), \quad (3.14)$$

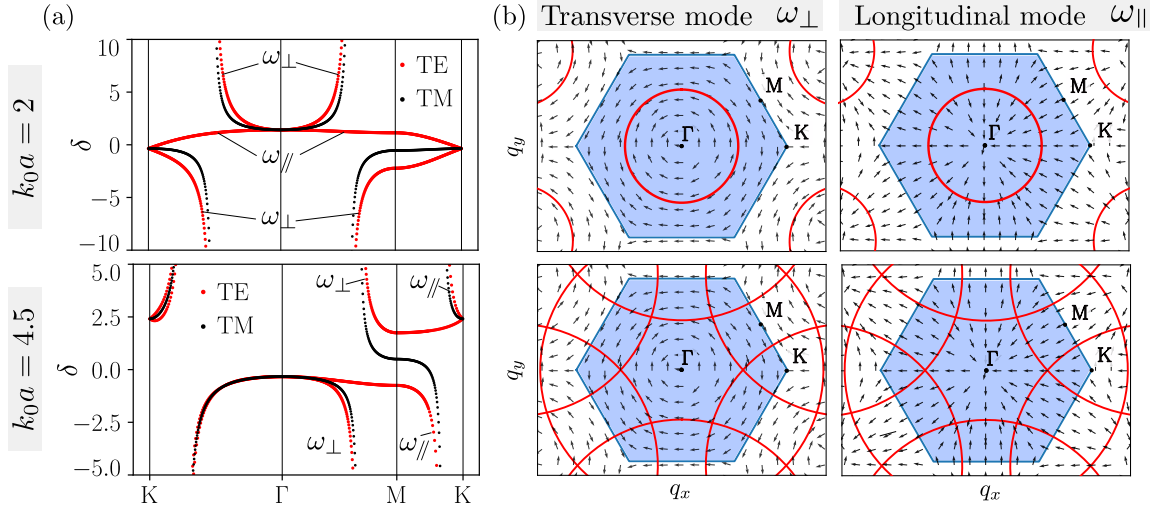


Figure 3.11: (a) Photonic band structure of the triangular lattice at high density ( $k_0a = 2$ , top) and moderate density ( $k_0a = 4.5$ , bottom), for both TM (black) and TE (red) polarisations. For the TE case, bands are marked as transverse ( $\omega_{\perp}$ ) or longitudinal ( $\omega_{\parallel}$ ). (b) View of the first Brillouin zone (shaded blue), together with the light circles  $|\mathbf{q}| = k_0$  and  $|\mathbf{q} - \mathbf{Q}| = k_0$ , at high density (top) and moderate density (bottom). Arrows represent the orientation  $\epsilon$  of the eigenstates corresponding to the transverse band ( $\omega_{\perp}$ , associated to  $\epsilon \perp \mathbf{q}$ ) and longitudinal band ( $\omega_{\parallel}$ , associated to  $\epsilon \parallel \mathbf{q}$ ) shown in (a).

when the light circles associated to two non-adjacent Brillouin zones first meet, either in M or M'. We plot these different conditions in Fig. 3.10 in terms of the density parameter  $k_0a = k_0a^* \sqrt{\sin \theta}$ . We also compare these predictions with the gaps found numerically for the different lattices (shaded blue domain). We get good agreement apart from a small domain near  $\theta = \pi/6$ , where the model overestimates the upper border. We may have missed another contact condition which would closes the TE gap below  $\theta = \pi/6$ .

Simple geometric considerations allow to predict the opening and closing condition for band gaps in resonant photonic crystals. The predictions regarding the gaps confirm the robustness of the TM gap, whose size varies little over the range of lattices. The intermediate density TE gap is more sensitive to the lattice parameters. It is maximal in the triangular lattice, and completely closed in the square one. The closing of the gap in the square lattice occurs because the opening and the closing conditions merge, as the edge containing M' is reduced to a single vertex of the BZ. We can also notice that the triangular lattice has the largest gaps in both TE and TM configurations. Apart from the direct vicinity of the square lattice, every compact orthorhombic lattice host both a high density TM gap and a low density TE one. This explains why they survive in the partially ordered systems.

### 3.5.3 Effect of the polarisation on the gaps

To understand better the underlying phenomenon leading to the opening of gaps, let us go back to the study of the triangular lattice and focus first on the high density regime ( $k_0a = 2$ ) where the TM setup has a gap and the TE setup does not.

The TM setup hosts a gap because of its polaritonic structure. This does not occur for the TE setup because an extra-band fills the gap. This extra band can be labelled as a longitudinal band  $\omega_{\mathbf{q}}$ , as its eigenstates are parallel to the wave-vector  $\mathbf{q}$ . The other two bands are transverse and labelled  $\omega_{\mathbf{q}^{\perp}}$ . The orientations of both types of eigenstates inside the BZ are shown in Fig. 3.11 (b). As a general guiding rule, a polaritonic splitting between the lower polariton and the upper polariton occurs for  $q = k_0$  when the polarisation of the

eigenstates is tangential to the light circle. The longitudinal band thus does not participate to the polaritonic band structure, but why does it close the gap? The answer lies at the point K, where there is a contact between three distinct BZ. At this point, the labels *longitudinal* and *transverse* become irrelevant because the same field cannot be aligned along three distinct directions. Mathematically, the degeneracy between  $\omega_{\mathbf{q}}^{\perp}$  and  $\omega_{\mathbf{q}}^{\parallel}$  at point K is due to the equal contributions of the three adjacent BZ. By selecting the corresponding components [ $\mathbf{Q} = \mathbf{0}$  and  $\mathbf{Q}^{\pm} = 2\pi/a^*(1, \pm 1/\sqrt{3})$  for the triangular lattice] in Eq. (3.2), we find that  $\tilde{G}_0(\mathbf{q}, \omega)$  is proportional to the identity at K, making the distinction between longitudinal and transverse modes indeed irrelevant. The same thing happens at  $\mathbf{q} = \mathbf{0}$ , creating two degeneracy constrains at  $\Gamma$  and K, forcing the flat longitudinal band to bend and fill the TM gap as in Fig. 3.11 (a).

By decreasing the density of scatterers, we reduce the size of the first Brillouin zone, which may become smaller than the domain encompassed by the light circle centred in  $\Gamma$ . This is typically what is shown in Fig. 3.11 (b) at  $k_0a = 4.5$ . As a result, the light circles belonging to adjacent zones now intersect the first Brillouin zone. The presence or absence of gap in this regime can be found by applying the general guiding rule mentioned above. By definition, TM eigenstates are always transverse to the light circles, so that the TM band diverges when crossing both the first circle along the path  $\Gamma \rightarrow M$  and the second one along the path  $M \rightarrow K$  [see Fig. 3.11 (a)]. This precludes the possibility to observe a polaritonic gap for TM polarisation. On the other hand, TE eigenstates cannot be transverse to both light circles. Eigenstates associated to  $\omega_{\mathbf{q}}^{\perp}$  are transverse to the first circle, while those associated to  $\omega_{\mathbf{q}}^{\parallel}$  are transverse to the second one. Having a single polaritonic divergence in each of the two bands  $\omega_{\mathbf{q}}^{\perp}$  and  $\omega_{\mathbf{q}}^{\parallel}$  allows the formation of a TE gap, while preserving the degeneracy at points  $\Gamma$  and K.

The polarisation of the field is a crucial feature to understand the existence of gaps in the band structures. In a given band, the orientation of the field with respect to the wave-vector is conserved, except at  $\Gamma$ , the centre of the BZ and its corners where the label collapses. It is the interplay between the field polarisation and the degeneracy conditions that determine whether a band gap can exist in the structure. These conditions, and in particular the degeneracy points at the corner of the Brillouin zone only exist because of periodicity and symmetry. Does this picture holds in partially ordered ensembles? We will answer this question in the next section.

### 3.5.4 Dispersion relation for hyperuniform patterns

Although Bloch modes are not proper eigenstates of the Hamiltonian (1.48) in the presence of disorder, we can still perform a Fourier analysis of the eigenstates  $\Psi_{\mathbf{n}}$ . The latter being defined at the disordered resonator locations  $\mathbf{r}_j$  only, the Fourier transform takes the form

$$\Psi_{\mathbf{n}}(\mathbf{q}) = \sum_{j=1}^N \psi_{n,j} e^{-i\mathbf{q}\cdot\mathbf{r}_j}. \quad (3.15)$$

Furthermore, we can define their degree of polarisation by looking at their longitudinal and transverse projections with respect to  $\mathbf{q}$ :

$$\Psi_{\mathbf{n}}^{\perp}(\mathbf{q}) = \Delta_{\mathbf{q}}^{\perp} \Psi_{\mathbf{n}}(\mathbf{q}) \quad \Psi_{\mathbf{n}}^{\parallel}(\mathbf{q}) = \Delta_{\mathbf{q}}^{\parallel} \Psi_{\mathbf{n}}(\mathbf{q}). \quad (3.16)$$

In Fig. 3.12 (a), we have represented the amplitudes of these projections in momentum space, for a typical eigenstate of the Hamiltonian. This shows that the  $\mathbf{q}$ -component of  $\Psi_{\mathbf{n}}$  are isotropic in both polarisations. We can thus average the norm of  $\Psi_{\mathbf{n}}^{\perp}$  and  $\Psi_{\mathbf{n}}^{\parallel}$  over the  $\mathbf{q}$ -directions to obtain Fig. 3.12 (b), which shows that  $\Psi_{\mathbf{n}}$  as a dominant  $\mathbf{q}$ -component and polarisation-component. A dispersion relation is thus found by plotting the frequency of

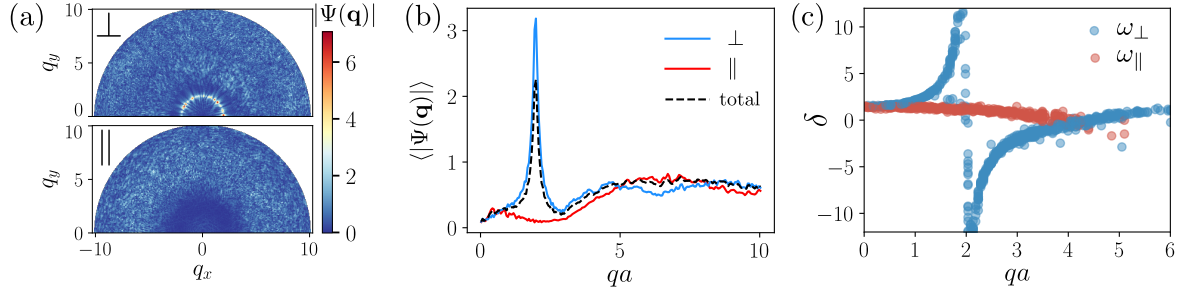


Figure 3.12: (a) Transverse and longitudinal projection (top and bottom) of the Fourier transform of a typical eigenvector of the Green's matrix for 2D TE waves propagating in an SHU system.. (b) Angular average of the Fourier transform shown in (a). (c) Frequency of each mode  $\Psi_n$  versus the dominant spatial frequency component. The labels refer to the dominant projection (either transverse or longitudinal). A single SHU configuration at  $\chi = 0.5$  and  $k_0a = 2$  containing  $N = 2372$  resonators has been considered in this computation.

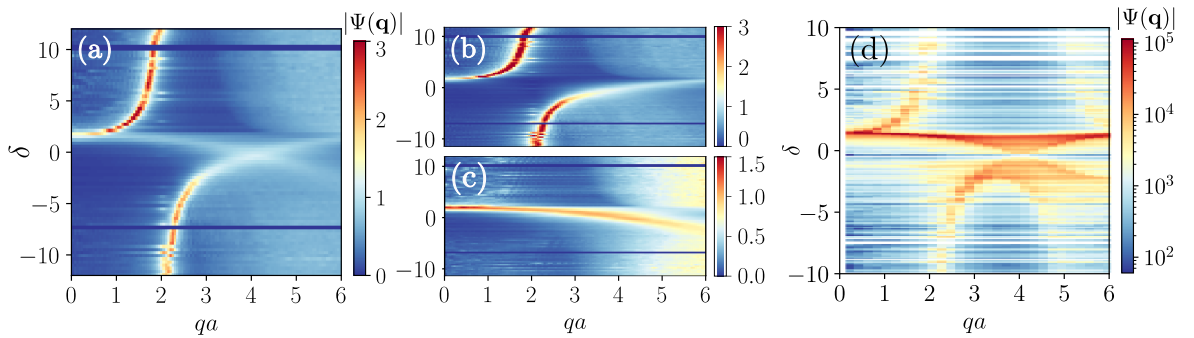


Figure 3.13: (a) Intensity map  $\Psi_n(q)$  of the eigenstates as function of their frequency (vertical axis) for a single SHU configuration of  $N = 2372$  resonators at  $\chi = 0.5$ . Same map for each polarisation component: transverse (b) and longitudinal (c). (d) Same map for a finite-size triangular lattice composed of  $N = 1000$  resonators at  $k_0a = 2$  in the TE (vector) polarisation.

each  $\Psi_n$  versus its dominant  $\mathbf{q}$ -component, as in Fig. 3.12 (c), where the polarisation label refers to the dominant polarisation. Alternatively, we can give a full representation of the  $\mathbf{q}$ -components by plotting the norm of  $\Psi_n$  versus  $\mathbf{q}$ . Repeating the operation for all modes of different frequency, we get the intensity maps shown in Fig. 3.13 (a, b, c). At  $k_0a = 2$ , we recover the polaritonic dispersion relation of transverse modes as well as the mostly flat-band of longitudinal modes.

When applied to a triangular lattice, the very same procedure leads to Fig. 3.13 (d). It turns out that the dispersion relation of ordered and partially ordered ensembles are similar in many ways. The polaritonic structure composed of transverse modes in the first BZ is clearly visible, as well as the longitudinal band [see Fig. 3.12 (c) and 3.13 (c)] which closes the gap through linear crossing of the two bands. Yet they also differ in some major points. In particular, both periodicity and band folding are only visible with ordered lattices, the bands becoming blurry for high wave-vectors in disordered systems. It is also important to mention that the well-resolved band structure of SHU patterns depends strongly on the correlation ratio. For uncorrelated patterns or at low  $\chi$ , the gapped polaritonic structure in TM is much less visible.

This Fourier analysis shows that we can build an effective dispersion relation for strongly correlated disordered systems that looks similar to the one found in ordered structures. In this respect, it corroborates the validity of the arguments used in the previous section to explain the opening and closing of gaps in SHU systems.

## 3.6 Expansion of the Hamiltonian in reciprocal space

We showed previously that the Hamiltonian of a periodic arrangement of resonators coupled by light can be reduced to an effective Hamiltonian parametrised by the wavevector  $\mathbf{q}$  and the frequency  $\omega$  of the plane-wave solutions. It reads  $\mathcal{H}_{\mathbf{q}}(\omega) = (\omega_0 - i\Gamma_0/2) \mathbb{1} - \tilde{\mathcal{G}}_0(\mathbf{q}, \omega)\Gamma_0/2$ , where

$$\tilde{\mathcal{G}}_0(\mathbf{q}, \omega) = -c_d k_0^{2-d} \left[ \rho \sum_{\mathbf{Q}} \mathbf{G}_0(\mathbf{q} - \mathbf{Q}, \omega) - \mathbf{G}_0(\mathbf{R} = \mathbf{0}, \omega) \right]. \quad (3.17)$$

In this sum, the different  $\mathbf{Q}$ -components correspond to contributions associated to different Brillouin zones centred in  $\mathbf{Q}$ . As the number density is reduced, more and more  $\mathbf{Q}$ -components will contribute to the dispersion relation inside the first Brillouin zone whose size gets larger. In the following, we will show that we can restrict this sum to one or few terms to get explicit analytical predictions for the dispersion relation.

### 3.6.1 Long wavelength limit

In the long wavelength limit ( $qa \ll 1$ ), the  $\mathbf{q}$ -dependence in each term of the Eq. (3.17) is small, except for the one at  $\mathbf{Q} = \mathbf{0}$ . We can then keep the wave-vector dependence in the zeroth order term and neglect it in the others. This is how the long wavelength limit was computed in Ref. Antezza and Castin (2009a) for 3D crystals. A more direct way is to go back to the expression of the Green's matrix in Fourier space. In 2D, it reads

$$\tilde{\mathcal{G}}_0(\mathbf{q}, \omega) = -2\beta \sum_{\mathbf{R} \neq \mathbf{0}} \mathbf{G}_0(\mathbf{R}, \omega) e^{-i\mathbf{q} \cdot \mathbf{R}}, \quad (3.18)$$

and we recall that  $\beta$  is the dimension of the field ( $\beta = 1$  in TM and  $\beta = 2$  in TE). In the high density limit, we ignore the local structuration of the medium and replace the sum by

an integral. It gives

$$\begin{aligned} \sum_{\mathbf{R} \neq \mathbf{0}} \mathbf{G}(\mathbf{R}, \omega) e^{i\mathbf{q} \cdot \mathbf{R}} &\underset{qa \ll 1}{\simeq} \frac{1}{a^2} \int d\mathbf{R} \mathbf{G}(\mathbf{R}, \omega) e^{-i\mathbf{q} \cdot \mathbf{R}} - \text{Im}[\mathbf{G}(\mathbf{R} = \mathbf{0}, \omega)] - \frac{1}{a^2} \int_{\delta\mathcal{A}} d\mathbf{R} \text{Re}[\mathbf{G}(\mathbf{R}, \omega)] \\ &\simeq \frac{1}{a^2} \mathbf{G}(\mathbf{q}, \omega) + \mathbb{1} \left( \frac{i}{4} - \frac{\delta_{\beta,2}}{2k_0^2 a^2} \right) + \mathbb{1} \frac{\delta\mathcal{A}}{a^2} \left[ \frac{2\gamma - 1 + \ln(\delta\mathcal{A}/2)}{8\pi} \right], \end{aligned} \quad (3.19)$$

where  $\delta\mathcal{A}$  is a small surface enclosing the origin. Taking the limit  $\delta\mathcal{A} \rightarrow 0$ , we obtain

$$\tilde{\mathbf{G}}_0(\mathbf{q}, \omega) \simeq \begin{cases} \frac{4}{(k_0 a)^2} \left( \frac{k^2}{q^2 - k^2} \right) - i & \text{in TM,} \\ \frac{8}{(k_0 a)^2} \left( \frac{k^2}{[q^2 - k^2]\mathbb{1} - q^2 \Delta_{\mathbf{q}}^{\parallel}} + \frac{\mathbb{1}}{2} \right) - i\mathbb{1} & \text{in TE.} \end{cases} \quad (3.20)$$

Inserting these expressions into Eq. (3.1), we find that the frequency associated with the scalar mode  $\omega_{\mathbf{q}}^0$  and the transverse and longitudinal ones of TE polarisation  $\{\omega_{\mathbf{q}}^{\perp}, \omega_{\mathbf{q}}^{\parallel}\}$ , are solutions of the following equations which determine the dispersion relation:

$$\begin{aligned} \omega_{\mathbf{q}}^0 &= \omega_0 - \frac{\Gamma_0}{2} \frac{4}{(k_0 a)^2} \frac{(\omega_{\mathbf{q}}^0/c)^2}{q^2 - (\omega_{\mathbf{q}}^0/c)^2}, \\ \omega_{\mathbf{q}}^{\perp} &= \omega_0 - \frac{\Gamma_0}{2} \frac{8}{(k_0 a)^2} \left[ \frac{(\omega_{\mathbf{q}}^{\perp}/c)^2}{q^2 - (\omega_{\mathbf{q}}^{\perp}/c)^2} + \frac{1}{2} \right], \\ \omega_{\mathbf{q}}^{\parallel} &= \omega_0 + \frac{\Gamma_0}{2} \frac{4}{(k_0 a)^2}. \end{aligned} \quad (3.21)$$

Interestingly, these solutions can be interpreted as eigenvalue solutions of an effective wave equation  $[-\nabla \times \nabla \times + k^2 \epsilon(\omega)] \mathbf{E}(\mathbf{r}, \omega) = \mathbf{0}$ . TM plane waves of vector  $\mathbf{q}$  obey the dispersion relation  $q^2 = k^2 \epsilon(\omega)$ , where the dielectric function,  $\epsilon(\omega) = 1 + \rho \alpha_e(\omega)$ , is expressed in terms of an effective polarisability  $\alpha_e(\omega) = 4\beta \tilde{\alpha}_e(\omega)/k_0^2$ , with  $\tilde{\alpha}_e(\omega) = -\Gamma_0/2(\omega - \omega_0)$ . In addition, longitudinal and transverse TE solutions satisfy  $\epsilon(\omega) = 0$  and  $q^2 = k^2 \epsilon(\omega)$ , respectively, with  $\epsilon(\omega) = 1 + \rho \alpha_e(\omega)/(1 - \rho \alpha_e(\omega)/2)$ . Hence, in the long-wavelength limit, the crystal rigorously behaves as an homogeneous medium of effective polarisability  $\alpha_e(\omega)$ . Note in particular the difference between the bare polarisability  $\alpha(\omega)$  and the effective polarisability  $\alpha_e(\omega)$ . The latter is real and does not contain any decay rate because there is no radiative loss for ballistic waves in infinite crystals.

This approach highlights the similarity between the TM mode and the transverse TE mode, as they both have a polaritonic structures, while the longitudinal remains flat. Close to the resonance frequency, the dispersion relations, expressed in the normalised unit  $\delta = 2(\omega - \omega_0)/\Gamma_0$ , read

$$\delta_{\mathbf{q}}^0 = \frac{4}{(k_0 a)^2 - (qa)^2}, \quad \delta_{\mathbf{q}}^{\perp} = \frac{8}{(k_0 a)^2 - (qa)^2} - \frac{4}{(k_0 a)^2}, \quad \delta_{\mathbf{q}}^{\parallel} = \frac{4}{(k_0 a)^2}. \quad (3.22)$$

These expressions predict a gap for both polarisations at high density. The TM gap lies in the range  $\delta \in [0, 4/(k_0 a)^2]$  while the TE gap is found for  $\delta \in [-4/(k_0 a)^2, 4/(k_0 a)^2]$ . The TE gap is expected to be twice larger than the TM gap, and symmetrical around  $\delta = 0$ . These predictions are in good agreement with what we observed in Fig. 3.11 (a) between  $\Gamma$  and M. Figure 3.14 shows the superposition of the DOS of the triangular lattice for both polarisations and the gap edges predictions. The agreement is quite good in the TM setup, but the long-wavelength approach fails at describing the longitudinal band which fills the gap. We also see that the prediction for the upper edge is more accurate than the prediction for the lower one.

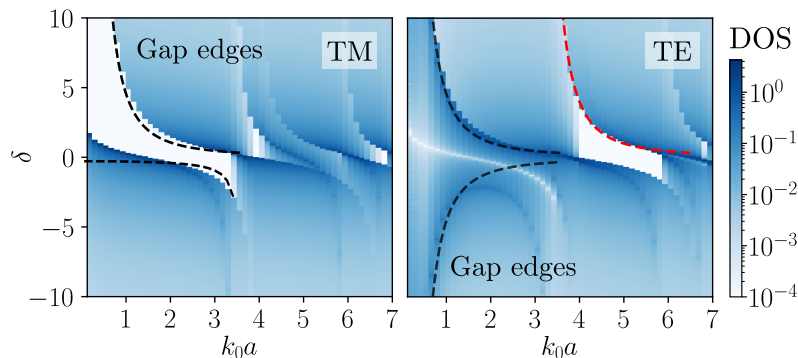


Figure 3.14: Density of states of the triangular lattice in the TM (left) and TE (right) polarisation. The predictions for the edges of the band gap computed using the long wavelength approximation are shown in black dashed lines. We also added the lower edge prediction  $\delta_{\min} = 4/[(k_0 a)^2 - (q_M a)^2]$  where  $q_M$  is the amplitude of  $q$  at point M [see Eq. (3.22)]. The borders predicted in TE do not encircle a band gap because of the behaviour of the longitudinal band is not well captured by the long wavelength approximation, yet they provide lines of maximal DOS. We also added a shifted version of the transverse TE prediction to capture the upper edge of the gap found at intermediate density.

These two discrepancies come from the fact that the long-wavelength approximation does not hold at large  $\mathbf{q}$  near the edge of the Brillouin zone. Large- $\mathbf{q}$  components are precisely those that contribute to the transverse lower polaritonic branch near the gap and to the bending of the longitudinal band. Translating the values obtained from Eq. (3.22) toward the TE gap (Fig. 3.14 in red) shows that the same kind of conditions could exist at lower densities.

### 3.6.2 Higher order expansion

In Sec. 3.5.2, we have identified the elementary processes which led to the opening or the closing of both the TM and the TE gaps. These processes involve an increasing number of Brillouin zones as they occur at lower and lower density.

Restricting the summation in Eq. (3.17) to the first BZ leads to the long-wavelength approximation which predicts a spurious gap at high density in TE. In Fig. 3.15 we have represented the dispersion relations obtained by taking into account an increasing number of BZ in Eq. (3.17). In these representations, we do not restrict the computation to an irreducible specific path but scan the full  $q$ -space. The long wavelength approximation corresponds to Fig. 3.15 (a). By keeping a wave-vector dependence in a second adjacent Brillouin zone, we obtain Fig. 3.15 (b), where the gap has been filled by the now extended longitudinal band. We have interpreted the existence of a gap at intermediate densities by the interplay between three Brillouin zones at K. Figure 3.15 (d) shows that two BZ are indeed not enough to recreate the said-gap, while three are [see (e)]. The last regime of interest is the closing of the TE gap by the quadruple overlap at M. Such a crossing is not possible with only three BZ, and it is indeed what we observe in Fig. 3.15 (h) where the TE gap remains open at  $k_0 a = 6$ . A fourth Brillouin zone is required to close it, this situation is shown in (i). We can also notice that restricting the Hamiltonian to the smallest number of BZ required to reproduce the opening and closing conditions for the gaps is sufficient to get good agreement with the full computation of the crystal in Fig. 3.15 (c,f,j).

The approach developed in this section not only reproduces qualitatively the dispersion relation of the triangular lattice, and especially the existence of gap, but also confirms the idea that the Hamiltonian 3.1 represented in Fourier space can be viewed as a series of correction terms to the homogenous long wave length approximation. Its zeroth order provides the high

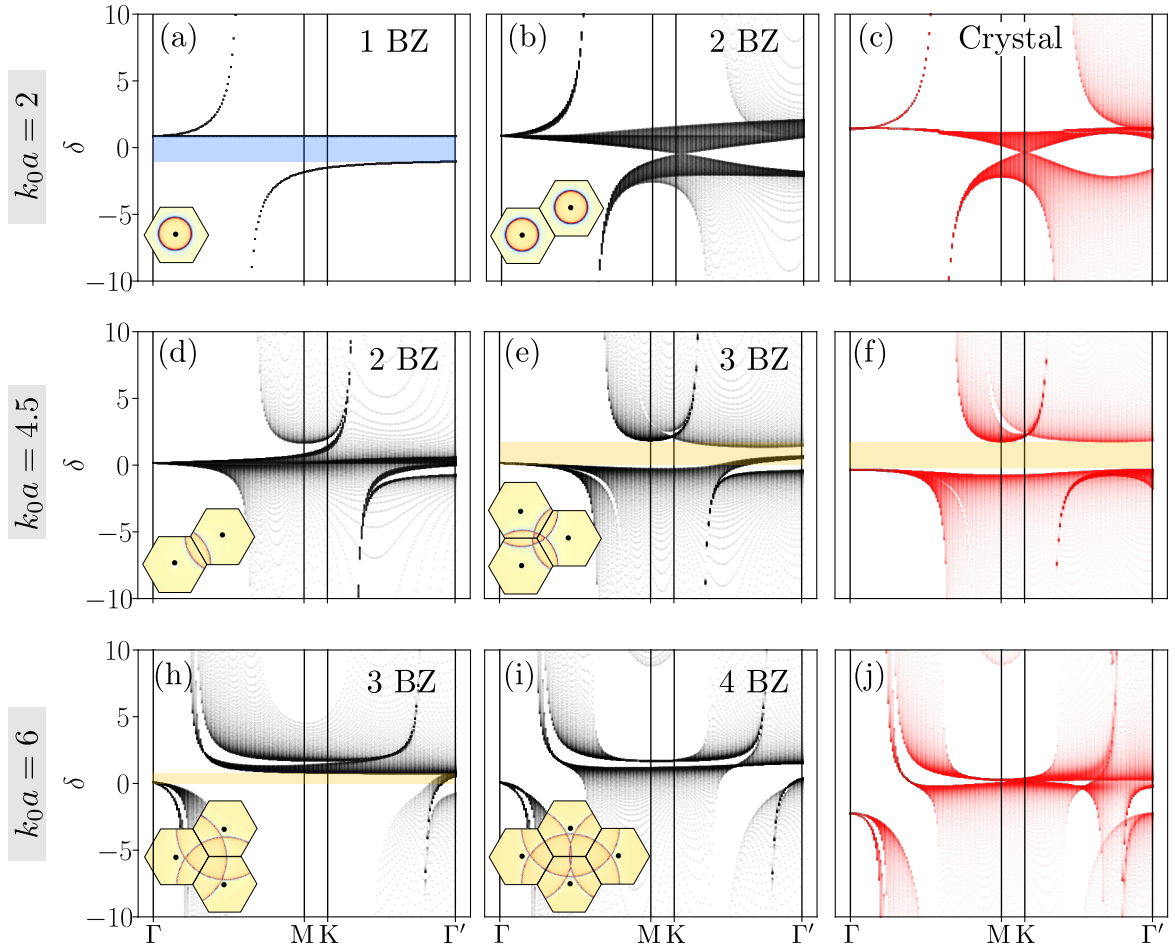


Figure 3.15: Dispersion relations of a triangular lattice in the TE polarisation for different degrees of approximations of Eq. (3.17). The number in the upper right corner, as well as the inset diagram, show the number of neighbouring Brillouin zone that were considered for each plot.  $\Gamma$  denotes the centre of the first Brillouin zones, and  $\Gamma'$  the centre of another in its vicinity. The dispersion relation deep inside the second BZ is not meaningful and  $\mathbf{q}$  far on the left of K will be disregarded. The complete computation for the infinite lattice is shown on the right in red. In each case, we also show in the inset the light circles centred in the middle of each BZ.



density behaviour where any spatial structure has been smoothed out, and each higher order term extends the validity of the model to lower density. Incidentally, this approach also indicates that the real space nearest neighbour tight-binding model used in Refs. Weaire (1971); Thorpe and Weaire (1971) to compute the electronic DOS of amorphous semiconductors is not relevant for Hamiltonian of the form (1.48) as the polaritonic dispersion relation builds upon long-range interaction in real space.

### 3.7 Conclusion

This chapter began with the observation of similar structural properties between strongly correlated SHU patterns and ensembles of small crystals without long-range orientational order. This leads us to study crystalline structures made of resonators. The analysis of the density of states confirmed the similitude with strongly correlated systems, as the gaps found in hyperuniform ensembles also exist, in photonic crystals. We extended our study to include a wide range of periodic structures similar to those found locally in SHU patterns. The DOS averaged over the ensemble of all these structures turned out to be very similar to the SHU DOS, confirming our initial intuition. Then we studied the underlying band structure of crystals to understand the elementary processes governing the physics of band gaps. The crucial role of the longitudinal band has been pointed out as responsible for both the absence of a high density gap and the presence of a high density one. We also identified geometric overlap conditions which were responsible for the opening and closing of both the TM and the TE gap in the arbitrary orthorhombic lattices and obtained very good agreement with the simulations. The precise understanding of those overlap conditions in Fourier space was supported by an analysis of the dispersion relation based upon a restriction of the Fourier-space Hamiltonian to the central BZ. Regarding SHU systems, we were able to build numerically effective dispersion relation by performing a Fourier analysis of the Hamiltonian eigenstates. At high enough correlation ratios, SHU ensembles develop a well-resolved band structure which is very similar to that of a crystalline lattice.

The generalisation of our findings to 3D systems is in principle possible following the same lines of thought. In dense 3D lattices coupled by a vector field, no bandgap is expected (see Fig. 1.20); these considerations are relevant only for scalar fields which makes this study less appealing. However, it would be interesting to consider general lattices different from the most compact one (face-centred-cubic). In 3D the band structure is composed of at least two transverse bands and a longitudinal one, the Brillouin zone has a more complex shape than in 2D with significantly more particular points, leaving more room for various overlaps. Spanning the space of the lattice parameters will also be more complicated as there are now four free parameters instead of two in 2D. A hyperuniform arrangement of point resonators is a good way to obtain gapped structure in 2D, even for vector fields, but does not seem to be the case in 3D. The close analysis of various 3D lattices using the tools developed in this chapter may help to identify the key ingredients for designing strongly correlated structures that support bandgaps in the absence of remnant periodicity.

## Chapter 4

# Mesoscopic description of the density of states in partially ordered media

In this chapter we lay out an approach to evaluate the average density of states (DOS) in the ensembles of resonant point-scatterers described in the previous chapters. We rely on the idea that the Green's matrix coupling gives an accurate description of the interaction between resonators and that its spectrum gives the density of collective resonances, at least close to the bare resonance of the resonators. First, we will express the distribution of modes in terms of the averaged total scattering operator of the system and the self-energy. This expression is exact as no assumption has been made at this point about the scattering processes taken into account.

We will then evaluate the self-energy operator up to the second order in density for arbitrary pair correlation function, and test explicitly our predictions for the DOS of SHU arrangements with 2D TE coupling. Finally we will comment our theoretical expression for the DOS and its relation with the commonly accepted expression involving the imaginary part of the average Green's function of the full scattering system.

### 4.1 Complex spectrum of $\mathbf{G}$ in the thermodynamic limit

We described in Chap. 1 how the Green's matrix can be used to study ensembles of coupled resonators. Under the assumption of a large quality factor, it captures all the resonances of the system “matter + waves”, close to the resonance. This constraint can be lifted in the case of photonic crystals as shown in Chap. 1. The DOS could also be computed directly from the determinant of the Hamiltonian as claimed in Ref. Gaspard and Sparenberg (2021). We will restrict ourselves in this chapter to the case of high quality factors where the Hamiltonian problem is linear and reads

$$\mathcal{H} = \left( \omega_0 - i \frac{\Gamma_0}{2} \right) - \frac{\Gamma_0}{2} \tilde{\mathbb{G}}(\omega_0), \quad (4.1)$$

where the Green's matrix  $\mathbb{G}$  has been defined in Sec. 1.5.1 such that its coefficients are

$$\tilde{\mathbb{G}}_{ij} = -c_d k_0^{2-d} \mathbf{G}_0(\mathbf{r}_i - \mathbf{r}_j, \omega_0). \quad (4.2)$$

The eigenvalues of  $\mathcal{H}$  are complex in general, but become real in the case of infinite systems ( $V \rightarrow \infty$ ). Indeed, the imaginary part accounts for loss and there cannot be a radiation loss in an infinite system. We will now focus on the eigenvalues of the Green's matrix itself, since the spectrum of Hamiltonian 4.1 can be obtained from the one of  $\tilde{\mathbb{G}}$  up to a shift and a rescaling. In a medium composed of  $N$  interacting particles, we define  $\Lambda_n$  the  $n^{\text{th}}$  eigenvalue of  $\tilde{\mathbb{G}}$ . It has been shown in Ref. Goetschy (2011) that they satisfy the condition  $\text{Im } \Lambda > -1$  and that

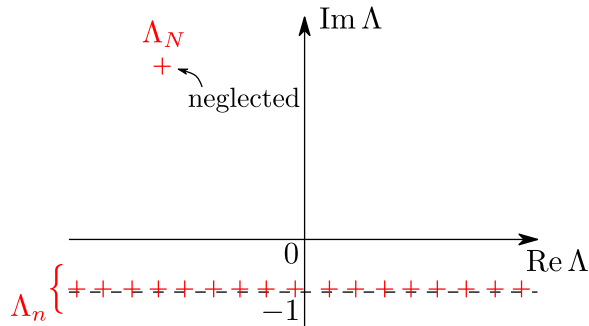


Figure 4.1: Schematic representation of the spectrum of the Green's matrix in the complex plane, where most of the eigenvalues have a imaginary part of -1.

they eventually collapse onto the axis  $\text{Im } \Lambda = -1$  in the large system limit. This means that the linewidths  $\gamma_n = \text{Im } \Lambda_n + 1$  tend to zero from above. Actually, they cannot all cancel because the trace of  $\mathbb{G}$  is zero, so that  $\sum_{n=1}^N \text{Im } \Lambda_n = 0$ . In practice, most of the eigenvalues have their imaginary part on the line  $\text{Im } \Lambda_n = -1 + 0^+$  except for one superradiant mode of the form  $\Lambda_N = \text{Re } \Lambda_N + (N - 1)i$ . The situation is represented in Fig. 4.1. In the limit of large systems, where  $N \rightarrow \infty$ , the contribution of the eigenvalue labelled  $\Lambda_N$  can be neglected when considering the DOS. We can thus write in the thermodynamic limit ( $N \rightarrow \infty, V \rightarrow \infty$ , at fixed density rho) that  $\Lambda_n = \text{Re } \Lambda_n - i + i0^+$ . Hence, the spectrum becomes real which significantly simplifies the computation of the DOS defined as the marginal density of the frequencies  $\omega_n$ .

## 4.2 DOS and resolvent of $\mathbb{G}$

To study the spectral properties of the Green's matrix, we can use some tools commonly defined in Random Matrix Theory [RMT, Mehta (2004)]. Let us first define the resolvent function

$$g(\delta) = \frac{1}{\beta N} \left\langle \text{Tr}_{\beta N} \left[ \frac{1}{\delta - i - \tilde{\mathbb{G}}} \right] \right\rangle, \quad (4.3)$$

where brackets denote ensemble averages over the positions degrees of freedom (later on, we might also use an overline if confusion is possible with brackets of the operator formalism).  $\text{Tr}_{\beta N}$  is the trace operator of size  $\beta N \times \beta N$ , with  $\beta$  the dimension of the field (1 for scalar, 2 or 3 for vector fields in two or three dimensions). The subscript will often be discarded in unequivocal situations. The distribution of the real part of the collective resonances  $p(\delta)$  can be obtained from the imaginary part of  $g(\delta)$ . Indeed, we have from Eq. (4.3)

$$g(\delta) = \frac{1}{\beta N} \left\langle \sum_{j=1}^{\beta N} \frac{1}{\delta - i - \Lambda_n} \right\rangle \underset{N \gg 1}{\approx} \frac{1}{\beta N} \left\langle \sum_{j=1}^{\beta N} \frac{1}{\delta - \text{Re } \Lambda_n - i0^+} \right\rangle \quad (4.4)$$

$$\approx \frac{1}{\beta N} \left\langle \sum_{j=1}^{\beta N} \text{PP} \left[ \frac{1}{\delta - \text{Re } \Lambda_n} \right] + i\pi \delta(\delta - \text{Re } \Lambda_n) \right\rangle. \quad (4.5)$$

By using the definition of the distribution of  $\text{Re } \Lambda_n$  as  $p(\delta) = \frac{1}{\beta N} \left\langle \sum_{j=1}^{\beta N} \delta(\delta - \text{Re } \Lambda_n) \right\rangle$  we directly have that

$$p(\delta) = \frac{1}{\pi} \text{Im } g(\delta). \quad (4.6)$$

Equation 4.3 is a standard relation, useful in RMT to evaluate the eigenvalue spectrum of Hermitian matrices. Note that in the limit  $N, V \rightarrow \infty$  at fixed  $N/R^d$ , the density of

resonances fills a compact support in the complex plane, and other techniques developed in Refs. Goetschy (2011) and Goetschy and Skipetrov (2013) for non-Hermitian matrices, can give access to the full distribution of complex eigenvalues.

In the following, instead of using a RMT framework adapted to matrices with correlated elements, we will relate  $g(\delta)$  to a physical quantity of our system: the total scattering operator  $\mathbf{T}$ , introduced in Eq. (1.11) of Sec. 1.3.2.

### 4.3 From the scattering operator to the resolvent

In this section, we will show that the total scattering operator can be written in a very similar form as the resolvent involved in the computation of the DOS. Let us first recall the expression of the average total scattering operator  $\overline{\mathbf{T}}$ . For point-like particles, the operator can be expanded in an operator representation as

$$\mathbf{T} = \sum_i \mathbf{t}_i + \sum_i \sum_{j \neq i} \mathbf{t}_i \mathbf{G}_0 \mathbf{t}_j + \sum_i \sum_{j \neq i} \sum_{k \neq j} \mathbf{t}_i \mathbf{G}_0 \mathbf{t}_j \mathbf{G}_0 \mathbf{t}_k + \dots, \quad (4.7)$$

where  $\mathbf{t}_i$  is the scattering operator of particle  $i$  and reads

$$\mathbf{t}_i(\mathbf{r}, \mathbf{r}') = t \mathbb{1} \delta(\mathbf{r} - \mathbf{r}_i) \delta(\mathbf{r}' - \mathbf{r}_i) = t \mathbb{1} |\mathbf{r}_i\rangle \langle \mathbf{r}_i|, \quad (4.8)$$

where the identity operator  $\mathbb{1}$  accounts here for the polarisation degrees of freedom, and  $t = -k^2 \alpha(\omega)$ . In this representation, we can rewrite Eq. (4.7) using Eq. (4.8), and

$$\mathbb{G}_{ij} = (1 - \delta_{ij}) \langle \mathbf{r}_i | \mathbf{G}_0 | \mathbf{r}_j \rangle = (1 - \delta_{ij}) \mathbf{G}_0(\mathbf{r}_j - \mathbf{r}_i), \quad (4.9)$$

where indices  $i, j$  run over the particles and  $\mathbf{G}_0$  is the free space Green's function. Equation 4.7 becomes

$$\mathbf{T} = t \sum_i |\mathbf{r}_i\rangle \langle \mathbf{r}_i| + \sum_{i,j} t \mathbb{G}_{ij} t |\mathbf{r}_i\rangle \langle \mathbf{r}_j| + \sum_{i,k,j} t \mathbb{G}_{ik} t \mathbb{G}_{kj} t |\mathbf{r}_i\rangle \langle \mathbf{r}_j| + \dots \quad (4.10)$$

$$\begin{aligned} &= t \sum_{ij} \left\{ \mathbb{1}_{ij} + t \mathbb{G}_{ij} + [(t \mathbb{G})^2]_{ij} + \dots \right\} |\mathbf{r}_i\rangle \langle \mathbf{r}_j| \\ &= \sum_{ij} \left[ \frac{t}{\mathbb{1} - t \mathbb{G}} \right]_{ij} |\mathbf{r}_i\rangle \langle \mathbf{r}_j|. \end{aligned} \quad (4.11)$$

To express Eq. (4.10) in terms of our usual Green's matrix  $\tilde{\mathbb{G}}$ , we need to recall the expression of the polarisability  $\alpha(\omega) = \alpha_0 \tilde{\alpha}(\omega)$  with

$$\tilde{\alpha} = -\frac{-\Gamma_0/2}{\omega - \omega_0 + i\Gamma_0/2} = \frac{1}{\delta + i}, \quad (4.12)$$

with  $\delta = 2(\omega - \omega_0)/\Gamma_0$  is the normalised detuning. From the definition of  $t = -k^2 \alpha(\omega)$  and  $\mathbb{G}$  in Eq. (1.48) we directly have that  $t \mathbb{G} = \tilde{\alpha} \tilde{\mathbb{G}}$ . Using Eq. (4.11) and 4.12, we finally get

$$\mathbf{T} = \alpha_0 \sum_{i,j} \left[ \frac{\tilde{\alpha}}{\mathbb{1} - \tilde{\alpha} \tilde{\mathbb{G}}} \right]_{ij} |\mathbf{r}_i\rangle \langle \mathbf{r}_j|. \quad (4.13)$$

The resolvent defined in Eq. (4.3) only selects the diagonal terms of  $\mathbf{T}$  as it can be written as

$$g(\delta) = \frac{1}{\beta N} \left\langle \sum_j \left[ \frac{1}{\delta - i - \tilde{\mathbb{G}}} \right]_{jj} \right\rangle. \quad (4.14)$$

In order to select the diagonal elements of the operator, we can express Eq. (4.13) in a Fourier representation using  $\langle \mathbf{r} | \mathbf{q} \rangle = \frac{1}{\sqrt{V}} e^{i\mathbf{q}\cdot\mathbf{r}}$ . Equation 4.13 becomes

$$\langle \mathbf{q} | \mathbf{T} | \mathbf{q} \rangle = -k_0^{2-d} \alpha_0 \sum_{ij} \left[ \frac{\tilde{\alpha}}{\mathbf{1} - \tilde{\alpha} \tilde{\mathbf{G}}} \right]_{ij} \frac{e^{-i\mathbf{q}\cdot(\mathbf{r}_i - \mathbf{r}_j)}}{V}. \quad (4.15)$$

From Eq. (4.15), an integration over the  $\mathbf{q}$  should enforce the condition  $i = j$  in the sums. A statistical average of this integration gives

$$\int \frac{d\mathbf{q}}{(2\pi)^d} \langle \mathbf{q} | \overline{\mathbf{T}} | \mathbf{q} \rangle = -\alpha_0 k_0^{2-d} \left\langle \sum_{ij} \left[ \frac{\tilde{\alpha}}{\mathbf{1} - \tilde{\alpha} \tilde{\mathbf{G}}} \right]_{ij} \frac{\delta(\mathbf{r}_i - \mathbf{r}_j)}{V} \right\rangle \quad (4.16)$$

$$= -\alpha_0 k_0^{2-d} \rho^2 \left\langle \frac{1}{N} \sum_i \left[ \frac{1}{\mathbf{1}/\tilde{\alpha} - \tilde{\mathbf{G}}} \right]_{ii} \right\rangle, \quad (4.17)$$

where  $d$  is the dimension of space and  $\delta(\mathbf{r}_i - \mathbf{r}_j) = \rho \delta_{ij}$  has been used to obtain Eq. (4.17). Comparing Eqs. 4.14 and 4.17, we directly see that

$$g(\delta) = \frac{-k_0^{d-2}}{\alpha_0 \rho^2} \int \frac{d\mathbf{q}}{(2\pi)^d} \langle \mathbf{q} | \overline{\mathbf{T}} | \mathbf{q} \rangle \Big|_{1/\tilde{\alpha} = \delta - i}. \quad (4.18)$$

Equation 4.18 gives an exact expression of the resolvent in terms of the T-operator, but it requires the evaluation of  $\mathbf{T}(q)$  for all  $q$ . An approximated expression can be obtained by noticing that in the limit of large  $\mathbf{q}$ , Eq. (4.15) should be dominated by the term  $i = j$ ,

$$\lim_{q \rightarrow \infty} \overline{\langle \mathbf{q} | \mathbf{T} | \mathbf{q} \rangle} \simeq \frac{-k_0^{2-d} \alpha_0}{V} \left\langle \sum_i \left[ \frac{\tilde{\alpha}}{\mathbf{1} - \tilde{\alpha} \tilde{\mathbf{G}}} \right]_{ii} \right\rangle = -k_0^{2-d} \alpha_0 \rho \left\langle \frac{1}{N} \sum_i \left[ \frac{\tilde{\alpha}}{\mathbf{1} - \tilde{\alpha} \tilde{\mathbf{G}}} \right]_{ii} \right\rangle, \quad (4.19)$$

such that we end up with

$$g(\delta) \simeq \frac{-k_0^{d-2}}{\alpha_0 \rho} \lim_{q \rightarrow \infty} \langle \mathbf{q} | \overline{\mathbf{T}} | \mathbf{q} \rangle, \quad (4.20)$$

where the medium is supposed statistically isotropic such that  $\langle \mathbf{q} | \mathbf{T} | \mathbf{q} \rangle$  only depends on the norm of  $\mathbf{q}$ . Equation 4.20 is much easier to compute as it only requires an evaluation of the total scattering operator in the large wavevector limit. The spectrum of the Green's matrix has thus been linked to the evaluation of a physical quantity of our system, the total scattering operator  $\mathbf{T}$ . We finally obtain

$$p(\delta) = \frac{-k_0^{d-2}}{\pi \rho \alpha_0} \text{Im} \lim_{q \rightarrow \infty} \langle \mathbf{q} | \overline{\mathbf{T}} | \mathbf{q} \rangle. \quad (4.21)$$

This result can be applied to systems of any dimension and polarisability, as we did not assume anything on both the Green's function and the polarisation  $\alpha$ . More generally, note that this result also holds for any coupling  $\mathbf{G}$ , eventually different from a Green's function. In the rest of this chapter, we will apply it to study the effect of correlated disorder on the photonic properties of 2D systems.

## 4.4 Density expansion of the DOS

In this section, we will express the total scattering operator  $\mathbf{T}$  in terms of the self-energy  $\Sigma$ , defined in Eq. (1.19) and compute it theoretically for moderate density of resonators.

#### 4.4.1 Expression of the scattering operator to the self-energy

According to Eq. (4.10),  $\bar{\mathbf{T}}$  is an iteration of the self-energy such that the average scattering operator  $\bar{\mathbf{T}}$  reads

$$\bar{\mathbf{T}} = \boldsymbol{\Sigma} + \boldsymbol{\Sigma} \mathbf{G}_0 \boldsymbol{\Sigma} + \boldsymbol{\Sigma} \mathbf{G}_0 \boldsymbol{\Sigma} \mathbf{G}_0 \boldsymbol{\Sigma} + \dots \quad (4.22)$$

$$= \frac{\boldsymbol{\Sigma}}{\mathbb{1} - \mathbf{G}_0 \boldsymbol{\Sigma}}. \quad (4.23)$$

In the limit of infinite and homogeneous systems, we have translational invariance such that  $\mathbf{G}_0$  and  $\boldsymbol{\Sigma}$  are diagonal in Fourier representation leading to

$$\langle \mathbf{q} | \bar{\mathbf{T}} | \mathbf{q} \rangle = \frac{\boldsymbol{\Sigma}(\mathbf{q})}{\mathbb{1} - \mathbf{G}_0(\mathbf{q}) \boldsymbol{\Sigma}(\mathbf{q})}. \quad (4.24)$$

This is in general a complicated object as  $\mathbf{G}_0$  and  $\boldsymbol{\Sigma}$  have in general a non-trivial dependence on  $\mathbf{q}$ .

#### 4.4.2 Low density evaluation of the density of modes

At the lowest order in density the scattering operator reduces to the independent scattering approximation (ISA) value,

$$\bar{\mathbf{T}} \simeq \boldsymbol{\Sigma}_{\text{ISA}} = \rho t \mathbb{1} = -\rho k^{2-d} \alpha_0 \tilde{\alpha} \mathbb{1}. \quad (4.25)$$

Using the exact expression 4.18 for the resolvent and the closure relation

$$\int \frac{d\mathbf{q}}{(2\pi)^d} \langle \mathbf{q} | \mathbf{q} \rangle = \sum_{\mathbf{q}} \frac{\Delta \mathbf{q}}{(2\pi)^d} = \frac{1}{V} \text{Tr}_N \mathbb{1} = \rho, \quad (4.26)$$

we obtain

$$g(\delta) = \frac{1}{\delta - i} \quad \Rightarrow \quad p(\delta) = \frac{1}{\pi} \frac{1}{\delta^2 + 1}, \quad (4.27)$$

which is a known result in dilute systems (see Ref. Skipetrov and Goetschy (2011)) and is in excellent agreement with numerical results both in 2D and 3D (not shown here).

#### 4.4.3 Density of states in 2D, beyond the ISA

In order to evaluate Eq. (4.21), it is convenient to use the decomposition

$$\boldsymbol{\Sigma}(\mathbf{q}, \omega) = \boldsymbol{\Sigma}^\perp(\mathbf{q}, \omega) \boldsymbol{\Delta}_{\mathbf{q}}^\perp + \boldsymbol{\Sigma}^\parallel(\mathbf{q}, \omega) \boldsymbol{\Delta}_{\mathbf{q}}^\parallel, \quad \mathbf{G}_0(\mathbf{q}, \omega) = G_0^\perp(\mathbf{q}, \omega) \boldsymbol{\Delta}_{\mathbf{q}}^\perp + G_0^\parallel(\mathbf{q}, \omega) \boldsymbol{\Delta}_{\mathbf{q}}^\parallel, \quad (4.28)$$

where  $\boldsymbol{\Delta}_{\mathbf{q}}^\perp$  and  $\boldsymbol{\Delta}_{\mathbf{q}}^\parallel$  are the projectors perpendicular and parallel to  $\mathbf{q}$ . We get

$$p(\delta) = -\frac{1}{4\pi\beta\rho} \lim_{q \rightarrow \infty} \text{Im} \left[ \frac{\boldsymbol{\Sigma}^\perp(\mathbf{q}, \omega)}{1 - G_0^\perp(\mathbf{q}, \omega) \boldsymbol{\Sigma}^\perp(\mathbf{q}, \omega)} + \frac{\boldsymbol{\Sigma}^\parallel(\mathbf{q}, \omega)}{1 - G_0^\parallel(\mathbf{q}, \omega) \boldsymbol{\Sigma}^\parallel(\mathbf{q}, \omega)} \right], \quad (4.29)$$

where we assumed that the space is two-dimensional. The vector fields situation is obtained by taking  $\beta = 2$ , while in the scalar case  $\beta = 1$  and  $\boldsymbol{\Sigma} = \boldsymbol{\Sigma}^\perp$ ,  $G_0 = G_0^\perp$  and  $\boldsymbol{\Sigma}^\parallel = 0$  and  $G_0^\parallel = 0$ . We will come back to the scalar situation later in this chapter.

As expressed in Eq. (1.20), the self-energy is a complicated object which includes every possible non factorisable diffusion sequence. Here we aim at providing an expansion of  $\boldsymbol{\Sigma}$  to study the effects of spatial correlations in resonant ensembles of scatterers of moderate

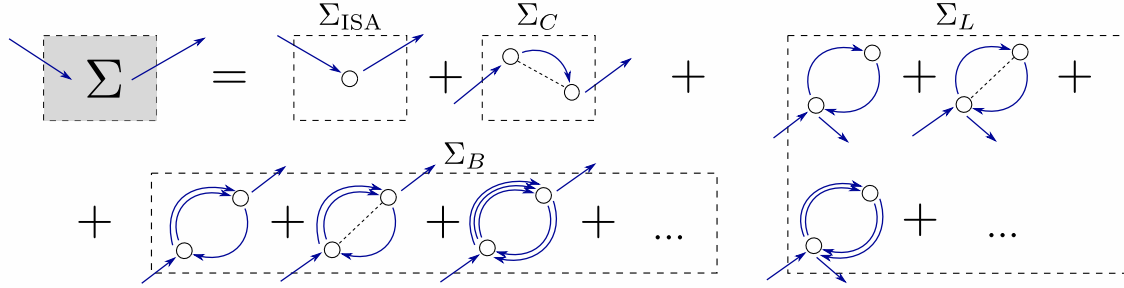


Figure 4.2: Pictorial representation of the scattering sequences included in the self-energy  $\Sigma$ . Open circles represent scatterers, arrows account for field propagation through  $\mathbf{G}_0$ , and dashed line connecting scatterers stand for the spatial correlation function  $h_2$ . Diagrams are classified into four classes discussed in the text.

density. The first non-zero contribution of spatial correlation to  $\Sigma$  has been analysed in in Ref. Fraden and Maret (1990) and much later reconsidered in Leseur et al. (2016) to study the *stealthy* regime, where SHU correlations expands the homogenisation regime towards low densities. It is labelled  $\Sigma_C$  in Fig. 4.2 and is the same diagram that has been used to derive Eq. (1.77), relating changes in the transport mean free path to the structure factor  $S(\mathbf{q})$ .

We will go one step further and consider *recurrent scattering*. The latter consists in scattering events bouncing back and forth between pairs of resonators. The model including arbitrary and infinite number of round-trips in 3D systems has been discussed in (van Tiggelen and Lagendijk, 1994; Cherroret et al., 2016). There are two reasons to go beyond  $\Sigma_C$ . First, it does not provide a consistent expansion in term of density: the self-energy is composed, at first order in density (term proportional to  $\rho$ ) of  $\Sigma_{\text{ISA}}$ , but at second order (terms proportional to  $\rho^2$ ) of more diagrams than just  $\Sigma_C$ . Secondly, we will see later in this chapter that  $\Sigma_C$  does not contribute to changes in the density of modes when taking the large  $\mathbf{q}$  limit in Eq. (4.20).

#### 4.4.4 Expansion of the self-energy to second order in density and recurrent scattering

In a more formal diagrammatic representation, we can write the self-energy, formerly defined in Eq. (1.19), as

$$\begin{aligned}
 \Sigma = & \underbrace{\circ}_{\Sigma_{\text{ISA}}} + \underbrace{\circ \text{---} \circ}_{\Sigma_C} + \underbrace{\circ \text{---} \circ \text{---} \circ}_{\Sigma_L} + \underbrace{\circ \text{---} \circ \text{---} \circ \text{---} \circ}_{\Sigma_L} + \dots + \underbrace{\circ \text{---} \circ \text{---} \circ \text{---} \circ \text{---} \circ}_{\Sigma_L} + \dots \\
 & + \underbrace{\circ \text{---} \circ \text{---} \circ \text{---} \circ \text{---} \circ}_{\Sigma_B} + \underbrace{\circ \text{---} \circ \text{---} \circ \text{---} \circ \text{---} \circ}_{\Sigma_B} + \dots + \underbrace{\circ \text{---} \circ \text{---} \circ \text{---} \circ \text{---} \circ}_{\Sigma_B} + \dots
 \end{aligned} \tag{4.30}$$

This diagrammatic representation is similar to the one shown in Fig. 4.2. Circles represent scattering events and horizontal solid lines stand for the free space Green's functions connecting these scattering events. Also, scatterers spatially correlated through  $h_2$ , are linked by dashed curved lines and identical scatterers involved in recurrent scattering sequences are linked by solid upper and lower lines. Equation (4.30) takes the compact form

$$\Sigma(\mathbf{q}, \omega) = \Sigma_{\text{ISA}}(\mathbf{q}, \omega) + \Sigma_C(\mathbf{q}, \omega) + \Sigma_L(\mathbf{q}, \omega) + \Sigma_B(\mathbf{q}, \omega), \tag{4.31}$$

which includes the four families of scattering events

- $\Sigma_{\text{ISA}}$  is the independent scattering term, dominating at low density and is given by  $\Sigma_{\text{ISA}}(\mathbf{q}, \omega) = \rho t(\omega) \mathbb{1}$ ,
- $\Sigma_C$  involves scattering between two statistically correlated particles and is sufficient to model the transparency regime of *stealthy* hyperuniform materials described in Ref. Leseur et al. (2016),
- $\Sigma_L$  captures recurrent scattering between two resonators, correlated or not. It includes every possible number of round-trip between them but with the condition that the sequence begins and ends at the same particle, hence their *Loop* denomination,
- $\Sigma_B$  is the counter-part of  $\Sigma_L$  where the entry and exit points correspond to different scatterers, making *Boomerang*-shaped diagrams.

The complete expression of the self-energy at second order in density is given by

$$\begin{aligned} \Sigma(\mathbf{q}, \omega) = & \rho t(\omega) \mathbb{1} + \rho^2 t(\omega)^2 \int d\mathbf{r} h_2(\mathbf{r}) \mathbf{G}_0(\mathbf{r}, \omega_0) e^{-i\mathbf{q}\cdot\mathbf{r}} \\ & + \rho^2 t(\omega)^3 \int d\mathbf{r} [1 + h_2(\mathbf{r})] \frac{\mathbf{G}_0^2(\mathbf{r}, \omega_0)}{\mathbb{1} - t(\omega)^2 \mathbf{G}_0^2(\mathbf{r}, \omega_0)} \\ & + \rho^2 t(\omega)^4 \int d\mathbf{r} [1 + h_2(\mathbf{r})] \frac{\mathbf{G}_0^3(\mathbf{r}, \omega_0)}{\mathbb{1} - t(\omega)^2 \mathbf{G}_0^2(\mathbf{r}, \omega_0)} e^{-i\mathbf{q}\cdot\mathbf{r}}, \end{aligned} \quad (4.32)$$

where the different terms will be computed in their order of appearance in the following sections.

#### 4.4.5 Evaluation of $\Sigma_C$

Let us explicitly compute the first correlated term of  $\Sigma$

$$\Sigma_C(\mathbf{r}, \mathbf{r}') = \overline{\sum_{i,j \neq i} t(\omega) \langle \mathbf{r} | \mathbf{r}_j \rangle \langle \mathbf{r}_j | \mathbf{G}_0 t(\omega) | \mathbf{r}_i \rangle \langle \mathbf{r}_i | \mathbf{r}' \rangle} \quad (4.33)$$

$$= \frac{N(N-1)}{V^2} t(\omega)^2 h_2(\mathbf{r} - \mathbf{r}') \mathbf{G}_0(\mathbf{r} - \mathbf{r}', \omega_0), \quad (4.34)$$

where we recall that  $N$  is the number of particles and  $V$  the volume occupied by the medium. In Fourier space, it reads

$$\Sigma_C(\mathbf{q}, \mathbf{q}', \omega) \simeq \rho^2 t(\omega)^2 \int d\mathbf{r} d\mathbf{r}' h_2(\mathbf{r} - \mathbf{r}') \mathbf{G}_0(\mathbf{r} - \mathbf{r}', \omega_0) e^{-i\mathbf{q}\cdot\mathbf{r}} e^{i\mathbf{q}'\cdot\mathbf{r}'} \quad (4.35)$$

$$\simeq \delta(\mathbf{q} - \mathbf{q}') \underbrace{\rho^2 t(\omega)^2 \int d\mathbf{r}'' h_2(\mathbf{r}'') \mathbf{G}_0(\mathbf{r}'') e^{-i\mathbf{q}\cdot\mathbf{r}''}}_{\equiv \Sigma_C(\mathbf{q}, \omega)}, \quad (4.36)$$

where we defined  $\Sigma(\mathbf{q})$  through the relation  $\Sigma(\mathbf{q}, \mathbf{q}') \equiv \delta(\mathbf{q} - \mathbf{q}') \Sigma(\mathbf{q})$ . To go further, we need to decompose the self-energy tensor in terms of projectors perpendicular or parallel to the wavevector, setting aside the delta-divergence related to the Lorentz-Lorenz effect. It reads

$$\Sigma_C(\mathbf{q}, \omega) = \Sigma_C^\perp(\mathbf{q}, \omega) \Delta_{\mathbf{q}}^\perp + \Sigma_C^\parallel(\mathbf{q}, \omega) \Delta_{\mathbf{q}}^\parallel + \Sigma_C^{\text{LL}}(\mathbf{q}, \omega) \mathbb{1}. \quad (4.37)$$

To find each term of this decomposition, we decompose the Green's function that shows up in Eq. (4.32) onto a basis of projectors, but this time in real space as

$$\mathbf{G}_0(\mathbf{r}, \omega) = G_0^t(\mathbf{r}, \omega) \Delta_{\mathbf{r}}^\perp + G_0^l(\mathbf{r}, \omega) \Delta_{\mathbf{r}}^\parallel + \frac{\delta(\mathbf{r})}{2k_0^2} \mathbb{1}, \quad (4.38)$$



where  $\Delta_{\mathbf{r}}^{\perp(\parallel)}$  are the transverse (longitudinal) projector with respect to the position  $\mathbf{r}$ . Using the relations

$$\int_0^{2\pi} d\theta \Delta_{\mathbf{r}}^{\perp} e^{-i\mathbf{q}\cdot\mathbf{r}} = 2\pi \left[ J_0(qr) - \frac{J_1(qr)}{qr} \right] \Delta_q^{\perp} + 2\pi \frac{J_1(qr)}{qr} \Delta_q^{\parallel}, \quad (4.39)$$

$$\int_0^{2\pi} d\theta \Delta_{\mathbf{r}}^{\parallel} e^{-i\mathbf{q}\cdot\mathbf{r}} = 2\pi \frac{J_1(qr)}{qr} \Delta_q^{\perp} + 2\pi \left[ J_0(qr) - \frac{J_1(qr)}{qr} \right] \Delta_q^{\parallel}, \quad (4.40)$$

where  $J_0(x)$  and  $J_1(x)$  are Bessel functions of the first kind, we find that the three terms of  $\Sigma_C$  take the form

$$\begin{aligned} \Sigma_C^{\perp}(\mathbf{q}, \omega) &= 2\pi\rho^2 t(\omega)^2 \int_0^{\infty} dr r h_2(r) \\ &\quad \times \left\{ G_0^t(r, \omega) \left[ J_0(qr) - \frac{J_1(qr)}{qr} \right] + G_0^l(r, \omega) \frac{J_1(qr)}{qr} \right\}, \end{aligned} \quad (4.41)$$

$$\begin{aligned} \Sigma_C^{\parallel}(\mathbf{q}, \omega) &= 2\pi\rho^2 t(\omega)^2 \int_0^{\infty} dr r h_2(r) \\ &\quad \times \left\{ G_0^t(r, \omega) \frac{J_1(qr)}{qr} + G_0^l(r, \omega) \left[ J_0(qr) - \frac{J_1(qr)}{qr} \right] \right\}, \end{aligned} \quad (4.42)$$

$$\Sigma_C^{\text{LL}}(\mathbf{q}, \omega) = \frac{\rho^2 t(\omega)^2 h_2(0)}{2k_0^2}. \quad (4.43)$$

Here the last term  $\Sigma_C^{\text{LL}}(\mathbf{q})$  is due to the singular part of the Green's function (last term of Eq. (4.38)).

#### 4.4.6 Computation of $\Sigma_L$

Whereas  $\Sigma_C$  involved a single scattering contribution,  $\Sigma_L$  is composed of an infinite series of scattering events. Let us first compute the first diagrams of the *looped*-recurrent scattering events

$$\begin{aligned} \Sigma_{L,1}(\mathbf{r}, \mathbf{r}') &= \text{Diagram 1} + \text{Diagram 2} \\ &= \sum_{i,j} \int d\mathbf{r}_i d\mathbf{r}_j dp(\mathbf{r}_i, \mathbf{r}_j) \langle \mathbf{r} | \mathbf{r}_i \rangle t(\omega) \langle \mathbf{r}_i | \mathbf{G}_0 | \mathbf{r}_j \rangle t(\omega) \langle \mathbf{r}_j | \mathbf{G}_0 | \mathbf{r}_i \rangle t(\omega) \langle \mathbf{r}_i | \mathbf{r}' \rangle \\ &= \rho^2 \delta(\mathbf{r} - \mathbf{r}') \int d\mathbf{r}'' [1 + h_2(\mathbf{r}'')] t(\omega)^3 \mathbf{G}_0^2(\mathbf{r}'', \omega_0). \end{aligned} \quad (4.44)$$

From the structure of the next diagrams in the self-energy, we see that it amounts at adding a closed loop to the previous one. This directly means that

$$\begin{aligned} \Sigma_L(\mathbf{r}, \mathbf{r}') &= \text{Diagram 1} + \text{Diagram 2} + \text{Diagram 3} + \text{Diagram 4} + \dots \\ &= \rho^2 \delta(\mathbf{r} - \mathbf{r}') \int d\mathbf{r}'' [1 + h_2(\mathbf{r}'')] t(\omega) \sum_{j=1}^{\infty} (t(\omega) \mathbf{G}_0(\mathbf{r}'', \omega))^2 \\ &= \rho^2 \delta(\mathbf{r} - \mathbf{r}') \int d\mathbf{r}'' [1 + h_2(\mathbf{r}'')] \frac{t(\omega)^3 \mathbf{G}_0^2(\mathbf{r}'', \omega_0)^2}{1 - t(\omega)^2 \mathbf{G}_0^2(\mathbf{r}'', \omega_0)^2}. \end{aligned} \quad (4.45)$$

One can notice that there is no explicit dependence on the positions  $\mathbf{r}$  and  $\mathbf{r}'$  apart from the delta function, contrary to  $\Sigma_C$ . Hence, as announced in Eq. (4.32), its expression in Fourier space reads

$$\Sigma_L(\mathbf{q}, \omega) = \rho^2 t(\omega)^3 \int d\mathbf{r} [1 + h_2(\mathbf{r})] \frac{\mathbf{G}_0^2(\mathbf{r}, \omega_0)}{\mathbb{1} - t(\omega)^2 \mathbf{G}_0^2(\mathbf{r}, \omega_0)}. \quad (4.46)$$

As before we can write the loop term  $\Sigma_L$  in the form

$$\Sigma_L(\mathbf{q}, \omega) = \Sigma_L^\perp(\mathbf{q}, \omega) \Delta_q^\perp + \Sigma_L^\parallel(\mathbf{q}, \omega) \Delta_q^\parallel + \Sigma_L^{\text{LL}}(\mathbf{q}, \omega) \mathbf{1}. \quad (4.47)$$

The first two terms follow from the decomposition

$$\begin{aligned} \frac{\mathbf{1}}{\mathbf{1} - t(\omega)^2 \mathbf{G}_0^2(\mathbf{r}, \omega_0)} &= \sum_{j=0}^{\infty} [t(\omega)^2 \mathbf{G}_0(\mathbf{r}, \omega_0)^2]^j \\ &= \sum_{j=0}^{\infty} [t(\omega)^2 G^t(r, \omega_0)^2]^j \Delta_r^\perp + [t(\omega)^2 G^l(r, \omega_0)^2]^j \Delta_r^\parallel \\ &= \frac{1}{1 - t(\omega)^2 G_0^t(r, \omega_0)^2} \Delta_r^\perp + \frac{1}{1 - t(\omega)^2 G_0^l(r, \omega_0)^2} \Delta_r^\parallel. \end{aligned} \quad (4.48)$$

Taking the limit  $\mathbf{q} \rightarrow \mathbf{0}$  in Eqs. (4.39) and (4.40), we get  $\int_0^{2\pi} d\theta \Delta_r^\perp = \int_0^{2\pi} d\theta \Delta_r^\parallel e = \pi \mathbf{1}$ , which leads to

$$\begin{aligned} \Sigma_L^\perp(\mathbf{q}, \omega) = \Sigma_L^\parallel(\mathbf{q}, \omega) &= \pi \rho^2 t(\omega)^3 \int_0^\infty dr r [1 + h_2(r)] \\ &\quad \times \left[ \frac{G_0^t(r, \omega_0)^2}{1 - t(\omega)^2 G_0^t(r, \omega_0)^2} + \frac{G_0^l(r, \omega_0)^2}{1 - t(\omega)^2 G_0^l(r, \omega_0)^2} \right], \end{aligned} \quad (4.49)$$

which is independent of  $q$  and will be noted  $\Sigma_L(\omega)$  later on. In addition, the contribution of the singular part of  $\mathbf{G}_0(\mathbf{r}, \omega)$  to  $\Sigma_L(\mathbf{q}, \omega)$  vanishes thanks to a simplification of the  $\delta$ -terms appearing in Eq. (4.46), leading to

$$\Sigma_L^{\text{LL}}(\mathbf{q}, \omega) = 0. \quad (4.50)$$

**Regularisation procedure** The first integrand involving  $G_0^t$  is regular at the origin, but not convergent for large argument. Indeed,  $r G_0^{t2}(r, \omega_0)$  is equivalent to  $i \exp[2ik_0 r]/8\pi$ . The integral can be computed nonetheless by setting a cut-off  $r_c$  in the following way Kwong et al. (2019):

$$\int_0^\infty dr r [1 + h_2(r)] \frac{G_0^t(r, \omega_0)^2}{1 - t(\omega)^2 G_0^t(r, \omega_0)^2} = \int_0^{r_c} dr r [1 + h_2(r)] \frac{G_0^t(r, \omega_0)^2}{1 - t(\omega)^2 G_0^t(r, \omega_0)^2} \quad (4.51)$$

$$+ \int_{r_c}^\infty dr r [1 + h_2(r)] \frac{G_0^t(r, \omega_0)^2}{1 - t(\omega)^2 G_0^t(r, \omega_0)^2}. \quad (4.52)$$

For a large enough value of  $r_c$ , the first integral is computed numerically and the second one is approximated by

$$\int_{r_c}^\infty dr r G_0^t(r, \omega_0)^2 = \lim_{\eta \rightarrow 0^+} \int_{r_c}^\infty dr r G_0^t(r, \omega_0 + i\eta)^2 \quad (4.53)$$

$$= \frac{i}{8\pi k_0} \int_{r_c}^\infty \exp[2ik_0 r] dr = \frac{\exp[2ik_0 r_c]}{16\pi k_0^2}. \quad (4.54)$$

The final result (4.52) is independent of  $r_c$ .

#### 4.4.7 Computation of $\Sigma_B$

We use the same approach as for the loop terms to sum the infinite series of diagrams contained in  $\Sigma_B$ , leading to

$$\Sigma_B(\mathbf{q}, \omega) = \rho^2 t(\omega)^4 \int d\mathbf{r} [1 + h_2(\mathbf{r})] \frac{\mathbf{G}_0^3(\mathbf{r}, \omega_0) e^{-i\mathbf{q}\cdot\mathbf{r}}}{\mathbf{1} - t(\omega)^2 \mathbf{G}_0^2(\mathbf{r}, \omega_0)}, \quad (4.55)$$

that we write in the form

$$\Sigma_B(\mathbf{q}, \omega) = \Sigma_B^\perp(\mathbf{q}, \omega) \Delta_q^\perp + \Sigma_B^\parallel(\mathbf{q}, \omega) \Delta_q^\parallel + \Sigma_B^{\text{LL}}(\mathbf{q}, \omega) \mathbf{1}. \quad (4.56)$$

Using Eqs. (4.48) and (4.39), we obtain

$$\begin{aligned} \Sigma_B^\perp(\mathbf{q}, \omega) &= 2\pi\rho^2 \int_0^\infty dr r [1 + h_2(r)] \\ &\times \left\{ \frac{t(\omega)^4 G_0^{t3}(r, \omega_0)}{1 - t(\omega)^2 G_0^{t2}(r, \omega_0)} \left[ J_0(qr) - \frac{J_1(qr)}{qr} \right] + \frac{t(\omega)^4 G_0^{l3}(r, \omega_0)}{1 - t(\omega)^2 G_0^{l2}(r, \omega_0)} \frac{J_1(qr)}{qr} \right\}, \end{aligned} \quad (4.57)$$

$$\begin{aligned} \Sigma_B^\parallel(\mathbf{q}, \omega) &= 2\pi\rho^2 \int_0^\infty dr r [1 + h_2(r)] \\ &\times \left\{ \frac{t(\omega)^4 G_0^{t3}(r, \omega_0)}{1 - t(\omega)^2 G_0^{t2}(r, \omega_0)} \frac{J_1(qu)}{qr} + \frac{t(\omega)^4 G_0^{l3}(r, \omega_0)}{1 - t(\omega)^2 G_0^{l2}(r, \omega_0)} \left[ J_0(qr) - \frac{J_1(qu)}{qr} \right] \right\}, \end{aligned} \quad (4.58)$$

$$\Sigma_B^{\text{LL}}(\mathbf{q}, \omega) = -\frac{\rho^2 t(\omega)^2 (1 + h_2(0))}{2k_0^2}. \quad (4.59)$$

It is interesting to note that the two terms coming from the singular part of the Green's function simplify which gives

$$\Sigma_B^{\text{LL}}(\mathbf{q}, \omega) = \Sigma_C^{\text{LL}}(\mathbf{q}, \omega) + \Sigma_B^{\text{LL}}(\mathbf{q}, \omega) = -\frac{\rho^2 t^2}{2k_0^2}, \quad (4.60)$$

independently of the precise value of  $h_2(0)$ . At the leading order in density, this contribution is identical to the one we would obtain considering point-like repulsion between scatterers and known as Lorentz-Lorenz correction.

## 4.5 Explicit evaluation of the density of states of 2D systems

### 4.5.1 Evaluation of the average density of states for TE waves

Let us go back to the computation of the distribution  $p(\delta)$  given by Eq. (4.29), using the explicit expressions for the different terms of the self-energy, established in the previous section. A first simplification comes from the fact that  $G_0^\perp(\mathbf{q}, \omega) \rightarrow 0$  when  $q \rightarrow \infty$ , reducing the first term to the numerator  $\Sigma^\perp$ . Secondly, in the limit  $q \rightarrow \infty$ , most terms in  $\Sigma_B$  and  $\Sigma_C$  vanish. We are left with

$$p(\delta) = -\frac{1}{8\pi\rho} \lim_{q \rightarrow \infty} \text{Im} \left[ \Sigma^\perp(\mathbf{q}, \omega) + \frac{\Sigma^\parallel(\mathbf{q}, \omega)}{1 - \Sigma^\parallel(\mathbf{q}, \omega)/k_0^2} \right], \quad (4.61)$$

with  $\lim_{q \rightarrow \infty} \Sigma^\perp(\mathbf{q}, \omega) = \lim_{q \rightarrow \infty} \Sigma^\parallel(\mathbf{q}, \omega) = \Sigma_{\text{ISA}}(\omega) + \Sigma_{\text{LL}}(\omega) + \Sigma_L(\omega)$ . The only term which needs to be computed numerically is  $\Sigma_L$  (see Eq. (4.49)).

We have represented in Fig. 4.3(a) maps of the DOS  $p(\delta)$  of TE waves in the regime of moderate density  $k_0 a \in [2.5, 7]$ , for two degrees of spatial correlation,  $\chi = 0$  (top) and  $\chi = 0.5$  (bottom). Numerical distributions obtained from the diagonalization of the Hamiltonian (1.48) (left panels) are compared with the theoretical prediction (4.21), evaluated at the second order in density with Eqs. 4.24 and 4.30 (right panels). Good agreement between numerics and theory is found over a broad range of densities and detunings, all the way from uncorrelated system ( $\chi = 0$ ) to strongly correlated one ( $\chi = 0.5$ ). This confirms the validity of the connection established in Eq. (4.21) between  $p(\delta)$  and the average collective  $\mathbf{T}$ -operator.

Figure 4.3(b) shows cuts of the two maps along the line  $k_0 a = 4.5$ . In the absence of spatial correlation (top),  $p(\delta)$  differs slightly from the Lorentzian profile 4.27 found in

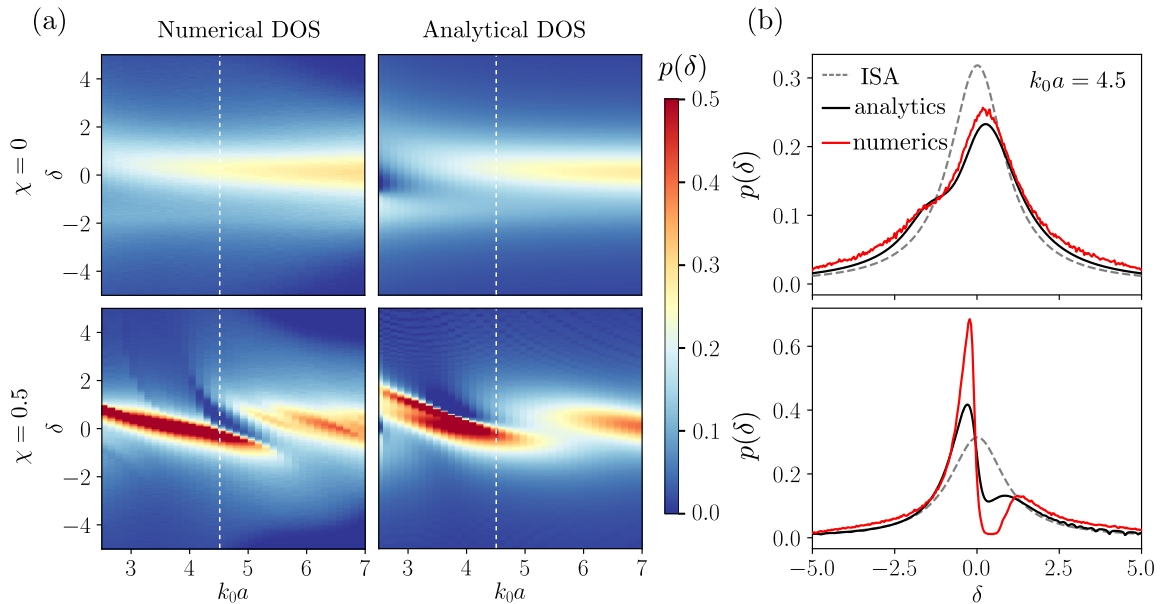


Figure 4.3: (a) Comparison between the numerical DOS  $p(\delta)$  of TE waves (left) and the theoretical prediction 4.21, including recurrent scattering and spatial correlation at the second order in density (right). Good agreement is found for  $k_0a \gtrsim 3$ , without (top) and with (bottom) spatial correlation. (b) Cuts along the line  $k_0a = 4.5$  of the maps shown in (a). The Lorentzian profile (4.27) for dilute uncorrelated system is shown with a dashed line for reference. Numerical results shown in (a) and (b) have been obtained with a system size  $k_0R = 55$  and a number of disorder realisations adjusted to have  $\sim 10^6$  eigenvalues for each  $k_0a$ .

the dilute limit (dashed line). In particular, the loop correction  $\Sigma_L$  is responsible for an antisymmetric contribution to  $p(\delta)$  through  $\text{Im}[t(\omega)^3]$ , which blue-shifts the maximum of  $p(\delta)$  and creates a depletion at  $\delta < 0$ . On the contrary, for a large degree of correlation (bottom),  $\Sigma_L$  is responsible for a dip in the DOS at  $\delta > 0$ , which coincides with the pseudo-gap found in simulations.

#### 4.5.2 Evaluation of the average density of states for TM waves

When considering the *a priori* simpler problem of scalar waves, the density of modes is still given by Eq. (4.21). Using that  $\lim_{q \rightarrow \infty} G_0(\mathbf{q}, \omega) = 0$ , we can write the DOS as

$$p(\delta) = -\frac{1}{4\pi\rho} \lim_{q \rightarrow \infty} \text{Im} [\Sigma(\mathbf{q}, \omega)], \quad (4.62)$$

where Eq. (4.30) still holds. Yet, in the limit  $q \rightarrow \infty$ , the contributions  $\Sigma_B$  and  $\Sigma_C$  vanish, as the Lorentz-Lorenz contribution, which arises from the delta-singularity of the vector Green's function, is absent for scalar waves. We thus find

$$\lim_{q \rightarrow \infty} \Sigma(\mathbf{q}, \omega) = \Sigma_{ISA}(\omega) + \Sigma_L(\omega) \quad (4.63)$$

with

$$\Sigma_{ISA}(\omega) = \rho t(\omega), \quad (4.64)$$

$$\Sigma_L(\omega) = 2\pi\rho^2 t(\omega)^3 \int_0^\infty dr r [1 + h_2(r)] \frac{G_0^2(r, \omega_0)}{1 - t(\omega)^2 G_0^2(r, \omega_0)}, \quad (4.65)$$

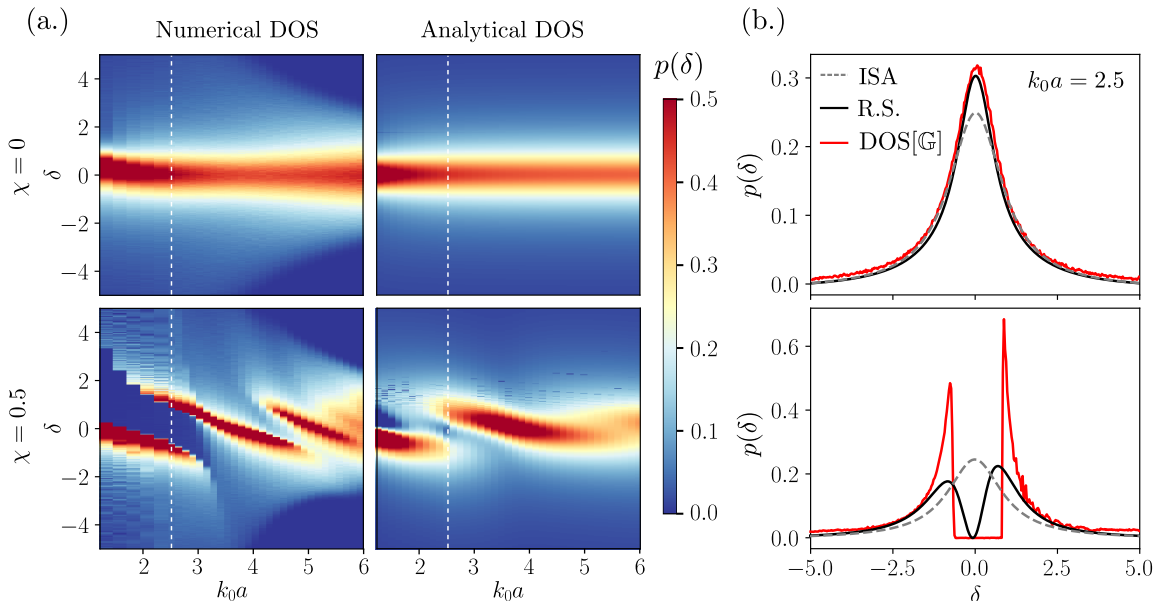


Figure 4.4: (a) Comparison between the numerical DOS  $p(\delta)$  of TM waves (left) and the theoretical prediction 4.62, including recurrent scattering and spatial correlation at the second order in density (right). Good agreement is found for  $k_0a \gtrsim 1$ , without (top) and with (bottom) spatial correlation. (b) Cuts along the line  $k_0a = 2.5$  of the maps shown in (a). The Lorentzian profile (4.27) for dilute uncorrelated system is shown with a dashed line for reference. Numerical results shown in (a) and (b) have been obtained with a system size  $k_0R = 55$  and a number of disorder realisations adjusted to have  $\sim 10^6$  eigenvalues for each  $k_0a$ .

where we recall that  $t(\omega) = -4/(\delta + i)$  close to the resonance. The integral giving  $\Sigma_L$  is regular at the origin and but the same regularisation as in 4.4.6 is necessary for large arguments. The resulting DOS is shown in Fig. 4.4.

The good agreement between the theory and the numerics holds for scalar fields as well, up to even higher densities. The numerical DOS at  $\chi = 0$  is closer to our prediction than to the ISA estimate. The difference is subtle as the blue shifted asymmetry found in the vector situation and due to Lorentz-Lorenz corrections, is now absent.

The effects of strong spatial correlations are also captured by our theory as Fig. 4.4 predicts the high density TM gap. The edges are smoothed out and not as sharp as in the real DOS, but we still capture the slight asymmetry between the two edges and the range of density where it occurs. The model seems to fail to reproduce the fine structures in the DOS appearing at lower densities ( $k_0a \sim 5$ ). These details seem to be averaged out. We still lack a simple explanation for this observation. We can notice that the distributions of modes are correctly normalised to 1 [ $\int p(\delta)d\delta = 1$ ]. It is trivially verified in the ISA [see Eq. (4.27)], it remains true at all order. Indeed, the frequency dependence of each diagram is only carried by a  $t(\omega)^j$ ,  $j \in \mathbb{N}, j > 1$  factor which once integrated over the detuning, gives a zero net contribution [ $\int t(\delta)^j d\delta = 0$  if  $j \in \mathbb{N}$  and  $j > 1$ ].

## 4.6 Single scattering versus double scattering

We show in this section that the infinite series of diffusion events involved in the self-energy can be very well approximated (except in one specific case) by the first diagram and its

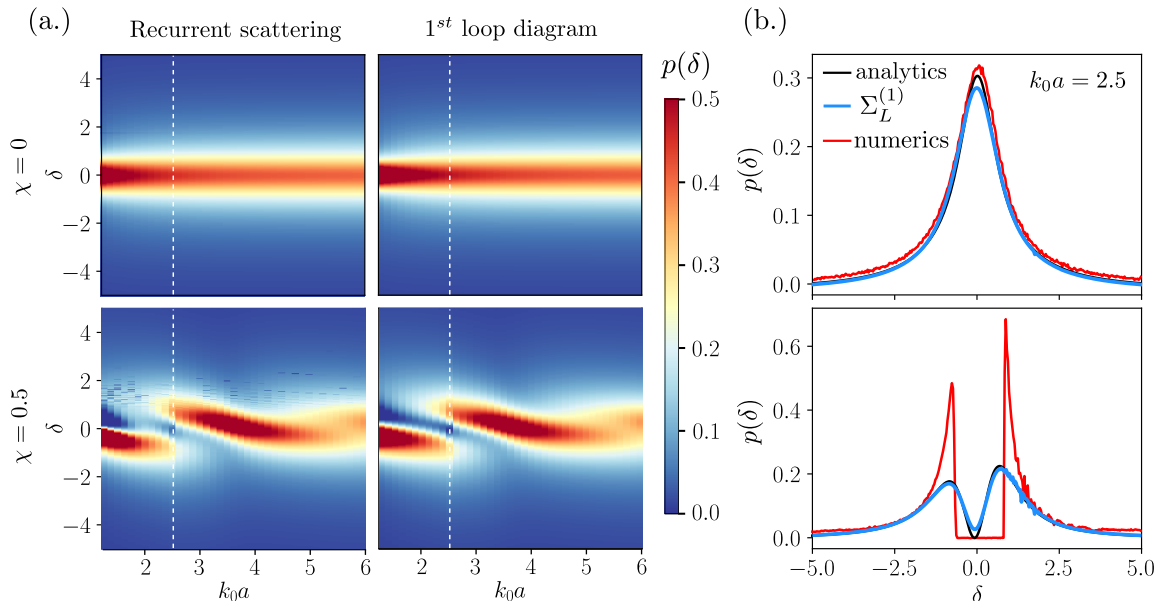


Figure 4.5: Comparison between maps of the density of states in frequency-density space of the TM (scalar) setup (a), at  $\chi = 0$  (top) and  $\chi = 0.5$  (bottom). We used the complete expression of the self-energy up to second order in density in the left column and the two leading terms [see Eq. (4.66)] in the right one. We show cuts at  $k_0a = 2.5$  (b) for both the uncorrelated (top) and strongly correlated arrangements (bottom). The model using the full expression of  $\Sigma_L$  is shown as a plain dark line, the one using only the first loop is shown in blue and the numerical evaluation is in red. For both degrees of correlation, the two models give very similar results.

correlated counterpart such that

$$\Sigma_L(\mathbf{r}, \mathbf{r}') \simeq \text{---} \text{---} \text{---} + \text{---} \text{---} \text{---} \quad (4.66)$$

The expressions read

$$\Sigma_L(\omega) \simeq \rho^2 t(\omega)^3 \begin{cases} 2\pi \int_0^\infty dr r g_2(r) G_0^2(r, \omega_0) & \text{in TM,} \\ \pi \int_0^\infty dr r g_2(r) [G_0^{t^2}(r, \omega_0) + G_0^{l^2}(r, \omega_0)] & \text{in TE.} \end{cases} \quad (4.67)$$

Approximating  $\Sigma_L$  by its first component has the advantage to split the terms involving the frequency from the ones involving the density. In Fig. 4.5, the DOS obtained from Eq. (4.67) is compared to one evaluated in the previous section, for scalar waves. The two models give almost the same results.

The domination of the first looped-diagram in the self-energy also holds for vector waves in correlated ensembles, as shown in Fig. 4.6.

Interestingly, one cannot make such an approximation if  $\chi = 0$ . The re-summation procedure involving the infinite number of scattering event regularises the expression, while the first diagram has a non-integrable divergence at the origin due to  $rG_t^2(r, \omega)$ . This issue does not occur for scalar waves as  $rG_0^2(r, \omega) \sim r \ln(r) + \mathcal{O}(r)$ , which is regular at  $\mathbf{0}$ . Similarly, this issue is circumvented in strongly correlated ensembles thanks to the effective hard-core behaviour, cancelling  $1 + h_2(r)$  over the singularity. Explicitly,  $g_2$  is mathematically zero over a finite domain around the origin for hard-core like point patterns. If we discard the potentially strong short range behaviour of  $\mathbf{G}$ , every extra round-trip between two particles adds a

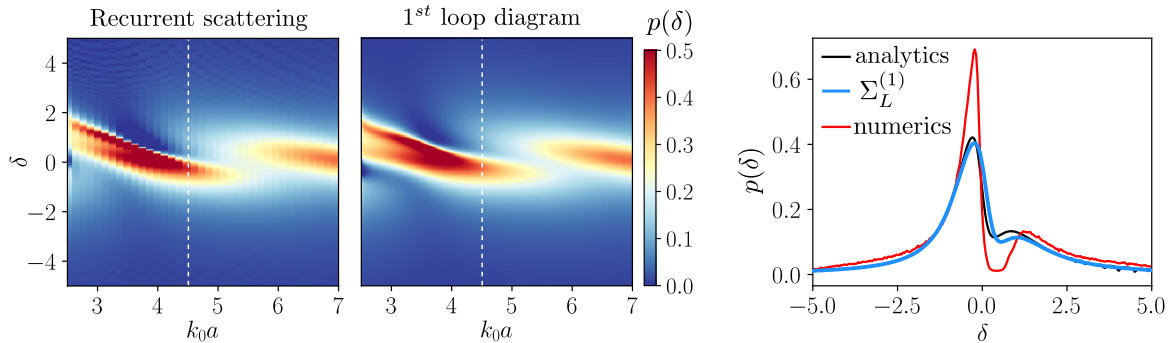


Figure 4.6: Comparison between maps of the density of states in frequency-density space of the TE (vector) setup (a), at  $\chi = 0.5$ . We used the complete expression of the self-energy up to second order in density in the left column and the two leading terms [see Eq. (4.66)] in the right one. We show cuts at  $k_0 a = 4.5$  (b) only for the strongly correlated arrangements because the uncorrelated one has a non-integrable divergence which happens to be smoothed out by  $g_2(r)$ . The model using the full expression of  $\Sigma_L$  is shown as a plain dark line, the one using only the first loop is shown in blue and the numerical evaluation is in red.

factor  $G^2 \underset{r \rightarrow \infty}{\sim} \sqrt{2/\pi k_0 r}$ , which at the densities we consider is smaller than 1, justifying the convergence of the geometrical series.

The good agreement between the numerical and the theoretical predictions indicates that we have correctly modelled the DOS and have in particular identified the crucial role of *Loop*-type recurrent scattering. The discrepancies, in particular regarding the accurate shape of the gap, could come from the approximation consisting in replacing the wavevector integral in Eq. (4.18) by a large wavevector limit to obtain Eq. (4.20), but are more likely to come from the density expansion of the self-energy. A full band gap is by definition a non-perturbative process and a second order density expansion can only provide a partial description. Higher order terms should probably be included in the self-energy. In the case where the self-energy is dominated by one or a few scattering events, it may be possible to evaluate their contribution and test this hypothesis.

## 4.7 Changes in the DOS seen as an interference process

We saw in the previous section that the self-energy appearing in the computation of the DOS was dominated by two distinct scattering events. This section will use this observation to discuss the effects of spatial correlations in terms of interferences between the single scattering and double scattering sequences.

Explicitly, the effects of spatial correlations on the density of states can be simply understood from  $\Sigma_{\text{ISA}}$  and  $\Sigma_L$ . The ISA term alone gives  $p(\delta) = -\text{Im } t(\omega)/4\pi\beta$ , which is a positive Lorentzian profile. The difference to the Lorentz profile thus depends on the sign of the  $\Sigma_L$  contribution, which takes the form  $-\text{Im } t^3(\omega) \int dr r g_2(r) G^2(r, \omega_0)$  when considering only the first loop. We plotted  $g_2$  and the rest of the integrand at the central frequency (where  $t = -4\beta i$ ), knowing that a positive result will give an increase in the DOS and reciprocally. We can see in Fig. 4.7, that the DOS reaches a high value whenever the first peak of  $g_2$  coincides with a positive arch of the rest of the integrand. Conversely,  $\Sigma_L$  will have a negative contribution, sometimes leading to a gap, when the peak of the pair correlation function coincides with a minimum of  $-\text{Im } r t(\omega_0)^3 G^2(r, \omega_0)$ . In the scalar case, at  $\delta = 0$  the TM gap roughly extends between  $k_0 a \sim 1.5$  and  $k_0 a \sim 3.5$ . Directly outside these values, the DOS reaches a local maximum, which is in perfect agreement with the above picture: the

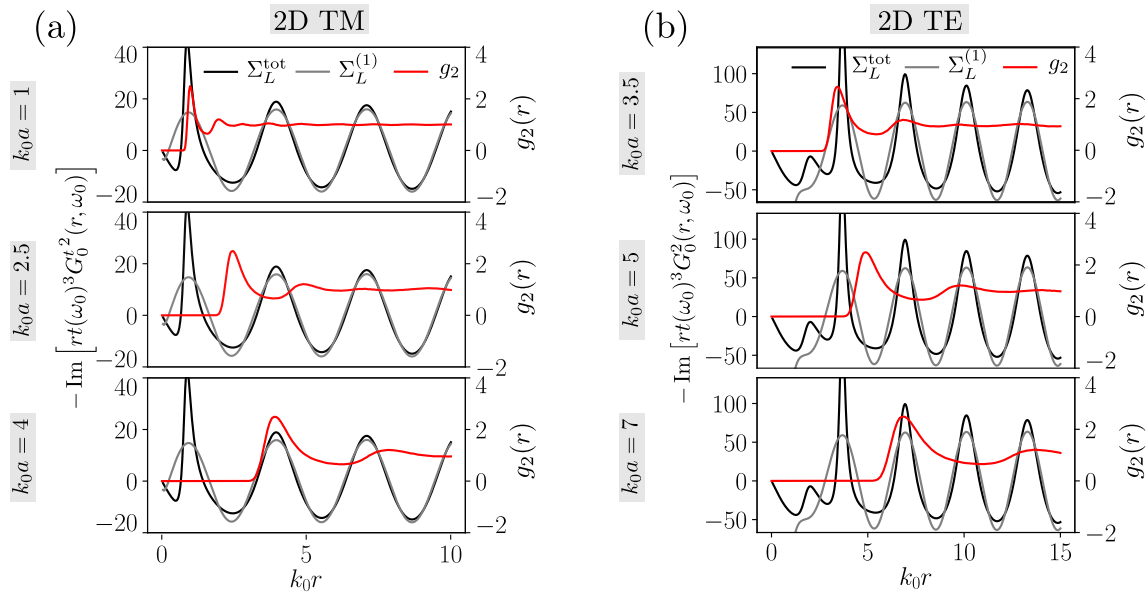


Figure 4.7: Imaginary part of the two components of the integrand of  $\Sigma_L$  at  $\delta = 0$  in TM (a) and TE polarisation (b) computed using the first term (gray,  $\Sigma_L^{(1)}$ ) or the full expression (black,  $\Sigma_L^{\text{tot}}$ ). The first component is given in the left axis and the second one in the right axis.

main peak of  $g_2$  overlaps with the first two maxima of the integrand roughly at  $k_0 a \sim 1$  and 4, leaving a gap in-between where the two scattering processes associated to  $\Sigma_{\text{ISA}}$  and  $\Sigma_L$  interfere destructively. The same effect occurs for vector waves but at a lower density since the first maximum of the integrand lies around  $k_0 a \sim 3.5$ .

We can notice that the only difference between all the plots of Fig. 4.7, is that  $g_2$  has been rescaled. It means, and we can already notice it, that its first peak gets broader and broader as the density decreases. This may explain why the changes in the DOS captured by this model seem to be more resolved at high density rather than at low density. For  $k_0 a > 7$ , the main peak of  $g_2$  becomes eventually broad enough that it overlaps many oscillations of the integrand, smoothing away any distinguishable effects on the DOS. We can also notice that the scalar and vector configurations have very similar integrand, except at short range, where the TE setup is missing the TM maximum.

## 4.8 The DOS as Im $\mathbf{G}$

We derived a model to predict and study analytically the density of collective resonances in ensembles of resonant scatterers coupled by electromagnetic field. A keen reader may notice that the expression we use for the density of modes differs from the usually accepted expression involving the imaginary part of  $\mathbf{G}$ , the average total Green's function. We will question here the limit of validity of the usual approach [see eg Lagendijk and van Tiggelen (1996) or more recently Carminati et al. (2015a)] by showing how it differs from our results.

In the case of homogeneous, lossless and non dispersive medium ( $n = \text{cst}$ ) the density of states of scalar waves defined as  $\rho_0(\omega) = \sum_n \delta(\omega - \omega_n)$  can be obtained from (Carminati and Schotland, 2021; Lagendijk and van Tiggelen, 1996)

$$\rho_0(\omega) = \frac{-2\omega}{\pi c^2} \text{Im Tr } G(\omega). \quad (4.68)$$

The derivation relies on an modal expansion of the Green's function, which are traced over



in Eq. (4.68).

In free space, it takes the explicit form of

$$\rho_0(\omega) = \begin{cases} \frac{V\omega^2}{2\pi^2c^3} & \text{in 3D} \\ \frac{V\omega}{2\pi c^2} & \text{in 2D.} \end{cases} \quad (4.69)$$

Let us now consider an ensemble of resonators. In that case, it is far from obvious that the relation (4.68) still holds. To show this, let us evaluate the right hand-side of Eq. (4.68) and compare it to our own results. We first recall the expression of the average Green's function, defining the self-energy.

$$\langle G \rangle = \frac{1}{\nabla^2 + \frac{\omega^2}{c^2} - \Sigma}. \quad (4.70)$$

The average dielectric constant is complex in the case of resonant particles and related to the self-energy by

$$\varepsilon(\omega) = 1 - \frac{\Sigma(\omega)}{\omega^2/c^2}, \quad (4.71)$$

so that we have  $\frac{\omega^2}{c^2} - \Sigma(\omega) = \frac{\omega^2}{c^2}\varepsilon(\omega)$ .

The expression  $\text{Im Tr } \overline{G}$  defines an integral over the entire Fourier space, which corresponds to  $G(\mathbf{r} = 0)$ . A simple calculation gives

$$\frac{\text{Im Tr } \langle G \rangle(\omega)}{\text{Im Tr } G_0(\omega)} = \begin{cases} \text{Re } \sqrt{\varepsilon(\omega)}, & \text{in 3D,} \\ 1 - \frac{1}{\pi} \arctan \left[ \frac{\text{Im } \varepsilon(\omega)}{\text{Re } \varepsilon(\omega)} \right] & \text{in 2D,} \end{cases} \quad (4.72)$$

where we assumed  $\text{Re}[\varepsilon(\omega)] > 0$  to obtain the expression in 2D. Even though the first result is widely known, the second much less. If we consider that Eq.(4.72) characterises the DOS, then we find that in 2D, no matter the shape of  $\varepsilon(\omega)$ , the DOS will be bounded by 0 and two times the value of the free space DOS, which is very different from the 3D case.

Let us give an explicit value for Eq.(4.72) at first order in density. The simplest expression of the self-energy is given by its ISA value  $\Sigma(\mathbf{q}, \omega) \simeq \Sigma_{\text{ISA}}(\omega)$ , accurate at low density.

For point-dipoles, the self-energy reads

$$\Sigma_{\text{ISA}}(\omega) = \rho t(\omega) = -\frac{\omega^2}{c^2} \rho \alpha(\omega). \quad (4.73)$$

Using that  $\text{Im } \varepsilon / \text{Re } \varepsilon = \rho \text{Im } \alpha / (1 + \rho \text{Re } \alpha) \simeq \rho \text{Im } \alpha$ , with  $\alpha$  given in Sec.1.5.1, we find

$$\frac{\text{Im Tr } \langle G \rangle(\omega)}{\text{Im Tr } G_0(\omega)} = \begin{cases} 1 + \frac{2\pi}{(k_0 a)^3} \frac{\delta}{1 + \delta^2}, & \text{in 3D,} \\ 1 - \frac{4}{\pi(k_0 a)^2} \frac{1}{1 + \delta^2} & \text{in 2D.} \end{cases} \quad (4.74)$$

The 2D and the 3D systems behave qualitatively different. Only the 3D system has the characteristic asymmetric shape of the polariton, with more mode below the resonance than above. The difference between 2D and 3D can also be understood by using the lowest order of the Dyson expansion,  $\langle G \rangle = G_0 + G_0 \Sigma G_0$ : for 3D scalar waves, the contribution of  $G_0^2$  is imaginary so that  $\text{Im Tr } \langle G \rangle$  is proportional to  $\text{Re}(\Sigma)$ , whereas for 2D scalar waves,  $G_0^2$  gives a real contribution and  $\text{Im Tr } \langle G \rangle$  is proportional to  $\text{Im}(\Sigma)$ . In 2D, Eq. (4.74) predicts a DOS depleted in a symmetric manner, around the resonance, which is in contradiction with both the numerical observation of the Green's matrix spectrum, and the theoretical approaches developed in Chap. 3. This indicates that Eq. (4.68) cannot describe the density of collective resonances in an ensemble of coupled resonators.

## 4.9 Conclusion

In this chapter, we first expressed the DOS of the light-matter effective Hamiltonian in terms of the total scattering operator  $\mathbf{T}$ . We then evaluated  $\mathbf{T}$  theoretically, up to the second order in density, and we computed the distribution of modes in 2D correlated systems, for both scalar (TM) and vector (TE) waves. We obtained good agreement between theory and numerics over a wide range of densities, frequencies, and correlation ratio.

In particular, the existence and locations of gaps, opened by strong spatial correlations are rather accurately predicted in our formalism. We also showed that most of the features of the DOS can be obtained by only considering the ISA contribution to the self-energy and the first looped diagram including its correlated counterpart. The DOS has been interpreted as an interference process between single and double scattering.

We finally indicate that the theoretical results of this chapter go beyond the study of electromagnetic waves, as the Green's function can be replaced by any coupling function in our formal treatment and analytical predictions. They thus apply to any Hamiltonian of the general form (4.1).



## Chapter 5

# Strong localization phenomenon in correlated resonant systems

This chapter will describe the link between the modification of the DOS induced by spatial correlations, and the observation of Anderson localized modes. We will first introduce a general transport equation satisfied by the average intensity. This will be the occasion to discuss the *transport mean free path*, which can differ from the already described *scattering mean free path*. Then, we will show in the same fashion as in Chap. 1, how localization features can be introduced through a self-consistent approach. We will in particular pay attention to the DOS dependence appearing in these equations that will lead to modified expressions for both the Ioffe-Regel's criterion in 3D and the localization lengths in both 2D and 3D which capture the impact of spatial correlation. The accuracy of our predictions will be tested in 2D and TE polarisation (vector fields), with two complementary approaches. The first one relies on the direct numerical estimation of the exponential decay of the eigenmodes of the coupled-dipole method used throughout this work. The second one is based on a numerical study of the statical properties of the field and intensity detected behind a disordered slab illuminated with coherent light. From these simulations we will extract both the localisation length and the scattering mean free path. Finally, the transport mean free path, found by combining the scattering mean free path with the scattering anisotropy factor evaluated analytically, will be used to compare our prediction for the localisation length with numerical results.

### 5.1 Diffusion equation for vector fields

This section aims at sketching the key steps to obtain a diffusion equation for the intensity of vector fields in 2D. For this purpose we will adapt the 3D results of Refs. Vynck et al. (2014, 2016); Akkermans and Montambaux (2007) to the 2D scenario. Neither correlations, nor the time dependence will be included at this point. We already presented a proof of the diffusion equation satisfied by the average intensity in Sec. 1.4, but without considering polarisation effects. Here we will explicitly compute the diffusion coefficients of each of the different propagation channels and show that transport is dominated by a single scalar-like channel at large distance.

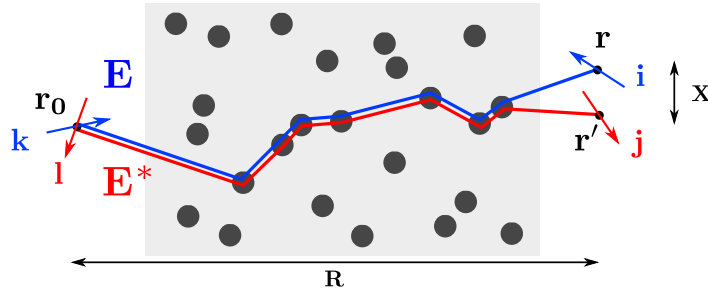


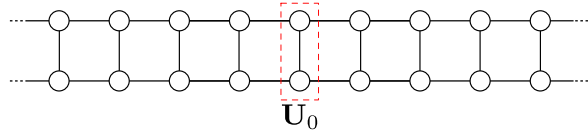
Figure 5.1: Schematic representation of the diffusion path considered in Sec. 5.1.1, where we compute the correlator between a field  $\mathbf{E}$ , diffusing from  $\mathbf{r}_0$  with a polarisation along the direction  $\mathbf{k}$ , with a field  $\mathbf{E}^*$  originating from the same location but with a polarisation along  $\mathbf{l}$ . The two fields follow the same diffusion process, but are then evaluated respectively at  $\mathbf{r}$  and  $\mathbf{r}'$ , in the polarisation  $\mathbf{i}$  and  $\mathbf{j}$ . The distance between the source and evaluation points is supposed large compared to the distance between the evaluation points themselves ( $R \gg X$ ).

### 5.1.1 Bethe-Salpether equation for vector Green's functions

The average two-fields correlator satisfies an equation similar to the Dyson's equation for the average field, called the Bethe-Salpether equation. It reads

$$\begin{aligned} \langle G_{ik}(\mathbf{r}, \mathbf{r}_0) G_{jl}^*(\mathbf{r}', \mathbf{r}_0) \rangle &= \langle G_{ik}(\mathbf{r}, \mathbf{r}_0) \rangle \langle G_{jl}^*(\mathbf{r}', \mathbf{r}_0) \rangle + \\ &\int \langle G_{im}(\mathbf{r}, \mathbf{r}_1) \rangle \langle G_{jn}^*(\mathbf{r}', \mathbf{r}_1') \rangle U_{mnr s}(\mathbf{r}_1, \mathbf{r}_1', \mathbf{r}_2, \mathbf{r}_2') \langle G_{rk}(\mathbf{r}_2, \mathbf{r}_0) G_{sl}^*(\mathbf{r}_2', \mathbf{r}_0) \rangle d\mathbf{r}_1 d\mathbf{r}_1' d\mathbf{r}_2 d\mathbf{r}_2', \end{aligned} \quad (5.1)$$

where the frequency dependence in the Green's function and summation over repeated indices have been omitted for simplicity.  $U_{mnr s}$  is the four-rank irreducible intensity vertex tensor which accounts for all the complexity of the two-field scattering process and  $G_{ij}(\mathbf{r}, \mathbf{r}_0)$  is the Green's function representing a field at  $\mathbf{r}$  polarised along the polarisation axis  $i$ , generated by a point dipole oriented along the axis  $j$  at  $\mathbf{r}_0$ . If we apply the so-called *ladder* approximation, each field and its complex conjugate visit the same scatterers along the propagation, so that the scattering sequences are formally represented by ladders:



Such scattering sequences are generated by the vertex

$$U_{mnr s}(\mathbf{r}_1, \mathbf{r}_1', \mathbf{r}_2, \mathbf{r}_2') \simeq \rho |t(\omega)|^2 \delta(\mathbf{r}_1 - \mathbf{r}_1') \delta(\mathbf{r}_1' - \mathbf{r}_2) \delta(\mathbf{r}_1' - \mathbf{r}_2') \delta_{mr} \delta_{ns}, \quad (5.2)$$

where  $t$  is the scattering amplitude of a single resonator. With this expression, Eq. (5.1) becomes

$$\begin{aligned} \langle G_{ik}(\mathbf{r}, \mathbf{r}_0) G_{jl}^*(\mathbf{r}', \mathbf{r}_0) \rangle &= \langle G_{ik}(\mathbf{r}, \mathbf{r}_0) \rangle \langle G_{jl}^*(\mathbf{r}', \mathbf{r}_0) \rangle + \\ &\rho |t(\omega)|^2 \int \langle G_{im}(\mathbf{r}, \mathbf{r}_1) \rangle \langle G_{jn}^*(\mathbf{r}', \mathbf{r}_1) \rangle \langle G_{mk}(\mathbf{r}_1, \mathbf{r}_0) G_{nl}^*(\mathbf{r}_1, \mathbf{r}_0) \rangle d\mathbf{r}_1. \end{aligned} \quad (5.3)$$

### 5.1.2 Diagonalization of the Bethe-Salpeter equation at large scales

Several approaches exist to solve the Bethe-Salpether equation. In order to treat the polarisation effects, we will apply the derivation found in Refs. Vynck et al. (2014, 2016);

Akkermans and Montambaux (2007). We see that Eq. (5.3) links the two point correlator  $W_{ijkl}(\mathbf{r}, \mathbf{r}') = \langle G_{ik}(\mathbf{r}, \mathbf{0})G_{jl}(\mathbf{r}', \mathbf{0}) \rangle$  to the one point correlator  $\langle G_{mk}(\mathbf{r}_1, \mathbf{0})G_{nl}^*(\mathbf{r}_1, \mathbf{0}) \rangle$  where we chose, without loss of generality, the origin at  $\mathbf{r}_0$ . The term can be computed using Eq. (5.3) evaluated at the same point. We obtain a closed equation which can be written simply in Fourier space by recognising a convolution product, as

$$W_{ijkl}(\mathbf{Q}) = S_{ijkl}(\mathbf{Q}) + \rho|t(\omega)|^2 S_{ijmn}(\mathbf{Q})W_{mnkl}(\mathbf{Q}), \quad (5.4)$$

where

$$W_{ijkl}(\mathbf{Q}) = \int W_{ijkl} \left( \mathbf{q} + \frac{\mathbf{Q}}{2}, \mathbf{q} - \frac{\mathbf{Q}}{2} \right) \frac{d\mathbf{q}}{(2\pi)^d} \quad (5.5)$$

$$S_{ijkl}(\mathbf{Q}) = \int \left\langle G_{ik} \left( \mathbf{q} + \frac{\mathbf{Q}}{2} \right) \right\rangle \left\langle G_{jl}^* \left( \mathbf{q} - \frac{\mathbf{Q}}{2} \right) \right\rangle \frac{d\mathbf{q}}{(2\pi)^d}, \quad (5.6)$$

with  $\mathbf{q}$  and  $\mathbf{Q}$  the Fourier variables associated to  $\mathbf{X} = \mathbf{r} - \mathbf{r}'$  and  $\mathbf{R} = (\mathbf{r} + \mathbf{r}')/2 - \mathbf{r}_0$ , shown in fig. 5.1.

Equation (5.4) can be solved by diagonalizing the operator  $\mathbf{S}$ . In 3D, the correlator is a  $(3 \times 3) \times (3 \times 3)$  tensor with 9 eigenvalues computed in Ref. Vynck et al. (2014). We treat here the 2D case, where  $\mathbf{S}$  is of size  $(2 \times 2) \times (2 \times 2)$  and has thus only 4 eigenmodes for TE polarisation.

The explicit form of  $\mathbf{S}(\mathbf{Q})$  follows from  $\langle G(\mathbf{q}) \rangle = [k_r^2 - q^2 - i \text{Im} \Sigma(\mathbf{q})]^{-1}$ , which gives

$$\left\langle G_{ik} \left( \mathbf{q} + \frac{\mathbf{Q}}{2} \right) \right\rangle \left\langle G_{jl}^* \left( \mathbf{q} - \frac{\mathbf{Q}}{2} \right) \right\rangle = (\delta_{ik} - \hat{q}_i \hat{q}_k)(\delta_{jl} - \hat{q}_j \hat{q}_l) \frac{\pi \delta(k_{\text{eff}}^2 - q^2)}{i \mathbf{q} \cdot \mathbf{Q} - \text{Im} \Sigma(\mathbf{q})}. \quad (5.7)$$

Here  $\Sigma(\mathbf{q})$  has been assumed isotropic such that  $\Sigma(\mathbf{q}) = \Sigma(q)\mathbf{1}$ .

We evaluate the  $q$ -integral in Eq. (5.6) to get

$$\frac{1}{2\pi} \int_0^\infty \left\langle G \left( \mathbf{q} + \frac{\mathbf{Q}}{2} \right) \right\rangle \left\langle G^* \left( \mathbf{q} - \frac{\mathbf{Q}}{2} \right) \right\rangle q dq = \frac{\ell_s}{8k_0} [1 - i \hat{\mathbf{q}} \cdot \mathbf{Q} \ell_s - (\hat{\mathbf{q}} \cdot \mathbf{Q})^2 \ell_s^2], \quad (5.8)$$

so that  $\mathbf{S}$  takes the form

$$S_{ijkl}(\mathbf{Q}) = \frac{\ell_s}{8k_0} \langle (\delta_{ik} - \hat{q}_i \hat{q}_k)(\delta_{jl} - \hat{q}_j \hat{q}_l)(1 - i \hat{q}_r Q_r \ell_s - \hat{q}_m \hat{q}_n Q_n Q_m \ell_s^2) \rangle_{\hat{\mathbf{q}}}, \quad (5.9)$$

where  $\langle \cdot \rangle_{\hat{\mathbf{q}}}$  accounts for an average over the normalised vector  $\hat{\mathbf{q}}$ . The tensor  $S$  can be computed analytically using  $\langle \hat{q}_i^2 \rangle_{\hat{\mathbf{q}}} = 1/2$ ,  $\langle \hat{q}_i^4 \rangle_{\hat{\mathbf{q}}} = 3/8$ ,  $\langle \hat{q}_i^6 \rangle_{\hat{\mathbf{q}}} = 5/16$ ,  $\langle \hat{q}_i^2 \hat{q}_j^2 \rangle_{\hat{\mathbf{q}}} = 1/8$  and  $\langle \hat{q}_i^4 \hat{q}_j^2 \rangle_{\hat{\mathbf{q}}} = 1/16$  ( $i \neq j$ ). We obtain a rather complicated matrix whose eigenmodes provide independent channels for intensity transport. Setting aside the constant term in Eq. (5.8), we diagonalise this matrix and rewrite it as

$$\frac{8k_0}{\ell_s} S_{ijkl}(\mathbf{Q}) = \sum_{p=1}^4 \lambda_p(\mathbf{Q}) |ij\rangle_p \langle kl|_p, \quad (5.10)$$

where the  $\lambda_p$  and  $|ik\rangle_p$  are its eigenvalues and eigenvectors. Since we are interested in the behaviour of the intensity at large scales, we can restrain ourselves to a study at small  $\mathbf{Q}$ . The eigen-elements of  $\mathbf{S}$  are, at second order in  $Q\ell_s$

$$\lambda_1(\mathbf{Q}) \simeq 1 - \frac{(Q\ell_s)^2}{2}, \quad \lambda_2(\mathbf{Q}) = \lambda_3(\mathbf{Q}) \simeq \frac{1}{2} - \frac{(Q\ell_s)^2}{4}, \quad \lambda_4(\mathbf{Q}) = 0 \quad (5.11)$$

$$\begin{aligned} |kl\rangle_1 &= \frac{1}{\sqrt{2}} \delta_{kl}, & |kl\rangle_2 &= \frac{1}{\sqrt{2}} (\delta_{ka} \delta_{la} - \delta_{kb} \delta_{lb}), \\ |kl\rangle_3 &= \frac{1}{\sqrt{2}} (\delta_{ka} \delta_{lb} + \delta_{kb} \delta_{la}), & |kl\rangle_4 &= \frac{1}{\sqrt{2}} (\delta_{ka} \delta_{lb} - \delta_{kb} \delta_{la}). \end{aligned} \quad (5.12)$$

$|kl\rangle_2$  and  $|kl\rangle_3$  form a degenerated subspace and hence the precise choice of  $|kl\rangle_2$  and  $|kl\rangle_3$  is arbitrary inside that subspace.

We can now express Eq. (5.4) in the eigenbasis of  $\mathbf{S}$  leading to

$$W_{ijkl}(\mathbf{Q}) = \sum_{p=1}^4 w_p(\mathbf{Q}) |ij\rangle_p \langle kl|_p, \quad \text{where} \quad w_p(\mathbf{Q}) = \frac{\ell_s}{8k_0} \frac{\lambda_p(\mathbf{Q})}{1 - \lambda_p(\mathbf{Q})}. \quad (5.13)$$

If we define  $A_p$  and  $B_p$  such that  $\lambda_p = A_p - B_p Q^2 \ell^2$  and expand  $w_p$  near  $Q = 0$ , we can rewrite the equation defining  $w_p(\mathbf{Q})$  as

$$\left( \frac{1}{A_p} - 1 + \frac{B_p^2}{A_p} Q^2 \ell_s^2 \right) \frac{8k_0}{\ell_s} w_p(\mathbf{Q}) = 1. \quad (5.14)$$

This equation shows that the quantity  $U_p(\mathbf{Q}) = w_p(\mathbf{Q}) 8k_0 / v_E$  ( $v_E$  is a velocity we will interpret later), is proportional to an energy density (Vynck et al., 2014), and satisfies a stationary diffusion equation with an damping term. In real space, it reads

$$-D_p \nabla^2 U_p(\mathbf{R}) + \mu_p v_E U_p(\mathbf{R}) = \delta(\mathbf{R}), \quad (5.15)$$

where  $D_p = \frac{B_p}{A_p^2} v_E \ell_s$  and  $\mu_p = \frac{1}{\ell_s} \left( \frac{1}{A_p} - 1 \right)$  are the diffusion constant and the attenuation coefficient of the  $p^{\text{th}}$  polarisation eigenchannel. The solution of Eq. (5.15) are of the form

$$U_p(\mathbf{R}) = \frac{Q_0(R/\ell_{\text{att}})}{2\pi}, \quad (5.16)$$

where  $Q_0$  is a modified Bessel function of zeroth order and  $\ell_{\text{att}} = \sqrt{D_p / \mu_p v_E}$  is the attenuation length. We have summarised the diffusion constants, the attenuation coefficients and lengths in the table below.

$p$	1	2, 3	4
$D_p$	$\frac{v_E \ell_s}{2}$	$v_E \ell_s$	*
$\mu_p$	0	$\frac{1}{\ell_s}$	$\infty$
$\ell_{p,\text{att}}$	$\infty$	$\ell_s$	$0^*$

We see that among the four polarisation channels, only the first one at  $p = 1$  is not attenuated and is purely diffusive, with the regular diffusion constant

$$D_0 = \frac{v_E \ell_t}{2} \quad (5.17)$$

of scalar waves in 2D, where  $v_E$  has the meaning of the energy transport velocity and  $\ell_t$  is the transport mean free path, equal to  $\ell_s$  in the present context because we considered the simplest situation of isotropic scattering. This particular mode is referred to as the scalar mode or Goldstone mode. The second and third modes have a larger diffusion constant than the scalar mode, yet they are exponentially attenuated over a single mean free path. These two channels therefore do not participate in large scale transport. The last channel is a bit peculiar as it corresponds to a zero-eigenvalue channel for the intensity transport. The diffusion constant is hence not defined, but it has an infinite attenuation coefficient. Even though the attenuation length cannot be properly defined without a diffusion coefficient, an infinite  $\mu_{\text{att}}$  implies an immediate attenuation in the time domain and hence an attenuation length of zero.

We showed in this section that even when considering fully polarised vector fields the transport is dominated at large distance by a single diffusive polarisation channel, the others being exponentially attenuated. This result has been obtained in the stationary regime and for 2D uncorrelated disordered systems. For 3D systems, we refer the reader to Ref. Akkermans and Montambaux (2007); Sheng (2006, 1990), for a proof of the same result in the non-stationary regime and to Ref. Vynck et al. (2016) in the presence of spatial correlations.

### 5.1.3 Diffusion equation

Now that we have shown that even in the case of vector fields, diffusion takes place at large distance, let us recall the more general space and time dependent diffusion equation satisfied by the average intensity. For this purpose, we introduce the correlator

$$I_{\alpha\gamma}(\mathbf{R}, \Omega) = \left\langle G_{\alpha\gamma} \left( \mathbf{r}, \mathbf{r} + \mathbf{R}, \omega + \frac{\Omega}{2} \right) G_{\alpha\gamma} \left( \mathbf{r}, \mathbf{r} + \mathbf{R}, \omega - \frac{\Omega}{2} \right)^* \right\rangle, \quad (5.18)$$

where  $\omega$  and  $\Omega$  are respectively the fast carrying frequency and the beating one characterising the envelope and  $(\alpha, \gamma)$  refer to output and input polarisation channels. In the long time limit ( $\Omega \rightarrow 0$ ) and large scale limit ( $R \gg \ell_t$ ),  $I_{\alpha\gamma}(\mathbf{R}, \Omega)$  is dominated by the scalar mode of the Bethe-Salpeter equation as shown in Sec. 5.1.2, which is independent of the polarisation channels:  $I_{\alpha\gamma}(\mathbf{R}, \Omega) \equiv I(\mathbf{R}, \Omega)$  Akkermans et al. (2008). In addition, in the regime of weak scattering ( $k\ell_s \gg 1$ , where  $\ell_s$  is the scattering mean free path discussed below), the mean intensity effectively obeys a diffusion equation. In the Fourier domain, it reads

$$(D_0 Q^2 - i\Omega)I(\mathbf{Q}, \Omega) = 0, \quad (5.19)$$

with  $I(\mathbf{Q}, \Omega)$  the Fourier transform of  $I(\mathbf{R}, \Omega)$  and  $D_0$  the scalar diffusion constant defined in Eq. (5.17).

For future purposes, we indicate that another correlator obeys the same equation. It is defined as

$$I_{\alpha\gamma}(\mathbf{R}, \omega) = \left\langle \mathcal{G}_{ij}^{\alpha\gamma} \left( \omega + \frac{\Omega}{2} \right) \mathcal{G}_{ij}^{\alpha\gamma} \left( \omega - \frac{\Omega}{2} \right)^* \right\rangle, \quad (5.20)$$

where  $(i, j)$  are positions indices with  $\mathbf{r}_i = \mathbf{r}_j + \mathbf{R}$ , and  $(\alpha, \gamma)$  refer to output and input polarisation channels. It is the intensity associated to the field operator

$$\mathcal{G}(\omega) = \frac{1}{\omega\mathbb{1} - \mathcal{H}(\omega_0)}, \quad (5.21)$$

where  $\mathcal{H}(\omega_0)$  is the Hamiltonian considered throughout this thesis and whose DOS is given by  $p(\delta)$ . Using Eq. (4.13), we can also express the intensity in terms of the collective  $\mathbf{T}$ -operator,

$$I_{\alpha\gamma}(\mathbf{R}, \Omega) \propto \left\langle T_{\alpha\gamma} \left( \mathbf{r}_i - \mathbf{r}_j, \omega + \frac{\Omega}{2} \right) T_{\alpha\gamma} \left( \mathbf{r}_i - \mathbf{r}_j, \omega - \frac{\Omega}{2} \right)^* \right\rangle, \quad (5.22)$$

where  $T_{\alpha\gamma}(\mathbf{r}_i - \mathbf{r}_j, \omega) = \left( [(\delta + i)\mathbb{1} + \tilde{\mathcal{G}}_0(\omega_0)]^{-1} \right)_{\alpha\gamma}(\mathbf{r}_i - \mathbf{r}_j)$ . One common way to find the expression of the correlator (5.22) is to write a Behte-Salper equation for  $\langle \mathbf{T}\mathbf{T}^\dagger \rangle$  and compute its irreducible vertex at a given order in density using the expansion (4.30). It gives an intensity dominated by the Goldstone mode, and satisfying Eq. (5.19).

## 5.2 Renormalisation of the diffusion constant using the self-consistent theory of localisation

As introduced in Sec. 1.6, the weak localisation correction to diffusion transport consists in including the maximally crossed diffusion events (see Fig. 1.9) in the diffusion sequence. It



reduces the diffusion coefficient by allowing the diffusion paths to form closed loops. Once this effect has been taken into account, nothing prevents us from iterating this process, allowing loops to form inside loops as shown in Fig. 1.9, (d). The resulting equations for the intensity constitute the self-consistent theory of localisation (Vollhardt and Wölfle, 1980a,b, 1982; Wölfle and Vollhardt, 2010; Sheng, 2006). The frequency-dependent intensity satisfies an effective diffusion equation,

$$[D(\omega)Q^2 - i\Omega] I(\mathbf{Q}, \Omega) = 0, \quad (5.23)$$

where  $\omega$  and  $\Omega$  are the frequencies associated with fast and slow dynamics already defined in Sec. 5.1.3 and  $\mathbf{Q}$  is the Fourier variable accounting for large distance behaviour as already defined in Sec. 1.4. The diffusion coefficient in Eq. (5.23) is defined self-consistently by

$$\frac{1}{D(\omega)} = \frac{1}{D_0(\omega)} \left[ 1 + \underbrace{\frac{1}{\pi p(\omega)} \int \frac{d\mathbf{Q}}{(2\pi)^d} \frac{1}{D(\omega)Q^2 - i\Omega}}_{P_0} \right], \quad (5.24)$$

$P_0$  represents the return probability to the origin. It is expressed in terms of the DOS  $p(\omega)$ , associated to the effective Hamiltonian defining the Green's function in Eq. (1.48). In our situation, this is precisely the DOS studied in previous chapters. This equation can be solved by computing the integral in  $P_0$  which presents convergence issues in 2D and 3D (we let aside the 1D case which will not be considered in this chapter). As already mentioned in Sec. 1.6, diffusion breaks down at distances shorter than  $\ell_t$ , leading to a natural upper cut-off  $q_{max} = 1/\ell_t$ .

### 5.2.1 Study in 2D

In two dimensions, the return probability  $P_0$  can be computed using the upper cut-off above-mentioned, leading to

$$P_0 = \frac{1}{(2\pi)^2 p(\omega) D(\omega)} \ln \left[ 1 + \frac{iD(\omega)}{\Omega \ell_t^2} \right]. \quad (5.25)$$

In the limit of large time ( $\Omega \rightarrow 0^+$ ), the diffusion coefficient  $D(\omega)$ , solution of Eq. (5.24), becomes purely imaginary and reads

$$D(\omega) = -i\Omega \xi^2, \quad (5.26)$$

where  $\xi$  is a characteristic length-scale defined as :

$$\xi = \ell_t e^{2\pi^2 p(\omega) D_0} = \ell_t e^{2\pi^2 \beta \rho \ell_t \ell_s p(\delta)}, \quad (5.27)$$

where  $\beta$  accounts for the dimension of the field,  $\beta = 1$  for scalar (TM) fields and  $\beta = 2$  for vector (TE) fields. This length describes the attenuation of the intensity inside the medium. Indeed, Eq. (5.23) now simplifies to  $(Q^2 + 1/\xi^2)I(\mathbf{Q}) = 0$ , whose real-space solution  $I(\mathbf{R})$  is providing an exponentially decreasing solution over the length  $\xi$ . This expression has been obtained using  $D_0 = v_E \ell_t / 2$ , and  $p(\omega) = \frac{2\beta\rho}{\Gamma_0} p(\delta)$  (see Eq. (1.53)). In the strongly resonant limit, the energy transport celerity is not given by  $c$  as in the non-resonant case, but rather by  $v_E = \Gamma_0 \ell_s$  (see Sec. 1.4). Indeed, the time spent by light interacting with a particle is much greater than the travelling time between two consecutive scattering events, such that a distance equal to  $\ell_s$  is covered after a time  $\Gamma_0^{-1}$ .

If we consider non-resonant systems instead, the density of states is that of free space (see Eq. (4.69)), and  $v_E = c$  we recover the expression of the localisation in 2D introduced in Chap.1 (see Eq. (1.61)) and given by

$$\xi = \ell_t e^{\frac{\pi}{2} \ell_t}. \quad (5.28)$$

### 5.2.2 3D case

In 3D, the return probability takes the form

$$P_0 = \frac{1}{2\pi^3 p(\omega) \ell_t D(\omega)} \left[ 1 - \sqrt{\frac{-i\ell_t^2 \Omega}{D(\omega)}} \arctan \sqrt{\frac{D(\omega)}{-i\ell_t^2 \Omega}} \right]. \quad (5.29)$$

Equation (5.24) now becomes

$$\frac{D(\omega)}{D_0} = 1 - \frac{1}{2\pi^3 p(\omega) \ell_t D_0} \left[ 1 - \frac{\pi}{2} \sqrt{\frac{-i\ell_t^2 \Omega}{D(\omega)}} \right]. \quad (5.30)$$

In the long time limit ( $\Omega \rightarrow 0$ ), Eq (5.30) displays two regimes. If we have

$$1 \geq 2\pi^3 p(\omega) \ell_t D_0, \quad (5.31)$$

then the diffusion constant is purely imaginary and defines, in the same fashion as in Sec. 5.2.1, a localisation length as

$$\xi = \ell_t \frac{\pi}{2} \frac{1}{1 - 2\pi^3 p(\omega) \ell_t D_0} = \ell_t \frac{\pi}{2} \frac{1}{1 - p(\delta) \rho \ell_t^2 \ell_s 4\pi^3 / 3}. \quad (5.32)$$

If  $1 < 2\pi^3 p(\omega) \ell_t D_0$ , we then obtain a real, yet renormalised diffusion coefficient of the form  $D(\omega) = D_0 - 1/(2\pi^3 p(\omega) \ell_t)$ . This transition from a diffusive (extended) to a localised transport regime is a true phase transition. Equation (5.31) actually defines an Ioffe-Regel criterion for this transition, with a non-trivial frequency dependence through the interplay of  $p(\omega)$ ,  $\ell_t$  and  $D_0$  which all strongly depend on frequency (Sheng, 2006).

The usual Ioffe-Regel criterion ( $k_0 \ell \leq 3/\pi$ ) is recovered by considering a free-space DOS as well as a non-resonant diffusive behaviour such that  $D_0 = \ell_t c/3$ . We then have for the localisation length in non-resonant systems

$$\xi = \ell_t \frac{3}{2} \frac{1}{3/\pi - (k_0 \ell_t)^2}. \quad (5.33)$$

We have derived expressions for the diffusion coefficient, as well as the localisation length which have an explicit dependence on the density of states. In particular, in the event of a pseudo-gap, the localisation length of the 2D system is expected to collapse. Similarly in 3D, a decrease in the DOS should induce a transition towards the localised phase.

## 5.3 Evaluation of the mean free paths

This section will tackle the problem of the computation of both the scattering and transport mean-free paths that enter explicitly in the expressions of the localisation length given in the previous section. We will focus on the problem of 2D vector waves but will try to give, when possible, expressions that will be valid in any dimension.

### 5.3.1 The mean free paths given by the structure factor

The first model to include spatial correlations in the expression of the transport mean free path, was given in Ref. Fraden and Maret (1990); Rojas-Ochoa et al. (2004). In 2D, it takes the form

$$\frac{1}{\ell_t} = \rho \int_0^{2\pi} \frac{d\sigma}{d\theta} S(q) (1 - \cos \theta) d\theta, \quad (5.34)$$

where  $d\sigma/d\theta$  is the differential cross-section of each particle, and  $S(q)$  is the structure factor of the spatially correlated medium. This approach can be formulated in a more modern fashion

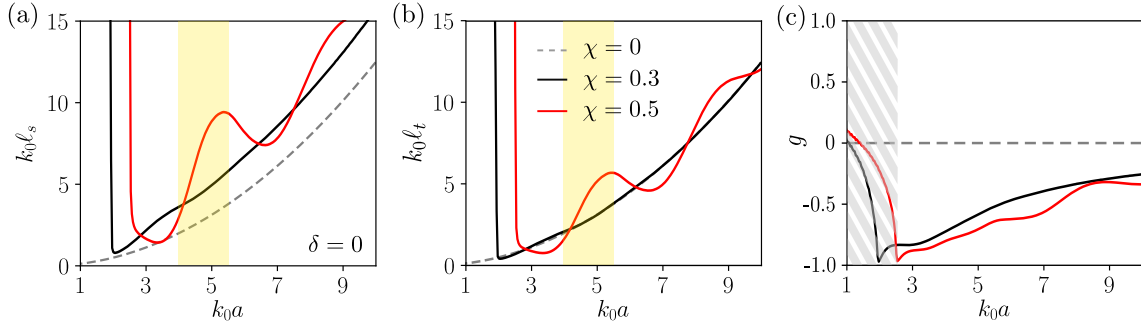


Figure 5.2: Scattering (a) and transport (b) mean free paths of 2D vector waves in SHU systems, between  $k_0 a = 1$  to 10 and at zero detuning ( $\delta = 0$ ). The corresponding anisotropy factor  $g$  is plotted in (c). In each case, the mean free paths have been evaluated at  $\chi = 0, 0.3$  and  $0.5$ . The yellow domain corresponds to the localisation window observed in Chap. 2. The sharp divergence of the mean free paths at high densities corresponds to the stealthy regime characterised by  $k_0 < K/2$ , where  $K$  is the hyperuniformity radius defined in Sec. 2.1.1. The values of  $g$  are not physical past this point and are hashed in grey.

in terms of the irreducible vertex  $\mathbf{U}$ . Transposing the 3D approach developed in Ref. Cherroret et al. (2016) to 2D, we get, in the limit of low number density,

$$\frac{1}{\ell_s} = \frac{\langle U^\perp(k_0 \mathbf{p}, k_0 \mathbf{p}', \omega) \rangle_{\mathbf{p}'}}{4k_0} \quad (5.35)$$

$$\frac{1}{\ell_t} = \frac{\langle (1 - \mathbf{p} \cdot \mathbf{p}') U^\perp(k_0 \mathbf{p}, k_0 \mathbf{p}', \omega) \rangle_{\mathbf{p}'}}{4k_0}, \quad (5.36)$$

with  $U^\perp(k_0 \mathbf{p}, k_0 \mathbf{p}', \omega) = \Delta_{\mathbf{p}}^\perp \cdot \mathbf{U}(k_0 \mathbf{p}, k_0 \mathbf{p}', \omega) \cdot \Delta_{\mathbf{p}'}^\perp = (\Delta_{\mathbf{p}}^\perp)_{ik} U_{ij,kl}(k_0 \mathbf{p}, k_0 \mathbf{p}', \omega) (\Delta_{\mathbf{p}'}^\perp)_{jl}$ , where repeated indices have been summed over. The  $1/4k_0$  is specific to the 2D; it should be replaced by the prefactor  $1/8\pi$  in 3D. Equation (5.34) can be obtained from Eq. (5.36) by including the following scattering events in  $\mathbf{U}$

$$\mathbf{U} = \underbrace{\circ}_{\mathbf{U}_0} + \underbrace{\circ}_{\mathbf{U}_C}. \quad (5.37)$$

Here the first diagram  $\mathbf{U}_0$  represents an elementary scattering process where the field and its conjugate visit the same resonator, whereas  $\mathbf{U}_C$  stands for scattering by two different but spatially correlated resonators through the pair correlation function  $g_2$ . For point-like resonators, we immediately obtain  $\mathbf{U}(k_0 \mathbf{p}, k_0 \mathbf{p}', \omega) = \mathbb{1} \rho |t(\omega)|^2 S(k_0 \mathbf{p} - k_0 \mathbf{p}')$  since  $S(\mathbf{q}) = 1 + \rho h_2(\mathbf{q})$  (cf Eq. (1.75) in Chap. 1). Equations (5.35) and (5.36) take the form

$$\frac{1}{\ell_s} = \frac{\rho |t|^2}{4k_0} \int_0^{2\pi} \frac{d\theta}{2\pi} S\left(2k_0 \left| \sin \frac{\theta}{2} \right| \right) \cos^2 \theta, \quad (5.38)$$

$$\frac{1}{\ell_t} = \frac{\rho |t|^2}{4k_0} \int_0^{2\pi} \frac{d\theta}{2\pi} S\left(2k_0 \left| \sin \frac{\theta}{2} \right| \right) \cos^2 \theta (1 - \cos \theta), \quad (5.39)$$

where we have used the fact that  $(\Delta_{\mathbf{p}}^\perp)_{ik} \mathbb{1}_{ij,kl} (\Delta_{\mathbf{p}'}^\perp)_{jl} = |\mathbf{p} \cdot \mathbf{p}'|^2$ . The values of  $\ell_s$  and  $\ell_t$  computed from Eqs. (5.38) and (5.39) and the numerical value of the structure factor of SHU patterns are given in Fig. 5.2. This model predicts an oscillating behaviour at large  $\chi$  because  $S(\mathbf{q})$  itself presents oscillations. In particular, it gives higher values of the mean free paths in the domain of density parametrised by  $k_0 a$  where we observed localisation. This finding indicates that the reduction of the localisation length is not determined by a reduction of the

mean free path. In particular, it is inconsistent with the expression of the localisation length in non-resonant media given by Eq. (5.28). However it is compatible with the expression for resonant media, given by Eq. (5.27), because of the strong DOS depletion in the range of  $k_0a$  where localisation is observed ( $\xi < R$ , where  $R$  is the system size). In Fig. 5.2, we also show the dependence on  $k_0a$  of the anisotropy factor  $g$ , which quantifies the difference between  $\ell_t$  and  $\ell_s$  through the relation  $\ell_t = \ell_s/(1 - g)$  [see Eq. (1.43)]. We find negative  $g$ , indicating that each scattering process is enhanced in the backward direction in the presence of strong spatial correlations. Similar phenomenon has also been observed in Refs. (Conley et al., 2014; Vynck et al., 2021).

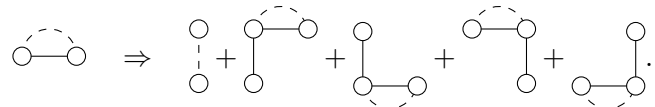
The choice to include in  $\mathbf{U}$  the two diagrams described in Eq. (5.37) only does not constitute a rigorous second-order density expansion, as recurrent scattering can also contribute at this order. Furthermore, this choice is not consistent with the Ward identity which ensures energy conservation in the absence of absorption. The latter relates the components of  $\Sigma$  and  $\mathbf{U}$ ; it is given by (van Tiggelen and Lagendijk, 1994; Lagendijk and van Tiggelen, 1996; Cherroret et al., 2016)

$$\text{Im } \Sigma^\perp(\mathbf{p}, \omega) (\Delta_{\mathbf{p}}^\perp)_{ik} (\Delta_{\mathbf{p}}^\perp)_{jl} = \int \frac{d\mathbf{p}'}{(2\pi)^d} \text{Im } \langle G^\perp(\mathbf{p}') \rangle U_{ij,kl}^\perp(\mathbf{p}, \mathbf{p}', \omega), \quad (5.40)$$

for vector waves. The scalar case is recovered by removing projectors and polarisation indices in this relation. This identity is useful to relate the scattering mean free path obtained through the intensity vertex and to the extinction length of the mean field:

$$\frac{1}{\ell_s} = \frac{\langle U^\perp(k_0\mathbf{p}, k_0\mathbf{p}', \omega) \rangle_{\mathbf{p}'}}{4k_0} = \frac{-\text{Im} [\Sigma^{(\perp)}(q = k_0, \omega)]}{\omega/v_\phi}. \quad (5.41)$$

where  $v_\phi = \omega/q$  is the phase velocity of the wave. This indicates that diagrammatic expansion of  $\Sigma$  and  $\mathbf{U}$  must be performed consistently to obtain reliable results. For correlated systems, we have seen in Chap. 4 that recurrent scattering contributions to  $\Sigma$  was crucial to capture the destructive interference process leading to the DOS depletion. This strongly suggests contributions beyond Eq. (5.37) must also be considered in the evaluation of  $\ell_s$  and  $\ell_t$ . Let us make this statement more precise. For continuous disorder, it can be shown that Eq. (5.41) translates into a direct equivalence between diagrams of  $\Sigma$  and diagrams of  $\mathbf{U}$ . Contrary to the case of particulate disorder we study here, where the Ward identity imposes to use the entire second order expansion for both irreducible operators, with continuous disorder, this consistency condition actually creates an equivalence between subsets diagrams of  $\Sigma$  with another sets in  $\mathbf{U}$  (Vynck et al., 2021). In particular, we have the correspondence



$$\text{Looped diagram} \Rightarrow \text{Diagram 1} + \text{Diagram 2} + \text{Diagram 3} + \text{Diagram 4} + \text{Diagram 5}. \quad (5.42)$$

Hence the first looped diagram of  $\Sigma$  (looped diagram) which plays an important role for the DOS, generates terms for  $\mathbf{U}$  that have not been considered in Eq. (5.37). Previous discussion shows that the evaluation of the mean free paths, requires to perform a proper density expansion of  $\mathbf{U}$  or  $\Sigma$ . While  $\mathbf{U}_C$  is indeed a first correlated contribution to the intensity vertex, it is not the only relevant one. Proper evaluations of  $\ell_s$  and  $\ell_t$  are presented in the next sections.

### 5.3.2 Density expansion of $\ell_s$

We have seen in Eqs. (5.36) and (5.41) that even though the transport mean free path requires the computation of the intensity vertex, the evaluation of  $\ell_s$  can be computed from either  $\mathbf{U}$  or  $\Sigma$ . The intensity vertex is complicated to evaluate as it is a four-rank tensor which contains

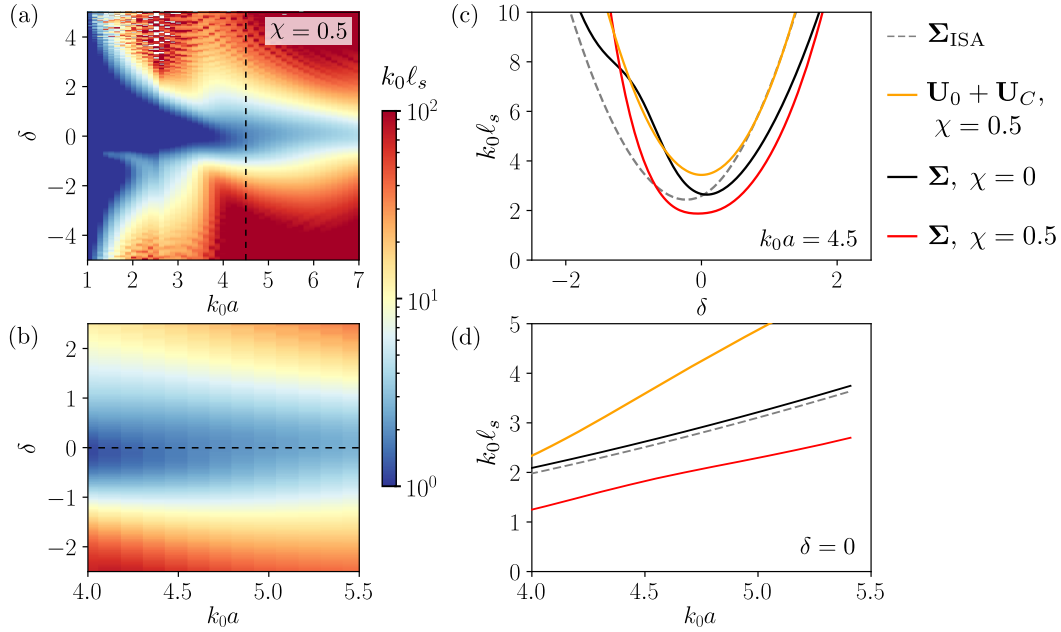


Figure 5.3: Analytical estimates of the scattering mean free path in density-frequency space (a) and a zoom over the localised region (b). We presents cuts of  $\ell_s$  over the detuning at  $k_0 a = 4.5$  (c) and over the densities at  $\delta = 0$  (d). The value computed from  $\Sigma_{\text{ISA}}$  (including the Lorentz-Lorenz term) is plotted in dashed grey line, the values obtained including recurrent scattering in the self-energy, with and without correlations are displayed respectively as red and dark plain lines ( $\Sigma = \Sigma_{\text{ISA}} + \Sigma_C + \Sigma_L + \Sigma_B$ ). As a reference we added the predictions of Eq. (5.38) where the scattering mean free path has been computed using the irreducible vertex as  $\mathbf{U} = \mathbf{U}_0 + \mathbf{U}_C$ , in orange.

more diagrammatic contributions than  $\Sigma$ , as can be seen by using the correspondence principle mentioned in the previous section and resulting from the Ward identity. We will thus compute  $\ell_s$  using the self-energy. On the other hand, the transport mean free path, will be found from  $\ell_s$  and the computation of the anisotropy factor  $g$  which turns out to be simpler than the full computation of  $\ell_t$ .

In the absence of absorption, the scattering mean free path is defined as the attenuation length of ballistic light. As explained in Sec. 1.3.3, only the transverse Green's function  $\langle G^{(\perp)}(\mathbf{q}, \omega) \rangle = [k^2 - q^2 - \Sigma^{(\perp)}(\mathbf{q}, \omega)]^{-1}$  contributes to the computation of  $\ell_s$ . At moderate density, we can replace the self-energy by its *on-shell* value  $\Sigma^{(\perp)}(\mathbf{q}, \omega) \simeq \Sigma^{(\perp)}(|\mathbf{q}| = k, \omega)$ . At second order in density, the inverse scattering mean free path takes the form

$$\frac{1}{\ell_s} = \frac{-\text{Im} [\Sigma^{(\perp)}(q = k_0, \omega)]}{\omega/v_\phi}, \quad (5.43)$$

where  $v_\phi = c \left[ 1 + \text{Re} \Sigma_{\text{ISA}}^{(\perp)}(\omega) \right]$ . Since the self-energy contains both first and second order terms, including only the zeroth and first order term of the phase velocity is enough to obtain the full second order expansion of  $\ell_s$ . More precisely, the phase velocity only contributes to the ISA term, as  $\Sigma$  does not contain a zero-order term.

The expression of each component of  $\Sigma^{(\perp)} = \Sigma_{\text{ISA}}^{(\perp)} + \Sigma_C^{(\perp)} + \Sigma_L^{(\perp)} + \Sigma_B^{(\perp)}$  has already been computed in Secs. 4.4.5, 4.4.6 and 4.4.7, for the evaluation of the density of states. But now, instead of evaluating the self-energy in the large wavevector limit, we take its value *on-shell*. The dependence of  $\ell_s$  on detuning and density, in correlated SHU systems excited with TE modes, is presented in Fig. 5.3. Cuts along  $k_0 a = 4.5$  (where localisation occurs) and  $\delta = 0$  are

also shown in Fig. 5.3 (c) and (d). Predictions based on  $\Sigma$  at  $\chi = 0.5$  (red line) are compared with the result of Eq. (5.38). For reference, we also show the result based on  $\Sigma$  at  $\chi = 0$  (black line), as well as the ISA approximation (dashed line). Rather counter-intuitively, the positive contribution of the spatial correlation (orange line) is balanced by the recurrent scattering diagrams and the overall mean free path (red line) ends up smaller than its ISA value. This result shows that the commonly accepted expression of Eq. (5.38) gives incorrect predictions; it predicts that correlations should increase the mean free path whereas a rigorous density expansion predicts a reduction of  $\ell_s$ .

### 5.3.3 Density expansion of $\ell_t$

We recall that the transport mean free path  $\ell_t$  can be linked to the scattering mean free path  $\ell_s$  through the anisotropy factor  $g$ . In 2D, it is given by

$$\frac{1}{\ell_t} = \frac{1-g}{\ell_s} = \frac{\langle (1 - \hat{\mathbf{q}} \cdot \hat{\mathbf{q}}') U^\perp(k_0 \hat{\mathbf{q}}, k_0 \hat{\mathbf{q}}', \omega) \rangle_{\hat{\mathbf{q}}'}}{4k_0}, \quad (5.44)$$

where  $\hat{\mathbf{q}} = \mathbf{q}/q$  with  $q = k_0$ ,  $\langle \dots \rangle_{\hat{\mathbf{q}}'}$  denotes an average over the direction of  $\hat{\mathbf{q}}'$ , and  $U^\perp(\mathbf{q}, \mathbf{q}', \omega) = \sum_{i,j,k,l} \Delta_{\mathbf{q},ij}^\perp U_{ij,kl}(\mathbf{q}, \mathbf{q}', \omega) \Delta_{\mathbf{q}',kl}^\perp$  is the transverse part of the irreducible vertex  $\mathbf{U}(\mathbf{q}, \mathbf{q}', \omega)$ . Here, we are specifically interested in the anisotropy factor evaluated on the shell  $|\mathbf{q}| = k_0$ , which reads

$$g = \ell_s \frac{\langle \hat{\mathbf{q}} \cdot \hat{\mathbf{q}}' U^\perp(k_0 \hat{\mathbf{q}}, k_0 \hat{\mathbf{q}}', \omega) \rangle_{\hat{\mathbf{q}}'}}{4k_0}, \quad (5.45)$$

where  $\ell_s$  is given by Eq. (5.43). At the second order in density, the angular average in the numerator of Eq. (5.45) has non-zero contributions only for correlated or recurrent scattering events which accumulate a phase difference between the propagating field and its conjugate. Among the many possible families of diagrams at second order, only the following ones contribute to  $g$  (van Tiggelen and Lagendijk, 1994; Cherroret et al., 2016):

$$\mathbf{U}_C = \begin{array}{c} \circ \\ | \\ \circ \end{array} \quad (5.46)$$

$$\begin{aligned} \mathbf{U}_L = & \begin{array}{c} \circ \text{---} \circ \text{---} \circ \\ | \\ \circ \end{array} + \begin{array}{c} \circ \text{---} \circ \text{---} \circ \\ | \\ \circ \end{array} + \begin{array}{c} \circ \text{---} \circ \text{---} \circ \text{---} \circ \\ | \\ \circ \end{array} + \begin{array}{c} \circ \text{---} \circ \text{---} \circ \text{---} \circ \\ | \\ \circ \end{array} + \dots + c.c. \\ & + \begin{array}{c} \circ \text{---} \circ \text{---} \circ \\ | \\ \circ \end{array} + \begin{array}{c} \circ \text{---} \circ \text{---} \circ \\ | \\ \circ \end{array} + \begin{array}{c} \circ \text{---} \circ \text{---} \circ \\ | \\ \circ \end{array} + \begin{array}{c} \circ \text{---} \circ \text{---} \circ \\ | \\ \circ \end{array} + \dots + c.c. \end{aligned} \quad (5.47)$$

$$\mathbf{U}_B = \begin{array}{c} \circ \text{---} \circ \\ | \\ \circ \end{array} + \begin{array}{c} \circ \text{---} \circ \\ | \\ \circ \end{array} + \begin{array}{c} \circ \text{---} \circ \text{---} \circ \\ | \\ \circ \end{array} + \begin{array}{c} \circ \text{---} \circ \text{---} \circ \\ | \\ \circ \end{array} + \begin{array}{c} \circ \text{---} \circ \text{---} \circ \\ | \\ \circ \end{array} + \dots + c.c. \quad (5.48)$$

where the notations are identical to those used in Eq. (4.30), with the upper and lower lines accounting for the propagating field and its conjugate, respectively. We recognise  $\mathbf{U}_C$ , already used in Eq. (5.37), and then two families of events where each field (top and bottom) undergoes recurrent scattering events.

Explicitly, the first term reads

$$\mathbf{U}_C(\mathbf{q}, \mathbf{q}', \omega) = \rho^2 |t(\omega)|^2 h_2(\mathbf{q} - \mathbf{q}') \mathbf{1}, \quad (5.49)$$

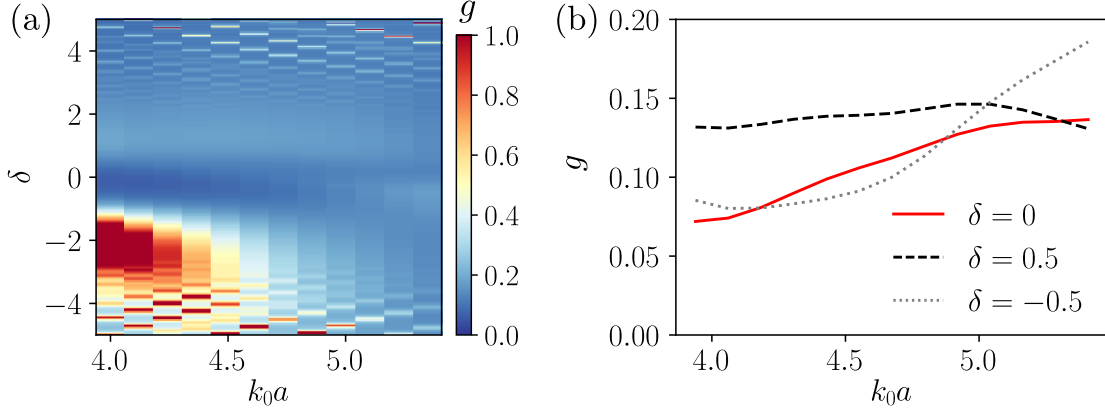


Figure 5.4: (a) Anisotropy factor  $g$  for TE waves propagating in a highly correlated ensemble of resonators ( $\chi = 0.5$ ) over the density ( $k_0a = 4$  to  $5.5$ ) and the detuning ( $\delta = -2.5$  to  $2.5$ ), and (b) cuts over the detuning  $\delta = 0$  (solid red line),  $\delta = 0.5$  (dashed black line), and  $\delta = -0.5$  (dotted grey line). The anisotropy factor fluctuates between 0.05 and 0.2 in the density window where localisation is prominent (see Fig. 5.12).

so that the angular average of its transverse part can be written in the form

$$\langle \hat{\mathbf{q}} \cdot \hat{\mathbf{q}}' U_C^\perp(\mathbf{q}, \mathbf{q}', \omega) \rangle_{\hat{\mathbf{q}}'} = \rho |t(\omega)|^2 \int_0^{2\pi} \frac{d\theta}{2\pi} h_2(2q |\sin(\theta/2)|) \cos^3 \theta. \quad (5.50)$$

The next terms,  $\mathbf{U}_L$  and  $\mathbf{U}_B$  are named *loop* and *boomerang* since the field and its conjugate follow looped or boomerang sequences exclusively. They read

$$\mathbf{U}_L(\mathbf{q}, \mathbf{q}', \omega) = \rho^2 |t(\omega)|^2 \int d\mathbf{r} [1 + h_2(r)] e^{i(\mathbf{q}-\mathbf{q}') \cdot \mathbf{r}} \left\{ \frac{\mathbb{1}}{[\mathbb{1} - t(\omega)^2 \mathbf{G}_0(\mathbf{r}, \omega_0)^2] \otimes [\mathbb{1} - t(\omega)^2 \mathbf{G}_0(\mathbf{r}, \omega_0)^2]^*} - \mathbb{1} \right\}, \quad (5.51)$$

$$\mathbf{U}_B(\mathbf{q}, \mathbf{q}', \omega) = \rho^2 |t(\omega)|^4 \int d\mathbf{r} [1 + h_2(r)] e^{i(\mathbf{q}+\mathbf{q}') \cdot \mathbf{r}} \frac{\mathbf{G}_0(\mathbf{r}, \omega_0) \otimes \mathbf{G}_0^*(\mathbf{r}, \omega_0)}{[\mathbb{1} - t(\omega)^2 \mathbf{G}_0(\mathbf{r}, \omega_0)^2] \otimes [\mathbb{1} - t(\omega)^2 \mathbf{G}_0(\mathbf{r}, \omega_0)^2]^*}. \quad (5.52)$$

The angular integrations over the directions of  $\mathbf{r}$  and  $\hat{\mathbf{q}}$  that appear in  $\langle \hat{\mathbf{q}} \cdot \hat{\mathbf{q}}' U_L^\perp(\mathbf{q}, \mathbf{q}', \omega) \rangle_{\hat{\mathbf{q}}'}$  and  $\langle \hat{\mathbf{q}} \cdot \hat{\mathbf{q}}' U_B^\perp(\mathbf{q}, \mathbf{q}', \omega) \rangle_{\hat{\mathbf{q}}'}$  can be performed using the decomposition defined by Eq. (4.28) and the relation Eq. (4.48). After a lengthy calculation, we find

$$\langle \hat{\mathbf{q}} \cdot \hat{\mathbf{q}}' U_L^\perp(\mathbf{q}, \mathbf{q}', \omega) \rangle_{\hat{\mathbf{q}}'} = -\rho^2 |t(\omega)|^2 \int_0^\infty dr r [1 + h_2(r)] \left\{ A(qr) \left| \frac{1}{1 - t(\omega)^2 G_0^t(r, \omega_0)^2} \right|^2 \right. \\ \left. + B(qr) \left| \frac{1}{1 - t(\omega)^2 G_0^l(r, \omega_0)^2} \right|^2 + 2C(qr) \operatorname{Re} \left[ \left( \frac{1}{1 - t(\omega)^2 G_0^t(r, \omega_0)^2} \right) \left( \frac{1}{1 - t(\omega)^2 G_0^l(r, \omega_0)^2} \right)^* \right] - D(qr) \right\}, \quad (5.53)$$

$$\langle \hat{\mathbf{q}} \cdot \hat{\mathbf{q}}' U_B^\perp(\mathbf{q}, \mathbf{q}', \omega) \rangle_{\hat{\mathbf{q}}'} = \rho^2 |t(\omega)|^4 \int_0^\infty dr r [1 + h_2(r)] \left\{ A(qr) \left| \frac{G_0^t(r, \omega_0)}{1 - t(\omega)^2 G_0^t(r, \omega_0)^2} \right|^2 \right. \\ \left. + B(qr) \left| \frac{G_0^l(r, \omega_0)}{1 - t(\omega)^2 G_0^l(r, \omega_0)^2} \right|^2 + 2C(qr) \operatorname{Re} \left[ \left( \frac{G_0^t(r, \omega_0)}{1 - t(\omega)^2 G_0^t(r, \omega_0)^2} \right) \left( \frac{G_0^l(r, \omega_0)}{1 - t(\omega)^2 G_0^l(r, \omega_0)^2} \right)^* \right] \right\}, \quad (5.54)$$

where  $A(x) = -2\pi [J_2(x) - xJ_1(x)]^2/x^2$ ,  $B(x) = C(x) = -2\pi J_2(x)^2/x^2$ ,  $D(x) = A(x) + 3B(x)$ , and  $J_1(x)$  and  $J_2(x)$  are Bessel functions of the first kind. We note that the remaining integration over  $r$  is not convergent for  $r \rightarrow \infty$  because of the term  $rA(qr)|G_0^t(r, \omega_0)|^2 \sim \cos(kr)^2/r$ . We regularise this logarithmic divergence by replacing the free space Green's function  $G_0^t(r, \omega_0)$  with the far-field expansion of the average Green's function,  $\langle G^t(r, \omega_0) \rangle \simeq G_0^t(r, \omega_0)e^{-r/2\ell_s}$ . It amounts at artificially including more diagrams in the irreducible vertex in order to force the convergence of the integral.

We show in Fig. 5.4 the anisotropy factor  $g$  evaluated from Eq. (5.43) and Eq. (5.45) with  $U^\perp = U_C^\perp + U_B^\perp + U_L^\perp$ , for the range of density where localisation is noticeable in our finite-size 2D simulations and different values of detuning  $\delta$ . In particular, at resonance ( $\delta = 0$ ), we find  $g \sim 0.07 - 0.13$ , which gives  $\ell_t \sim 1.07 - 1.15 \ell_s$ . Note the important difference between this result and the one presented in Fig. 5.2, which only included the contribution of  $\mathbf{U}_C$  in  $g$ : the addition of the recurrent scattering contributions,  $\mathbf{U}_B$  and  $\mathbf{U}_L$ , make now  $g$  slightly positive, which corresponds to an enhanced forward scattering situation.

### 5.3.4 Impact of the mean free path on the localisation length

We have evaluated theoretically both the scattering and the transport mean free path in Sec. (5.3.2) and 5.3.3 through a second order-density expansion of both the self-energy and the intensity vertex. The motivation was to understand their role in the localisation observed for 2D TE waves at intermediate density: is localisation triggered by a reduction of  $\ell_t$  and  $\ell_s$ ? Indeed, if we rely on the commonly accepted expression for the localisation length [see Eq. (5.28)], the only way to get  $\xi$  smaller than the system size is to reduce  $\ell_t$ . This is the argument developed in Ref. Laurent et al. (2007a); Conley et al. (2014). However, the fine analysis of  $\ell_s$  and  $\ell_t$  does not reveal any strong reduction at intermediate density. Equation (5.34) actually predicts the opposite (see Fig. 5.2), while a better model based on Eq. (5.41) and (5.42) shows a moderate reduction of  $\ell_s$  and  $\ell_t$  with respect to the case without correlation and a monotonic behaviour as function of density (Figs. 5.3 and 5.4). This confirms the idea that in resonant materials, we must rely on the expression (5.27) for the localisation length, which presents an explicit dependence on the DOS.

Equation (5.27) seems to explain localisation of 2D vector waves by a collapse of the localisation length triggered by the emergence of pseudo-gaps due to correlations. To support this explanation, we will now evaluate the localisation length as well as  $\ell_s$  numerically.

## 5.4 Evaluation of $\xi$ and $\ell_s$ from numerical simulation

We present two methods to estimate numerically the localisation length. The first one is an *ab initio* numerical simulation where  $\xi$  is estimated using fits of the attenuation of the intensity through a slab. While the second one directly fits the profile of the modes obtained from the coupled-dipole method.

### 5.4.1 Evaluation of $\xi$ and $\ell_s$ from transport simulation

#### Transmission through a slab

The numerical estimation of the scattering mean-free path  $\ell_s$  and of the localisation length  $\xi$  is performed through *ab initio* computations using the coupled-dipole method. We place a SHU pattern into a rectangle of length  $L$  (typically  $kL \in [10, 60]$ , with  $k = \omega/c$ ) and transverse size  $D$ . In order to mimic a slab geometry, which is the most convenient geometry to have access to estimates of  $\ell_s$  and  $\xi$ , we choose  $D \gg L$  (typically  $D = 20L$ , see Fig. 5.5). This



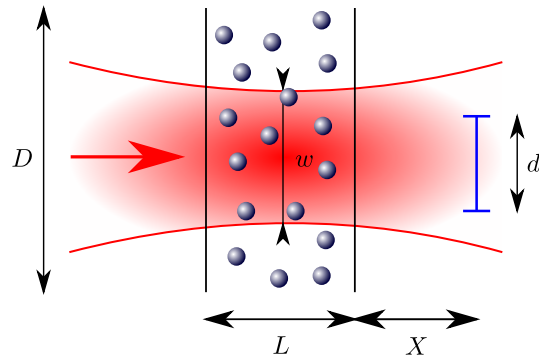


Figure 5.5: Numerical setup used to estimate  $\ell_s$  and  $\xi$ . Red: gaussian beam illuminating the medium. Blue: screen on which the transmitted field is computed.

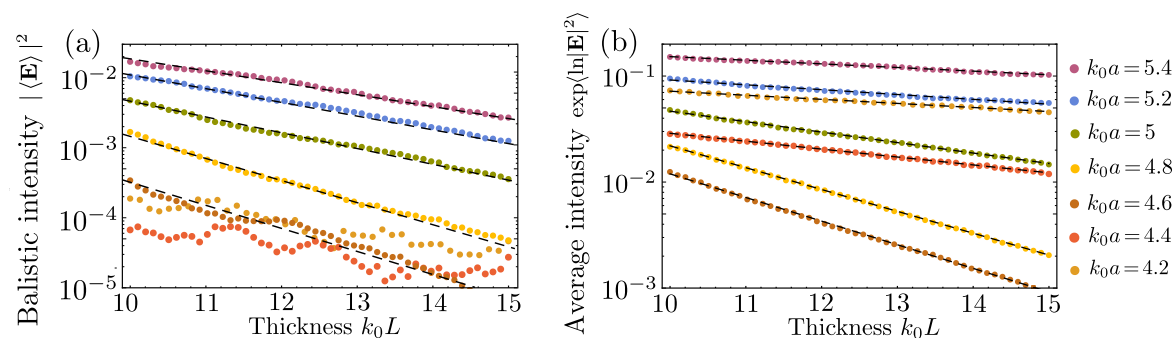


Figure 5.6: Intensity of the average field (a) and mean of the intensity logarithm (b) for strongly correlated SHU slabs at  $\chi = 0.5$  as function of the slab thickness. The scatterer density is varied from  $k_0 a = 4.2$  to  $k_0 a = 5.4$ . The markers show the raw data, while the dashed lines display the best exponential fit for each set of points. For  $k_0 a < 4.6$ , mean field data are too noisy to extract a reliable  $\ell_s$ .

system is shined using a gaussian beam of waist  $w \gg \lambda$  (typically  $kw = 200$ ) given by

$$\mathbf{E}(\mathbf{r}, \omega) = \frac{\mathbf{E}_0}{\sqrt{1 + i\alpha}} \exp \left[ ikx - \frac{y^2}{w^2(1 + i\alpha)} \right] \quad (5.55)$$

for TE waves.  $\mathbf{E}_0$  is the amplitude and  $\alpha = 2x/(kw^2)$ . This specific illumination is chosen such that it smoothes the transverse finite-size effects. The transmitted electric field is computed for each disordered configurations on a screen of size  $d$  lying at a distance  $X$  from the output interface of the slab. We take  $X > \lambda$  (typically  $kX = 10$ ) in order to avoid potential near-field effects close to the interface.

### Fitting procedure and results

In order to estimate  $\ell_s$ , we average the transmitted field over many SHU configurations. To accelerate the numerical convergence, we also perform a spatial average over the observation screen assuming ergodicity and a size  $d > \lambda$  (typically  $kd = 10$ ). Then we compute the intensity of this average field and perform a fit with the formula

$$|\langle \mathbf{E} \rangle|^2 = A \exp \left[ -\frac{L}{\ell_s} \right] \quad (5.56)$$

as a function of the thickness of the slab  $L$ .  $A$  and  $\ell_s$  are the fitted parameters.

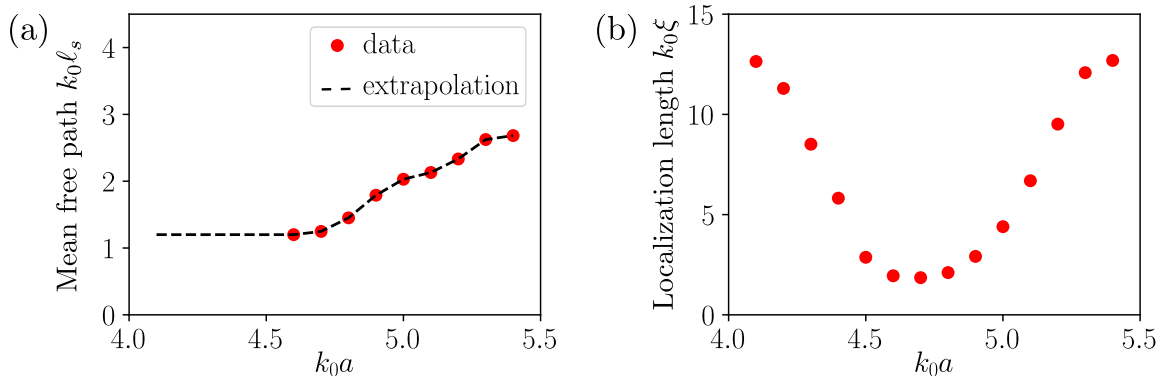


Figure 5.7: Value of the scattering mean free path (a) and of the localisation length (b) obtained from an exponential fit of the data shown in Fig. 5.6. Due to the fluctuations in the mean field data below  $k_0 a = 4.5$ , we extrapolated the last trustworthy value around  $k_0 a = 4.6$ . It is shown as a dashed line.

The estimation of the localisation length  $\xi$  is performed from the fit of the average of the intensity logarithm as a function of  $L$ . The fitting formula is given by

$$\langle \ln |\mathbf{E}|^2 \rangle = B - \frac{L}{\xi} \quad (5.57)$$

where  $B$  and  $\xi$  are the fitted parameters.

Some of the numerical results are shown in Fig. 5.6. Both  $\langle E \rangle$  and  $\exp(\langle \ln |\mathbf{E}|^2 \rangle)$  display a clear exponential profile as function of the thickness  $L$ , apart for  $\langle E \rangle$  at  $k_0 a < 4.6$ . The values obtained from the fit are summarised in Fig. 5.7. The mean free path, of the order of the wave-length, is very small in these systems. The fluctuations found for  $\langle E \rangle$  versus  $L$  at  $k_0 a < 4.6$  do not allow to extract a value for  $\ell_s$ . We cannot attribute these fluctuations to noise only because smaller and less fluctuating signals have been measured at higher  $k_0 a$ . We think that these fluctuations are associated to a break-down of the on-shell approximation of the self-energy at large density. In that case, the dielectric constant of the effective medium is non-local and the extinction of the ballistic component is no more exponential. On the other hand, we find that the transport localisation length is strongly reduced in the regime of density identified in Chap. 2 as the localisation domain through the study of the smallest collective decay rates.

#### 5.4.2 Evaluation of $\xi$ from the eigenvectors

To further validate the previous results, we also directly evaluate the localisation length from the spatial attenuation of the eigenmodes of the effective Hamiltonian introduced in Eq. (1.48).

##### Shape of the modes

The eigenmodes of the effective Hamiltonian (1.48) are defined at the dipole locations only. However, we can find the field radiated by these collective excitations anywhere inside the system by solving Eq. (1.45). In this way, we obtain the intensity maps shown in Fig. 5.8 (a-d). This procedure is tedious and computationally expensive. We see in Fig. 5.8 (e-h) that we can work directly with the eigenvectors instead of the radiated fields, as they share the same spatial profiles.

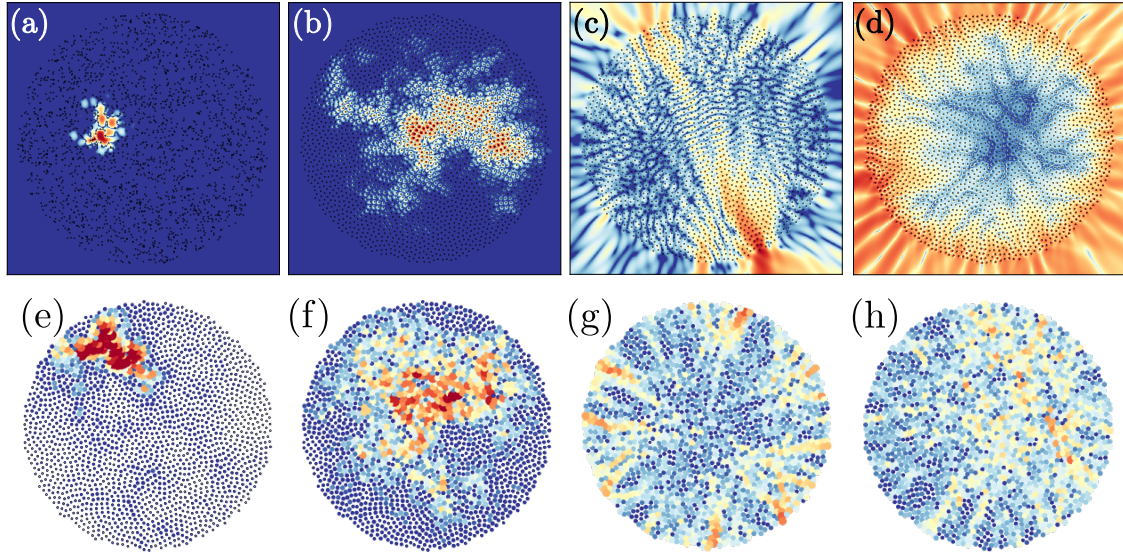


Figure 5.8: (a-d) Intensity maps produced by exciting selectively the eigenmodes of the Hamiltonian (1.48). (e-h) Plot of the magnitude of the eigenvectors of the same Hamiltonian but for different modes. In these 2D simulations,  $k_0a = 2$  and  $\chi = 0.5$ . The localised eigenmode (e) corresponds to a TM polarisation and eigenmodes (f-h) to a TE polarisation.

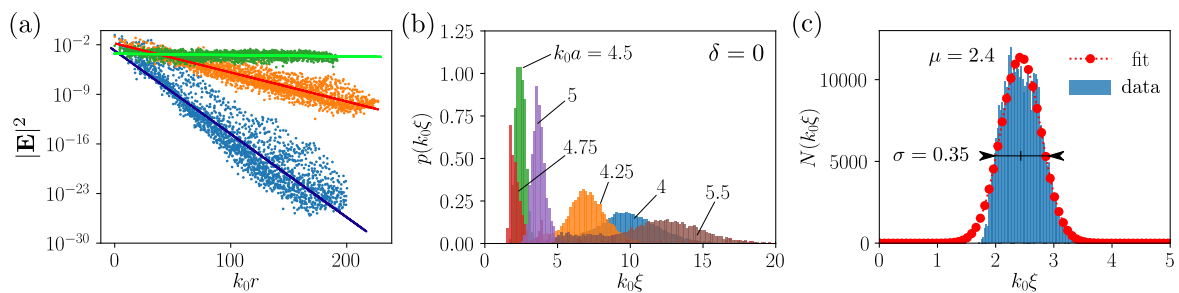


Figure 5.9: (a) Intensity of some typical eigenmodes of the effective Hamiltonian, plotted as function of the distance to their maximum value, with the best exponential fit. (b) Normalised distributions of the localisation lengths for densities ranging from  $k_0a = 4$  to 5.5, using values for  $\delta \in [-0.05, 0.05]$ . (c) Each distribution is fitted using a Gaussian kernel to estimate the most probable value ( $\mu$ ) of  $k_0\xi$  and the standard deviation ( $\sigma$ ). The data are shown as a blue histogram and the best fit is shown in red markers.

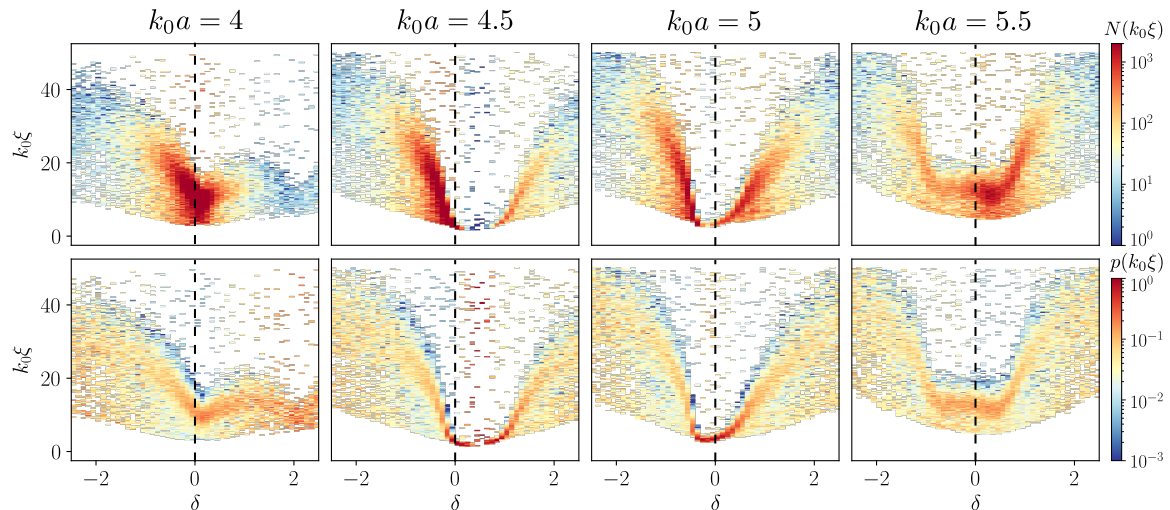


Figure 5.10: (Top): Histograms of the localisation lengths  $k_0\xi$  for different  $\delta$  and  $k_0a$  in TE polarisation. (Bottom) Distribution of localisation length in each frequency window, normalised to unity.

### Evaluation of $\xi$ from the eigenvectors

To extract a localisation length from the eigenvectors, we plot for each mode the intensity as a function of the distance to the maximum of the mode. We obtain for modes localised in the bulk [see Fig. 5.8 (a),(e)] a strong exponential decay with the distance, as shown in Fig. 5.9. Modes localised on the edges [see Fig. 5.8 (c),(g)], will have a different localisation length than the bulk ones [see Maximo et al. (2019)]. Their proportion in large systems is small and we will disregard their contributions. Only modes fully delocalised [see Fig. 5.8 (d),(h)], will display no decay. The three situations are summarised in Fig. 5.9 (a).

We thus blindly fit the eigenvectors profile by a exponentially decaying function and obtain for each set of densities and frequencies, an ensemble of localisation lengths. The distributions of  $k_0\xi$  for  $k_0a$  between 4 and 5.5 associated to modes near  $\delta = 0$  is shown in Fig. 5.9. They are all rather narrow and do not extend further than  $k_0\xi = 50$  which is smaller than the system size,  $100 < k_0R < 140$ . Distributions for different detunings are also shown in Fig. 5.10. They collapse towards low values of  $k_0\xi$ , for the same range of parameters where the linewidth  $\gamma$  of the collective modes drops (see Chap. 2). The participation of each mode in the transport decays with the detuning from the source (Guerin and Kaiser, 2017) indicating that we can focus on small frequency windows.

The most probable values of the localisation length are obtained through a Gaussian deconvolution of the distributions as shown in Fig. 5.10 (c). The results for different  $k_0a$  and  $\delta$  are shown in Fig. 5.11. The localisation length is minimum in a domain of density and detuning that coincides with the pseudo-gap in the density of states observed in Fig. 2.21.

We have computed the localisation length in strongly correlated SHU patterns from two different approaches. One uses the statistical properties of the average transmitted intensity, while the other performs a direct estimate from the eigenmodes of the system. In the following we will compare these values to the theory developed in Sec. 5.2. We can use the scattering mean free path obtained from the transport simulation, but we still need a way to evaluate the transport mean free path  $\ell_t$ . For practical reasons, we decided to evaluate it numerically.

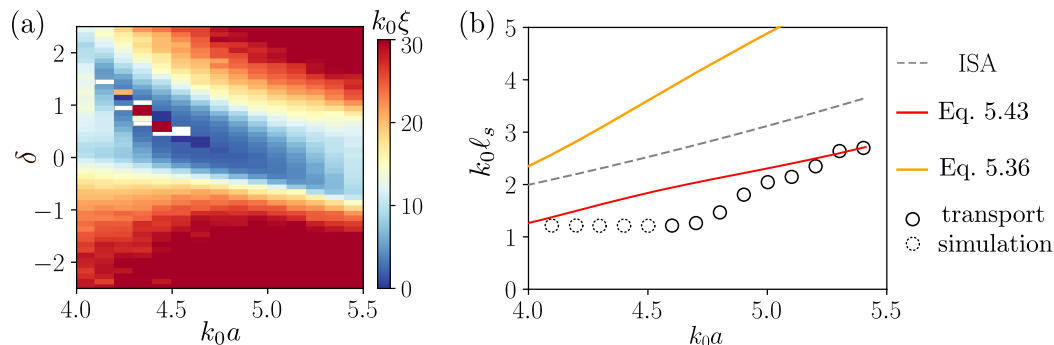


Figure 5.11: (a) Map of the localisation length obtained using the method described in Fig. 5.9, (c), for  $k_0 a$  in the range 4 to 5.5 and a detuning smaller than 2.5 in the TE polarisation. The island of larger values in the small  $k_0 \xi$  area accounts for the full band gap, where no bulk mode exists, not even localised ones, and only extended edge modes are present. (b) Comparison between the different estimates for the scattering mean free path between analytical predictions using  $\Sigma_{\text{ISA}}$  in dashed grey line, Eq. (5.37) in plain orange line and the complete second order expansion of  $\Sigma$  including recurrent scattering in red, and the results of transport simulations described in Sec. 5.4.1 in (dark markers). The dashed markers denotes the values for which we extrapolated the last clean value of the scattering mean free path.

## 5.5 Comparison between theory and numerics

Our objective is to compare the prediction (5.27) for the localisation length with simulations. Since Eq. (5.27) is expressed in terms of  $l_s$ , we first compare our model for  $l_s$  with numerical values found from a fit of the mean field (see Sec. 5.3). Figure 5.11(b) shows a relatively good agreement with Eq. (5.43), but is not fully quantitative. In the following, we thus evaluate Eq. (5.27) with the numerical values of  $l_s$ , and the theoretical value of  $g$  [see Eq. (5.45)]. In Fig. 5.12 we compare numerical values of  $\xi$  with the non-resonant prediction [Eq. (5.28)] and the resonant one [Eq. (5.27)]. The prediction based on Eq. (5.28), fails at describing the localisation, predicting values an order of magnitude larger than the two independent numerical computations of  $\xi$ . The situation where  $k_0 l_t$  has been replaced by  $k_0 l_s$  is shown in Fig. 5.12(a), to show that the mismatch cannot be due to an error in  $g$ . The model nonetheless predicts a dip in the localisation lengths of the system, but not much else.

On the other hand the formula (5.27), shows an excellent agreement between both simulations which gives very similar values. The concordance between all of them is especially impressive in the middle of the localised domain, where they are almost indistinguishable. This domain is also the same where  $p(\delta)$  exhibits a pseudo-gap confirming the critical dependence of  $\xi$  on  $p(\delta)$ . Hence, formula (5.27) justifies quantitatively why localised states form when the DOS is depleted.

## 5.6 Conclusion

In this chapter we presented the relation between the density of states and the localisation properties in a resonant medium. An analysis of the propagation including the fields polarisations concluded that long range diffusion is preserved. Using a frequency-dependent self-consistent approach to the diffusion theory adapted to resonant systems, we obtained a diffusion coefficient depending on the density of states and the scattering and transport mean free paths. We recovered in the long time limit the localisation behaviour observed in non resonant media. The 3D Ioffe-Regel criterion, along with the localisation length predicted by the theory now both explicitly depend on the density of states, favouring localisation in

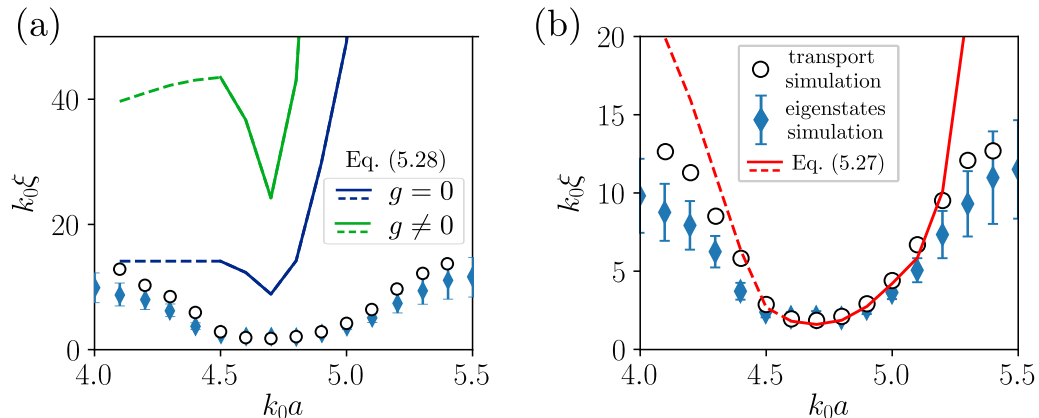


Figure 5.12: Comparison between the localisation lengths  $\xi$  obtained from transport simulation (open circles, Sec. 5.4.1) and from the eigenstate profile (filled diamonds with error bars, Sec. 5.4.2), with the non resonant formula (5.28) (a) (solid and dashed line) and with the resonant one Eq. (5.27) (b), in an ensemble of correlated resonant dipoles ( $\chi = 0.5$ ,  $\delta = 0$ ) and illuminated with TE polarisation in 2D. The localisation length is strongly reduced when the DOS  $p(\delta)$  is depleted. In both cases,  $\ell_t$  has been computed using the numerical values inferred from the transport simulation, and the analytical anisotropy factor  $g$ . For the density of states  $p(\delta)$ , appearing in Eq. (5.27), we used the numerical values obtained from the Green's matrix spectra. For  $k_0a < 4.6$ , reliable values of  $\ell_s$  cannot be found, which is attributed to non-locality of the effective dielectric constant (see text for details); the value of  $\ell_s$  obtained at  $k_0a = 4.6$  is thus extrapolated to get  $\xi$  at lower  $k_0a$  (dashed line). Details about transport simulation and eigenstate analysis are given in Secs. 5.4.2 and 5.4.

the presence of a pseudo-gap. We tested this dependence numerically in 2D in the TE polarisation, with a transport simulation estimating from the decay of the mean field and the average intensity, the scattering mean free path and the localisation length respectively. The latter have been compared with direct estimates of the localisation length of the eigenstates of our Hamiltonian. Without a convenient way to measure the transport mean free path, we used the numerical value of the scattering mean free path with the theoretical expression of the anisotropy factor. We obtain quantitative agreement between both simulations and the analytical expression over the TE gap region. A comparison with the non resonant model proves that the changes in the transport mean free path due to the spatial correlation is not the main drive for the localisation, but rather the changes in the DOS.



## Chapter 6

# Towards an experimental validation

This chapter will summarise our first attempts to experimentally validate some of the observations made in the previous chapters. The correlation-driven intermediate density gap observed in 2D systems with vector coupling is in this regard particularly interesting as we also expect strongly localised modes in its vicinity.

We will show how a waveguide geometry can mimic a two-dimensional setup in the microwave regime and how the TE polarisation is not required to exhibit vector coupling. The resonators modelled in the previous chapters are chosen as high-index ceramics cylinders. We will work in the TM polarisation which is the only one propagating at large scale in a metallic waveguide at the target frequencies, and will take advantage of the multiple Mie resonances of ceramics resonators to obtain both the scalar and the vector behaviour in a single setup.

Similar experiments have been already carried out in Ref. Dalichaouch et al. (1991) and more recently in Ref. Aubry et al. (2020) showing interesting results regarding Anderson localisation. The second reference characterizes the different transport regimes that can be achieved by tuning the frequency near a bandgap induced by spatial correlations. Yet, these two references do not emphasize the important role of the individual Mie resonances in the collective scattering process and do not discuss the qualitative differences between scalar and vector coupling identified in the previous chapters.

One objective of this chapter is to convince the reader that the collective resonance framework used throughout this manuscript is relevant in the case of finite-sized dielectric objects.

### 6.1 Two-dimensional propagation in a waveguide

To realise a 2D system, one needs to obtain a translationally invariant setup. The invariance direction will be taken as a reference and be labelled as the transverse direction. It could be reached by using long cylinders, which is unpractical as it requires bulky setups, especially in a direction without physical interest. Another and more judicious solution is to impose continuity boundary conditions that mimic an infinite system. This is easily reached using a thin waveguide geometry.

Between two parallel metallic plates, electromagnetic wave propagation is strongly constrained by the interface conditions of the metal. The field is found to propagate in two independent polarisations: called the TM polarisation where the electric and magnetic fields are respectively transverse and aligned with the plates, and conversely in the TE polarisation. Continuity of the tangential component of the electric field at the interfaces imposes a node of the electric field near the metal in TE, but not in TM where a mode of constant amplitude along the transverse direction exists. The dispersion relation of electromagnetic waves in an empty waveguide takes the form

$$\frac{\omega}{c} = \sqrt{q_{\parallel}^2 + \left(\frac{m\pi}{h}\right)^2}, \quad (6.1)$$



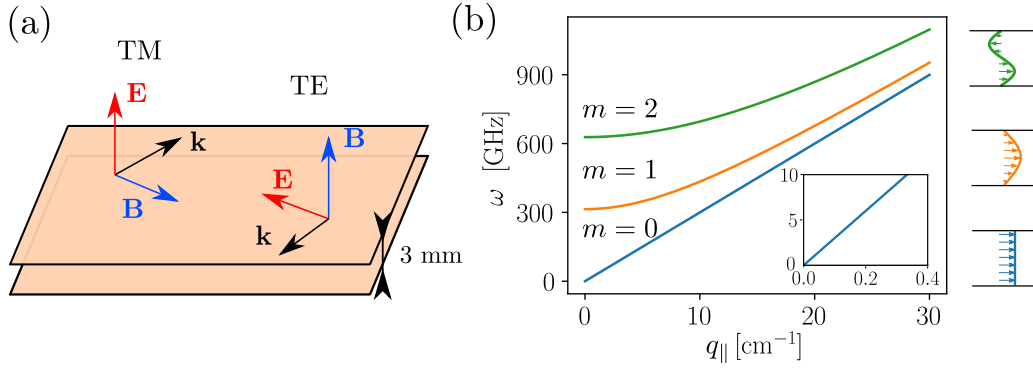


Figure 6.1: (a) Figurative representation of the 2D waveguide used for experiments. In the TM polarisation, the electric and magnetic fields are oriented respectively out-of and in-plane; in the TE polarisation, this is the opposite. (b) Dispersion relation of the planar waveguide shown in Fig. (a) for 0, 1 and 2 nodes in the transverse direction with for each, a different cut-off frequency. The mode  $m = 0$  only exists in the TM polarisation. The inset shows a zoom over the 0 to 10 GHz frequency range which contains only a zero-order TM mode.

where  $q_{\parallel}$  is the in-plane projection of the wave-vector,  $h$  is the distance between the two plates and  $m$  is an integer ( $m \neq 0$  in TE). The TM polarisation in the range of frequencies below the first TE mode at  $\omega_{\text{TE}} = \pi c/h$  can be used to study wave propagation in 2D. The dispersion relation in a waveguide of width 3 mm is shown in Fig. 6.1 (b).

## 6.2 Resonance of high dielectric cylinders and the coupled dipole approach

Most of this thesis deals with highly resonant object which can be described either by a monopolar resonance, or by a dipolar one. Cold atoms provide a very good experimental platform, but arranging cold atoms in 2D SHU patterns is obviously experimentally challenging. We will prefer high index ceramic objects which exhibit Mie resonances.

We chose dielectric cylinders of BaSmTi-oxide, of 4 mm diameter, 3 mm height and  $\varepsilon = 78$  marketed by Exxelia. They host strong Mie resonances whose scattering efficiency can be computed using standard harmonic expansion (Bohren and Huffman, 1993). The Mie series relies on a cylindrical harmonics expansion defined as

$$\mathbf{E}_s = - \sum_{n \in \mathbb{Z}} E_n [b_n \mathbf{N}_n + ia_n \mathbf{M}_n], \quad (6.2)$$

$$\mathbf{H}_s = \frac{ik}{\omega\mu} \sum_{n \in \mathbb{Z}} E_n [b_n \mathbf{M}_n + ia_n \mathbf{N}_n]. \quad (6.3)$$

Here  $\mathbf{E}_s$  and  $\mathbf{H}_s$  are the scattered electric and magnetic fields and  $\mathbf{M}_n$  and  $\mathbf{N}_n$  are the cylindrical harmonics defined by the relations

$$\mathbf{M}_n = \nabla \times (\hat{\mathbf{e}}_z \psi_n), \quad \mathbf{N}_n = \frac{\nabla \times \mathbf{M}_n}{k}, \quad \psi_n = Z_n(kr) e^{in\phi} \quad (6.4)$$

where  $\hat{\mathbf{e}}_z$  is the unit vector along the transverse direction and  $Z_n$  a solution of the Bessel equation  $u \frac{d}{du} \left( u \frac{d}{du} Z_n(u) \right) + (u^2 - n^2) Z_n(u) = 0$ . The functions  $\mathbf{N}_n$  are out-of-plane while the functions  $\mathbf{M}_n$  are in-plane. We represent them for indices ranging from 0 to 3 in Fig. 6.2. By applying the proper continuity relations at the cylinder boundaries, we can compute the  $a_n$  and  $b_n$  coefficients. The TE and the TM polarisation do not mix under

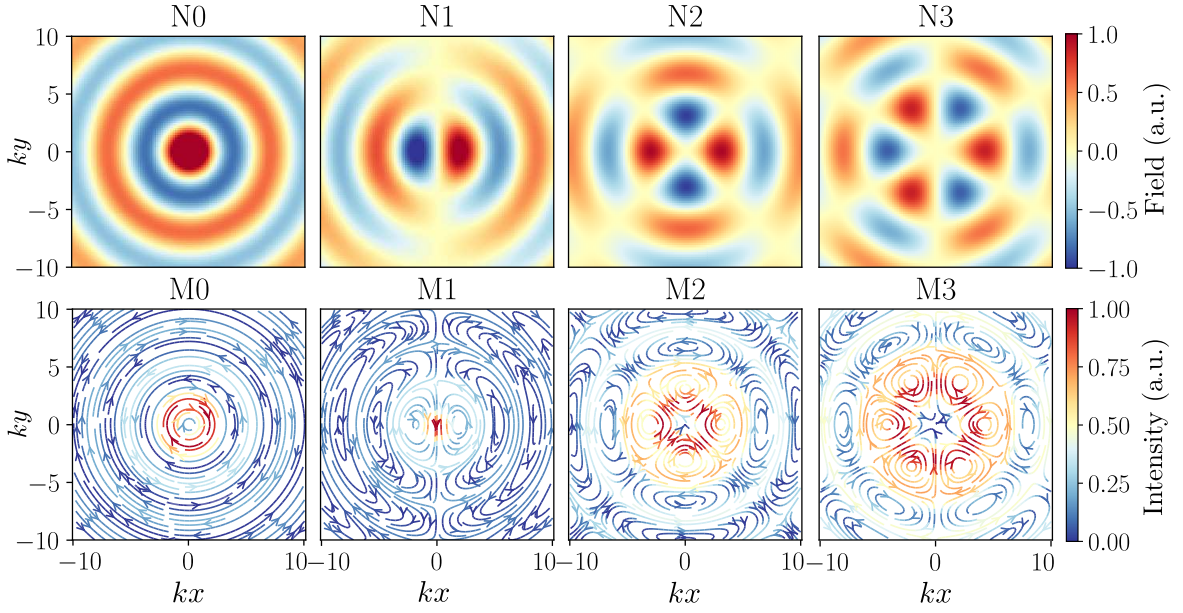


Figure 6.2: First four modes ( $\mathbf{N}_n, \mathbf{M}_n$ ) of Eq. (6.4), with respect to index  $n$ . The upper and lower lines represent respectively the electric and magnetic fields in the TM polarisation, and inversely in the TE polarisation.

normal incidence, such that the coefficients read

$$a_n = 0, \quad b_n = \frac{J_n(mx)\dot{J}_n(x) - m\dot{J}_n(mx)J_n(x)}{J_n(mx)\dot{H}_n^{(1)}(x) - m\dot{J}_n(mx)H_n^{(1)}(x)} \quad \text{in TM polarisation,} \quad (6.5)$$

$$a_n = \frac{mJ_n(mx)\dot{J}_n(x) - \dot{J}_n(mx)J_n(x)}{mJ_n(mx)\dot{H}_n^{(1)}(x) - \dot{J}_n(mx)H_n^{(1)}(x)}, \quad b_n = 0 \quad \text{in TE polarisation,} \quad (6.6)$$

with  $m = \sqrt{\varepsilon_{\text{rod}}/\varepsilon_m}$  the ratios of the permittivity of the rod to that of the outer medium and  $x = kR$  the radius of the rods normalised by the wavelength. The  $a_n$  coefficients are trivially zero in TM as they are associated to an in-plane electric field, incompatible with the TM geometry. In the same way, the  $b_n$  coefficients are zero in the TE polarisation. We can define the normalised scattering cross-section in 2D as (Bohren and Huffman, 1993):

$$C_{sca}^{TM} = \frac{2}{x} \left[ |a_0|^2 + 2 \sum_{n=1}^{\infty} |a_n|^2 \right], \quad C_{sca}^{TE} = \frac{2}{x} \left[ |b_0|^2 + 2 \sum_{n=1}^{\infty} |b_n|^2 \right] \quad (6.7)$$

Plugging the characteristics of our resonators in Eq. (6.7), we obtain Fig. 6.3(b). Only two resonances exist below 10 GHz, an out-of plane electric dipole that looks like an effective in plane monopole around 3 GHz followed by a dipolar one at 6 GHz. The first resonance is hence a good physical support for our study of out-of plane dipoles in the TM polarisation. We expect it to behave accordingly to the numerical simulations of Sec. 2.3.3 in Chap. 2. The second peak is a dipolar mode in TM polarisation, and is not described by the scalar framework of the coupled dipoles in TM polarisation. However, it can still be described by coupled in-plane dipoles by considering the magnetic field. Indeed, this out-of-the plane dipolar TM resonance turns into an in-plane magnetic one for the magnetic field. The analogy between the dipoles coupled in two dimensions by scalar or vector couplings, and the TM or TE polarisation only works for the first resonances. If we go consider magnetic dipole resonances or higher order multipoles resonances, the equivalence breaks down. Recalling the

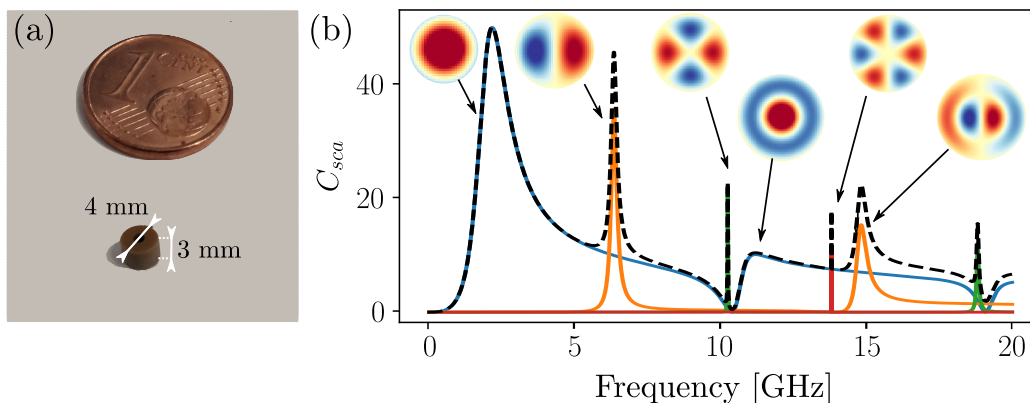


Figure 6.3: (a) Photography of one of the resonators with its dimensions. (b) Scattering cross-section of the dielectric cylinders of Fig. (a), for  $\varepsilon = 78$ , computed using Eqs. (6.5) and (6.7). The colours refer to modes with the same angular number: 0 in blue, 1 in orange, 2 in green, and three in red. The hole in the middle of the cylinder has been neglected, leading us to expect a red-shift by the lower average index. The transverse component of the electric field in the resonator is represented on top of each resonance.

fact that Green's function propagating the magnetic field from a magnetic dipole takes the exact same form as the one propagating the electric field from an electric dipole, we can apply the vector version of the coupled-dipoles equations to the case of an in-plane magnetic dipole described by the second resonance of Fig. 6.3 (b). We then expect the dipolar resonance to act in accordance with the results of Sec. 2.4 of Chap. 2 and in particular, to give rise to a pseudo-gap and localisation triggered by spatial correlations.

There are several factors which make the case of physical Mie resonances more complicated than the model of high quality factor Lorentzian resonances considered in the previous chapters. The first one is their quality factor. While the dipolar peak centred at  $f = 6.4$  GHz, has a quality factor of  $Q = 30$ , the lower frequency monopolar one ( $f = 2.5$  GHz) only has a quality factor of  $Q = 1.5$ . To verify the robustness of our predictions regarding the gaps with lower quality factors, we can rely on the similarities between highly correlated SHU patterns and photonic crystals presented in Chap. 3 and evaluate the DOS of a triangular structure for these values of  $Q$ . We computed the DOS using the general Hamiltonian for crystal of arbitrary quality factor [see Eq. (1.70) from Chap. 1] and obtained Fig. 6.4. We can see that a quality factor of  $Q = 30$  is enough to well reproduce the DOS map obtained by assuming a large quality factor. The scalar bandgap, even if very distorted for  $Q = 1.5$ , is also expected to survive in the physical system when considering scalar and vector coupling independently. But we still need to verify that the frequency overlap we observe in Fig. 6.3 (b) does not change the physics of the individual resonances.

### 6.3 Numerical study of a system composed of two resonances

We present in this section two different approaches to model the behaviour of the resonators described in Sec.6.2. The first one extends the coupled-dipole method by including both an electric and a magnetic resonance. The second one will directly evaluate the DOS through a Finite-Element Method (FEM) simulation.

#### 6.3.1 Electromagnetic Green's function and generalised coupled-dipole method

Let us derive here the basic propagation equations for a particle having both a magnetic and an electric moment. Following Ref. Amorim et al. (2017) we can write the two inhomogeneous

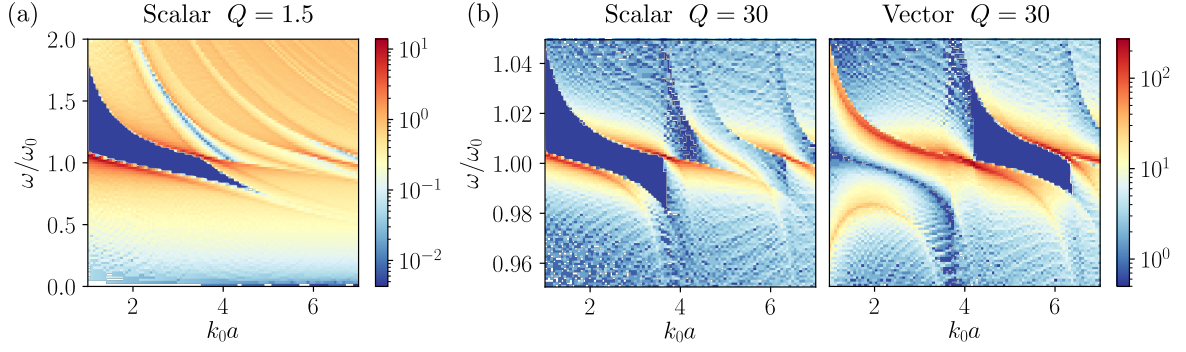


Figure 6.4: (a) Density of states of the triangular lattice, computed using Eq. (1.70) for scalar coupling and for a quality factor of  $Q = 1.5$ . (b) Densities of states for scalar (left) and vector (right) coupling, using a quality factor of  $Q = 30$ . Fig. (a) describe a situation one would obtain in a crystal composed of resonators having for sole resonance, the monopolar one from Fig. 6.3 at 3 GHz, while Fig. (b) describes the same system for the dipolar resonance at 6 GHz. The decrease in the DOS observed at  $\omega < 0.5\omega_0$  in (a) is an artefact associated to a failure of the solver. At low frequency, the function to minimise to find the eigenfrequencies is already small and real roots are more difficult to find.

Helmholtz equations for both the electric and the magnetic fields

$$-\nabla^2 \mathbf{E}(\mathbf{r}, \omega) - k^2 \mathbf{E}(\mathbf{r}, \omega) = i\omega\mu_0 \left[ \mathbf{j}(\mathbf{r}, \omega) + \frac{1}{k^2} \nabla (\nabla \cdot \mathbf{j}(\mathbf{r}, \omega)) \right] \quad (6.8)$$

$$-\nabla^2 \mathbf{B}(\mathbf{r}, \omega) - k^2 \mathbf{B}(\mathbf{r}, \omega) = \mu_0 \nabla \times \mathbf{j}(\mathbf{r}, \omega), \quad (6.9)$$

where  $\mathbf{j}$  is the current density. Using the Green's formalism, we recover the Lippman-Schwinger equations for the fields

$$\mathbf{E}(\mathbf{r}, \omega) = \mathbf{E}_0(\mathbf{r}, \omega) + i\omega\mu_0 \int d^3\mathbf{r}' G_0(\mathbf{r} - \mathbf{r}', \omega) \left( \mathbb{1} + \frac{1}{k^2} \nabla' \nabla' \right) \mathbf{j}(\mathbf{r}', \omega) \quad (6.10)$$

$$\mathbf{B}(\mathbf{r}, \omega) = \mathbf{B}_0(\mathbf{r}, \omega) + \mu_0 \int d^3\mathbf{r}' G_0(\mathbf{r} - \mathbf{r}', \omega) \nabla' \times \mathbf{j}(\mathbf{r}', \omega) \quad (6.11)$$

with  $G_0(\mathbf{r} - \mathbf{r}', \omega)$  the free space Green function of the scalar wave equation. Decomposing the current in terms of polarisation  $\mathbf{P}_f$  and magnetisation  $\mathbf{M}_f$  densities as

$$\mathbf{j}(\mathbf{r}, \omega) = -i\omega \mathbf{P}_f(\mathbf{r}, \omega) + \nabla \times \mathbf{M}_f(\mathbf{r}, \omega), \quad (6.12)$$

equations (6.10) and (6.11) become

$$\begin{aligned} \mathbf{E}(\mathbf{r}, \omega) = & \mathbf{E}_0(\mathbf{r}, \omega) + \omega^2 \mu_0 \int d^3\mathbf{r}' G_0(\mathbf{r} - \mathbf{r}', \omega) \left( \mathbb{1} + \frac{1}{k^2} \nabla' \nabla' \right) \mathbf{P}_f(\mathbf{r}', \omega) \\ & + i\omega \mu_0 \int d^3\mathbf{r}' G_0(\mathbf{r} - \mathbf{r}', \omega) \nabla' \times \mathbf{M}_f(\mathbf{r}', \omega) \end{aligned} \quad (6.13)$$

$$\begin{aligned} \mathbf{B}(\mathbf{r}, \omega) = & \mathbf{B}_0(\mathbf{r}, \omega) - i\omega \mu_0 \int d^3\mathbf{r}' G_0(\mathbf{r} - \mathbf{r}', \omega) \nabla' \times \mathbf{P}_f(\mathbf{r}', \omega) \\ & + \mu_0 \int d^3\mathbf{r}' G_0(\mathbf{r} - \mathbf{r}', \omega) (-\nabla'^2 + \nabla' \nabla') \mathbf{M}_f(\mathbf{r}', \omega). \end{aligned} \quad (6.14)$$

These equation can be written in terms of Green tensors as

$$\begin{aligned} \mathbf{E}(\mathbf{r}, \omega) &= \mathbf{E}_0(\mathbf{r}, \omega) + \omega^2 \mu_0 \int d^3 \mathbf{r}' \mathbf{G}_0^{\text{EE}}(\mathbf{r} - \mathbf{r}', \omega) \mathbf{P}_f(\mathbf{r}', \omega) \\ &\quad + i\omega \mu_0 k \int d^3 \mathbf{r}' \mathbf{G}_0^{\text{EM}}(\mathbf{r} - \mathbf{r}', \omega) \mathbf{M}_f(\mathbf{r}', \omega), \end{aligned} \quad (6.15)$$

$$\begin{aligned} \mathbf{B}(\mathbf{r}, \omega) &= \mathbf{B}_0(\mathbf{r}, \omega) - i\omega \mu_0 k \int d^3 \mathbf{r}' \mathbf{G}_0^{\text{ME}}(\mathbf{r} - \mathbf{r}', \omega) \mathbf{P}_f(\mathbf{r}', \omega) \\ &\quad + \mu_0 k^2 \int d^3 \mathbf{r}' \mathbf{G}_0^{\text{MM}}(\mathbf{r} - \mathbf{r}', \omega) \mathbf{M}_f(\mathbf{r}', \omega), \end{aligned} \quad (6.16)$$

where  $\mathbf{G}_0^{\text{EE}} = \mathbf{G}_0^{\text{MM}}$  is the dyadic Green's function for the propagation of the electric field from an electric dipole and reciprocally for a magnetic one.  $\mathbf{G}_0^{\text{EM}} = \mathbf{G}_0^{\text{ME}}$  is the Green's function for the propagation of the electric field from a magnetic dipole and conversely. They take the general form

$$\mathbf{G}_0^{\text{EM}}(\mathbf{r}, \omega) = \frac{1}{k_0} \nabla \times G_0(\mathbf{r}, \omega) \mathbb{1} = \begin{cases} \frac{e^{ik_0 R}}{4\pi r} \left[ i - \frac{1}{k_0 R} \right] \begin{pmatrix} 0 & \hat{r}_z & -\hat{r}_y \\ -\hat{r}_z & 0 & \hat{r}_x \\ \hat{r}_y & -\hat{r}_x & 0 \end{pmatrix} & \text{in 3D,} \\ -\frac{i}{4} \text{H}_1^{(1)}(k_0 r) \begin{pmatrix} 0 & 0 & -\hat{r}_y \\ 0 & 0 & \hat{r}_x \\ \hat{r}_y & -\hat{r}_x & 0 \end{pmatrix} & \text{in 2D,} \end{cases} \quad (6.17)$$

with  $\hat{r}_j$  the  $j^{\text{th}}$  component of  $\hat{\mathbf{r}} = \mathbf{r}/r$ , and where the 2D setup is actually a 3D one invariant under translation along the  $z$ -axis.

**Remark:** It is important to notice that, whereas  $\mathbf{G}_0^{\text{EE}}(-\mathbf{r}, \omega) = \mathbf{G}_0^{\text{EE}}(\mathbf{r}, \omega)$ ,  $\mathbf{G}_0^{\text{EM}}(-\mathbf{r}, \omega) = -\mathbf{G}_0^{\text{EM}}(\mathbf{r}, \omega)$  because of the curl term which depends on the sign of  $\mathbf{r}$ . It is linked to the loss of the usual Rayleigh reciprocity relation for point-like sources  $\mathbf{j}_1 \cdot \mathbf{E}_2 = \mathbf{j}_2 \cdot \mathbf{E}_1$  which is now replaced by the Rayleigh-Carson reciprocity relation (Jackson, 1999). It takes the form

$$\mathbf{j}_1 \cdot \mathbf{E}_2 - \mathbf{H}_1 \cdot \mathbf{M}_2 = \mathbf{j}_2 \cdot \mathbf{E}_1 - \mathbf{H}_2 \cdot \mathbf{M}_1. \quad (6.18)$$

### Generalised Coupled-dipoles method

With the behaviour of a field generated by an arbitrary source in mind, we can consider an ensemble of point-like electric and magnetic dipoles. As for the regular coupled-dipole method, we write a closed set of equation relating both the electric and magnetic excitation fields of each particle to the other as

$$\mathbf{E}_i(\omega) = -k^2 \alpha^E(\omega) \sum_{j \neq i} [\mathbf{G}_0^{\text{EE}}(\mathbf{r}_i - \mathbf{r}_j, \omega) \mathbf{E}_j(\omega) - \mathbf{G}_0^{\text{EM}}(\mathbf{r}_i - \mathbf{r}_j, \omega) \mathbf{M}_j(\omega)], \quad (6.19)$$

$$\mathbf{M}_i(\omega) = -k^2 \alpha^M(\omega) \sum_{j \neq i} [\mathbf{G}_0^{\text{EE}}(\mathbf{r}_i - \mathbf{r}_j, \omega) \mathbf{M}_j(\omega) + \mathbf{G}_0^{\text{EM}}(\mathbf{r}_i - \mathbf{r}_j, \omega) \mathbf{E}_j(\omega)], \quad (6.20)$$

where the polarisabilities take the form

$$\alpha^{\text{E,M}}(\omega, \omega_0^{\text{E,M}}) = -\frac{c_d}{(k_0^{\text{E,M}})^d} \frac{\Gamma_0^{\text{E,M}}}{\omega - \omega_0^{\text{E,M}} + i\Gamma_0^{\text{E,M}}/2}, \quad (6.21)$$

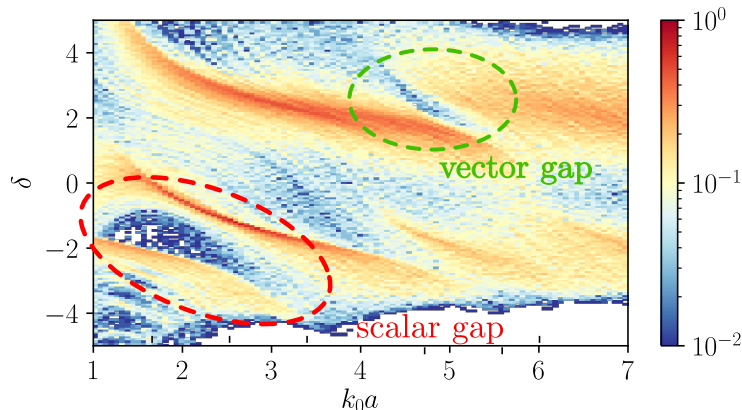


Figure 6.5: Density of states of a SHU system at  $\chi = 0.5$  composed of an out-of plane electric dipole and an in-plane magnetic one. The two resonances are detuned by  $\delta = 4$ , but have the same linewidth for the two resonances for visibility. The scalar gap is highlighted in red and the vector one in green. The data have been obtained by considering  $N = 2400$  eigenvalues for each density.

with  $\omega_0^{\text{E,M}} = k_0^{\text{E,M}} c$  and  $\Gamma_0^{\text{E,M}}$  are respectively the central frequency and linewidth of the electric or magnetic resonance and  $c_d$  a coefficient only depending on the density and defined in Sec. 1.5.1. The resonant solutions are found by solving

$$\det \left[ \mathbb{A}^{-1}(\omega) + \tilde{\mathbb{G}}(\omega) \right] = 0, \quad (6.22)$$

where

$$(\mathbb{A}^{-1})_{i,j}^{\mu,\nu}(\omega) = \left( \frac{\omega - \omega^\mu}{\Gamma_0^\mu/2} - i \right) \delta_{\mu,\nu} \delta_{ij} \mathbb{1}, \quad (6.23)$$

and

$$\tilde{\mathbb{G}}_{i,j}^{\mu,\nu}(\omega) = -c_d \frac{k^2}{(k_0^\mu)^d} \mathbf{G}^{\mu,\nu}(\mathbf{r}_i - \mathbf{r}_j, \omega). \quad (6.24)$$

the indices  $i, j$  runs over the particles and  $\mu, \nu$  account for the electric or magnetic field (E and M).

Equation (6.22), contrary to Eq. (1.48), is not a linear eigenvalue problem. Indeed, the Green's matrix defined by Eq. (6.24) depends non linearly on the frequency. Freezing it, like in the usual coupled-dipole method amounts to assuming that the quality factor is high enough so that, the frequency dynamics are driven by the polarisability, and also that the two resonances are close. In the following, we will only keep the frequency dependences in  $\mathbb{A}$ . Equation (6.22) becomes a linear eigenvalue problem for which we need to specify the detuning between the electric and magnetic resonances, as well as their respective linewidth.

### 6.3.2 Application to the first two Mie resonances

We apply the formalism described above to our initial experimental problem. The spectrum below 10 GHz of a Mie cylinder of dielectric constant  $\varepsilon = 78$  is composed of a broad out-of plane electric dipole resonance followed by a narrow in-plane magnetic dipole resonance. From the characteristics of the spectrum of Fig. 6.3, we can extract  $\omega_0^E, \Gamma_0^E, \omega_0^M, \Gamma_0^M$  and compute the DOS of the system by solving Eq. 6.22 for a SHU system at  $\chi = 0.5$ . For clarity, in Fig. 6.5 we neglected the difference between  $\Gamma^E$  and  $\Gamma^M$ . We find that the DOS looks composed of a juxtaposition of two individual DOS (see Chap. 2). It nonetheless preserves the gaps in the

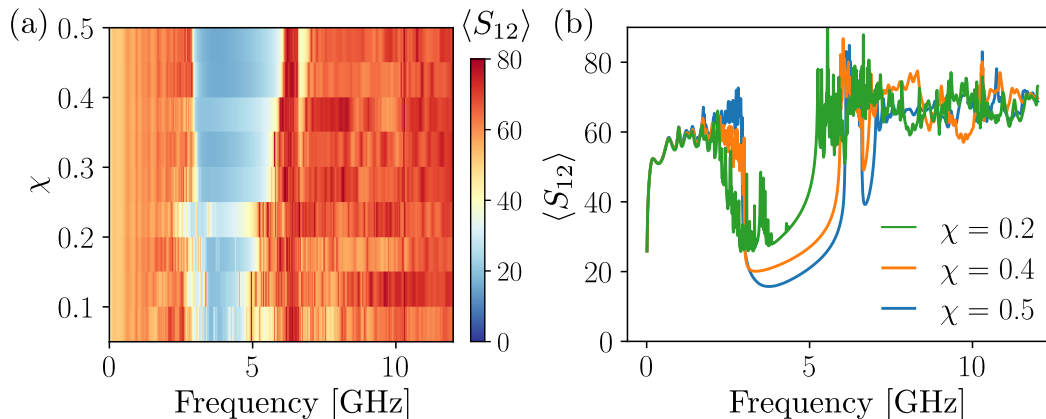


Figure 6.6: (a) Finite-element simulations of the  $S_{12}$  transmission coefficient in an ensemble of increasingly correlated SHU patterns made of the dielectric resonators described in Fig. 6.1 and spaced by a distance  $a = \rho^{-1/2} = 1.5$  cm. (b) Cuts of the map shown in (a) for  $\chi = 0.2$ , 0.4 and 0.5.

region where they overlap. These preliminary results could indicate that the coupling of the two resonances is not expected to prevent the formation of neither band gaps.

This model still presents some flaws. The first one regards the high quality factor assumptions, which is far from filled for the first Mie resonance ( $Q = 1.5$ ). It should be possible to use the framework developed for crystals of arbitrary quality factors and include the two resonances studied here. In addition, our treatment assumes that the difference between the two resonance frequencies is much smaller than the resonant frequencies, which is not satisfied for the parameters of Fig. 6.3. It can also be noted that this model is equivalent to considering the first two terms of the T-matrix expansion of our dielectric cylinder.

In the following, we will compare these preliminary results with the ones obtained by a more *brut-force* approach using Finite-Element Method (FEM) simulation.

## 6.4 Finite-element method

Instead of computing the collective modes of a complex system of electric and magnetic resonances, we turn to a different approach. We directly modelled the experimental setup using finite-element methods. The computation has been done on *COMSOL* with a code initially written by Fabrice Lemoult from Institut Langevin.

In a microwave experiment, we do not access directly to the density of states but rather to reflection and transmission coefficients measured thanks to a vector network analyser, and antennas placed inside the medium. The reflection coefficient is called  $S_{11}$  and the transmission one  $S_{12}$ . The reflection coefficient  $S_{11}$  is proportional to the local density of electromagnetic states (LDOS) in the system as shown in Ref. Rosny et al. (2010), while  $S_{12}$  is a measure of the cross-density of states (CDOS). Both the LDOS and the CDOS are described in Refs. Carminati et al. (2015b); Canaguier-Durand et al. (2019) and average spatially to the DOS. We compute the transmission coefficient  $S_{11}$  over the frequency range  $[0, 12.5]$  GHz (to capture the first two Mie resonances) and average its value over the source position inside the SHU medium to obtain a measure of the relative DOS. The results for different  $\chi$  are shown in Fig. 6.6. Fully uncorrelated configurations are impossible to make, due to the physical exclusion radius of the objects. Yet we can reach values below  $\chi = 0.1$  due to their relatively small size (few mm) compared to the working wavelength (cm).

Figure 6.6 (a) shows that spatial correlations have two effects. First they deepen an already

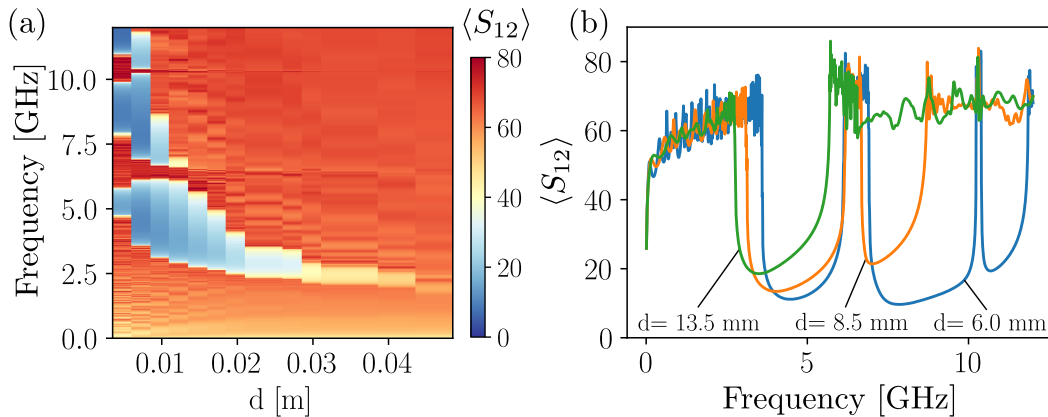


Figure 6.7: (a) Finite-element simulation of the  $S_{12}$  transmission coefficient in ensembles of highly correlated of SHU patterns ( $\chi = 0.5$ ) made with the dielectric resonators described in Fig. 6.1. We vary the average distance between the resonators from 3 mm up to 5 cm. (b) Cuts of the map shown in (a) for  $d = 6$  mm, 8.5 mm and 13.5 mm.

visible, yet noisy, gap between 3 and 4 GHz. Second, an-extra gap opens above  $\chi = 0.4$ . It is narrow, but clearly visible on Fig. 6.6(b). The behaviour of the two gaps are consistent with the study of respectively the TM and the TE gap in Chap. 2. Explicitly, the TM gap is observed at high density even without correlations. The latter only broaden it and remove defects modes inside it. The second gap centred at 7 GHz only appears above  $\chi = 0.4$  and is much narrower than the first one. This is again consistent with the TE gap. We can notice that these numerical results are similar to the ones obtained experimentally in Ref. Aubry et al. (2020), in a slightly blue-shifted frequency regime.

If we now look at the  $S_{12}$  of SHU configurations at  $\chi = 0.5$ , for different densities, we obtain Fig. 6.7. The lowest frequency gap is the most robust as it exists from high to relatively low densities. There exists a critical density at which the second gap opens and there is even a third gap that is visible at high density. The high density regime is more difficult to understand in a coupled-Mie resonance picture, as the average index of the medium changes due to the concentration of high index elements. Maxwell-Garnet formula could be used to correct for it (see Sec. 1.3.4).

These numerical simulations (seem to) confirm that the setup composed of spatially correlated dielectric cylinders displays the features of both the TM and the TE resonances we studied in the previous chapters. The third gap appearing at high frequency may be interpreted as a coupling with the first quadrupolar Mie resonance expected near 10 GHz in the Mie spectrum (see Fig. 6.3).

## 6.5 Towards an experimental implementation

After proving numerically the possibility to observe a gap driven by vector-wave coupling between resonators, we worked on building an experimental setup. Conducting copper layer of circuit board plates were used to build the cavity. The bottom of the waveguide is shown in Fig. 6.8, with absorbing foam on the edges to mimic an infinite system. An antenna peeks through the bottom level directly inside the guide (not visible in Fig. 6.8) to act as a source. The top layer is drilled with holes to allow for a mechanically controlled scanning antenna, to penetrate the space between the plate and measure the transmission coefficient from the source.

First attempts at measuring the effect of single resonators failed in the TM geometry. We



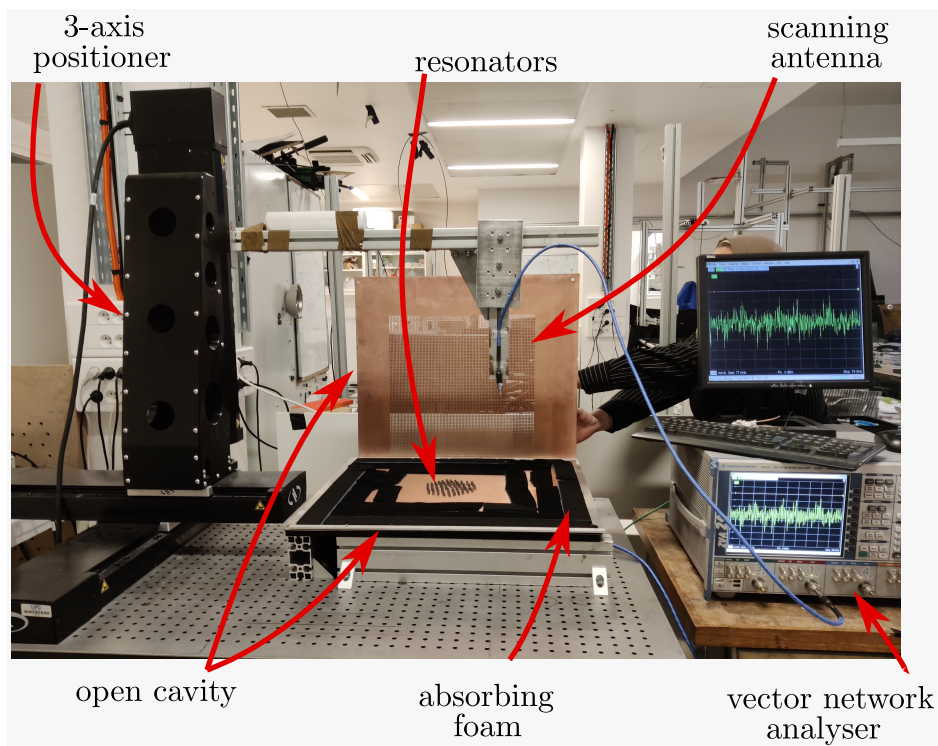


Figure 6.8: Photography of the experimental setup, showing the cavity enclosing the ceramic resonators, the scanning antenna positioned by the 3-axis positioner, and the vector network analyser measuring the reflection/transmission coefficients.

only managed to distinguish resonances at 7 GHz and up, by removing the top plate. This open geometry does not reproduce a system in the TM polarisation, and the signal has been interpreted as the first TE resonance of the cylinder. Signs of the presence of resonators have not been found, even in configurations where band gaps were expected.

In this preliminary study we overlooked a few factors, one of which is the good electrical contact between the ground plates and the resonators. It has been pointed out to be crucial to allow for a good coupling. Another issue may be the weak coupling between the antennas and the waveguide, which induces strong losses at both the input and the output. In this regard, the design of efficient strongly sub-wavelength antennas is challenging.

A collaboration with the group of F. Mortessagne at Institut de Physique de Nice (IN-PHYNI) in Nice, who already built a working setup, is in preparation. Hopefully it will allow to fix some of the above-mentioned issues, and test our vision of the physics at stake.

## 6.6 Conclusion

In this chapter, we summarised the preliminary results obtained in view of realising an experimental validation of the findings of this thesis. We focused on 2D systems with vector coupling which have been observed numerically to exhibit a band gap driven by structural correlations. The two-dimensionality has been reached by using the zeroth order TM mode in a planar waveguide. This propagation channel has the advantage of being uniform along the transverse direction, effectively mimicking an infinite system along one direction. We showed how the model of coupled electric resonators in TE polarisation can be applied to the case of in-plane magnetic dipoles in TM polarisation. The scalar and vector setup in 2D can both be achieved in TM polarisation, by the coupling of different Mie resonances of a cylinder. The

idea is to use high dielectric constant cylinders in the TM polarisation, which host successively an out-of plane electric dipole and an in-plane magnetic one. We showed that at the cost of unrealistic assumptions on the quality factors and the splitting of the two resonances, the behaviour of an ensemble of cylinders can be computed using a modified version of the coupled-dipole method, by including a magnetic resonance. This computation, supported by finite-element simulation, predicted the existence of two band gaps in the frequency range of interest. Their behaviour is consistent with the simulations in Chap. 2, especially regarding the second higher frequency gap which appears above a critical correlation ratio.

An experimental setup adapted to probe the behaviour near the first two resonances of high index material is in development. We have, to this day, not been able to reproduce the results obtained through simulation. Room is left to improve the setup and identify the issues at stake.



# General conclusion

Throughout this thesis, we have presented a systematic study of the influence of spatial correlations on the collective photonic properties of resonant particles. Spatially correlated materials act as intermediate systems between fully disordered and regular arrangements. In this respect, they have been observed to harbour band gaps, an essentially crystalline property, and to favour Anderson localisation, a property of disordered systems. For scalar light-mediated coupling between resonators, these phenomena generically occur at high density, both in 2D and 3D. However, in the case of vector coupling, the picture changes quite drastically. In finite-size 2D correlated systems, bandgap and localisation are found at intermediate density but absent at high density. And in 3D, neither bandgap nor localisation have been identified, whatever the density or the amount of spatial correlation. These observations have been made through a study of the density of states and the mode lifetimes of the collective resonances supported by the open disordered assembly of coupled resonators

The changes in the density of states have been understood from two opposite perspectives. In a first approach we considered the correlated structure as an assembly of small crystals and applied the band structure framework. This approach has highlighted the crucial role of the longitudinal band in vector configurations. In 2D and 3D, this band fills the polaritonic gap found at high density for scalar coupling, but also allows another polaritonic gap to open up at lower densities in 2D. This approach allows the density of states to be modelled with a very good level of accuracy in the different regimes of density and polarisation. In the second approach we develop the opposite point of view by considering uncorrelated disorder as a reference system. Starting from this situation, partial order is added and taken into account in the theoretical evaluation of the collective scattering operator of the system. We establish a connection between the properties of this operator and the density of states that allows us to reproduce theoretically the main features observed on the densities of states of correlated disordered systems with a good qualitative agreement all the way from full disorder to full order. In particular, we have identified the microscopic scattering processes responsible for a strong depletion in the density of states.

These two approaches allow the gap formation in the density of states to be understood from two complementary points of view: either as interferences between polaritonic waves from different Brillouin zones in the crystalline interpretation, or between two scattering processes involving pairs of spatially correlated resonators in the mesoscopic physics picture. The role of correlations for the appearance of these processes is crucial in both cases. It is indeed the similarity between the local environment of a correlated pattern and a crystal that allows the development of the band structure and the existence of a well-defined distance between neighbouring scatterers that makes the destructive interference between single and double scattering paths an efficient process.

By focusing on the question of the change in the density of states due to spatial correlations, we have also highlighted its role in localisation phenomena. By going back to the fundamental principles of the self-consistent localisation theory, we kept track of the explicit role of the density of states in the localisation criteria. In particular, the density of states appears explicitly in the expression of the localisation length and makes it collapse in the case of a pseudo-gap. This process, well documented for electrons, has somehow been overlooked for

light. Our treatment of the light-matter interaction problem in terms of an effective Hamiltonian makes the analogy with electron quite natural and the identification of the relevant density of states easy. The theoretical expression for the localisation length has been validated by direct numerical computations using transport simulations through disordered slabs as well as direct analysis of the eigenstates of the effective Hamiltonian. Our analytical and numerical analysis also showed that the transport mean free path is not the main driver of the collapse of the localisation length near a bandgap.

The theoretical treatment of spatial correlations in ensembles of resonant particles has required some simplifying assumptions. We assumed in particular that the resonators have a single resonance with a very large quality factor. These two assumptions, valid in the case of cold atoms, may be questionable when considering Mie particles with overlapping multipolar modes. To validate the practical relevance of the predictions made during this thesis, we turned to the realisation of an experiment based on resonant high-index ceramic scatterers coupled by microwaves. Different simulations of the experimental system, as well as some results of the recent literature, seem to confirm the results obtained in two dimensions. The realisation of an experimental setup is in progress.

The continuation of this project will first consist in the deepening of the experimental work. In particular, the possible observation of a pseudo-gap phase and localisation solely induced by strong spatial correlations in a system with vector coupling motivates the realisation. But such an experimental setup is much more versatile and can serve as an excellent support for the study of any collective resonant phenomena. At the theoretical level, it will be relevant to extend and apply the general formalism developed in this thesis to scattering systems that differ from point-like scatterers. We have in mind decorated random network structures whose behaviour differs from the one of point-like scatterers, exhibiting strong bandgap and localisation, not only in 2D but also in 3D.

## Appendix A

# Polarizabilities in 2D and 3D for scalar and vector fields

This appendix summarizes the the expressions of the polarizabilities used in this manuscript. We define  $\tilde{\omega} = \omega/\omega_0$ ,  $Q = \omega_0/\Gamma_0$  and  $\delta = 2(\omega - \omega_0)/\Gamma_0$ .

### A.1 3D vector

General expression

$$\alpha(\omega) = \frac{-6\pi\Gamma c^3}{\omega_0^2} \frac{1}{\omega^2 - \omega_0^2 + i\Gamma_0\omega^3/\omega_0^2} = \frac{-6\pi}{Qk_0^3} \frac{1}{\tilde{\omega}^2 - 1 + i\tilde{\omega}^3/Q} \quad (\text{A.1})$$

Near resonance

$$\alpha(\omega) = \frac{-6\pi}{k_0^3} \frac{\Gamma_0/2}{\omega - \omega_0 + i\Gamma_0/2} = \frac{-6\pi}{k_0^3} \frac{1}{\delta + i} \quad (\text{A.2})$$

### A.2 3D scalar

General expression

$$\alpha(\omega) = \frac{-4\pi\Gamma c^3}{\omega_0^2} \frac{1}{\omega^2 - \omega_0^2 + i\Gamma_0\omega^3/\omega_0^2} = \frac{-4\pi}{Qk_0^3} \frac{1}{\tilde{\omega}^2 - 1 + i\tilde{\omega}^3/Q} \quad (\text{A.3})$$

Near resonance

$$\alpha(\omega) = \frac{-4\pi}{k_0^3} \frac{\Gamma_0/2}{\omega - \omega_0 + i\Gamma_0/2} = \frac{-4\pi}{k_0^3} \frac{1}{\delta + i} \quad (\text{A.4})$$

### A.3 2D vector

General expression

$$\alpha(\omega) = \frac{-8\Gamma c^2}{\omega_0} \frac{1}{\omega^2 - \omega_0^2 + i\Gamma_0\omega^2/\omega_0} = \frac{-8}{Qk_0^2} \frac{1}{\tilde{\omega}^2 - 1 + i\tilde{\omega}^2/Q} \quad (\text{A.5})$$

Near resonance

$$\alpha(\omega) = \frac{-8}{k_0^2} \frac{\Gamma_0/2}{\omega - \omega_0 + i\Gamma_0/2} = \frac{-8}{k_0^2} \frac{1}{\delta + i} \quad (\text{A.6})$$

## A.4 2D scalar

### General expression

$$\alpha(\omega) = \frac{-4\Gamma c^2}{\omega_0} \frac{1}{\omega^2 - \omega_0^2 + i\omega^2\Gamma_0/\omega_0} = \frac{-4}{Qk_0^2} \frac{1}{\tilde{\omega}^2 - 1 + i\tilde{\omega}^2/Q} \quad (\text{A.7})$$

### Near resonance

$$\alpha(\omega) = \frac{-4}{k_0^2} \frac{\Gamma_0/2}{\omega - \omega_0 + i\Gamma_0/2} = \frac{-4}{k_0^2} \frac{1}{\delta + i} \quad (\text{A.8})$$

## Appendix B

# Regularization of the crystalline Hamiltonian

We summarise the regularisation of the crystalline Hamiltonian in every space and field geometry. The basis equations can be found in Sec. 3.2.2. We simply recall that the regularized Green's function in momentum space takes the form

$$\mathbf{G}_0^*(\mathbf{q}, \omega) = \mathbf{G}_0(\mathbf{q}, \omega) e^{-\frac{q^2 b^2}{2}}, \quad (\text{B.1})$$

where  $b$  is the regularization parameter. It gives in 2D TM polarisation

$$\begin{aligned} \mathbf{G}_0^*(\mathbf{R} = \mathbf{0}, \omega) &= -\frac{i}{4} \int d\mathbf{r} H_0^{(1)}(k_0 r) \frac{e^{-\frac{r^2}{2b^2}}}{2\pi b^2} \\ &\underset{k_0 b \ll 1}{\simeq} -\frac{1}{\pi} \left[ \gamma + \ln \left( \frac{k_0^2 b^2}{2} \right) \right] - \frac{i\mathbb{1}}{4}. \end{aligned} \quad (\text{B.2})$$

Here the Hankel function has been approximated at small values by

$$H_0^{(1)}(x) \underset{x \ll 1}{\simeq} 1 + \frac{i}{\pi} \left[ 2\gamma + \ln \left( \frac{x^2}{4} \right) \right], \quad (\text{B.3})$$

where  $\gamma$  is the Euler's constant. In the TE polarization, using  $\int_0^{2\pi} d\theta (\mathbb{1} - \hat{\mathbf{r}} \otimes \hat{\mathbf{r}}) = \pi\mathbb{1}$  and  $\int_0^{2\pi} d\theta (\mathbb{1} - 2\hat{\mathbf{r}} \otimes \hat{\mathbf{r}}) = 0$  where  $\hat{\mathbf{r}} = \mathbf{r}/r$ , we get

$$\begin{aligned} \mathbf{G}_0^*(\mathbf{R} = \mathbf{0}, \omega) &= -\frac{i\pi\mathbb{1}}{4} \int_0^\infty dr r H_0^{(1)}(k_0 r) \frac{e^{-\frac{u^2}{2b^2}}}{2\pi b^2} + \frac{\mathbb{1}}{4\pi k_0^2 b^2} \\ &\underset{k_0 b \ll 1}{\simeq} -\frac{\mathbb{1}}{2\pi} \left[ \gamma + \ln \left( \frac{k_0^2 b^2}{2} \right) \right] - \mathbb{1} \left( \frac{i}{8} - \frac{1}{4\pi k_0^2 b^2} \right). \end{aligned}$$

In 3D for scalar waves we have

$$\begin{aligned} \mathbf{G}_0^*(\mathbf{R} = \mathbf{0}, \omega) &= \int d\mathbf{r} \mathbf{r} \frac{-e^{ik_0 r}}{4\pi r} \frac{e^{-\frac{u^2}{2b^2}}}{(\sqrt{2\pi}b)^3} \\ &= \frac{k_0}{8\pi} \left\{ e^{-\frac{(kb)^2}{2}} \left[ \text{Erfi} \left( \frac{k_0 b}{\sqrt{2}} \right) - i \right] - \sqrt{\frac{2}{\pi}} \frac{1}{k_0 b} \right\}, \end{aligned} \quad (\text{B.4})$$

where  $\text{Erfi}(x) = -i \frac{2}{\sqrt{\pi}} \int_0^{ix} e^{-t^2} dt$  is the imaginary error function. Similarly for vector fields



we obtain

$$\begin{aligned}
 \mathbf{G}_0^*(\mathbf{R} = \mathbf{0}, \omega) &= \int_0^\infty dr r^2 \frac{e^{-\frac{r^2}{2b^2}}}{(\sqrt{2\pi}b)^3} \int d\Omega \mathbf{G}_0(\mathbf{r}, \omega) \\
 &= \frac{k_0}{6\pi} \left\{ e^{-\frac{(k_0b)^2}{2}} \left[ \operatorname{Erfi} \left( \frac{k_0b}{\sqrt{2}} \right) - i \right] - \sqrt{\frac{2}{\pi}} \frac{1}{k_0b} + \frac{1}{\sqrt{2\pi}(k_0b)^3} \right\}, \quad (\text{B.5})
 \end{aligned}$$

where we have used that  $\int d\Omega (\mathbf{1} - \mathbf{u} \otimes \mathbf{u}) = 8\pi \mathbf{1}/3$  and  $\int d\Omega (\mathbf{1} - 3\mathbf{u} \otimes \mathbf{u}) = \mathbf{0}$ .

## Appendix C

# Diagrammatic approach: drawing rules




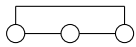
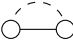
Feynman diagrams are routinely used in the framework of multiple scattering theory to account for diffusion sequences. They are used in the computation of the self energy  $\Sigma$  from Dyson's equation written diagrammatically as

$$\text{---} = \text{---} \Sigma \text{---}. \quad (\text{C.1})$$


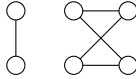

In the same way, the Bethe-Salpether equation reads

$$\blacksquare = \text{---} \text{U} \blacksquare. \quad (\text{C.2})$$

The drawing rules for one-line diagrams appearing in average fields are

Circle		scattering by a particle	$t$
Horizontal line		field propagator	$\mathbf{G}_0$
Thick horizontal line		average field propagator	$\langle \mathbf{G} \rangle$
Crooked line		scatterer 1 and 3 are identical	$\delta(\mathbf{r}_1 - \mathbf{r}_3)$
Dashed line		scatterer 1 and 2 are statistically correlated	$h_2(\mathbf{r}_1 - \mathbf{r}_2)$

For diagrams in two lines used in the computation of field correlations, the above rules still apply with the addition of specific two-liners showed below.

Gray box		Average intensity propagator	$\langle \mathbf{G} \mathbf{G}^* \rangle$
Vertical or oblique line		Identical scatterer	$\delta(\mathbf{r}_1 - \mathbf{r}_2)$
Dashed vertical line		Correlated scatterers	$h_2(\mathbf{r}_1 - \mathbf{r}_2)$



# Bibliography

- Abrahams, E., Anderson, P. W., Licciardello, D. C., and Ramakrishnan, T. V. (1979). Scaling theory of localization: Absence of quantum diffusion in two dimensions. *Phys. Rev. Lett.*, 42(10):673–676.
- Akkermans, E., Gero, A., and Kaiser, R. (2008). Photon localization and dicke superradiance in atomic gases. *Phys. Rev. Lett.*, 101:103602.
- Akkermans, E. and Montambaux, G. (2007). *Mesoscopic Physics of Electrons and Photons*. Cambridge University Press.
- Akkermans, E., Wolf, P. E., and Maynard, R. (1986). Coherent backscattering of light by disordered media: Analysis of the peak line shape. *Phys. Rev. Lett.*, 56:1471–1474.
- Amorim, B., Gonçalves, P. A. D., Vasilevskiy, M. I., and Peres, N. M. R. (2017). Impact of graphene on the polarizability of a neighbour nanoparticle: A dyadic green’s function study. *Appl. Sci.*, 7(11):1158.
- Anderson, P. W. (1985). The question of classical localization a theory of white paint? *Philosophical Magazine B*, 52(3):505–509.
- Antezza, M. and Castin, Y. (2009a). Fano-hopfield model and photonic band gaps for an arbitrary atomic lattice. *Phys. Rev. A*, 80(1):013816.
- Antezza, M. and Castin, Y. (2009b). Spectrum of light in a quantum fluctuating periodic structure. *Phys. Rev. Lett.*, 103:123903.
- Antezza, M. and Castin, Y. (2013). Photonic band gap in an imperfect atomic diamond lattice: Penetration depth and effects of finite size and vacancies. *Phys. Rev. A*, 88(3):033844.
- Aubry, G. J., Froufe-Pérez, L. S., Kuhl, U., Legrand, O., Scheffold, F., and Mortessagne, F. (2020). Experimental tuning of transport regimes in hyperuniform disordered photonic materials. *Phys. Rev. Lett.*, 125:127402.
- Badon, A., Barolle, V., Irsch, K., Boccara, A. C., Fink, M., and Aubry, A. (2020). Distortion matrix concept for deep optical imaging in scattering media. *Sci. Adv.*, 6(30):eaay7170.
- Baus, M. and Colot, J. L. (1987). Thermodynamics and structure of a fluid of hard rods, disks, spheres, or hyperspheres from rescaled virial expansions. *Phys. Rev. A*, 36:3912–3925.
- Beenakker, C. W. J. (1997). Random-matrix theory of quantum transport. *Rev. Mod. Phys.*, 69:731–808.
- Bekshaev, A. Y., Bliokh, K. Y., and Nori, F. (2013). Mie scattering and optical forces from evanescent fields: A complex-angle approach. *Opt. Express*, 21(6):7082–7095.
- Bellando, L., Gero, A., Akkermans, E., and Kaiser, R. (2014). Cooperative effects and disorder: A scaling analysis of the spectrum of the effective atomic hamiltonian. *Phys. Rev. A*, 90:063822.

- Bohren, C. F. and Huffman, D. R. (1993). *Absorption and Scattering of Light by Small Particles*. Wiley (New York).
- Canaguier-Durand, A., Pierrat, R., and Carminati, R. (2019). Cross density of states and mode connectivity: Probing wave localization in complex media. *Phys. Rev. A*, 99:013835.
- Cardy, J. (1996). *Scaling and Renormalization in Statistical Physics*. Cambridge University Press, 1 edition.
- Carminati, R., Cazé, A., Cao, D., Peragut, F., Krachmalnicoff, V., Pierrat, R., and De Wilde, Y. (2015a). Electromagnetic density of states in complex plasmonic systems. *Surf. Sci. Rep.*, 70(1):1–41.
- Carminati, R., Cazé, A., Cao, D., Peragut, F., Krachmalnicoff, V., Pierrat, R., and Wilde, Y. D. (2015b). Electromagnetic density of states in complex plasmonic systems. *Surf. Sci. Rep.*, 70(1):1–41.
- Carminati, R. and Schotland, J. C. (2021). *Principles of Scattering and Transport of Light*. Cambridge University Press.
- Chandrasekhar, S. (1960). *Radiative Transfer*. Dover Books on Intermediate and Advanced Mathematics. Dover Publications.
- Cherroret, N., Delande, D., and van Tiggelen, B. A. (2016). Induced dipole-dipole interactions in light diffusion from point dipoles. *Phys. Rev. A*, 94:012702.
- Chong, Y. D., Ge, L., Cao, H., and Stone, A. D. (2010). Coherent perfect absorbers: Time-reversed lasers. *Phys. Rev. Lett.*, 105:053901.
- Conley, G. M., Burrelli, M., Pratesi, F., Vynck, K., and Wiersma, D. S. (2014). Light transport and localization in two-dimensional correlated disorder. *Phys. Rev. Lett.*, 112(14):143901.
- Cottier, F., Cipris, A., Bachelard, R., and Kaiser, R. (2019). Intensity fluctuations signature of 3d anderson localization of light. *Phys. Rev. Lett.*, 123(8):083401. arXiv: 1812.10313.
- Dal Negro, L., Chen, Y., and Sgrignuoli, F. (2019). Aperiodic photonics of elliptic curves. *Crystals*, 9:482.
- Dalichaouch, R., Armstrong, J. P., Schultz, S., Platzman, P. M., and McCall, S. L. (1991). Microwave localization by two-dimensional random scattering. *Nature*, 354(6348):53–55.
- Edagawa, K., Kanoko, S., and Notomi, M. (2008). Photonic amorphous diamond structure with a 3d photonic band gap. *Phys. Rev. Lett.*, 100:013901.
- Fabry, C. and Perot, A. (1899). Theorie et applications d’une nouvelle methode de spectroscopie interferentielle. *Ann. Chim. Phys.*, 16(7).
- Facchinetti, G., Jenkins, S. D., and Ruostekoski, J. (2016). Storing light with subradiant correlations in arrays of atoms. *Phys. Rev. Lett.*, 117:243601.
- Feng, S., Kane, C., Lee, P. A., and Stone, A. D. (1988). Correlations and fluctuations of coherent wave transmission through disordered media. *Phys. Rev. Lett.*, 61:834–837.
- Foldy, L. L. (1945). The multiple scattering of waves. i. general theory of isotropic scattering by randomly distributed scatterers. *Phys. Rev.*, 67(3-4):107.
- Fraden, S. and Maret, G. (1990). Multiple light scattering from concentrated, interacting suspensions. *Phys. Rev. Lett.*, 65:512–515.

- Froufe-Pérez, L. S., Engel, M., Damasceno, P. F., Muller, N., Haberko, J., Glotzer, S. C., and Scheffold, F. (2016). Role of short-range order and hyperuniformity in the formation of band gaps in disordered photonic materials. *Phys. Rev. Lett.*, 117:053902.
- Froufe-Pérez, L. S., Engel, M., Sáenz, J. J., and Scheffold, F. (2017). Band gap formation and anderson localization in disordered photonic materials with structural correlations. *Proc. Natl. Acad. Sci. U.S.A.*, 114(36):9570–9574.
- Gaspard, D. and Sparenberg, J.-M. (2021). Resonance distribution in the quantum random lorentz gas. arXiv:2111.04410.
- Ge, L., Chong, Y. D., and Stone, A. D. (2010). Steady-state ab initio laser theory: Generalizations and analytic results. *Phys. Rev. A*, 82:063824.
- Ghosh, S., Cherroret, N., Grémaud, B., Miniatura, C., and Delande, D. (2014). Coherent forward scattering in two-dimensional disordered systems. *Phys. Rev. A*, 90(6):063602.
- Goetschy, A. (2011). *Light in disordered atomic systems: Euclidean matrix theory of random lasing*. PhD thesis. J. Fourier University–Grenoble 1, France.
- Goetschy, A. and Skipetrov, S. (2011a). Non-hermitian euclidean random matrix theory. *Phys. Rev. E*, 84:011150.
- Goetschy, A. and Skipetrov, S. E. (2011b). Euclidean matrix theory of random lasing in a cloud of cold atoms. *Europhys. Lett.*, 96:34005.
- Goetschy, A. and Skipetrov, S. E. (2013). Euclidean random matrices and their applications in physics. arXiv:1303.2880.
- Guerin, W. and Kaiser, R. (2017). Population of collective modes in light scattering by many atoms. *Phys. Rev. A*, 95(5):053865.
- Haberko, J., Froufe-Pérez, L. S., and Scheffold, F. (2020). Transition from light diffusion to localization in three-dimensional amorphous dielectric networks near the band edge. *Nat. Commun.*, 11(1):4867.
- Hainaut, C., Manai, I., Clément, J.-F., Garreau, J. C., Szriftgiser, P., Lemarié, G., Cherroret, N., Delande, D., and Chicireanu, R. (2018). Controlling symmetry and localization with an artificial gauge field in a disordered quantum system. *Nat. Commun.*, 9(1):1382.
- Hasan, S. B., Mosk, A. P., Vos, W. L., and Lagendijk, A. (2018). Finite-size scaling of the density of states in photonic band gap crystals. *Phys. Rev. Lett.*, 120:237402.
- Huxley, M. N. (2003). Exponential sums and lattice points iii. *Proc. London Math. Soc.*, (3):591–609.
- Huygens, C., Fresnel, A. J., and Young, T. (1900). *Wave Theory of Light, Memoirs by Huygens, Young and Fresnel*. Cincinnati American Book Company, New York.
- Imagawa, S., Edagawa, K., Morita, K., Niino, T., Kagawa, Y., and Notomi, M. (2010). Photonic band-gap formation, light diffusion, and localization in photonic amorphous diamond structures. *Phys. Rev. B*, 82:115116.
- Ioffe, A. F. and Regel, A. R. (1960). Non-crystalline, amorphous and liquid electronic semiconductors. *Prog. Semicond.*, 4:237–291.
- Ishimaru, A. (1985). *The Radiative Transfer Approach in Electromagnetic Imaging*. Series C: Mathematical and Physical Sciences. Springer.

- Jackson, J. (1999). *Classical Electrodynamics*. Wiley (New York), New York, NY, 3rd ed. edition.
- Jacqmin, T., Carusotto, I., Sagnes, I., Abbarchi, M., Solnyshkov, D. D., Malpuech, G., Galopin, E., Lemaître, A., Bloch, J., and Amo, A. (2014). Direct observation of dirac cones and a flatband in a honeycomb lattice for polaritons. *Phys. Rev. Lett.*, 112:116402.
- Jacucci, G., Vignolini, S., and Schertel, L. (2020). The limitations of extending nature’s color palette in correlated, disordered systems. *Proc. Natl. Acad. Sci. U.S.A.*, 117(38):23345–23349.
- Jiao, Y., Lau, T., Hatzikirou, H., Meyer-Hermann, M., Corbo, J. C., and Torquato, S. (2014). Avian photoreceptor patterns represent a disordered hyperuniform solution to a multiscale packing problem. *Phys. Rev. E*, 89:022721.
- Jin, C., Meng, X., Cheng, B., Li, Z., and Zhang, D. (2001). Photonic gap in amorphous photonic materials. *Phys. Rev. B*, 63:195107.
- Joannopoulos, J., Johnson, S., Winn, J., and Meade, R. (2008). *Photonic Crystals: Molding the Flow of Light (Second Edition)*. Princeton University Press.
- John, S. (1984). Electromagnetic absorption in a disordered medium near a photon mobility edge. *Phys. Rev. Lett.*, 53:2169–2172.
- John, S. (1987). Strong localization of photons in certain disordered dielectric superlattices. *Phys. Rev. Lett.*, 58(23):2486.
- Karpiuk, T., Cherroret, N., Lee, K. L., Grémaud, B., Müller, C. A., and Miniatura, C. (2012). Coherent forward scattering peak induced by anderson localization. *Phys. Rev. Lett.*, 109:190601.
- Katz, O., Heidmann, P., Fink, M., and Gigan, S. (2014). Non-invasive single-shot imaging through scattering layers and around corners via speckle correlations. *Nat. Photonics*, 8(10).
- Kirkwood, J. G. (1936). On the theory of dielectric polarization. *J. Chem. Phys.*, 4(9):1442–1459.
- Klatt, M. A., Steinhardt, P. J., and Torquato, S. (2021). Gap sensitivity reveals universal behaviors in optimized photonic crystal and disordered networks. *Phys. Rev. Lett.*, 127:037401.
- Klugkist, J. A., Mostovoy, M., and Knoester, J. (2006). Mode softening, ferroelectric transition, and tunable photonic band structures in a point-dipole crystal. *Phys. Rev. Lett.*, 96(16):163903.
- Kwong, C. C., Wilkowski, D., Delande, D., and Pierrat, R. (2019). Coherent light propagation through cold atomic clouds beyond the independent scattering approximation. *Phys. Rev. A*, 99(4):043806.
- Labeyrie, G., de Tomasi, F., Bernard, J.-C., Müller, C. A., Miniatura, C., and Kaiser, R. (1999). Coherent backscattering of light by cold atoms. *Phys. Rev. Lett.*, 83:5266–5269.
- Legendijk, A. and van Tiggelen, B. A. (1996). Resonant multiple scattering of light. *Phys. Rep.*, 270(3):143–215.
- Laurent, D., Legrand, O., Sebbah, P., Vanneste, C., and Mortessagne, F. (2007a). Localized modes in a finite-size open disordered microwave cavity. *Phys. Rev. Lett.*, 99(25):253902.

- Laurent, D., Legrand, O., Sebbah, P., Vanneste, C., and Mortessagne, F. (2007b). Localized modes in a finite-size open disordered microwave cavity. *Phys. Rev. Lett.*, 99:253902.
- Lax, M. (1951). Multiple scattering of waves. *Rev. Mod. Phys.*, 23(4):287.
- Lax, M. (1952). Multiple scattering of waves. ii. the effective field in dense systems. *Phys. Rev.*, 85(4):622.
- Lehmberg, R. H. (1970). Radiation from an  $n$ -atom system. i. general formalism. *Phys. Rev. A*, 2:883–888.
- Lemarié, G., Grémaud, B., and Delande, D. (2009). Universality of the anderson transition with the quasiperiodic kicked rotor. *Europhys. Lett.*, 87(3):37007.
- Leseur, O. (2016). *Diffusion, localisation et absorption de lumière en milieux désordonnés. Impact des corrélations spatiales du désordre. PhD thesis*. P. and M. Curie University–Paris VI, France.
- Leseur, O., Pierrat, R., and Carminati, R. (2016). High-density hyperuniform materials can be transparent. *Optica*, 3(7):763–767.
- Liew, S. F., Noh, H., Trevino, J., Negro, L. D., and Cao, H. (2011). Localized photonic band edge modes and orbital angular momenta of light in a golden-angle spiral. *Opt. Express*, 19(24):23631–23642.
- Lippmann, B. A. and Schwinger, J. (1950). Variational principles for scattering processes. i. *Phys. Rev.*, 79:469–480.
- Lorentz, H. A. (1880). Ueber die refractionsconstante. *Ann. Phys.*, 245(4):641–665.
- Lorenz, L. (1869). Ueber die beziehung zwischen der fortpflanzungsgeschwindigkeit des lichtetes und der körperdichte. *Ann. Phys.*, 247(9):70–103.
- Man, W., Florescu, M., Matsuyama, K., Yadak, P., Nahal, G., Hashemizad, S., Williamson, E., Steinhardt, P., Torquato, S., and Chaikin, P. (2013). Photonic band gap in isotropic hyperuniform disordered solids with low dielectric contrast. *Opt. Express*, 21(17):19972–19981.
- Maurice, D. M. (1957). The structure and transparency of the cornea. *J. Physiol.*, 136(2):263–286.
- Maxwell Garnett, J. (1904). Xii. colours in metal glasses and in metallic films. *Philosophical Transactions of the Royal Society of London. Series A, Containing Papers of a Mathematical or Physical Character*, 203(359-371):385–420.
- Mayer, A., Balasubramanian, V., Mora, T., and Walczak, A. M. (2015). How a well-adapted immune system is organized. *Proc. Natl. Acad. Sci. U.S.A.*, 112(19):5950–5955.
- Mehta, M. L. (2004). *Random matrices*. Pure Appl. Math. 142. Academic Press, 3rd ed edition.
- Mello, P. A., Akkermans, E., and Shapiro, B. (1988). Macroscopic approach to correlations in the electronic transmission and reflection from disordered conductors. *Phys. Rev. Lett.*, 61:459–462.
- Michaelis de Vasconcellos, S., Calvar, A., Dousse, A., Suffczyński, J., Dupuis, N., Lemaître, A., Sagnes, I., Bloch, J., Voisin, P., and Senellart, P. (2011). Spatial, spectral, and polarization properties of coupled micropillar cavities. *Appl. Phys. Lett.*, 99(10):101103.



- Mie, G. (1908). Beiträge zur optik trüber medien, speziell kolloidaler metallösungen. *Ann. Phys.*, 303(3):377–445.
- Mirlin, A. D. (2000). Statistics of energy levels and eigenfunctions in disordered systems. *Phys. Rep.*, 326(5):259–382.
- Miyazaki, H., Hase, M., Miyazaki, H. T., Kurokawa, Y., and Shinya, N. (2003). Photonic material for designing arbitrarily shaped waveguides in two dimensions. *Phys. Rev. B*, 67:235109.
- Monsarrat, R. and Stone, A. D. (2016). Salt method applied to high quality factor cavities. unpublished.
- Mosk, A. P., Lagendijk, A., Lerosey, G., and Fink, M. (2012). Controlling waves in space and time for imaging and focusing in complex media. *Nat. Photonics*, 6(5):283–292.
- Muller, N., Haberko, J., Marichy, C., and Scheffold, F. (2017). Photonic hyperuniform networks obtained by silicon double inversion of polymer templates. *Optica*, 4(3):361–366.
- Máximo, C. E., Moreira, N. A., Kaiser, R., and Bachelard, R. (2019). Anderson localization of light in dimension  $d - 1$ . *Phys. Rev. A*, 100(6):063845. arXiv: 1909.12269.
- Máximo, C. E., Piovella, N., Courteille, P. W., Kaiser, R., and Bachelard, R. (2015). Spatial and temporal localization of light in two dimensions. *Phys. Rev. A*, 92(6):062702.
- Müller, C. A. and Delande, D. (2016). Disorder and interference: localization phenomena. *arXiv:1005.0915 [cond-mat, physics:quant-ph]*. arXiv: 1005.0915 version: 3.
- Nieuwenhuizen, T. M., Burin, A. L., Kagan, Y., and Shlyapnikov, G. V. (1994). Light propagation in a solid with resonant atoms at random positions. *Phys. Lett. A*, 184(4):360–365.
- Novotny, L. and Hecht, B. (2012). *Principles of Nano-Optics*. Cambridge University Press, 2 edition.
- Percus, J. K. and Yevick, G. J. (1958). Analysis of classical statistical mechanics by means of collective coordinates. *Phys. Rev.*, 110:1–13.
- Percel, J., Borregaard, J., Chang, D. E., Pichler, H., Yelin, S. F., Zoller, P., and Lukin, M. D. (2017). Photonic band structure of two-dimensional atomic lattices. *Phys. Rev. A*, 96:063801.
- Philip J., C. and Francis C., E. (1954). Distance to nearest neighbor as a measure of spatial relationships in populations. *Ecology*, 35(4):445–453.
- Pine, D. J., Weitz, D. A., Chaikin, P. M., and Herbolzheimer, E. (1988). Diffusing wave spectroscopy. *Phys. Rev. Lett.*, 60:1134–1137.
- Pnini, R. and Shapiro, B. (1989). Fluctuations in transmission of waves through disordered slabs. *Phys. Rev. B*, 39:6986–6994.
- Prum, R. O. and Torres, R. H. (2004). Structural colouration of mammalian skin: convergent evolution of coherently scattering dermal collagen arrays. *J. Exp. Biol.*, 207(12):2157–2172.
- Puyo, L., Paques, M., Fink, M., Sahel, J.-A., and Atlan, M. (2019). Choroidal vasculature imaging with laser doppler holography. *Biomed. Opt. Express*, 10(2):995–1012.

- Rayleigh, L. (1899). Xxxiv. on the transmission of light through an atmosphere containing small particles in suspension, and on the origin of the blue of the sky. *Lond. Edinb. Dubl. Phil. Mag.*, 47(287):375–384.
- Rechtsman, M., Szameit, A., Dreisow, F., Heinrich, M., Keil, R., Nolte, S., and Segev, M. (2011). Amorphous photonic lattices: Band gaps, effective mass, and suppressed transport. *Phys. Rev. Lett.*, 106:193904.
- Rockstuhl, C., Peschel, U., and Lederer, F. (2006). Cassociatedelation between single-cylinder properties and bandgap formation in photonic structures. *Opt. Lett.*, 31(11):1741–1743.
- Rohfritsch, A., Conoir, J.-M., Valier-Brasier, T., and Marchiano, R. (2020). Impact of particle size and multiple scattering on the propagation of waves in stealthy-hyperuniform media. *Phys. Rev. E*, 102:053001.
- Rojas-Ochoa, L. F., Mendez-Alcaraz, J. M., Sáenz, J. J., Schurtenberger, P., and Scheffold, F. (2004). Photonic properties of strongly correlated colloidal liquids. *Phys. Rev. Lett.*, 93:073903.
- Rosny, J., Lerosey, G., and Fink, M. (2010). Theory of Electromagnetic Time-Reversal Mirrors. *IEEE Transactions on Antennas and Propagation*, 58:3139–3149.
- Russell, P. (2003). Photonic crystal fibers. *Science*, 299(5605):358–362.
- Salameh, C., Salviat, F., Bessot, E., Lama, M., Chassot, J.-M., Moulongui, E., Wang, Y., Robin, M., Bardouil, A., Selmane, M., Artzner, F., Marcellan, A., Sanchez, C., Giraud-Guille, M.-M., Faustini, M., Carminati, R., and Nassif, N. (2020). Origin of transparency in scattering biomimetic collagen materials. *Proc. Natl. Acad. Sci. U.S.A.*, 117(22):11947–11953.
- Saranathan, V., Forster, J. D., Noh, H., Liew, S.-F., Mochrie, S. G. J., Cao, H., Dufresne, E. R., and Prum, R. O. (2012). Structure and optical function of amorphous photonic nanostructures from avian feather barbs: a comparative small angle X-ray scattering (SAXS) analysis of 230 bird species. *J. R. Soc. Interface*, 9(75):2563–2580.
- Scheffold, F., Lenke, R., Tweer, R., and Maret, G. (1999). Localization or classical diffusion of light? *Nature*, 398(6724):206–207.
- Sellers, S. R., Man, W., Sahba, S., and Florescu, M. (2017). Local self-uniformity in photonic networks. *Nat. Commun.*, 8(1):14439.
- Sgrignuoli, F. and Dal Negro, L. (2021). Hyperuniformity and wave localization in pinwheel scattering arrays. *Phys. Rev. B*, 103:224202.
- Shapiro, B. (1986). Large intensity fluctuations for wave propagation in random media. *Phys. Rev. Lett.*, 57:2168–2171.
- Sheng, P. (1990). *Scattering and Localization of Classical Waves in Random Media*. WORLD SCIENTIFIC.
- Sheng, P. (2006). *Introduction to Wave Scattering, Localization and Mesoscopic Phenomena (Second Edition)*. Springer.
- Skipetrov, S. and Sokolov, I. (2015). Magnetic-field-driven localization of light in a cold-atom gas. *Phys. Rev. Lett.*, 114(5):053902.
- Skipetrov, S. E. (2016). Finite-size scaling analysis of localization transition for scalar waves in a three-dimensional ensemble of resonant point scatterers. *Phys. Rev. B*, 94:064202.

- Skipetrov, S. E. (2020). Localization of light in a three-dimensional disordered crystal of atoms. *Phys. Rev. B*, 102:134206.
- Skipetrov, S. E. and Beltukov, Y. M. (2018). Anderson transition for elastic waves in three dimensions. *Phys. Rev. B*, 98(6):064206.
- Skipetrov, S. E. and Goetschy, A. (2011). Euclidean random matrices for waves in random media. *J. Phys. A*, 44:065102.
- Skipetrov, S. E. and Page, J. H. (2016). Red light for anderson localization. *New J. Phys.*, 18(2):021001.
- Skipetrov, S. E., Peuser, J., Cerbino, R., Zakharov, P., Weber, B., and Scheffold, F. (2010). Noise in laser speckle correlation and imaging techniques. *Opt. Express*, 18(14):14519–14534. Publisher: Optical Society of America.
- Skipetrov, S. E. and Sokolov, I. M. (2014). Absence of anderson localization of light in a random ensemble of point scatterers. *Phys. Rev. Lett.*, 112:023905.
- Skipetrov, S. E. and van Tiggelen, B. A. (2004). Dynamics of weakly localized waves. *Phys. Rev. Lett.*, 92:113901.
- Skipetrov, S. E. and van Tiggelen, B. A. (2006). Dynamics of Anderson Localization in Open 3D Media. *Phys. Rev. Letters*, 96(4):043902. Publisher: American Physical Society.
- Slevin, K. and Ohtsuki, T. (1999). Corrections to scaling at the anderson transition. *Phys. Rev. Lett.*, 82:382–385.
- Stavenga, D. G., Tinbergen, J., Leertouwer, H. L., and Wilts, B. D. (2011). Kingfisher feathers – colouration by pigments, spongy nanostructures and thin films. *J. Exp. Biol.*, 214(23):3960–3967.
- Thorpe, M. F. and Weaire, D. (1971). Electronic density of states of amorphous si and ge. *Phys. Rev. Lett.*, 27:1581–1584.
- Thouless, D. J. (1974). Electrons in disordered systems and the theory of localization. *Phys. Rep.*, 13(3):93–142.
- Torquato, S. (2018). Hyperuniform states of matter. *Phys. Rep.*, 745:1–95.
- Torquato, S. and Kim, J. (2021). Nonlocal effective electromagnetic wave characteristics of composite media: Beyond the quasistatic regime. *Phys. Rev. X*, 11:021002.
- Torquato, S., Kim, J., and Klatt, M. A. (2021). Local number fluctuations in hyperuniform and nonhyperuniform systems: Higher-order moments and distribution functions. *Phys. Rev. X*, 11:021028.
- Torquato, S. and Stillinger, F. H. (2003). Local density fluctuations, hyperuniformity, and order metrics. *Phys. Rev. E*, 68:041113.
- Torquato, S., Uche, O., and Stillinger, F. (2006). Random sequential addition of hard spheres in high euclidean dimensions. *Phys. Rev. E*, 74:061308.
- Tsang, L. and Ishimaru, A. (1984). Backscattering enhancement of random discrete scatterers. *J. Opt. Soc. Am. A*, 1(8):836–839.
- Van Albada, M. P. and Lagendijk, A. (1985). Observation of weak localization of light in a random medium. *Phys. Rev. Lett.*, 55:2692–2695.

- 
- van Coevorden, D. V., Sprik, R., Tip, A., and Lagendijk, A. (1996). Photonic band structure of atomic lattices. *Phys. Rev. Lett.*, 77:2412–2415.
- van Tiggelen, B. A. and Lagendijk, A. (1994). Resonantly induced dipole-dipole interactions in the diffusion of scalar waves. *Phys. Rev. B*, 50:16729–16732.
- van Tiggelen, B. A. and Skipetrov, S. E. (2021). Longitudinal modes in diffusion and localization of light. *Phys. Rev. B*, 103:174204.
- Vollhardt, D. and Wölfle, P. (1980a). Anderson localization in  $d \sim 2$  dimensions: A self-consistent diagrammatic theory. *Phys. Rev. Lett.*, 45:842–846.
- Vollhardt, D. and Wölfle, P. (1980b). Diagrammatic, self-consistent treatment of the anderson localization problem in  $d \leq 2$  dimensions. *Phys. Rev. B*, 22:4666–4679.
- Vollhardt, D. and Wölfle, P. (1982). Scaling equations from a self-consistent theory of anderson localization. *Phys. Rev. Lett.*, 48:699–702.
- Vynck, K., Burrelli, M., Riboli, F., and Wiersma, D. S. (2012). Photon management in two-dimensional disordered media. *Nat. Mater.*, 11(12):1017–1022.
- Vynck, K., Pierrat, R., and Carminati, R. (2014). Polarization and spatial coherence of electromagnetic waves in uncorrelated disordered media. *Phys. Rev. A*, 89:013842.
- Vynck, K., Pierrat, R., and Carminati, R. (2016). Multiple scattering of polarized light in disordered media exhibiting short-range structural correlations. *Phys. Rev. A*, 94:033851.
- Vynck, K., Pierrat, R., Carminati, R., Froufe-Pérez, L. S., Scheffold, F., Sapienza, R., Vignolini, S., and Sáenz, J. J. (2021). Light in correlated disordered media. arXiv:2106.13892.
- Wan, D. and Glotzer, S. C. (2021). Unexpected dependence of photonic band gap size on randomness in self-assembled colloidal crystals. *Phys. Rev. Lett.*, 126:208002.
- Weaire, D. (1971). Existence of a gap in the electronic density of states of a tetrahedrally bonded solid of arbitrary structure. *Phys. Rev. Lett.*, 26:1541–1543.
- Wiersma, D. S., Bartolini, P., Lagendijk, A., and Righini, R. (1997). Localization of light in a disordered medium. *Nature*, 390(6661):671–673.
- Wolf, P.-E. and Maret, G. (1985). Weak localization and coherent backscattering of photons in disordered media. *Phys. Rev. Lett.*, 55:2696–2699.
- Wölfle, P. and Vollhardt, D. (2010). Self-consistent theory of anderson localization: General formalism and applications. *Int. J. Mod. Phys. B*, 24(12n13):1526–1554.
- Xiong, L., Forsythe, C., Jung, M., McLeod, A. S., Sunku, S. S., Shao, Y. M., Ni, G. X., Sternbach, A. J., Liu, S., Edgar, J. H., Mele, E. J., Fogler, M. M., Shvets, G., Dean, C. R., and Basov, D. N. (2019). Photonic crystal for graphene plasmons. *Nat. Commun.*, 10(1):4780.
- Yablonovitch, E. (1987). Inhibited spontaneous emission in solid-state physics and electronics. *Phys. Rev. Lett.*, 58(20):2059.
- Yu, S., Qiu, C.-W., Chong, Y., Torquato, S., and Park, N. (2021). Engineered disorder in photonics. *Nat. Rev. Mater.*, 6(3):226–243. Number: 3 Publisher: Nature Publishing Group.

- Yvon, J. (1937). *Recherches sur la théorie cinétique des liquides: fluctuations en densité et diffusion de la lumière*. Hermann et cie, (Paris).
- Zdetsis, A. D., Soukoulis, C. M., Economou, E. N., and Grest, G. S. (1985). Localization in two- and three-dimensional systems away from the band center. *Phys. Rev. B*, 32:7811–7816.
- Zheng, Y., Liu, L., Nan, H., Shen, Z. X., Zhang, G., Chen, D., He, L., Xu, W., Chen, M., Jiao, Y., and Zhuang, H. (2020). Disordered hyperuniformity in two-dimensional amorphous silica. *Sci. Adv.*, 6(16).



## RÉSUMÉ

---

Cette thèse, principalement théorique et numérique, s'intéresse à la propagation d'ondes lumineuses dans des milieux désordonnés présentant différents degrés de corrélation structurale. Le développement récent du concept d'hyperuniformité comme une classe de systèmes corrélés dont le degré d'ordre peut être choisi arbitrairement, permet de sonder continûment la transition entre systèmes complètement désordonnés et cristaux photoniques. Dans ce cadre, nous nous sommes intéressés à des ensembles de particules résonnantes couplées par le champ électromagnétique et agencées sous forme de systèmes hyperuniformes 2D ou 3D ouverts sur leur environnement. Dans un premier temps, nous avons réalisé une analyse systématique des propriétés spectrales et spatiales de ces systèmes pour une large gamme de densités, de fréquences et de taux de corrélation. Nous avons en particulier observé que des corrélations spatiales prononcées permettent d'induire une forte localisation d'ondes dans des systèmes 2D peu denses avec couplage vectoriel. Cet effet est radicalement différent de la localisation d'ondes scalaires qui se produit uniquement à haute densité et quel que soit le degré de corrélation spatiale. De plus, l'observation d'états localisés coïncide avec l'ouverture d'un pseudo-gap dans la densité d'états des excitations collectives, également contrôlé par le degré d'ordre partiel. Dans un deuxième temps de cette thèse, nous avons modélisé l'impact des corrélations sur la répartition spectrale des modes collectifs au moyen de deux approches théoriques complémentaires. La première est une approche mésoscopique basée sur la prise en compte de la diffusion récurrente dans l'opérateur *énergie propre* pilotant la densité d'états. La seconde approche est basée sur l'étude de cristaux photoniques résonnants. Nous montrons que les ensembles désordonnés fortement corrélés conservent les propriétés photoniques d'une distribution de réseaux cristallins ayant les mêmes propriétés statistiques. Dans un troisième temps, nous démontrons à partir d'une théorie auto-consistante de la localisation adaptée aux systèmes résonnants corrélés, le lien explicite entre longueur de localisation et densité d'états dans les systèmes 2D et 3D. Cette approche explique notamment l'observation d'états localisés par la diminution de leur longueur de localisation suite à une forte déplétion de la densité d'états à la fois en 2D, mais aussi marginalement en 3D. Enfin, la thèse s'ouvre sur la modélisation et la mise en place d'une expérience de propagation de micro-ondes dans un ensemble désordonné de céramiques résonnantes en géométrie de guide d'ondes qui permettrait de confirmer expérimentalement nos prédictions théoriques dans le cas bidimensionnel.

## MOTS CLÉS

---

Propagation d'ondes, milieux désordonnés corrélés, hyperuniformité, cristaux photoniques, structure de bandes, densité d'états, localisation d'Anderson

## ABSTRACT

---

This thesis, mainly theoretical and numerical, focuses on the propagation of light waves in disordered media with different degrees of structural correlation. The recent development of the concept of hyperuniformity as a class of correlated systems whose degree of order can be chosen arbitrarily, allows to continuously probe the transition between completely disordered systems and photonic crystals. In this framework, we are interested in ensembles of resonant particles coupled by the electromagnetic field and arranged as 2D or 3D hyperuniform systems open on their environment. First, we performed a systematic analysis of the spectral and spatial properties of these systems for a wide range of densities, frequencies and correlation ratios. In particular, we have observed that strong spatial correlations can induce strong wave localization in low density 2D systems with vector coupling. This effect is radically different from scalar wave localization which only occurs at high density and regardless of the degree of spatial correlation. Moreover, the observation of localized states coincides with the opening of a pseudo-gap in the density of states of collective excitations, also controlled by the degree of partial order. In a second step of this thesis, we have modelled the impact of correlations on the spectral distribution of collective modes by means of two complementary theoretical approaches. The first one is a mesoscopic approach based on the consideration of the recurrent scattering in the *self-energy* operator driving the density of states. The second approach is based on the study of resonant photonic crystals. We show that strongly correlated disordered ensembles preserve the photonic properties of a distribution of crystal lattices with the same statistical properties. In a third step, we demonstrate from a self-consistent localization theory adapted to correlated resonant systems, the explicit link between localization length and density of states in 2D and 3D systems. This approach explains in particular the observation of localized states by the decrease of their localization length following a strong depletion of the density of states both in 2D, but also marginally in 3D. Finally, the thesis opens on the modelling and the implementation of a microwave propagation experiment in a disordered set of resonant ceramics in waveguide geometry that would allow to experimentally confirm our theoretical predictions in the two-dimensional case.

## KEYWORDS

---

Wave propagation, correlated disordered media, hyperuniformity, photonic crystals, band structure, density of states, Anderson localization